TESIS DE LA UNIVERSIDAD DE ZARAGOZA
2022
72

Jorge Alda Gallo

A Glance into Flavour Physics with Effective Field Theories and Machine Learning

Director/es
Peñaranda Rivas, Siannah

ISSN 2254-7606

Prensas de la Universidad
Universidad Zaragoza

ISSN 2254-7606

Universidad Zaragoza
1542

Tesis Doctoral

A GLANCE INTO FLAVOUR PHYSICS WITH EFFECTIVE FIELD THEORIES AND MACHINE LEARNING

Autor

Jorge Alda Gallo

Director/es

Peñaranda Rivas, Siannah

UNIVERSIDAD DE ZARAGOZA
Escuela de Doctorado

sica

2022

Universidad Zaragoza

Departamento de Física Teórica
Centro de Astropartículas y Física de Altas Energías
Facultad de Ciencias, Universidad de Zaragoza

A Glance into Flavour Physics with Effective Field Theories and Machine Learning

Jorge Alda Gallo

Ph.D. Thesis opting to International Mention.
Supervisor:

Dra. Siannah Peñaranda Rivas

February 2022

Contents

Agradecimientos

I watch the ripples change their size
but never leave the stream of warm impermanence.

David Bowie

La ciencia es una aventura colectiva y colaborativa. Quisiera aprovechar estas líneas para agradecer a todo el mundo que ha contribuido en mayor o menor medida para que esta tesis sea una realidad.

En primer lugar me gustaría agradecer enormemente a mi directora, Siannah, por tu esfuerzo, dedicación y confianza. Contigo he aprendido mucho acerca de física, pero más aún sobre todo lo necesario para desarrollar una carrera de investigación. Ha sido un gran placer trabajar contigo, y espero seguir haciéndolo durante mucho tiempo más.

Igualmente ha sido un placer colaborar en gran parte de mi investigación con Jaume Guasch, siempre con una solución para cualquier problema que pudiera surgir. Thanks to this thesis I got to know and work with Stefano Rigolin and Alfredo Guerrera, who introduced me into the fascinating world of axions. Grazie di tutto!

I would want to thank Pepe Cortés, Paride Paradisi, Maurizio Giannotti and Javier Redondo for very interesting discussions, that have shaped parts of this thesis. Also to David Straub and Peter Stangl for their assistance with the codes of `flavio` and `smelli`.

Por supuesto no me puedo olvidar del Departamento de Físcica Teórica, que ha sido y siempre será mi segunda casa. Tampoco del CAPA, un gran proyecto con un futuro brillante por delante, y me siento muy orgulloso de haber formado parte de sus inicios. And a very special thanks to Università degli Studi di Padova and INFN for welcoming me in these complicated times of masks and green passes.

Finalmente, quiero dedicarle esta tesis a mis padres y a mi hermana. Me habéis dado la fuerza para seguir adelante incluso en los momentos más difíciles, no podría hacer hecho nada de esto sin vosotros. Gracias por vuestro apoyo y vuestra ayuda, pero más que nada, por vuestra enorme paciencia. Sabéis que os quiero más que a nada o nadie en este Universo.

Esta tesis ha sido realizada gracias al contrato predoctoral para la formación de personal investigador concedido por el Gobierno de Aragón por resolución de 19 de Julio de 2017, y cofinanciado por el Fondo Social Europeo. Asimismo, la investigación que aquí se presenta también ha sido parcialmente financiada por los proyectos de investigación FPA2015-65745-P (Ministerio de Economía y Competitividad/FEDER), PGC2018-095328-B-I00 (FEDER/Agencia Estatal de Investigación) y por el Grupo Teórico de Altas Energías, referencia DGIID-DGA No. 2015-E24/2. La estancia de investigación necesaria para la Mención Internacional ha sido realizada gracias al Programa Ibercaja-CAI de Estancias de Investigación, beca CB 5/21.

Summary

In the last years there has been a growing interest in the study of deviations from the predictions of the Standard Model of particle physics in the context of Flavour Physics. This dissertation is devoted to the study of these deviations, with special focus on those involving B mesons.

The interest on deviations from the Standard Model predictions is twofold: theoretical questions not yet solved and recent experimental measurements showing this kind of deviations. On the theoretical side, the Standard Model does not attemp to explain why the flavour structure is what we observe, with three generations of matter particles which only differ on their masses. On the experimental side, flavour is a remarkable hunting ground for hints of new physics, since many processes are affected by suppressions that could be lifted by new interactions, leading to clear experimental signatures. In this regard, the most important development is the number of precise flavour experimental measurements in tension with the Standard Model in the last few years. In our research we study two classes of these experimentally-interesting observables: the semileptonic decays of B mesons into K or K^* mesons and a pair of charged leptons through flavour-changing neutral currents, characterized by the $R_{K^{(*)}}$ ratios between the muonic and the electronic branching ratios; and the semileptonic decays of B mesons into D or D^* mesons, a charged lepton and a neutrino through flavour-changing charged currents, characterized by the $R_{D^{(*)}}$ ratios between the tauonic and the light branching ratios.

These anomalous experimental results have spurred numerous proposals for physics beyond the Standard Model. Effective Field Theories offer a model-independent way to analyze those New Physics effects. The idea is to integrate out the heavy fields appearing only in the internal lines of the Feynman diagrams, leaving a set of non-renormalizable interactions including just the light fields and their symmetries. We have used in this thesis the framework of Effective Field Theories, being able to obtain constraints on New Physics contributions to the Wilson coefficients of the effective Lagrangian from the experimental results.

Quantum corrections contained in the Renormalization Group have the effect of mixing the non-renormalizable interactions. As a consequence, the deviations from the Standard Model introduced through Effective Field Theories tend to propagate also to physical observables differents from the ones we are interested in. The solution is to determine the coefficients entering the Effective Field Theory through means of global fits including

observables from all affected sectors. The sheer number of observables involved makes mandatory the use of numerical calculations, and in the most extreme cases, even using Machine Learning tools such as regression trees and SHAP (SHAPley Additive exPlanation) values. We use for the first time in the flavour context a Montecarlo analysis to extract the confidence intervals and correlations between observables, showing that it constitutes a suitable strategy to use in this kind of analysis.

Although most of the dissertation deals with the framework of Effective Field Theories, we have also extrapolated our results to specific models of New Physics; in particular to leptoquarks, hypothetical particles that could turn quarks into leptons or vice-versa, and to W' and Z' bosons, hypothetical gauge mediators that could exhibit non-universal couplings to each fermion. We have also performed a more in-deep analysis of a model for Axion-Like Particles, pseudoscalars that could appear as pseudo-Nambu-Goldstone bosons for new global $U(1)$ symmetries. Unlike the traditional approaches, we have examined the case where the Axion-Like Particles have a non-trivial flavour structure in their couplings to quarks and leptons.

This dissertation is structured as follows:

- We start with a general introduction in Chapter 1 that motivates our work.

- In Chapter 2, the basics of the Standard Model are reviewed, with special focus on the flavour aspects of the different interactions, and the sources of suppression affecting flavour-changing processes. After that, the flavour observables which will be used in the rest of the dissertation will be presented. Finally, the experiments exploring B meson physics and the results that they have obtained are summarized.

- In Chapter 3, the model-independent approach of Effective Field Theories is presented. The traditional top-down is presented first, where one starts with a high energy theory and explicitly integrates out some heavy particles. Then the opposite approach is presented, bottom-up, where one starts with a low energy theory and extends it by adding all the compatible effective operators. Then, the intricacies of dealing with several Effective Field Theories are explained: matching between two theories defined at the same energy scale, and changing the energy scale with the Renormalization Group equations. Finally, the two theories that we will use are presented: Standard Model Effective Field Theory (SMEFT) containing all the Standard Model particles, and the Weak Effective Theory (WET) where the top quark and the W, Z and Higgs bosons have been also integrated out.

- In Chapter 4, some of the models of new physics are introduced: leptoquarks, new heavy gauge bosons and Axion-like particles. Finally we discuss the Minimal Flavour Violation *ansatz* that proposes a general structure for any New Physics affecting the flavour sector.

- Chapter 5 contains our first incursion in the analysis of New Physics violating Lepton Flavour Universality, by using fits in the framework of Effective Field Theories. We work in the WET with complex coefficients and consider relations between the operators motivated by models of leptoquarks and Z'. This first fit only includes a limited amount of observables related to $b \to s\mu^+\mu^-$ decays and ΔM_s. The inclusion of complex couplings provides a slightly improved global fit, and a marginally improved ΔM_s prediction.

- In Chapter 6, we work in the SMEFT framework, and consider several scenarios of effective operators including two left-handed $SU(2)_L$ quark doublets and lepton doublets. In this analysis we include a set of different scenarios in which the New Physics contributions to the Wilson coefficients are present in one, two or three of the Wilson coefficients at a time. For the global fits, we consider a large range of different physical observables, including electroweak and nuclear precision tests. We analyze the most descriptive scenario using a Hessian approximation. The scenario in which New Physics modifies three independent Wilson coefficients is the favoured one for the explanation of the tension between Standard Model predictions and B physics anomalies, but a specific, more restricted scenario can provide similar goodness of fit with a smaller set of free parameters. Finally, we discuss the impact of future measurements of electroweak precision tests from linear colliders on our results.

- In Chapter 7, we consider a different arrangement of SMEFT operators including two quarks and two leptons. The motivation is a new interaction affecting only the third generation particles, that are then rotated to the mass basis. We use the same set of physical observables for our fits than in the previous chapter. We found that, in this case, the Hessian approximation is no longer useful, and in consequence we need to use Machine Learning tools to analyze the scenarios. According to our results, the $R_{K^{(*)}}$ anomalies can be described as the interplay between tree-level and loop-level contributions to the effective operators, while the $R_{D^{(*)}}$ are purely tree-level phenomena, manifesting in an interesting correlation between $R_{D^{(*)}}$ and the semileptonic decays of B mesons into a kaon and a pair of neutrinos.

- In Chapter 8, we turn our attention to Axion-like particles. We study the leptonic decays of mesons into a lepton and a neutrino in search of hints of an invisible Axion-like particle present in the branching ratios or the differential distributions. We consider a generic flavour structure for the couplings of the Axion-like particle to quarks and leptons and we compare our results with the previous one. Our bounds for the couplings of ALPs to leptons are the most stringent to date.

- Finally, in Chapter 9, the main results of the thesis are collected and summarized.

The dissertation also includes several appendices. Appendix A collects the expressions for the differential observables for B meson decays in the WET. In Appendix B we comment on the computer codes used to calculate our results, both the public codes and the codes written *ad-hoc* for this thesis. Appendix C contains the predictions for the observables in Chapters 6 and 7.

Resumen

En los últimos años se ha dedicado especial atención a investigar algunas desviaciones con respecto a las predicciones del Modelo Estándar de la física de partículas en el contexto de la física del sabor. El objetivo de esta tesis es el estudio de estas desviaciones, haciendo especial énfasis en las desviaciones que involucran los mesones B.

El interés en las desviaciones con respecto a las predicciones del Modelo Estándar está fundamentado tanto en aspectos téoricos aún sin esclarecer como en medidas experimentales recientes que muestran tales desviaciones. Desde el punto de vista teórico, el Modelo Estándar no explica por qué la estructura del sabor es tal y como la observamos, con tres generaciones de partículas constituyentes de la materia que difieren entre sí solo en sus masas. Desde el punto de vista experimental, el sabor es un excepcional coto de caza de indicios de nueva física, ya que muchos procesos están suprimidos en el Modelo Estándar y la introducción de nuevas interacciones podría dar lugar a señales experimentales claras. En este respecto, es importante notar la proliferación en los últimos años de mediciones experimentales precisas en el ámbito del sabor en tensión con el Modelo Estándar. En esta tesis nos centramos en el estudio de dos clases de estos observables que muestran anomalías en la física de sabor: las desintegraciones semileptónicas de mesones B en mesones K o K^* y un par de leptones cargados, mediadas por corrientes neutras con cambio de sabor y caracterizadas por el cociente $R_{K^{(*)}}$ entre las razones de desintegración muónica y electrónica; y las desintegraciones semileptónicas de mesones B en mesones D o D^*, un leptón cargado y un neutrino, mediadas por corrientes cargadas con cambio de sabor y caracterizadas por el cociente $R_{D^{(*)}}$ entre las razones de desintegración tauónica y en fermiones ligeros.

La existencia de estas anomalías ha motivado numerosas propuestas de modelos de Nueva Física como candidatos para explicar tales desviaciones. Un análisis independiente de modelo requiere el uso de las Teorías de Campos Efectivas. En estas teorías se integran los campos cuánticos más pesados, que corresponden únicamente a las líneas internas de los diagramas de Feynman, dejando un conjunto de interacciones no-renormalizables que incluyen solo los campos ligeros y sus simetrías. En esta tesis hemos usado este marco teórico de las Teorías de Campos Efectivas, y hemos obtenido límites a las contribuciones de Nueva Física en los coeficientes de Wilson del Lagrangiano efectivo partiendo de resultados experimentales.

Las correcciones cuánticas contenidas en el Grupo de Renormalización tienen el efec-

to de mezclar las interacciones no-renormalizables. Como consecuencia, las desviaciones respecto del Modelo Estándar introducidas a través de las Teorías de Campos Efectivas suelen propagarse también a observables físicos diferentes de los que estamos estudiando. La solución a este problema es determinar los coeficientes de la Teoría de Campos Efectiva mediante un ajuste estadístico global que incluya observables de todos los sectores afectados. El gran número de observables que aparecen en estos análisis hace necesario el uso de cálculos numéricos, y en los casos más extremos es necesario utilizar algunas herramientas de "Machine Learning", como los árboles de regresión y los valores SHAP (del inglés *SHAPley Additive exPlanation*). En esta tesis utilizamos por primera vez en el marco de la física de sabor un análisis de Montecarlo para extraer los intervalos de confianza y las correlaciones entre observables, y demostramos que estas herramientas constituyen una estrategia útil y adecuada en este tipo de análisis.

Aunque la mayor parte de esta tesis se desarrolla dentro del marco teórico de las Teorías de Campos Efectivas, también hemos extendido nuestro análisis a modelos específicos de Nueva Física. Concretamente, a modelos de leptoquarks, partículas hipotéticas que podrían transformar quarks en leptones o viceversa, y a bosones W' y Z', bosones gauge hipotéticos que podrían exhibir acoplamientos no universales a cada fermión. Además, hemos hecho un análisis en más profundidad de un modelo de *partículas similares* a los Axiones –ALPs, del inglés *Axion Like Particles*–, partículas pseudoescalares que podrían aparecer como pseudo-bosones de Nambu-Goldstone de nuevas simetrías $U(1)$ globales. A diferencia de los enfoques tradicionales, hemos examinado el caso en el que los ALPs tienen una estructura de sabor no trivial en sus acoplamientos a quarks y leptones.

Esta tesis está organizada como sigue:

- El Capítulo 1 está destinado a una introducción general al tema de la tesis.
- En el Capítulo 2 se expone una vista general del Modelo Estándar, con un especial énfasis en los aspectos relacionados con el sabor de las distintas interacciones y en los orígenes de la supresión que afectan a los procesos con cambio de sabor. A continuación, se introducen los observables de sabor que serán usados a lo largo de la tesis. Finalmente se resumen los experimentos que exploran la física de los mesones B y los resultados que han obtenido.
- El Capítulo 3 se centra en el enfoque independiente de modelo ofrecido por las Teorías de Campos Efectivas. Primero presentamos la visión tradicional (de *arriba* a *abajo*), en la que se empieza con una teoría formulada a una alta escala de energía y se integran explícitamente las partículas pesadas. Continuamos presentando la visión opuesta (de *abajo* a *arriba*), en la que se empieza con una teoría a baja energía que se extiende añadiendo todos los operadores efectivos compatibles. Posteriormente, se explican los pormenores necesarios para tratar con las Teorías de Campos Efectivas: el procedimiento de "matching" entre dos teorías definidas en la misma

escala de energía, y el cambio de escala usando las ecuaciones del Grupo de Renormalización. Finalmente se presentan las dos teorías en que nos centramos en esta tesis: SMEFT –del inglés *Standard Model Effective Field Theory*– que contiene todas las partículas del Modelo Estándar, y WET –del inglés *Weak Effective Theory*– donde se integran el quark top y los bosones W, Z y Higgs.

- En el Capítulo 4 se introducen algunos de los modelos de nueva física: leptoquarks, nuevos bosones gauge pesados y partículas similares a los axiones. Finalmente discutimos la hipótesis de la Violación Mínima de Sabor, que propone una estructura general para cualquier propuesta de Nueva Física que afecte a la física del sabor.

- El Capítulo 5 contiene nuestra primera incursión en el análisis de Nueva Física que viole la Universalidad del Sabor Leptónico mediante el uso de ajustes estadísticos en el marco de las Teorías de Campos Efectivas. Trabajamos en la teoría WET con coeficientes complejos, y consideramos relaciones entre operadores motivadas por modelos de leptoquarks y Z'. Este primer ajuste estadístico solamente incluye un número limitado de observables relacionados con desintegraciones $b \to s\mu^+\mu^-$ y ΔM_s. La inclusión de coeficientes de Wilson complejos en el análisis proporciona un ajuste global ligeramente mejorado, no siendo tan favorable la predicción en el caso de ΔM_s.

- En el Capítulo 6, trabajamos en el marco de la teoría SMEFT, y consideramos varios escenarios de operadores efectivos que incluyen dos dobletes de $SU(2)_L$ de quarks y leptones levógiros. En este análisis proponemos diferentes escenarios en los cuales las contribuciones de Nueva Física a los coeficientes de Wilson están presentes en uno, dos o tres coeficientes simultáneamente. Para este ajuste estadístico global consideramos una gran variedad de observables físicos, incluyendo tests de precisión electrodébiles y nucleares. Analizamos el escenario más descriptivo usando una aproximación Hessiana. Los resultados muestran que un escenario en el que Nueva Física modifique tres coeficientes de Wilson simultáneamente es el escenario preferido para explicar las tensiones entre las predicciones del Modelo Estándar y las anomalías en la física de mesones B. Un escenario específico, más restringido, es capaz de proporcionar un ajuste similar con un menor número de parámetros libres. Finalmente, discutimos el impacto que tendrían en nuestros resultados las futuras mediciones de tests electrodébiles de precisión en los colisionadores lineales.

- En el Capítulo 7, consideramos una configuración diferente de los operadores SMEFT que contienen dos quarks y dos leptones. La motivación es considerar una nueva interacción que afecte solamente a las partículas de la tercera generación, antes de calcular la rotación a la base de masa. Usamos el mismo conjunto de observables en los ajustes estadísticos que en el capítulo previo. En este caso encontramos que

la aproximación Hessiana no es satisfactoria, y en consecuencia necesitamos usar herramientas de "Machine Learning". Según nuestros resultados, las anomalías en los cocientes $R_{K^{(*)}}$ necesitarían de contribuciones de Nueva Física a los operadores efectivos tanto a "nivel árbol" como a "nivel de un bucle", mientras que las anomalías en los cocientes $R_{D^{(*)}}$ precisarían solo de las correcciones a "nivel árbol", lo cual se manifiesta en una correlación entre las predicciones para $R_{D^{(*)}}$ y para las desintegraciones semileptónicas de un mesón B en un kaón y un par de neutrinos.

- En el Capítulo 8, nos centramos en las partículas similares a axiones, ALPs. Estudiamos las desintegraciones leptónicas de mesones en un leptón y un neutrino en busca de indicios de ALPs presentes en las razones de desintegración o en las distribuciones diferenciales. Consideramos una estructura de sabor genérica para los acoplamientos a quarks y leptones, y comparamos nuestros resultados con resultados previos en la literatura. Obtenemos los límites a los acoplamientos de ALPs a leptones más restrictivos publicados hasta el momento.

- Finalmente, en el Capítulo 9 se resumen los principales resultados de la tesis.

La tesis incluye además varios apéndices: En el Apéndice A están incluidas las expresiones para los observables diferenciales de las desintegraciones de mesones B en la teoría WET. En el Apéndice B se comentan los códigos informáticos empleados para calcular nuestros resultados, tanto los códigos públicos como los escritos *ad-hoc* para esta tesis. El Apéndice C contiene las predicciones de los observables en los Capítulos 6 y 7.

Part of the research presented in this dissertation has been published in the following articles:

- [1] J. Alda, J. Guasch, S. Peñaranda,
  Some Results on Lepton Flavour Universality Violations,
  Eur. Phys. J. C 79.7 (2019), p. 588, arXiv:1805.03636 [hep-ph].

- [2] J. Alda, J. Guasch, S. Peñaranda,
  Anomalies in B meson decays: A phenomenological approach,
  Eur. Phys. J. Plus 137 (2022), p. 217, arXiv: 2012.14799 [hep-ph].

- [3] J. Alda, J. Guasch, S. Peñaranda,
  Anomalies in B meson decays: Present status and future collider prospects, Contribution to the International Workshop on Future Linear Colliders 2021 (LCWS2021), C21-03-15.1, arXiv:2105.05095 [hep-ph].

- [4] J. Alda, J. Guasch, S. Peñaranda,
  Using Machine Learning techniques in phenomenological studies in flavour physics,
  arXiv:2109.07405 [hep-ph].

- [5] J. Alda, J. Guasch, S.Peñaranda,
  Exploring B-physics anomalies at colliders,
  Contribution to the European Physical Society conference on high energy physics 2021, PoS(EPS-HEP2021)494, arXiv:2110.12240 [hep-ph].

- [6] J. Alda, A. W. M. Guerrera, S. Peñaranda, S. Rigolin,
  Leptonic Meson Decays into invisible ALP,
  arXiv:2111.02536 [hep-ph].

Note that, in order to keep a consistent style throughout the thesis, some notations may have been altered with respect to the published versions.

Chapter 1

Introduction

Since the dawn of humankind, we have tried to find explanations for the world that surround us, using a series of theories, a term derived from the Greek θεωρία, originally meaning "looking at, observing". One of the earliest observations of humanity is that there are many materials with diverse properties. This led us to a question that has pressed thinkers, philosophers and scientists for millennia, that of the composition of matter. We have made huge advances in this topic, starting with simplistic theories like the four elements in the classical Greece, and culminating at the start of the twentieth century with the radical paradigm shift of the quantum theory. Once that the quantum nature of reality was established, the task was to find a unified description of the elemental particles and their interactions. This was accomplished by the Standard Model (SM) of particle physics, formulated in the decade of 1960s and passing its final experimental verification in 2012 with the discovery of the Higgs boson.

The SM is, by far, the most successful scientific theory in physics. It has been able to predict, with incredible precision, the observed phenomena from the early Universe to our everyday lives to collider events. Although the SM is in great shape, there are still some issues, both theoretical and experimental, that indicate that the SM can not be the ultimate theory.

The problem for us, particle physicists, is that there is not a single and clear thread to follow in the quest for that ultimate theory, in part due to the "unreasonable" success of the SM. If we expect that there is New Physics (NP) that will guide us to that ultimate goal, and that this NP is "around the corner", at the TeV energy scale, there are three possible strategies to follow.

The first one is pushing the energy frontier, achieving collisions with higher center-of-mass energies with the hopes of finding a resonance for a new elemental particle. The second strategy is to study the cosmic frontier, using the Universe as a laboratory to study ultra-relativistic cosmic particles.

The third, more subtle approach, is to push the intensity frontier, by increasing the number of events. This is done in order to explore rare processes and increase the precision, in the search for tiny deviations from the SM predictions. In a quantum theory, the

particles and interactions occurring at very high energies, even if not directly accessible, modify the dynamics at lower energies through virtual particles encoded in the internal lines of Feynman diagrams. The hope is, therefore, that improving the precision of our experimental measurements, we will be able to gain sensitivity to the quantum effects induced by new particles and interactions. This is precisely the main motivation for the research contained in this thesis dissertation.

Naturally, not every physical process is equally amenable to the intensity frontier. Flavour physics is an obvious candidate, with many rare processes where quantum effects might be comparable in magnitude to the SM predictions. Historically, flavour has been a very fruitful area for indirect discoveries, starting with the proposals of both the neutrino and the W boson to explain β decays, continuing with the discovery of CP violation in kaon decays anticipating the need for a third generation of fermions, or the suppression of $K_L \to \mu^+\mu^-$ decays compared to $K^+ \to \mu^+\bar{\nu}_\mu$ decays indicating the existence of the charm quark. We expect to continue the trend by examining the leptonic and semileptonic decays of B mesons, processes with branching ratios of less than one in a million.

In addition to know *where* to look for the hints of new physics, it is also essential to know *how* to look for them. Effective theories are the tool to extend in a systematic way a low-energy theory, in this case the SM, in order to characterize any possible deviation. The results are model-independent, meaning that they are valid regardless of the physics happening above the energy scale at which the effective theory is defined.

Once our attack plan has been laid out, let us get into action!

Chapter 2

Standard Model Flavour Physics

This chapter is devoted to the phenomenology of Flavour Physics within the SM of particle physics, which constitutes the foundation for the rest of the thesis. We start by examining the fields and interactions of the SM, and how do they relate to the flavour symmetry. This introduction to the SM will allow us to discuss some of its open questions, and realize that many of them are related to flavour. We then turn our attention to a class of processes that are very interesting to us, those that change the flavour of one quark. Some of the flavour-changing physical observables for the B mesons are presented, as well as their experimental determinations.

2.1 Standard Model and Flavour Symmetry

The SM is the quantum field theory that describes the elemental particles of matter and their interactions [7–9]. Matter is composed of fermions, which can be either quarks or leptons. The Higgs field is responsible for the generation of masses of the particles through the Electroweak Spontaneous Symmetry Breaking (EWSSB) mechanism [10, 11]. Interactions are mediated by gauge fields, eight massless gluons for the strong interactions, one massless photon for the electromagnetic interactions, and three massive bosons, $W^{\pm}$ and Z for the weak interaction. The photon, $W^{\pm}$ and Z are the result of the EWSSB for the massless electroweak W and B bosons. The Higgs boson was the last missing piece of the puzzle, until it was discovered in 2012 by the ATLAS [12] and CMS [13].

The SM is invariant under Poincaré symmetry and local $SU(3)_C \times SU(2)_L \times U(1)_Y$ gauge symmetry, where $SU(3)_C$ is the color symmetry of Quantum Chromodynamics (QCD) and $SU(2)_L \times U(1)_Y$ is the chiral electroweak symmetry. At energies below the electroweak scale, the Brout-Englert-Higgs mechanism causes the EWSSB, only remaining the electromagnetic gauge group $U(1)_{em}$. The SM is also invariant under the CPT transformation, the combination of a charge conjugation C, a parity transformation P and a time reversal T. The individual transformations C, P, and T and their pair-wise combinations such as Charge and Parity symmetry (CP), are not symmetries of the full SM. Lastly, the SM also has an accidental global symmetry $U(1)_B \times U(1)_e \times U(1)_\mu \times U(1)_\tau$ at the classical level that

leads to the conservation of the baryonic number B and the lepton flavour numbers L_e, L_μ and L_τ. At the quantum level, these global symmetries are not exact due to the chiral anomaly [14].

Fields in the SM are classified according to their representation of the Poincaré group, given by their spin, and the representation of the $SU(3)_C \times SU(2)_L \times U(1)_Y$ group [15–18]. Additionally, fermions come in three identical copies of the gauge representation called generations, and consequently each fermion has to be identified by one more label, which is its flavour. The three generations differ only by their mass and their flavour quantum numbers. Due to the chiral nature of the electroweak interactions, fermion fields have different quantum numbers depending on their chiralities: left-handed quarks and leptons are grouped in their corresponding $SU(2)_L$ doublets while the right-handed fermions are singlets:

$$\begin{aligned} q'_i &= \begin{pmatrix} u'_{i\,L} \\ d'_{i\,L} \end{pmatrix}, & u'_{i\,R}, & & d'_{i\,R}, \\ \ell_i &= \begin{pmatrix} \nu_{i\,L} \\ e_{i\,L} \end{pmatrix}, & e_{i\,R}. \end{aligned} \tag{2.1}$$

The flavours of the quarks are $u'_i = \{u', c', t'\}$ and $d'_i = \{d', s', b'\}$ and the leptons $e_i = \{e, \mu, \tau\}$ and $\nu_i = \{\nu_e, \nu_\mu, \nu_\tau\}$, in increasing order of generations. Each quark and lepton has a corresponding antiparticle with opposite quantum numbers. Fermions must come in complete generations with their weak isospin and hypercharge assignments, in order to cancel quantum anomalies of the gauge symmetries [19, 20]. A summary of the fields of the SM can be found in Table 2.1.

In any quantum field theory, the dynamics of the particles and their interactions can be obtained from the Lagrangian. The complete Lagrangian of the SM can we written as

$$\mathscr{L}_{\text{SM}} = \mathscr{L}_\varphi + \mathscr{L}_{\text{kin}} + \mathscr{L}_{\text{Yuk}}, \tag{2.2}$$

where $\mathscr{L}_\varphi$ is the scalar potential, $\mathscr{L}_{\text{kin}}$ contains the kinetic terms and gauge interactions of the fields, and $\mathscr{L}_{\text{Yuk}}$ represents the Yukawa interactions of the Higgs boson with the massive fermions. In more detail:

- The scalar potential is contained in $\mathscr{L}_\varphi$:

$$\mathscr{L}_\varphi = -\mu^2 \varphi^\dagger \varphi - \lambda (\varphi^\dagger \varphi)^2, \tag{2.3}$$

  with $\mu^2 < 0$ and $\lambda > 0$. This potential attains a minimum when the Higgs field is in its Vacuum Expectation Value (vev) given by

$$v = \sqrt{\frac{-\mu^2}{\lambda}}. \tag{2.4}$$

Particle	Symbol	Spin	$SU(3)_C$	$SU(2)_L$	T_3	Y	Q
Higgs boson	φ	0	**1**	**2**	$\pm\frac{1}{2}$	$\frac{1}{2}$	0
Gluon	G^A	1	**8**	**1**	0	0	0
Electroweak bosons	W^I	1	**1**	**3**	$-1, 0, +1$	0	$-1, 0, +1$
	B	1	**1**	**1**	0	0	0
Quarks	u'_L, c'_L, t'_L	$\frac{1}{2}$	**3**	**2**	$\frac{1}{2}$	$\frac{1}{6}$	$\frac{2}{3}$
	u'_R, c'_R, t'_R	$\frac{1}{2}$	**3**	**1**	0	$\frac{2}{3}$	$\frac{2}{3}$
	d'_L, s'_L, b'_L	$\frac{1}{2}$	**3**	**2**	$-\frac{1}{2}$	$\frac{1}{6}$	$-\frac{1}{3}$
	d'_R, s'_R, b'_R	$\frac{1}{2}$	**3**	**1**	0	$-\frac{1}{3}$	$-\frac{1}{3}$
Leptons	ν_{eL}, $\nu_{\mu L}$, $\nu_{\tau L}$	$\frac{1}{2}$	**1**	**2**	$\frac{1}{2}$	$-\frac{1}{2}$	0
	e_L, μ_L, τ_L	$\frac{1}{2}$	**1**	**2**	$-\frac{1}{2}$	$-\frac{1}{2}$	-1
	e_R, μ_R, τ_R	$\frac{1}{2}$	**1**	**1**	0	-1	-1

Table 2.1: Particles of the SM before EWSSB, classified according to their quantum numbers: Spin, representation under the colour group $SU(3)_C$, representation under the weak isospin $SU(2)_L$ and the corresponding third component of the weak isospin T_3, weak hypercharge Y and electromagnetic charge $Q = T_3 + Y$. Each quark and lepton has a corresponding antiparticle with opposite quantum numbers.

While the Lagrangian is invariant under $SU(2)_L \times U(1)_Y$, the vacuum of the Higgs is not, prompting the EWSSB. In the unitarity gauge, the perturbations h of the Higgs field around the minimum occur only in the $T_3 = -1/2$ component,

$$\varphi = \frac{1}{\sqrt{2}} \begin{pmatrix} 0 \\ v + h \end{pmatrix}. \tag{2.5}$$

- The kinetic terms of the Lagrangian and gauge interactions are described by $\mathscr{L}_{\text{kin}}$, given by

$$\begin{aligned} \mathscr{L}_{\text{kin}} = &-\frac{1}{4} G^A_{\mu\nu} G^{A\mu\nu} - \frac{1}{4} W^I_{\mu\nu} W^{I\mu\nu} - \frac{1}{4} B_{\mu\nu} B^{\mu\nu} - (D_\mu \varphi)^\dagger (D^\mu \varphi) \\ &- i \overline{q}'_i \gamma_\mu D^\mu q'_i - i \overline{u}'_{i\,R} \gamma_\mu D^\mu u'_{i\,R} - i \overline{d}'_{i\,R} \gamma_\mu D^\mu d'_{i\,R} \\ &- i \overline{\ell}_i \gamma_\mu D^\mu \ell_i - i \overline{e}_{i\,R} \gamma_\mu D^\mu e_{i\,R}, \end{aligned} \tag{2.6}$$

  where $G^A_{\mu\nu}$, $W^I_{\mu\nu}$ and $B_{\mu\nu}$ are the field strength tensors for the gluons, W bosons and B bosons respectively, D_μ is the gauge covariant derivative and γ_μ the Dirac matrices.

  The gauge covariant derivative contains the usual derivative, which would correspond to pure kinetical terms, and interactions with the gauge bosons, which de-

pend on the representation of the gauge group for the field,

$$D_\mu = \partial_\mu + i g_s T^A G^A_\mu + i g S^I W^I_\mu + i g' Y \,, \tag{2.7}$$

where g_s, g and g' are the coupling constants for the gauge groups $SU(3)_C$, $SU(2)_L$ and $U(1)_Y$ respectively. T^A and S^I are the generators of the representation of the $SU(3)_C$ and $SU(2)_L$, respectively, for the field the derivative is acting on: T^A is proportional to the structure constants of the group f^{ABC} if the derivative acts on the gluons on the adjoint representation, proportional to the Gell-Mann matrices if the derivative acts on the quarks on the fundamental representation, or zero if the derivative acts on a non-coloured field; and S^I is proportional to the totally antisymmetric tensor ε^{IJK} if the derivative acts on the W bosons on the adjoint representation, proportional to the Pauli matrices if the derivative acts on the left-handed fermions or the Higgs boson on the fundamental representation, or zero if the derivative acts on the right-handed fermions, gluons or B boson.

The field strength tensors are given by the commutators of two gauge covariant derivatives. As such, in the Abelian case they only contain pure derivative terms, but in the non-Abelian case there is also a term involving two gauge fields. The specific forms for each tensor are

$$\begin{aligned} G^A_{\mu\nu} &= \partial_\mu G^A_\nu - \partial_\nu G^A_\mu - g_s f^{ABC} G^B_\mu G^C_\nu \,, \\ W^I_{\mu\nu} &= \partial_\mu W^I_\nu - \partial_\nu W^I_\mu - g\, \varepsilon^{IJK} W^J_\mu W^K_\nu \,, \\ B_{\mu\nu} &= \partial_\mu B_\nu - \partial_\nu B_\mu \,. \end{aligned} \tag{2.8}$$

The kinetic term of the B boson is described by a Maxwell Lagrangian, while the gluon and W kinetic terms and self-interactions of three and four bosons are governed by non-Abelian Yang-Mills Lagrangians. The interaction of the gauge fields with the scalar and fermions are included through the gauge covariant derivative D_μ.

The EWSSB affects the gauge interactions of the Higgs field, creating terms in the Lagrangian that are proportional to $v^2 W_{\mu\nu} W^{\mu\nu}$ and $v^2 B_{\mu\nu} B^{\mu\nu}$, i.e., mass terms for the gauge bosons. The charged components of the W gain a mass M_W, and a linear combination of W^0 and B, called the Z boson, gains a mass M_Z, while the orthogonal combination, the photon A of the unbroken electromagnetism, remains massless:

$$\begin{pmatrix} Z \\ A \end{pmatrix} = \begin{pmatrix} \cos\theta_W & -\sin\theta_W \\ \sin\theta_W & \cos\theta_W \end{pmatrix} \begin{pmatrix} W^0 \\ B \end{pmatrix}. \tag{2.9}$$

$$M_W = M_Z \cos\theta_W = \frac{1}{2} v g, \tag{2.10}$$

where $\theta_W = \tan^{-1}(g'/g)$ is the Weinberg weak mixing angle.

In the fermionic part, above the EWSSB all kinetic and gauge terms are diagonal in the generation labels: gluons, B and W^0 bosons only interact with two fermions of

the same flavour, and $W^\pm$ interact with the two components of each $SU(2)_L$ doublets, connecting u-type and d-type or charged lepton and neutrino of the same generation.

- The Yukawa interactions of the Higgs boson with fermions are included in $\mathscr{L}_{\text{Yuk}}$:

$$\mathscr{L}_{\text{Yuk}} = (y_d)_{ij}\overline{q}'_i\varphi d'_{jR} + (y_u)_{ij}\overline{q}'_i\widetilde{\varphi}u'_{jR} + (y_e)_{ij}\overline{\ell}_i\varphi e_{jR} + \text{h.c.}, \tag{2.11}$$

where the Yukawa matrices y_d, y_u and y_e are in general non-diagonal and complex, thus providing the only flavour-dependant interactions in the SM above EWSSB and the only source of CP violation.

When the Higgs doublet defined in Eq. (2.5) is introduced in the Yukawa Lagrangian, the fermions gain mass terms:

$$\mathscr{L}_M = (M_d)_{ij}\overline{d}'_{iL}d'_{jR} + (M_u)_{ij}\overline{u}'_{iL}u'_{jR} + (M_e)_{ij}\overline{e}_{iL}\varphi e_{jR} + \text{h.c.}, \tag{2.12}$$

where the mass matrices $M_f = \frac{v}{\sqrt{2}}y_f$ are non-diagonal, which means that the eigenstates of $SU(2)_L \times U(1)_Y$ are not mass eigenstates. We can diagonalize the mass matrices using a bi-unitary transformation. For example, in the quark sector,

$$M_d = U^\dagger_{dL}\mathscr{M}_d U_{dR}, \qquad M_u = U^\dagger_{uL}\mathscr{M}_u U_{uR}, \tag{2.13}$$

where the new mass matrices $\mathscr{M}_d$ and $\mathscr{M}_u$ are diagonal. The mass eigenstates are obtained by the corresponding unitary rotation of the interaction eigenstates,

$$\begin{aligned} d_{iL} &= (U_{dL})_{ij}d'_{jL}, & d_{iR} &= (U_{dR})_{ij}d'_{jR}, \\ u_{iL} &= (U_{uL})_{ij}u'_{jL}, & u_{iR} &= (U_{uR})_{ij}u'_{jR}. \end{aligned} \tag{2.14}$$

The introduction of the Higgs doublet of Eq. (2.5) also induces interactions between the field h and the fermions, collected in the Lagrangian $\mathscr{L}_h$. Since the U matrices simultaneously diagonalize the Yukawa matrices and the mass matrices, all Higgs interactions to the mass eigenstates f are flavour-diagonal,

$$\mathscr{L}_h = -\frac{1}{v}\sum_f m_f \overline{f}_L h f_R + \text{h.c.} \tag{2.15}$$

Clearly, the Yukawa Lagrangian includes the Higgs-fermion interactions too, which turn out to be proportional to the fermion mass. After EWSSB, all the SM fermions acquire masses (except the neutrinos), which is given by $m_f = y_f\frac{v}{2}$.

Once that we have reviewed all the interactions in the SM, we can conclude that the only source of mixing between different flavours are the Yukawa interactions. This fact can be interpreted as a hint of a deeper flavour symmetry, and the Yukawa interactions as an spontaneous breaking of said symmetry. We will be back on this subject in section 4.4.

2.1.1 Is New Physics needed? Open questions in the Standard Model

The SM is an extremely successful theory of the elemental particles and interactions of our universe, which has been producing for more than sixty years precise and accurate predictions for phenomena in a large range of energy scales. However, there is the general belief that the SM cannot be the ultimate theory of Fundamental Physics. There are several aspects where the SM does not provide a satisfactory answer, some of them closely related to flavour physics. Some unresolved questions within the SM, that require going beyond the SM, are:

- Fermions in nature come in exactly three generations of particles with the same quantum numbers: three up-type quarks, three down-type quarks, three charged leptons and three neutrinos. We also know that the number of light neutrinos must be three, both from particle physics [21, 22] and from cosmology [23]. But we don't know the reason why nature works in exactly three generations.

- We observe an imbalance of matter and antimatter in the universe, which makes possible the formation of large matter structures, including us. Shakarov in [24] gave three conditions: interactions out of thermal equilibrium, violation of the baryonic number B, and CP violation. Related to the previous point, three is the minimum number of generations needed to violate the CP in the mixing of quarks or leptons, even though the amount of CP violation in the SM is not enough to explain this imbalance [25].

- While the Higgs mechanism [10, 11] explains how elemental particles acquire mass, it does not provide any insight in their specific values. The Yukawa couplings show a clearly hierarchical pattern spanning multiple orders of magnitude, with only the top Yukawa coupling displaying a "natural" $\mathcal{O}(1)$ value.

- In the SM, neutrinos are described as left-handed fermions, as indicated in Eq. (2.1) and Table 2.1. Therefore, according to Eq. (2.12), the SM neutrinos are massless. However, this is incompatible with the non-zero mass differences needed to explain the observations [26–28] of neutrino oscillations [29–31]. There is no clear consensus in which kind of extension of the SM would be needed regarding the Dirac or Majorana nature of the neutrinos and the role of right-handed neutrinos in seesaw mechanisms.

- The SM does not present any violation of the CP symmetry in the QCD interaction, although there is no fundamental reason for this conservation. This is commonly referred to as the "strong CP problem". A popular NP solution to the strong CP problem are the axions.

- The SM does not provide any insight in the nature of the Dark Matter or the Dark Energy. However, the prevalent cosmological model, ΛCDM [23, 32], establishes that the matter composed by SM fermions, or "baryonic matter", only comprises a fraction $\Omega_b \approx 0.049$ of the total density of the universe, with neutrinos and photons corresponding to negligible fractions. Cold Dark Matter comprises a fraction $\Omega_c \approx 0.26$ and the rest of the density corresponds to Dark Energy in the form of a cosmological constant Λ, with $\Omega_\Lambda \approx 0.68$.

- On the formal theoretical side, the SM does not contain gravity. There is no known theory of quantum gravity combining the SM and General Relativity. Both theories have several conceptual disagreements, as the roll played by spacetime, the fate of information contained in an object crossing the event horizon of a Black Hole (information paradox), or the huge disparity between the strength of gravity and the rest of known interactions (hierarchy problem). Besides, the SM does not provide gauge coupling unification. A fundamental theory that unifies all known gauge interactions must go beyond the SM.

- On the experimental front, there are some results that are in tension with the SM predictions, most notably the anomalous magnetic moment of the muon $(g-2)_\mu$ and the Leptonic Flavour Universality (LFU) of semileptonic B meson decays $R_{K^{(*)}}$ and $R_{D^{(*)}}$. For a recent review of experimental anomalies see [33] and references therein.

From this list, it is clear that the answer to the question "Is New Physics needed?" is a resounding yes. There are still many things that we do not know about particle physics in general, and flavour physics in particular. Flavour physics is also a very welcoming testground for NP, since models that do not respect the flavour symmetry produce clear signatures. This is specially true for the processes that proceed through the change of flavour, that we will present in the rest of this chapter.

2.2 Flavour changing processes

The $SU(2)_L \times U(1)_Y$ structure of the electroweak interactions implies that flavour changing processes will have different phenomenology depending on whether the initial and final fermion have the same electrical charge. Flavour-Changing Charged Currents (FCCC) are mediated by the $W^\pm$ boson at tree level. Flavour-Changing Neutral Currents (FCNC), as we shall see, are not allowed at tree level in the SM, and are remarkably suppressed at the loop level [34–36].

In the interaction basis for fermions, the $W^\pm$ bosons are coupled to fermions as

$$\mathscr{L}_{\text{FCCC}} = -\frac{g}{\sqrt{2}}\overline{\nu}_{iL}\gamma^\mu W^+_\mu e_{iL} - \frac{g}{\sqrt{2}}\overline{u}'_{iL}\gamma^\mu W^+_\mu d'_{iL} + \text{h.c.} \tag{2.16}$$

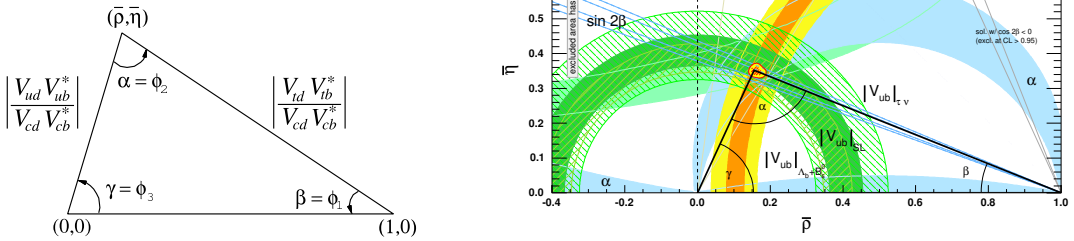

(a) (b)

Figure 2.1: Unitarity triangle in the complex plane from $\sum_i V_{id}V_{ib}^* = 0$. (a) Diagram showing the sides and angles of the triangle in terms of CKM parameters [37]. (b) Experimental determination [38]

.

We can rewrite this Lagrangian in the mass basis previously found,

$$\mathscr{L}_{\text{FCCC}} = -\frac{g}{\sqrt{2}}\overline{\nu}_{iL}\gamma^{\mu}W_{\mu}^{+}(U_{\nu L})_{ij}(U_{eL}^{\dagger})_{jk}e_{kL} - \frac{g}{\sqrt{2}}\overline{u}_{iL}\gamma^{\mu}W_{\mu}^{+}(U_{uL})_{ij}(U_{dL}^{\dagger})_{jk}d_{kL} + \text{h.c.} \quad (2.17)$$

If we assume that neutrinos are massless, we can absorb the unitary matrices in the leptonic sector with a redefinition of the neutrinos, $\nu_i \to (U_{eL})_{ij}(U_{\nu L}^{\dagger})_{jk}\nu_k$. In the quark sector, however, we obtain the Cabibbo-Kobayashi-Maskawa (CKM) matrix V connecting the different flavours,

$$V = U_{uL}U_{dL}^{\dagger}. \quad (2.18)$$

The CKM matrix is non-diagonal, and therefore FCCC can cause the interaction of fermions of different generations at tree level. With three generations of fermions, the CKM matrix is parameterized by three mixing angles between generations and one complex phase, responsible for CP violation. The unitarity of the CKM matrix is expressed by the constraint of the orthogonality of its rows and its columns,

$$\sum_i V_{ij}V_{ik}^* = \delta_{jk} \qquad \sum_j V_{ij}V_{kj}^* = \delta_{ik}. \quad (2.19)$$

This relation can be represented in the complex plane as a unitarity triangle, as shown in Fig. 2.1(a). The lengths and angles of the unitarity triangles are determined experimentally from several flavour processes, as illustrated in Fig. 2.1(b). The area of the triangle is the Jarlskog invariant J, that is a measure of the CP violation.

In order to appreciate the degree of mixing between generations, it is useful to write the CKM matrix using the Wolfenstein parameterization [39],

$$V = \begin{pmatrix} 1-\lambda^2/2 & \lambda & A\lambda^3(\rho-i\eta) \\ -\lambda & 1-\lambda^2/2 & A\lambda^2 \\ A\lambda^3(1-\rho-i\eta) & -A\lambda^2 & 1 \end{pmatrix} + \mathscr{O}(\lambda^4), \quad (2.20)$$

with $\lambda = 0.22650 \pm 0.00048$, $A = 0.790^{+0.017}_{-0.012}$, $\overline{\rho} = \rho(1-\lambda^2/2+\cdots) = 0.141^{+0.016}_{-0.017}$ and $\overline{\eta} = \eta(1-\lambda^2/2+\cdots) = 0.357 \pm 0.011$. Mixing is important between the first and second generations, with a mixing given by the Cabibbo angle $\sin\theta_C \approx \lambda$, and less important between the second and third generations with a mixing angle of order λ^2, and between the second and third generation, where the mixing angle is of order λ^3.

While FCCC are possible for quarks, charged currents in the leptonic sector in the SM are both flavour conserving and Leptonic Flavour Universality (LFU), due to the neutrinos being massless. If we supplement the SM with massive neutrinos, lepton flavour changes are possible for the neutrino mass eigenstates ν_1, ν_2 and ν_3, which are experimentally observed in the form of neutrino oscillations. In an analogous fashion to the CKM matrix, neutrino oscillations are governed by the Pontecorvo-Maki-Nakawa-Sakata (PMNS) matrix [30, 40], parameterized by three angles (solar, atmospheric and reactor angles) and one CP-violating complex phase.

The LFU of the charged currents can be experimentally observed in the decay modes of the W boson [37],

$$\begin{aligned} \mathrm{BR}(W^+ \to e^+\nu) &= (10.71 \pm 0.16)\%, \\ \mathrm{BR}(W^+ \to \mu^+\nu) &= (10.63 \pm 0.15)\%, \\ \mathrm{BR}(W^+ \to \tau^+\nu) &= (11.38 \pm 0.21)\%. \end{aligned} \tag{2.21}$$

The neutral electroweak interactions arising from the Lagrangian of Eq. (2.6) are

$$\mathscr{L}_{\mathrm{NC}} = -g\sum_{f'} T_3^{f'}\overline{f'}\gamma^\mu W_\mu^0 f' - g'\sum_{f'} Y_{f'}\overline{f'}\gamma^\mu B_\mu f', \tag{2.22}$$

where f' is summed over all interaction eigenstates. We have to rewrite this Lagrangian in terms of the mass eigenstates for fermions defined in Eq. (2.14) and electroweak bosons defined in Eq. (2.9). It is important to note that the rotation of the fermion basis does not induce flavour changing interactions,

$$\overline{f}'_i\gamma_\mu f'_i = \overline{f}_i\gamma_\mu (U^\dagger_{f\,L/R})_{ij}(U_{f\,L/R})_{jk} f_k = \overline{f}_i\gamma_\mu \delta_{ik} f_k = \overline{f}_i\gamma_\mu f_i. \tag{2.23}$$

Therefore, the SM does not allow electroweak FCNC at tree level,

$$\mathscr{L}_{\mathrm{NC}} = e\sum_f Q_f \overline{f}\gamma_\mu A^\mu f + \frac{g}{\cos\theta_W}\sum_f (T_3^f - \sin^2\theta_W Q_f)\overline{f}\gamma_\mu Z^\mu f. \tag{2.24}$$

Neutral currents are not only diagonal, but the couplings are also universal, since all generations have the same quantum numbers Q and T_3. LFU can be checked in the branching ratios of the different decays modes of the Z boson [37] to leptons,

$$\begin{aligned} \mathrm{BR}(Z \to e^+e^-) &= (3.363 \pm 0.004)\%, \\ \mathrm{BR}(Z \to \mu^+\mu^-) &= (3.366 \pm 0.007)\%, \\ \mathrm{BR}(Z \to \tau^+\tau^-) &= (3.370 \pm 0.008)\%, \end{aligned} \tag{2.25}$$

to u-type quarks,

$$\frac{1}{2}\left[\mathrm{BR}(Z\to u\overline{u})+\mathrm{BR}(Z\to c\overline{c})\right]=(11.6\pm0.6),\%$$
$$\mathrm{BR}(Z\to c\overline{c})=(12.0\pm0.2)\%, \tag{2.26}$$

and to d-type quarks,

$$\frac{1}{3}\left[\mathrm{BR}(Z\to d\overline{d})+\mathrm{BR}(Z\to s\overline{s})+\mathrm{BR}(Z\to b\overline{b})\right]=(15.6\pm0.4)\%,$$
$$\mathrm{BR}(Z\to b\overline{b})=(15.12\pm0.05)\%. \tag{2.27}$$

Since the neutral bosons can not change the flavour of fermions, FCNC can only appear through the exchange of at least two W bosons, in the topologies known as penguin and box Feynman diagrams. This creates three sources of suppression for these processes:

- **Loop suppression:** The integration over the internal momentum in the loop present in box and penguin Feynman diagrams introduces a factor of $(2\pi)^{-4}$ (see, for example [41]).

- **CKM suppression:** The diagrams include two W vertices, each with a factor V_{ij}, and at least one of them are off-diagonal. These CKM elements are small numbers, in the Wolfenstein parameterization they are proportional to some power of λ. For example, the $b\to s\ell^+\ell^-$ transitions are dominated by $|V_{tb}^*V_{ts}|\sim\lambda^2$. For a recent review, see [42].

- **Glashow-Iliopoulos-Maiani (GIM) mechanism [43]:** If all u-type quarks or all d-type in quarks were degenerate in mass, the interaction eigenstates would be also mass eigenstates. That would rule out flavour changing W interactions, and therefore FCNC interactions at the loop level. In the SM this symmetry between quarks is violated by their masses, and therefore the amplitudes of FCNC processes must be proportional to the breaking, so it vanishes when the symmetry is restored. For example, the decay of the kaon $\overline{K^0}\to\mu^+\mu^-$ is described by two box diagrams, with an internal u or c line (the diagram with an internal t line has a negligible contribution due to CKM suppression), as shown in Fig. 2.2. The amplitudes for these diagrams are

$$A_u\propto\frac{m_u^2}{M_W^2}\sin\theta_C\cos\theta_C,\qquad A_c\propto-\frac{m_c^2}{M_W^2}\sin\theta_C\cos\theta_C,$$
$$A_u+A_c\propto\frac{m_u^2-m_c^2}{M_W^2}\sin\theta_C\cos\theta_C. \tag{2.28}$$

  In fact, the suppression of the $\Delta S=2$ processes such as kaon mixing, $K\to\mu^+\mu^-$ and $K^+\to\pi^+\ell^+\ell^-$ was what led Glashow, Iliopoulos and Maiani to predict the existence of the c quark.

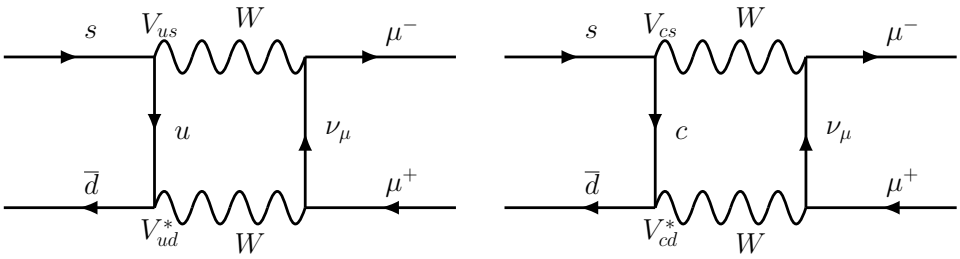

Figure 2.2: One-loop box diagrams for the decay $\overline{K^0} \to \mu^+\mu^-$ (a) with an internal u quark, (b) with an internal c quark.

The GIM mechanism only suppresses FCNCs when there is a small mass splitting between the quarks in the loops. If one of the external quarks is b, then the dominant contribution comes from the exchange of t (since $V_{tb} \approx 1$) and the FCNC is consequently enhanced by m_t^2/M_W^2 [42].

In the lepton sector, even if we enlarge the SM with massive neutrinos that would allow for non-diagonal $W^\pm$ vertices, FCNCs for the charged leptons would be extremely suppressed by a GIM factor of $\Delta m_\nu^2/M_W^2$ [44, 45].

To sum up, in the SM, the electroweak interactions involving leptons must always be flavour-conserving and flavour-universal, so it predict no Leptonic Flavour Violation (LFV) and no Leptonic Flavour Universality Violation (LFUV). On the other hand, electroweak interactions involving quarks can be flavour-changing and even CP-violating, with flavour-changing neutral currents suffering large suppressions.

2.3 Flavour observables

In the past decades, kaons, mesons composed by one s quark and one light u or d quark, have been the testground of flavour physics [46]. The suppression of kaon FCNC led to the prediction of the c quark, and the violation of CP symmetry in the neutral kaon $K^0 - \overline{K}^0$ oscillations led to the prediction of the third generation of quarks to accommodate a complex phase in the CKM matrix. Kaon physics is in agreement with the SM predictions, and puts stringent constraints on any kind of new physics that modifies the mixing between the first and second generation of quarks.

With the advent of new, more powerful colliders and detectors, much of the focus of flavour physics has shifted towards B mesons. B mesons are composed by one b quark and one lighter quark, $B^0 = d\overline{b}$, $B^+ = u\overline{b}$ and $B_s = s\overline{b}$, and their antiparticles $\overline{B}^0$, B^-, $\overline{B}_s$. B mesons have "long" lives $\tau_B \sim 10^{-12}$ s, compared to the ephemerous charmed D mesons $\tau_D \sim 10^{-15}$ s [37]. This discrepancy is due to CKM suppression, as B decays are dominated by $V_{cb} = A\lambda^2$, while D decays proceed through $V_{cd} = -\lambda$. Longer lives allows experimental

access to rarer decay modes, such as FCNC decays [47].

2.3.1 FCNC observables

Depending on the final products, FCNC processes for B mesons can be classified as [48–53]:

- **Neutral meson oscillations:** The oscillations $B^0 - \overline{B^0}$ and $B_s - \overline{B_s}$ occur through W box diagrams, similar to the well-known kaon oscillations [54]. The oscillation frequency is determined by the mass splitting ΔM between meson and anti-meson. Oscillations in $B_s - \overline{B_s}$ are notably large, with $\Delta M_{B_s}/\Gamma_{B_s} \approx 27$ [37] due to smaller CKM suppressions.

  B decays exhibit both direct CP violation and indirect CP violation through the interference between the decays $B \to f$ and $B \to \overline{B} \to f$, where the final state is a CP eigenstate $\overline{f} = f$. The time-dependant CP asymmetry is given by [37, 47]

  $$A_{CP}^{f}(t) = \frac{\Gamma(\overline{B} \to f) - \Gamma(B \to f)}{\Gamma(\overline{B} \to f) + \Gamma(B \to f)} = S_f \sin(\Delta M_B\, t) - C_f \cos(\Delta M_B\, t), \tag{2.29}$$

  where the coefficient S_f of the oscillation is due to indirect CP violation and C_f due to direct violation.

  The angles α and β of the unitarity triangle in Fig. 2.1 are extracted from CP asymmetries in $B \to \pi\pi$, $\rho\rho$, $\rho\pi$ and $B \to J/\psi K_S$ respectively. The CP asymmetry in the decay $B_s \to J/\psi\phi$ is used for the experimental determination of the angle $\beta_s = \arg(-V_{ts}V_{tb}^*/V_{cs}V_{cb}^*)$ of the $\sum_i V_{is}V_{ib}^*$ unitarity triangle [37, 47, 55].

- **Radiative decays:** The final state contains a light hadron and one photon. At the quark level, the decays are $b \to s\gamma$ or $b \to d\gamma$, which in the SM are described by electromagnetic penguin loops. The exclusive decay $\mathrm{BR}(B \to K^*\gamma)$ and the inclusive decay $\mathrm{BR}(B \to X_s\gamma)$ were measured by CLEO [56, 57]. Inclusive radiative decays are theoretically very clean and impose constraints on NP Models that predict lepton-universal FCNC, like 2 Higgs-doublet model.

- **Leptonic decays:** The leptonic modes $B_s \to \mu^+\mu^-$ and $B^0 \to \mu^+\mu^-$ have been experimentally detected by LHC [58, 59]. In the SM, leptonic decays are described by W box and Z penguin diagrams. In addition to the usual CKM and loop suppressions, leptonic decays suffer from helicity suppression, as B_s and B^0 are pseudo-scalar particles decaying into a pair of fermions [50, 60]. The decay rate is

  $$\Gamma(B_{(s)} \to \ell^+\ell^-) = \frac{G_F^2 M_W^2 m_{B_{(s)}}^3 f_{B_{(s)}}^2}{8\pi^5} |V_{tb}^* V_{tq}|^2 \frac{4m_\ell^2}{M_{B_{(s)}}^2} \sqrt{1 - \frac{4m_\ell^2}{M_{B_{(s)}}^2}} |C_{10}^{\mathrm{SM}}|^2, \tag{2.30}$$

  where $q = d$, s and $f_{B_{(s)}}$ is the meson decay constant and C_{10} is a Wilson coefficient (see Section 3.5).

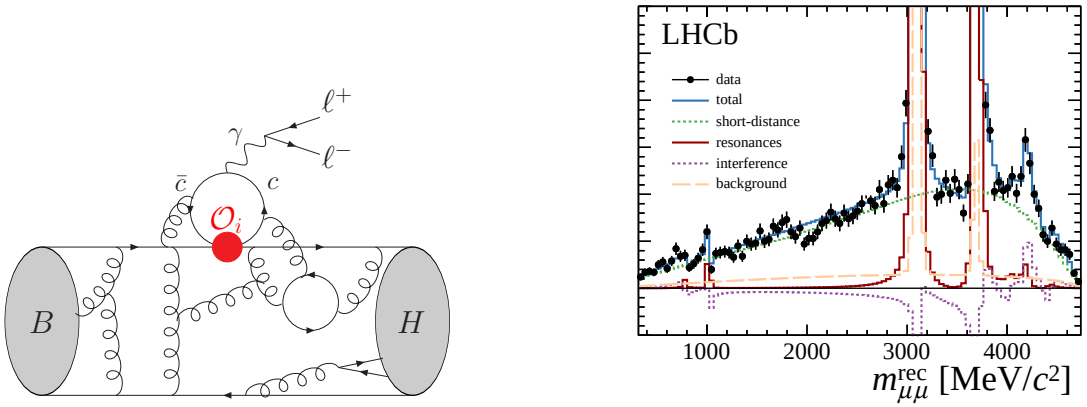

(a) (b)

Figure 2.3: Effects of charm loops in semileptonic B decays. (a) Example of a Feynman diagram illustrating a charm loop via an effective four-quark operator $\mathcal{O}_i$, mediated by a W exchange [51]. (b) Dimuon invariant mass distribution in the $B^+ \to K^+\mu^+\mu^-$ decay measured by LHCb. The solid red line represents the fit to resonances: one small peak at 1020 GeV corresponding to the ϕ meson ($s\bar{s}$ resonance) and two big peaks at 3096 GeV and 3686 GeV corresponding to the charmonium resonances J/ψ and $\psi(2S)$ [77].

The experimental results are in good agreement with the SM predictions [61–63], which will restrict the helicity structure of NP. Leptonic decays to a pair of taus are not possible because of the difficulty to reconstruct them from their decay products [47, 64, 65], and leptonic decays to a pair of electrons have too low branching ratio to be detected in the current generation of experiments [66, 67]. Therefore, leptonic decays are not suited for studies of potential LFUV.

- **Semileptonic decays:** The final states includes a pair of leptons and one hadron, from the decay $b \to s\ell^+\ell^-$. The b decay is described in the SM by electroweak penguins or W boxes, with the light quark of the meson acting as an spectator quark. The main modes are $B^+ \to K^+\ell^+\ell^-$ and $B^0 \to K^{*0}\ell^+\ell^-$, with $\ell = e,\ \mu$ (semileptonic $\tau^+\tau^-$ suffer from the same experimental challenges as the leptonic modes [68]). Other semileptonic $b \to s\ell^+\ell^-$ decays have been also observed in $B_s \to \phi\mu^+\mu^-$ [69–73] and in the baryonic transition $\Lambda_b \to \Lambda\mu^+\mu^-$ [74–76]. Semileptonic B decays thusly provide an exceptional avenue to test LFU.

The decay rates for the semileptonic B modes are expressed as functions of the dilepton invariant mass-squared $q^2 = m^2_{\ell\ell}$. The final state can also be reached through $B \to K^{(*)}\psi \to K^{(*)}\ell^+\ell^-$, where ψ denotes any charmonium state, as depicted in the example of the Feynman diagram illustrating this kind of processes in Fig. 2.3(a). This background is specially prominent in the q^2 regions corresponding to resonant production of J/ψ and $\psi(2S)$ [51, 53, 78–80], as illustrated in Fig. 2.3(b). We can integrate the decay rates in q^2

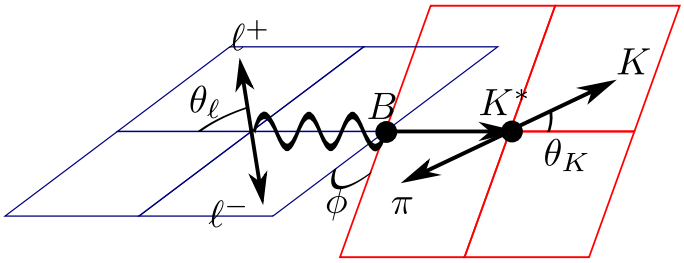

Figure 2.4: Definition of the angles in the $B \to K^*(\to K\pi)\ell^+\ell^-$ decay.

bins,

$$\Gamma^{[q^2_{\min},q^2_{\max}]} = \int_{q^2_{\min}}^{q^2_{\max}} \frac{d\Gamma(q^2)}{dq^2} dq^2 \,. \tag{2.31}$$

It is possible to reduce the impact of the charmonium resonances by selecting only the clean q^2 bins and discarding the region $8\ \text{GeV}^2 \le q^2 \le 15\ \text{GeV}^2$.

The decays into the pseudoscalar kaon K have a simple angular structure, depending only on the angle θ_ℓ between the positively-charged lepton and the B meson momenta in the rest frame of the dilepton system. The angular distribution is given by [81]

$$\frac{d^2\Gamma(B \to K\ell^+\ell^-)}{d\cos\theta_\ell\, dq^2} = \frac{3}{4}(1-F_H)(1-\cos^2\theta_\ell) + \frac{1}{2}F_H + A^\ell_{\text{FB}}\cos\theta_\ell, \tag{2.32}$$

where A^ℓ_{FB} is the forward-backward asymmetry, and F_H is the flat term, both of them are very close to zero in the SM.

The decays into the vector excited kaon K^* exhibit a richer angular structure. The polarization of the kaon can be obtained from its decay $K^* \to K^+\pi^-$ [82]. In total there are three relevant angles: θ_ℓ between the positively-charged lepton and the B meson momenta in the rest frame of the dilepton system, θ_K between the K^+ and the B meson momenta in the rest frame of the K^*, and ϕ between the planes that contain $K^+\pi^-$ and $\ell^+\ell^-$. These angles are depicted in Fig. 2.4. The angular distribution in terms of the angular coefficients I_i reads [83, 84]

$$\begin{aligned}\frac{d^4\Gamma(\overline{B}^0 \to \overline{K}^{*0}\ell^+\ell^-)}{d\cos\theta_\ell\, d\cos\theta_K\, d\cos\phi\, dq^2} = \frac{9}{32\pi}\Big[& I_1^s\sin^2\theta_K + I_1^c\cos^2\theta_K + (I_2^s\sin^2\theta_K + I_2^c\cos^2\theta_K)\cos 2\theta_l \\ & + I_3\sin^2\theta_K\sin^2\theta_\ell\cos 2\phi + I_4\sin 2\theta_K\sin 2\theta_\ell\cos\phi \\ & + I_5\sin 2\theta_K\sin\theta_\ell\cos\phi + (I_6^s\sin^2\theta_K + I_6^c\cos^2\theta_K)\cos\theta_\ell \\ & + I_7\sin 2\theta_K\sin\theta_\ell\sin\phi + I_8\sin 2\theta_K\sin 2\theta_\ell\sin\phi \\ & + I_9\sin^2\theta_K\sin^2\theta_\ell\sin 2\phi\Big].\end{aligned} \tag{2.33}$$

The angular distribution of the CP-reversed process $B^0 \to K^{*0}\ell^+\ell^-$ is obtained by the replacement $\overline{I}_i \to I_i$ for $i = 1,2,3,4,7$, and $\overline{I}_i \to -I_i$ for $i = 5,6,8,9$. The CP-averaged coefficients S_i and the CP asymmetries A_i are obtained as

$$S_i = \frac{I_i + \overline{I}_i}{d(\Gamma+\overline{\Gamma})/dq^2}, \qquad A_i = \frac{I_i - \overline{I}_i}{d(\Gamma+\overline{\Gamma})/dq^2}, \tag{2.34}$$

and the Forward-Backward asymmetry and the K^* longitudinal and transverse polarization fractions F_L, F_T are

$$A_{\rm FB} = \frac{3}{8}(2S_6^s + S_6^c), \qquad F_L = -S_2^c \qquad F_T = 4S_2^s. \tag{2.35}$$

The differential decay rate is obtained by integrating the angular distribution over the angular variables,

$$\frac{d\Gamma(\overline{B}^0 \to \overline{K}^{*0}\ell^+\ell^-)}{dq^2} = \frac{1}{4}(3I_1^c + 6I_1^s - I_2^c - 2I_2^s). \tag{2.36}$$

"Folding" is a procedure used to reduce the number of angular coefficients in the distribution and extracting all the S_i from small datasets. For example, the transformation $\phi \to \phi+\pi$ if $\phi < 0$ cancels all terms with a $\cos\phi$ or $\sin\phi$, leaving terms with $\cos 2\phi$ or $\sin 2\phi$ unaffected. Reference [85] includes a list of the folding transformations needed to extract all S_i observables.

The theoretical calculations for decay rates and angular distributions involve the evaluation of the matrix element $\langle K^{(*)}\ell^+\ell^-|J_\ell \cdot J_q|B\rangle$, where J_ℓ and J_q are leptonic and quark currents. In the large hadron recoil limit $q^2 \ll 4m_c^2$, the matrix element factorizes in leptonic and hadronic elements

$$\langle K^{(*)}\ell^+\ell^-|J_\ell \cdot J_q|B\rangle \sim \langle K^{(*)}|J_q|B\rangle \cdot \langle \ell^+\ell^-|J_\ell|0\rangle. \tag{2.37}$$

The leptonic elements are easily evaluated using the solutions of the Dirac equation. On the other hand, hadronic elements require knowledge of the non-perturbative regime of QCD. The hadronic matrix elements are usually written in terms q^2-dependent form factors [86–89]. For a B meson with momentum p decaying into a pseudoscalar kaon $P = K$ with momentum k, with $q = p - k$, the matrix elements are

$$\begin{aligned}
\langle P(k)|\bar{s}\gamma_\mu b|B(p)\rangle &= \left(p_\mu + k_\mu + q_\mu \frac{M_B^2 - M_P^2}{q^2}\right) f_+(q^2) + q_\mu \frac{M_B^2 - M_P^2}{q^2} f_0(q^2), \\
\langle P(k)|\bar{s}\sigma_{\mu\nu}q^\nu b|B(p)\rangle &= \frac{i}{M_B + M_P}\Big[q^2(p_\mu + k_\mu) - (M_B^2 - M_P^2)q^2\Big] f_T(q^2),
\end{aligned} \tag{2.38}$$

and for a B meson decaying into a vector meson $V = K^*$ with polarization ε,

$$\begin{aligned}
\langle V(k,\varepsilon)|\bar{s}\gamma_\mu b|B(p)\rangle &= \epsilon^{\mu\nu\rho\sigma}\varepsilon_\nu^* p_\rho k_\sigma \frac{2V(q^2)}{M_B + M_V}, \\
\langle V(k,\varepsilon)|\bar{s}\gamma_\mu\gamma_5 b|B(p)\rangle &= i\varepsilon_\mu^*(M_B + M_V)A_1(q^2) - i\varepsilon_\nu^* q^\nu (p_\mu + k_\nu)\frac{A_2(q^2)}{M_B + M_V} \\
&\quad - iq^\nu \varepsilon_\nu^* q_\mu \frac{2M_V}{q^2}\Big[A_3(q^2) - A_0(q^2)\Big], \\
\langle V(k,\varepsilon)|\bar{s}\sigma^{\mu\nu}\gamma_\nu b|B(p)\rangle &= 2\epsilon^{\mu\nu\sigma\rho}\varepsilon_\nu^* p_\rho k_\sigma T_1(q^2), \\
\langle V(k,\varepsilon)|\bar{s}\sigma^{\mu\nu}\gamma_\nu\gamma_5 b|B(p)\rangle &= i\varepsilon^{*\mu}(M_B^2 - M_V^2)T_2(q^2) - i\varepsilon_\nu^* q^\nu (p^\mu + k^\mu)T_2(q^2) \\
&\quad + i\varepsilon_\nu^* q^\nu \left(q^\mu - \frac{q^2}{M_B^2 - M_V^2}(p^\mu + k^\mu)\right) T_3(q^2).
\end{aligned} \tag{2.39}$$

The form factors are obtained at low hadron recoil (large q^2) from Lattice QCD computations [90–92], and at $q^2 \approx 0$ from Light-Cone Sum Rules (LCSR) [86, 89]. Both sets of results can be combined together and interpolated to the whole kinematic range of q^2.

Form factors are the main source of uncertainty in the SM predictions for the semileptonic B decays. It is therefore useful to define a new set of observables where the hadronic uncertainties largely cancel out. A set of clean angular observables was presented in [84],

$$\begin{aligned} P_1 &= \frac{2S_3}{F_T}, & P_2 &= \frac{S_6^s}{2F_T}, & P_3 &= -\frac{S_9}{F_T} \\ P_4' &= \frac{2S_4}{\sqrt{F_T F_L}}, & P_5' &= \frac{S_5}{\sqrt{F_T F_L}}, & P_6' &= \frac{-S_7}{\sqrt{F_T F_L}}. \end{aligned} \tag{2.40}$$

Clean observables for the decay rates can be obtained from the ratios of the decay modes to muons and electrons [93],

$$R_{K^{(*)}}^{[q^2_{\min}, q^2_{\max}]} = \frac{\int_{q^2_{\min}}^{q^2_{\max}} \frac{d\Gamma(B\to K^{(*)}\mu^+\mu^-)}{dq^2} dq^2}{\int_{q^2_{\min}}^{q^2_{\max}} \frac{d\Gamma(B\to K^{(*)}e^+e^-)}{dq^2} dq^2}. \tag{2.41}$$

We will use the notation $R_{K^{(*)}}$ to denote the set of all the LFU ratios in $b \to s\ell^+\ell^-$ semileptonic decays. Each individual LFU ratio will be identified by the kaon in the final state, so for example R_{K^+} denotes the LFU ratios for the $B^+ \to K^+\ell^+\ell^-$ decays, and $R_{K^{*0}}$ the LFU ratios for the $B^0 \to K^{*0}\ell^+\ell^-$ decays. Isospin-averaged measurements will be denoted as R_K and R_{K^*}. The B meson always has the same electric charge as the kaon. The $R_{K^{(*)}}$ observables are of uttermost interest, as they offer a theoretically-clean test of lepton flavour universality. The SM prediction for the whole q^2 range is $R_{K^{(*)}} = 1 + \mathcal{O}(m_\mu^2/m_b^2)$, where the mass corrections are well below 1%.

It is also possible to define clean angular observables sensitive to LFUV [94],

$$Q_i = P_i^\mu - P_i^e, \tag{2.42}$$

where P_i are the angular observables defined in Eq. (2.40). A non-zero value for any of the Q_i observables would mark a deviation from LFU.

2.3.2 FCCC observables

FCCC transitions are tree level processes in the SM without large suppressions, and consequently NP was expected to have a lesser impact in these observables. In fact, the branching ratios of $B \to D\mu\nu$ and $B \to De\nu$ are in agreement with LFU, and are used to perform measurements of the $|V_{cb}|$ element of the CKM matrix and to extract hadronic form factors. However, measurements involving tau leptons have found tensions with the universality predictions.

The main semitauonic modes are $B \to D\tau\nu$ and $B \to D^*\tau\nu$. Semitauonic decays are free from charm loops and therefore the factorization in hadronic and leptonic elements

is exact. The hadronic elements have the same general structure in Eq. (2.38) for the pseudoscalar D meson and Eq. (2.39) for the vector D^* meson [95, 96]. $B \to D$ form factors are obtained from lattice calculations [97, 98], and the $B \to D^*$ form factors are calculated using Heavy Quark Expansion (HQE) [99].

A set of important observables used to study the $B \to D^{(*)}\ell\nu$ decays are LFU ratios R_D and R_{D^*} ratios, defined as [99, 100]

$$R^{\mu}_{D^{(*)}} = \frac{\mathrm{BR}(B \to D^{(*)}\tau\nu)}{\mathrm{BR}(B \to D^{(*)}\mu\nu)},$$
$$R^{\ell}_{D^{(*)}} = \frac{\mathrm{BR}(B \to D^{(*)}\tau\nu)}{[\mathrm{BR}(B \to D^{(*)}e\nu) + \mathrm{BR}(B \to D^{(*)}\mu\nu)]/2} \tag{2.43}$$

In this case, the ratios deviate from unity due to the large mass of the tau lepton [101]. The branching ratios for $B \to D^*\mu\nu$ and $B \to D^*e\nu$ have been measured to be equal to great precision [102–104]. The determinations of these ratios that assume universality in the two lightest generations will be denoted by R_D and R_{D^*} respectively. The SM predictions for these ratios, assuming lepton flavour universality between the first and second generations, are [105]

$$R^{\mathrm{SM}}_D = 0.299 \pm 0.004, \qquad R^{\mathrm{SM}}_{D^*} = 0.257 \pm 0.005. \tag{2.44}$$

The experimentally available angular observables in $B \to D^*\tau\nu$ decays are the D^* longitudinal polarization $F_L^{D^*}$ (defined analogously as in Eq. (2.35)), and the τ longitudinal polarization. Semitauonic decays also exist for B_c mesons, with the LFU ratio

$$R_{J/\psi} = \frac{\mathrm{BR}(B_c \to J\psi\tau\nu)}{\mathrm{BR}(B_c \to J\psi\mu\nu)}, \tag{2.45}$$

where the SM prediction is $R^{\mathrm{SM}}_{J/\psi} = 0.267 \pm 0.016$, that has larger uncertainties from the hadronic form factors [106].

The leptonic decay $B_c \to \tau\nu$ has an additional helicity suppression, and therefore is not expected to be measured in the foreseeable future. However, it is possible to constraint its branching ratio from the precise determination of the B_c lifetime [107]. The leptonic $B \to \ell\nu$ decays, together with similar channels for the D, D_s and K mesons, will be analyzed in detail in Chapter 8.

2.4 B physics experimental results

Following the experimental discovery of long-lived B mesons and large $B^0 - \overline{B}^0$ meson mixing during the decade of 1980, and a notable increase in collider luminosity, the two "B factories", BaBar at the SLAC National Accelerator Laboratory (USA) [108–111] and Belle at the KEK (Japan) [112], were commissioned. Their goal was to test the flavour mixing mechanism of the CKM as a source of CP violation. Both experiments used e^+e^- collisions to achieve resonant production of the bottonium state $\Upsilon(4S)$, which decays into a

pair of $B^0\overline{B}^0$ or B^+B^- mesons entangled in a P-wave state. The e^+ and e^- beams had different energies, so the Υ would not be at rest in the lab frame, and the produced B mesons would be Lorentz-boosted so it was possible to carry out time-dependant measurements [108]. BaBar was in operation from 1999 until 2008, when it was shut down due to budgetary reasons. Belle was in operation from 1999 to 2010, and later was upgraded to Belle-II [113, 114], which started taking data in 2018.

Although not a B factory *per se*, Large Hadron Collider (LHC) collisions produce a huge number of B mesons, as well as B_s mesons, B_c mesons and bottom-flavoured baryons. One of the four main experiments in the LHC tunnel, LHCb [115–117], is devoted to look for possible NP effects in flavour physics and CP violations, providing complementary results to those of BaBar and Belle. In addition, the two general-purpose experiments, ATLAS and CMS, also have their own flavour programme. LHC has been active in Run 1, from 2009 to 2013, operating at center-of-mass energies of $\sqrt{s} = 7$ and 8 TeV, and in Run 2, from 2015 to 2018 at $\sqrt{s} = 13$ TeV. Run 3, operating at $\sqrt{s} = 14$ TeV, is expected to run from March 2022 until 2025. After that, an upgrade of the collider and detectors, High Luminosity Large Hadron Collider (HL-LHC), will increase the luminosity by a factor of around 7.

2.4.1 $b \to s\ell^+\ell^-$ decays

Belle was the first experiment that reported observations of $b \to s\ell^+\ell^-$ decays [118, 119]. The first measurements of the $R_{K^{(*)}}$ ratios defined in Eq. (2.41), with large uncertainties, were compatible with the SM [120],

$$\begin{aligned} R_K &= 0.83 \pm 0.17 \pm 0.08, \\ R_{K^*} &= 1.03 \pm 0.19 \pm 0.06. \end{aligned} \tag{2.46}$$

Measurements of the $R_{K^{(*)}}$ ratios in the low-q^2 region were reported by BaBar in 2012 [121]. They were compatible with the SM predictions within large uncertainties,

$$\begin{aligned} R_K^{[0.1,8.12]} &= 0.74^{+0.40}_{-0.31} \pm 0.06, \\ R_{K^*}^{[0.1,8.12]} &= 1.06^{+0.48}_{-0.33} \pm 0.08. \end{aligned} \tag{2.47}$$

The measurements in LHCb for the muonic and electronic modes are affected by different experimental efficiencies. In order to reduce experimental uncertainties caused by this fact, LHCb does not measure directly the $R_{K^{(*)}}$ ratios. Instead, the measured observables are the double ratios $\mathscr{R}_{K^{(*)}}$ defined as [122]

$$\mathscr{R}_{K^{(*)}} = \frac{\mathrm{BR}(B \to K^{(*)}\mu^+\mu^-)}{\mathrm{BR}(B \to K^{(*)}J/\psi(\to \mu^+\mu^-))} \Big/ \frac{\mathrm{BR}(B \to K^{(*)}e^+e^-)}{\mathrm{BR}(B \to K^{(*)}J/\psi(\to e^+e^-))}. \tag{2.48}$$

The resonant $J/\psi \to \ell^+\ell^-$ decays are used to normalize the lepton efficiencies. LHCb has determined the ratio [123]

$$r_{J/\psi} = \frac{\mathrm{BR}(B \to K^{(*)}J/\psi(\to \mu^+\mu^-))}{\mathrm{BR}(B \to K^{(*)}J/\psi(\to e^+e^-))} = 1.014 \pm 0.035, \tag{2.49}$$

which is lepton flavour universal, and therefore $R_{K^{(*)}} = \mathscr{R}_{K^{(*)}}$ to great accuracy. For our studies, we will consider both types of ratios to be equivalent.

LHCb reported a discrepancy in the $\mathscr{R}_K$ ratio in 2014, analyzing $3\,\text{fb}^{-1}$ of data taken at $\sqrt{s} = 7\,\text{TeV}$ and $\sqrt{s} = 8\,\text{TeV}$ [122],

$$\mathscr{R}_{K^+}^{[1,6]} = 0.745^{+0.090}_{-0.074} \pm 0.036\,. \tag{2.50}$$

Another deviation in the $\mathscr{R}_{K^*}$ ratio was found in 2017, also analyzing the $3\,\text{fb}^{-1}$ data sample [124–126]

$$\begin{aligned} \mathscr{R}_{K^{*0}}^{[0.045,1.1]} &= 0.66^{+0.11}_{-0.07} \pm 0.03\,, \\ \mathscr{R}_{K^{*0}}^{[1.1,6]} &= 0.685^{+0.113}_{-0.069} \pm 0.047\,. \end{aligned} \tag{2.51}$$

In 2019, LHCb reported a new value for $\mathscr{R}_K$, including an additional $2\,\text{fb}^{-1}$ of data obtained during Run 2 at $\sqrt{s} = 13\,\text{TeV}$. The value is closer to the SM prediction, but the uncertainty has notably improved, so the overall significance remains at the $2.5\,\sigma$ level [123],

$$\mathscr{R}_{K^+}^{[1.1,6]} = 0.846^{+0.060+0.016}_{-0.054-0.014}. \tag{2.52}$$

The 2019 Belle results still were compatible with the SM within the large uncertainties [127, 128],

$$\begin{aligned} &R_K^{[0.1,4]} = 1.01^{+0.28}_{-0.25} \pm 0.02\,, && R_{K_S^0}^{[0.1,4]} = 1.62^{+1.31}_{-1.01} \pm 0.02\,, && R_{K^+}^{[0.1,4]} = 0.98^{+0.29}_{-0.26} \pm 0.02\,, \\ &R_K^{[1,6]} = 1.03^{+0.28}_{-0.24} \pm 0.01\,, && R_{K_S^0}^{[1,6]} = 0.55^{+0.46}_{-0.34} \pm 0.01\,, && R_{K^+}^{[1,6]} = 1.39^{+0.36}_{-0.33} \pm 0.02\,, \\ &R_{K^*}^{[0.045,1.1]} = 0.52^{+0.36}_{-0.26} \pm 0.06\,, && R_{K^{*0}}^{[0.045,1.1]} = 0.46^{+0.55}_{-0.27} \pm 0.13\,, && R_{K^{*+}}^{[0.045,1.1]} = 0.62^{+0.60}_{-0.36} \pm 0.09\,, \\ &R_{K^*}^{[1.1,6]} = 0.96^{+0.45}_{-0.29} \pm 0.11\,, && R_{K^{*0}}^{[1.1,6]} = 1.06^{+0.63}_{-0.38} \pm 0.14\,, && R_{K^{*+}}^{[1.1,6]} = 0.72^{+0.99}_{-0.44} \pm 0.15\,. \end{aligned} \tag{2.53}$$

A new analysis in 2021, including the full run 2 data set from LHCb set the value [129]

$$\mathscr{R}_{K+}^{[1.1,6]} = 0.846^{+0.042+0.013}_{-0.039-0.012}, \tag{2.54}$$

that had the same central value as the 2019 result but reduced uncertainty, increasing the tension with the SM prediction to $3.1\,\sigma$.

Also in 2021, LHCb reported the LFU ratios for the $B^0 \to K_S^0 \ell^+ \ell^-$ and $B^+ \to K^{*+} \ell^+ \ell^-$ decays, which are the isospin partners of $B^+ \to K^+ \ell^+ \ell^-$ and $B^0 \to K^{*0} \ell^+ \ell^-$ respectively, but are affected by reduced experimental efficiency at LHCb [130].

$$\begin{aligned} \mathscr{R}_{K_S^0} &= 0.66^{+0.20+0.02}_{-0.14-0.04}\,, \\ \mathscr{R}_{K^{*+}} &= 0.70^{+0.18+0.03}_{-0.13-0.04}\,. \end{aligned} \tag{2.55}$$

Angular analyses of the $B \to K^* \mu^+ \mu^-$ were performed by LHC and Belle in [71, 131–138]. A good agreement with the SM predictions was found for all observables except P_5' in the medium-q^2 region, collected in Table 2.2. The measurements show a discrepancy of around $3\,\sigma$ with the values predicted in [139],

$$P_5^{\prime\,[1,6]} = -0.412^{+0.042+0.026+0.096+0.014}_{-0.070-0.045-0.089-0.017}. \tag{2.56}$$

Experiment	q^2 bin	P_5'	Ref.
2013 LHCb	[1,6]	$0.21^{+0.20}_{-0.21} \pm 0.03$	[131]
2015 LHCb	[1.1,6]	$-0.049^{+0.107}_{-0.108} \pm 0.014$	[133]
2016 Belle	[1,6]	$0.385^{+0.276}_{-0.285} \pm 0.099$	[134, 135]
2018 ATLAS	[1.1,6]	$0.01 \pm 0.21 \pm 0.07$	[137]
2020 LHCb	[1.1,6]	$-0.114 \pm 0.068 \pm 0.026$	[138]

Table 2.2: Measurements of the angular observable P_5'.

Experiment	R_D^ℓ	$R_{D^*}^\ell$	$R_{D^*}^\mu$	Ref.
2009 Belle	$0.48^{+0.22+0.06}_{-0.19-0.05}$	$0.47^{+0.11+0.06}_{-0.10-0.07}$	—	[142]
2012 BaBar	$0.440 \pm 0.058 \pm 0.042$	$0.332 \pm 0.024 \pm 0.018$	—	[141]
2015 Belle	$0.375 \pm 0.064 \pm 0.026$	$0.293 \pm 0.038 \pm 0.015$	—	[143]
2015 LHCb	—	—	$0.336 \pm 0.027 \pm 0.030$	[144]
2016 Belle	—	$0.270 \pm 0.035^{+0.028}_{-0.025}$	—	[145]
2017 LHCb	—	—	$0.291 \pm 0.019 \pm 0.026 \pm 0.013$	[146]
2019 Belle	$0.307 \pm 0.037 \pm 0.016$	$0.283 \pm 0.018 \pm 0.014$	—	[147]

Table 2.3: Belle, BaBar and LHCb measurements of the $R_{D^{(*)}}$ ratios.

2.4.2 $b \to c\ell\nu$ decays

Belle reported in 2007 the observation of $b \to c\tau\nu$ decays [140]. Since then, Belle and BaBar have made several measurements of the ratios $R_{D^{(*)}}^\ell$ of the muon and electron decay modes combined, while LHCb has measured the ratio R_D^μ only to the muonic decay mode. All of these measurements can be found in Table 2.3.

BaBar was the first experiment to report an excess in the R_D and R_{D^*} ratios [141]. Belle and LHCb have reproduced these anomalies.

The average experimental values for the $R_{D^{(*)}}$ ratios, as obtained by Heavy Flavour Averaging Group (HFLAV), is [148]

$$\begin{aligned} R_D^{\text{ave}} &= 0.340 \pm 0.027 \pm 0.013, \\ R_{D^*}^{\text{ave}} &= 0.295 \pm 0.011 \pm 0.008. \end{aligned} \tag{2.57}$$

R_D exceeds the SM value by 1.4σ, and R_{D^*} by 2.5σ. When combined together, included their correlation, the excess is 3.08σ. The combined analysis is plotted in Fig. 2.5. The ellipses BaBar12 [141], Belle15 [143] and Belle19 [147] correspond to the 1 σ allowed regions in correlated measurements of R_D and R_{D^*}, while the horizontal bands LHCb15 [144],

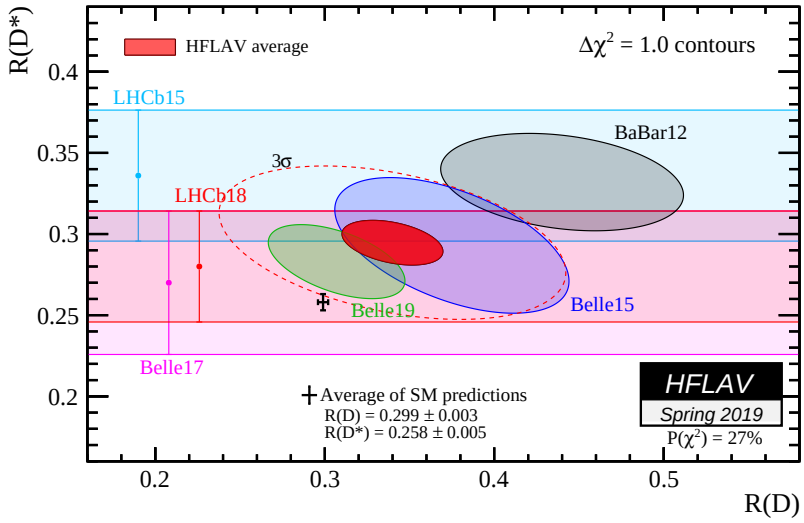

Figure 2.5: Combined R_D and $R_{D^{(*)}}$ analysis by Heavy Flavour Averaging Group (HFLAV) in Spring 2019. Solid contours correspond to $1\,\sigma$ compatibility, and the dashed contour to $3\,\sigma$ compatibility with the averaged values [148].

Belle17 [145] and LHCb18 [146] are the 1 σ values for measurements of R_{D^*} only. The average obtained by HFLAV, including the correlation between both observables, is indicated by the red ellipse at 1 σ and by the dashed ellipse at 3 σ. The average of SM predictions is marked by a cross. In general, recent measurements are closer to the SM values than older measurements.

The integrated longitudinal polarization of the D^* meson in $B^0 \to D^{*-}\tau^+\nu$ decays has been measured by Belle [149],

$$F_L^{D^*} = 0.60 \pm 0.08 \pm 0.04, \tag{2.58}$$

which is $1.6\,\sigma$ larger than the SM prediction.

The ratio $R_{J/\psi}$ defined in Eq. (2.45) has been reported by LHCb [150],

$$R_{J/\psi}^{\mu} = 0.71 \pm 0.17 \pm 0.18, \tag{2.59}$$

that lies within $2\,\sigma$ of the SM predictions. This observable is currently not included in our analysis, although we are planning to implement it in the future.

Chapter 3

Effective Field Theories

Physics phenomena at different energy scales generally can be decoupled from each other. For example, one does not need to know a thing about QCD in order to understand the energy levels of the Hydrogen atom. While this fact might seem obvious, Effective Theories provide the formalism needed to perform this decoupling in a rigorous and consistent way. In particular, we will make use of Effective Field Theory (EFT), since Quantum Field Theory is the natural language to describe many-body relativistic quantum processes.

This Chapter contains the theoretical foundations of the EFTs used in the thesis. First, we focus on the top-down approach[1], where one starts with a theory valid up to a certain high energy scale, and integrates out the heaviest fields to obtain a simpler theory valid only at low energies. The Heisenberg theory for light-by light scattering is presented as a pedagogical example of this approach. Then we discuss the bottom-up approach, where one starts with a theory valid at low energies, and extend it in the more general possible way using effective operators with no previous knowledge of the physics at higher scales. An example of historical importance of this approach is the Fermi theory for the β decays. The theoretical apparatus is completed with the discussion of the matching and running procedures used to relate two different EFTs, which are common to both approaches.

For our analyses we will mostly use the bottom-up approach, starting with the SM, or a low-energy version of the SM, as the initial theory, and constructing a basis of dimension-6 effective operators to capture the effects of any possible heavy particle. The last part of this chapter is devoted to the initial theory, the Standard Model Effective Field Theory (SMEFT), and to the Weak Effective Theory (WET), where the top, Higgs boson and W and Z gauge bosons are also integrated out.

3.1 Top-down approach

The original approach to EFT was top-down [151–153]: one would start with a theory valid up to a high energy scale, commonly denoted as the "ultraviolet (UV) theory". We then

[1] Here, top-down and bottom-up mean directions on the energy scale, not the quark flavours.

define the energy scale Λ that sets the limit of validity of the EFT. One can then identify which degrees of freedom have masses lower than Λ, that will be the only ones appearing in the EFT. The heavy degrees of freedom, that in the UV theory can only appear through internal lines in Feynman diagrams, are "integrated out" when going down to the EFT.

Let us consider a UV theory with n_H heavy fields $\Phi_1,\dots,\Phi_{n_H}$, and n_L light fields $\phi_1,\dots,\phi_{n_L}$. We can write the partition function as [152, 153]

$$Z_{\rm UV}[J_\Phi,J_\phi]=\int[\mathscr{D}^{n_H}\Phi][\mathscr{D}^{n_L}\phi]\exp\left[i\int d^4x\left(\mathscr{L}_{\rm UV}(\Phi,\phi)+\sum_{i=1}^{n_H}J_{\Phi_i}\Phi_i+\sum_{i=1}^{n_L}J_{\phi_i}\phi_i\right)\right], \tag{3.1}$$

where $[\mathscr{D}^{n_H}\Phi]=[\mathscr{D}\Phi_1]\cdots[\mathscr{D}\Phi_{n_H}]$ and $[\mathscr{D}^{n_L}\phi]=[\mathscr{D}\phi_1]\cdots[\mathscr{D}\phi_{n_L}]$ denote the functional integration over the heavy and light fields respectively and $\mathscr{L}_{\rm UV}(\Phi,\phi)$ is the Lagrangian of the UV theory depending both on the heavy and light fields. The partition function fully determines the theory, as any n-point correlation function can be obtained by taking the functional derivative with respect to the currents J_Φ and J_ϕ. In the EFT, the heavy fields are not present in the correlation functions since they can not be initial or final states of the process below the energy Λ. Therefore we can simply set the effective partition function as

$$Z_{\rm EFT}[\phi]=Z_{\rm UV}[0,J_\phi]. \tag{3.2}$$

Now we would want to write the effective partition function as the integral of some Lagrangian $\mathscr{L}_{\rm EFT}(\phi)$ depending only on the light fields,

$$Z_{\rm EFT}[J_\phi]=\int[\mathscr{D}^{n_L}\phi]\exp\left[i\int d^4x\left(\mathscr{L}_{\rm EFT}(\phi)+\sum_{i=1}^{n_L}J_{\phi_i}\phi_i\right)\right], \tag{3.3}$$

so we can extract the Feynman rules from the Lagrangian and use them to compute the amplitudes contributing to any physical observable. It is clear that we can not just simply set $\mathscr{L}_{\rm EFT}(\phi)=\mathscr{L}_{\rm UV}(0,\phi)$, as that would mean switching off any interaction where the light fields exchange one or more heavy fields. If we compare the expressions for the partition functions in Eq. (3.1) and Eq. (3.3), we notice that the EFT Lagrangian is given by

$$\exp\left(i\int d^4x\mathscr{L}_{\rm EFT}(\phi)\right)=\int[\mathscr{D}^{n_H}\Phi]\exp\left(i\int d^4x\mathscr{L}_{\rm UV}(\Phi,\phi)\right), \tag{3.4}$$

where we have integrated out the heavy fields, as promised. The price to pay is that $\mathscr{L}_{\rm EFT}(\phi)$ now is non-local, *i.e.* it includes terms that are not polynomial in the fields or their derivatives. The non-local terms include one or several propagators of the heavy fields. At leading order, the heavy fields configurations that contribute to the integral above are the classical fields, obtained by extremizing the action:

$$\mathscr{L}_{\rm EFT}(\phi)=\mathscr{L}_{\rm UV}(\Phi_{\rm cl},\phi)\qquad\qquad \left.\frac{\delta S}{\delta\Phi}\right|_{\Phi=\Phi_{\rm cl}}=0. \tag{3.5}$$

For example, let us examine a toy model with one light scalar ϕ of mass m ($m<\Lambda$) and one heavy scalar Φ of mass M ($M\gg\Lambda$) with a cubic interaction,

$$\mathscr{L}(\Phi,\phi)=\frac{1}{2}\partial_\mu\phi\partial^\mu\phi-\frac{m^2}{2}\phi^2+\frac{1}{2}\partial_\mu\Phi\partial^\mu\Phi-\frac{M^2}{2}\Phi^2+\kappa\Phi\phi^2, \tag{3.6}$$

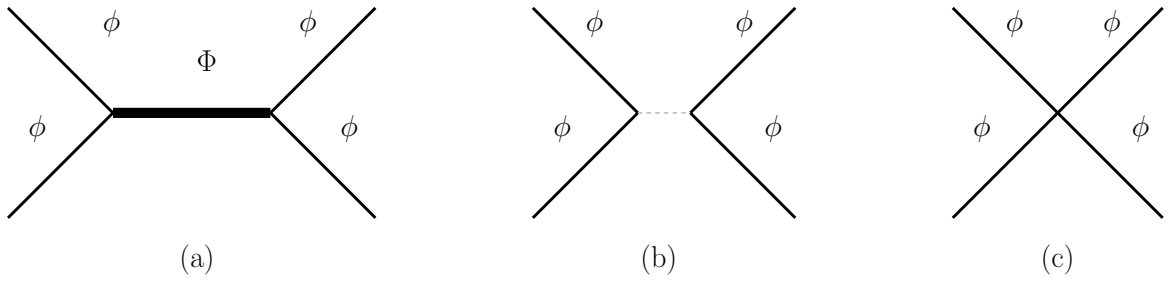

Figure 3.1: (a) Light fields ϕ exchanging a heavy field Φ in the UV theory. (b) In the EFT, the heavy field is integrated out, and the result is a non-local interaction. (c) Performing a series expansion in p/M, the non-local interaction is replaced by an infinite number of local interactions.

where κ corresponds to the coupling of the cubic interaction.

Since we are working at the energy scale Λ, the heavy field can not appear in any external line, but it will be present in the internal lines, for example mediating the $\phi\phi \to \phi\phi$ scattering depicted in Fig. 3.1(a). We obtain the classical configuration of Φ using the Euler-Lagrange equations

$$\partial_\mu\left(\frac{\partial\mathscr{L}}{\partial(\partial_\mu\Phi)}\right)-\frac{\partial\mathscr{L}}{\partial\Phi}=0\,,\qquad \Box\Phi+M^2\Phi-\kappa\phi^2=0\,, \tag{3.7}$$

where $\Box=\partial_\mu\partial^\mu$ is the Laplacian operator. The solution is

$$\Phi_{\rm cl}=\kappa^2\phi(\Box+M^2)^{-1}\phi. \tag{3.8}$$

The factor $(\Box+M^2)^{-1}$ is the propagator of the heavy field. By inserting the classical field into the Lagrangian of Eq. (3.6), we obtain non-local terms of Fig. 3.1(b):

$$\begin{aligned}\mathscr{L}(\Phi_{\rm cl},\phi)=&\frac{1}{2}\partial_\mu\phi\partial^\mu\phi-\frac{m}{2}\phi^2+\frac{\kappa^2}{2}\partial_\mu[\phi(\Box+M^2)^{-1}\phi]\partial^\mu[\phi(\Box+M^2)^{-1}\phi]\\&-\frac{\kappa^2M^2}{2}[\phi(\Box+M^2)^{-1}\phi]^2+\kappa^2[\phi(\Box+M^2)^{-1}\phi]\phi^2.\end{aligned} \tag{3.9}$$

The mass M of the heavy fields are much larger than the masses of the lights fields and their momenta. This allows us to perform a series expansion in the derivatives (*i.e.* in the momenta) of the propagators

$$(\Box+M^2)^{-1}=\frac{1}{M^2}-\frac{1}{M^4}\Box+\frac{1}{M^6}\Box^2+\cdots. \tag{3.10}$$

When we insert this series expansion in the EFT Lagrangian, each propagator contributes with a infinite number of local terms.

In our example of two light fields exchanging a heavy field, the Lagrangian now includes the following terms, shown in Fig. 3.1(c):

$$\mathscr{L}_{\rm EFT}(\phi)\supset\frac{2\kappa^2}{M^4}\phi^2\partial_\mu\phi\partial^\mu\phi+\frac{\kappa^2}{2M^2}\phi^4+\mathscr{O}\left(\frac{\Box}{M^4}\right). \tag{3.11}$$

The first term can be simplified by first integrating by parts, $\partial_\mu\phi\partial^\mu\phi = -\frac{1}{3}\phi\Box\phi$, and then using the equation of motion for ϕ, $\Box\phi+m^2\phi = \mathcal{O}(M^{-2})$. With these transformations, we can rewrite the effective Lagrangian as

$$\mathscr{L}_{\text{EFT}}(\phi) \supset \frac{\kappa^2}{M^2}\left(\frac{2}{3}\frac{m^2}{M^2}+\frac{1}{2}\right)\phi^4 + \mathcal{O}\left(\frac{\Box}{M^4}\right). \tag{3.12}$$

The effects of the particles that were integrated out are suppressed by negative powers of the UV scale. This fact is known as the decoupling theorem, established by Appelquist and Carazzone [154]. The theorem states that under certain conditions in a given Quantum Field Theory with light and heavy particles, if the heavy particles are integrated out to all orders in perturbation theory, the remaining effective action to be valid at energies much lower that the heavy particle masses does not show any trace of these heavy particles. Then, they are said to decouple from the low energy theory. More specifically, all the quantum effects of the heavy particles that are left in the effective action can be either absorbed into a redefinition of the parameters of the original theory or wave function renormalization referring to the light fields, or they are suppressed by inverse powers of the heavy masses and, therefore, vanish in the infinite mass limit.

We obviously can not work in a theory with an infinite number of terms, so we have to choose a criterion in order to retain only some of them. The terms in the Lagrangian come from (3.10), an expansion in p/M_Φ when the momenta of the processes are always $p \ll M_\Phi$. In this regime, the dominant terms are the lower orders in p/M_Φ. Let us make this classification in a systematic way [155–158]: we can write every term in the Lagrangian as a product of an operator $\mathcal{O}_k$ and its corresponding Wilson coefficient C_j.

$$\mathscr{L}_{\text{EFT}} = \sum_j C_j\mathcal{O}_j. \tag{3.13}$$

An operator is a monomial in the fields and derivatives, and describes the local physics. The Wilson coefficient is some function of the couplings and masses, and condensates the non-local physics coming from the integration of the heavy fields. The energy behaviour of any term of the Lagrangian is set, using dimensional analysis, by the mass dimension of its operator. The mass dimension of a derivative is $[\partial] = 1$, and in a 4-dimensional space-time, the mass dimensions of the fields are $[\phi] = 1$ for scalars, $[A] = 1$ for vectors and $[\psi] = 3/2$ for fermions. If an operator has dimension D, its coefficient must have dimension $4-D$, since the Lagrangian has dimension 4 and the action is non-dimensional (it has the same dimensions as $\hbar$, which in natural units is $\hbar = 1$), an we can write

$$C_j \sim c_j\Lambda^{4-D}, \tag{3.14}$$

where c_j is a dimensionless constant. According to their dimension, we can classify operators in [155, 156][2]:

[2]The names for the classes of operators come from their low-energy behaviour. Since this thesis is focused on high-energy phenomenology, the names are somewhat a misnomer, and "irrelevant" operators will be absolutely relevant for our work.

- **"Relevant":** Operators with $D < 4$, and their coefficients have positive dimension. They describe the physics at low energies $E \ll \Lambda$, but their effects become negligible at higher energies. The only relevant operators in a relativistic theory in four spacetime dimensions are a cosmological constant (dimension 0), boson mass terms (dimension 2), fermion mass terms (dimension 3) and 3 scalars interactions (dimension 3). In the SM, the only relevant term is the mass of the Higgs boson, as the mass terms of fermions and other bosons are not allowed by gauge symmetries.

- **"Marginal":** Operators with $D = 4$, and their coefficients are dimensionless. In a classical theory they would be equally important at all energy scales. Quantum corrections, however, generate an anomalous dimension γ for all operators. In the case of marginal operators, they become relevant if $\gamma < 0$ and irrelevant if $\gamma > 0$. Some usual marginal operators are gauge interactions, Yukawa interactions and 4 scalars interactions. In the case of the SM, electroweak gauge interactions have $\gamma > 0$ and become stronger at higher energies, while QCD gauge interactions have $\gamma < 0$ and become weaker at higher energies, a fact known as asymptotic freedom [159, 160].

- **"Irrelevant":** Operators with $D > 4$, and their coefficients have negative dimension. At low energies these operators provide corrections to the observables, suppressed by powers of E/Λ. Their effects become larger at higher energies.

By dimensional analysis, a single insertion of an operator of dimension D_i contributes to the amplitude as

$$A \sim (E/\Lambda)^{D_i-4}. \tag{3.15}$$

When multiple insertions are included, even in the presence of loops, the total contribution is [158]

$$A \sim (E/\Lambda)^{\sum_i (D_i-4)}. \tag{3.16}$$

When working at a fixed energy scale E, we can just truncate the EFT Lagrangian to operators with dimension up to D, and compute any amplitude with accuracy

$$\epsilon \lesssim \left(\frac{E}{\Lambda}\right)^{D-4}. \tag{3.17}$$

If the experimental uncertainties of the physical observables improve, it is then necessary to increase the precision of the theoretical calculations, which is achieved by including more terms in the EFT expansion.

Irrelevant operators are non-renormalizable, and as the energy scale grows, the theory needs counterterms of increasing dimension. Combining (3.15) and (3.16), the dimension of the counterterm for a given diagram is

$$D - 4 = \sum_i (D_i - 4). \tag{3.18}$$

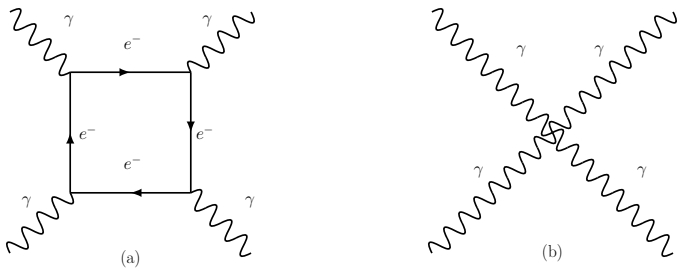

Figure 3.2: (a) Light-by-light scattering at one loop in QED. (b) Effective operator contributing to light-by-light scattering in the Euler-Heisenberg Lagrangian.

For example, let us imagine a Lagrangian truncated to operators up to dimension 5. A diagram with two insertions of dimension 5 operators scales as $A \sim (E/\Lambda)^{(1+1)}$, and therefore dimension 6 counterterms are needed to renormalize it. If we include dimension 6 operators, dimension 8 counterterms are needed, etc. The need for counterterms of ever-increasing dimension would be a fatal flaw for a fundamental theory, as it would loose its predictive power. In the case of an EFT, however, it is totally expected: the theory was designed from the beginning to be valid up to a certain scale Λ, and the breaking down of renormalizability is just a sign that we are getting closer to this scale, and therefore we must use instead the full UV theory, which is free of these troubles.

3.1.1 Example: Euler-Heisenberg Lagrangian for light-by-light scattering

One traditional textbook example of a top-down EFT is the Euler-Heisenberg Lagrangian [161, 162] that describes light-by-light scattering, see for example [151, 153]. The UV theory is Quantum Electrodynamics (QED), where the lowest order of photon scattering proceeds through one loop of charged fermions, as shown in Fig. 3.2(a). The Euler-Heisenberg Lagrangian is obtained by integrating out all the charged fermions, so the only surviving field in the EFT is the photon. The lowest order corresponds to the free Maxwell Lagrangian, with dimension 4, and the next order to dimension-8 operators including four photons, shown in Fig. 3.2(b). Note that is not possible to construct gauge-invariant operators with odd-numbered dimension (since the only gauge-invariant object containing only photons is the field strength tensors, of dimension 2), and all dimension-6 combinations vanish through the equations of motion. The Lagrangian up to dimension-8 operators is

$$\mathscr{L}_{\text{E–H}} = -\frac{1}{4}F_{\mu\nu}F^{\mu\nu} + \frac{\alpha_{\text{em}}^2}{m_e^4}\left[\frac{1}{90}(F_{\mu\nu}F^{\mu\nu})^2 + \frac{7}{360}(F_{\mu\nu}\widetilde{F}^{\mu\nu})^2\right] + \cdots, \tag{3.19}$$

where $F_{\mu\nu} = \partial_\mu A_\nu - \partial_\nu A_\mu$ is the field strength tensor, $\widetilde{F}^{\mu\nu} = \frac{1}{2}\epsilon^{\mu\nu\alpha\beta}F_{\alpha\beta}$ its dual tensor and $\alpha_{\text{em}} = e^2/(4\pi)$ the electromagnetic fine-structure constant.

In the Euler-Heisenberg Lagrangian, the m_e^4 factor is set by the order of the EFT expansion. The rest of the coefficient depends on the details of the UV theory. In particular,

since the light-by-light scattering diagram have 4 electromagnetic vertices, each with one electromagnetic coupling e, the effective Lagrangian must have a factor $e^4 \sim \alpha_{\rm em}^2$. Just by knowing this, we deduce that the amplitude for the scattering of two photons of energy $\sim E_\gamma$ is

$$A(\gamma\gamma \to \gamma\gamma) \sim \frac{\alpha_{\rm em}^2 E_\gamma^4}{m_e^4}. \tag{3.20}$$

The cross section is proportional to $|A|^2$ and has dimension -2, so the phase space must be proportional to E_γ^{-2}:

$$\sigma(\gamma\gamma \to \gamma\gamma) \sim \frac{1}{E_\gamma^{-2}} \left(\frac{\alpha_{\rm em}^2 E_\gamma^4}{m_e^4} \right)^2 = \frac{\alpha_{\rm em}^4 E_\gamma^6}{m_e^8}. \tag{3.21}$$

The full calculation yields [163]

$$\sigma(\gamma\gamma \to \gamma\gamma) = \frac{973}{10125\pi} \frac{\alpha_{\rm em}^4 E_\gamma^6}{m_e^8}. \tag{3.22}$$

3.2 Bottom-up approach

In the Euler-Heisenberg example, the EFT formalism has allowed us to deduce a non-trivial piece of information, that the scattering cross section of two photons depends on E_γ^6, just from the fact that the lowest effective operator has dimension 8 and gauge invariance. This is a general feature of effective theories, and one that we can exploit in the case when we do not know the full UV theory. It is always possible to write down an Effective Lagrangian starting from the low-energy physics in a bottom-up way [157, 158, 164]. The ingredients needed are:

- Energy scale Λ, that sets the limit of validity of the EFT.
- Physical degrees of freedom below Λ. If the EFT is a weakly coupled version of some UV theory, it is clear that the physical degrees of freedom are just the particles with mass $m < \Lambda$. This might not be true in strongly coupled theories: for example, Chiral Perturbation Theory is a EFT of QCD where the physical degrees of freedom are pions rather than quarks and gluons [165–167].
- Symmetries in the low-energy regime. Note that symmetries at low energy are a remnant of symmetries in the UV theory, but not necessary the same. For example, an EFT might exploit an approximate symmetry not present in the full theory.
- Desired accuracy ϵ. Using (3.17), the accuracy fixes the maximum dimension D in the EFT expansion.

All we have to do now is to construct all the local operators $\mathcal{O}_j$ with dimension $D_j \leq D$ from the physical fields and that are compatible with the symmetries. The Effective

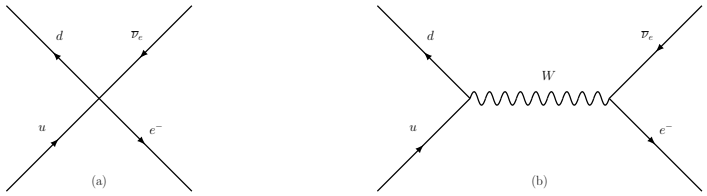

Figure 3.3: Tree-level Feynman diagrams describing β decay in (a) Fermi EFT and (b) SM.

Lagrangian will be the sum of all these allowed operators multiplied by Wilson coefficients of dimension $4 - D_j$. The result is a Lagrangian of the form of Eq. (3.13).

In the simplest case, the energy scale Λ is much higher than any energy experimentally accessible, so we can compute amplitudes to any desired accuracy. In this case, we can retain just the relevant and marginal operators. For example, if there is no NP up to the Grand Unification scale $\Lambda_{\text{GUT}} \sim 10^{16}$GeV, the SM would be a EFT consisting only of relevant and marginal operators capable of accuracies of $\epsilon \sim 10^{-14}$.

The set of all allowed operators of dimension D is a vector space. The operators appearing in the Effective Lagrangian must be a basis in that space, that is, a complete set of independent vectors. Independent means that there cannot be redundant operators when applying the equations of motion, partial integration, Fierz rearrangements, Ward identities, etc. We already saw an example in our toy model of operators that superficially looked different, but were in fact equivalent after applying integration by parts and the equations of motion, with the operators $\phi^2\partial_\mu\phi\partial^\mu\phi$ and ϕ^4 that appeared in Eq. (3.11). The task to obtain an independent set of operators is highly non-trivial[3], but it can be done in a systematic way using the properties of the on-shell amplitudes [170, 171]. One further complication is the number of independent operators up to dimension D grows in an approximately exponential way with D [172], and EFTs expanded to high orders become hard to use in practice.

It is important to remark that the condition of gauge anomaly cancellation depends only on the charge assignment of the fermions of the low-energy theory, and is not spoilt by the presence of effective operators of higher dimension [173].

3.2.1 Example: Fermi theory of the β decay

One historical example of a bottom-up EFT is the Fermi theory of the β decays [174, 175]. The only particles known at the time were the proton, neutron, electron, and the newly-theorized neutrino (actually anti-neutrino), and the energies experimentally accessible were well below the electroweak scale $\Lambda \sim M_W$. The Lagrangian proposed by Fermi, written in terms of the constituent quarks instead of proton and neutron, takes the form [157,

[3] For example, the first attempt [168] to find a basis of dimension-6 operators for the SMEFT theory, that we will study in Section 3.4, included a large number of redundant operators, and one operator was missing. A correct basis was later found in [169].

158]

$$\mathscr{L}_F = C_F(\bar{u}\gamma^\mu P_L d)(\bar{e}\gamma_\mu P_L \nu_e), \tag{3.23}$$

where C_F is a Wilson coefficient of mass dimension -2, and $P_L = \frac{1-\gamma_5}{2}$ is the chiral projector. The tree-level Feynman diagram is shown in Fig. 3.3(a). The cross section of the process $u \to de\bar{\nu}_e$ must be proportional to the square of the Wilson coefficient, and by dimensional analysis it should be

$$\sigma(u \to de\bar{\nu}_e) \sim C_F^2 s, \tag{3.24}$$

where s is the Mandelstam variable corresponding to the center-of-mass energy. This cross section reproduced the low-energy behaviour observed at the time. However, the cross section in the Fermi theory grows without bound as the energy increases, and eventually violates unitarity, marking the end of the validity of the EFT.

The Weinberg-Salam electroweak theory, which is part of the SM, includes a massive gauge boson $W^\pm$ that mediates the β decay. The tree-level amplitude, shown in Fig. 3.3(b), is

$$A(u \to de\bar{\nu}_e) = \left(\frac{-ig}{\sqrt{2}}\right) V_{ud}(\bar{u}\gamma^\mu P_L d)(\bar{e}\gamma^\nu P_L \nu_e)\left(\frac{-ig_{\mu\nu}}{p^2 - M_W^2}\right), \tag{3.25}$$

where g is the $SU(2)$ electroweak coupling and V_{ud} is the element of the CKM matrix. When $p \ll M_W$, we can expand the W propagator, and the amplitude at first order of the expansion is

$$A(u \to de\bar{\nu}_e) = \frac{i}{M_W^2}\left(\frac{-ig}{\sqrt{2}}\right) V_{ud}(\bar{u}\gamma^\mu P_L d)(\bar{e}\gamma_\mu P_L \nu_e) + O(M_W^{-4}). \tag{3.26}$$

This amplitude corresponds to a Lagrangian of the form (3.23) where the Wilson coefficient takes the value

$$C_F = -\frac{g^2}{2M_W^2} V_{ud} = -\frac{4G_F}{\sqrt{2}} V_{ud}. \tag{3.27}$$

G_F is the so-called Fermi constant, and historically was used as the low-energy parameter describing the electroweak interactions. Its numerical value was determined much earlier [176] that the discovery of the W [177, 178] , using the muon decay $\mu^- \to e^- \nu_\mu \bar{\nu}_e$ described by the effective Lagrangian

$$\mathscr{L}_\mu = -\frac{4G_F}{\sqrt{2}}(\bar{\nu}_\mu \gamma^\alpha P_L \mu)(\bar{e}\gamma_\alpha P_L \nu_e). \tag{3.28}$$

3.3 Matching and Running

Let us consider an EFT valid up to a certain energy scale Λ, and another theory that completes it in the UV (either a fundamental theory or another EFT) valid up to $\Lambda' > \Lambda$. Both theories must reproduce the same low-energy physics, that is, the S-matrix elements between light particles must agree. This imposes a set of relations between the parameters of both theories, known as matching conditions. The matching procedure allows us to

obtain the low-energy parameters in terms of the high-energy parameters, but not the other way, since the matching conditions are not bijective (as the high energy theory has more parameters than the low-energy theory).

In order to match the full S-matrix, it is sufficient to match all one-light-particle-irreducible Feynman diagrams, that is, all diagrams that cannot be split by removing only one internal propagator of the particles present in the low-energy theory. Thusly, the matching is performed perturbatively, order by order. When calculating diagrams with quantum loops, the results of the matching will depend on the regularization scheme used. It is better to work in a mass independent scheme, such as dimensional regularization with MS or $\overline{\text{MS}}$ substraction, in order to avoid additional mass scales (*e.g.* a cutoff) that spoil the dimensional power-counting [158]. At one loop, the general form of the matching conditions of the low-energy Wilson coefficient C in terms of the high-energy parameters λ in the $\overline{\text{MS}}$ scheme will be

$$C(\lambda;\mu) = C^{(0)}(\lambda) + \frac{1}{16\pi^2} C^{(1)}(\lambda) \log\frac{\mu}{\Lambda}, \tag{3.29}$$

where μ is introduced by dimensional regularization. Note that the loops introduce a logarithm $\log\mu/\Lambda$. In order to avoid large logarithms, matching is usually performed at the scale $\mu \approx \Lambda$.

After dimensional regularization, Wilson coefficients, the same as any other parameter in the Lagrangian, will depend on μ. Operators will also depend on μ through the wavefunction renormalization of the fields $Z_{ij}(\mu)$,

$$Z_{ij}(\mu)\mathcal{O}_i(\mu) = \mathcal{O}_j^{\text{B}}, \tag{3.30}$$

where $\mathcal{O}_j^{\text{B}}$ is the operator composed of bare fields and $\mathcal{O}_i$ is composed of renormalized fields. Since there can be several operators with the same quantum numbers, the $Z_{ij}(\mu)$ are in general non-diagonal. Requiring that the matrix element of the bare operator $\langle\mathcal{O}_i^{\text{B}}\rangle$ be independent of μ results in the well-known Callan-Symanzik Renormalization Group (RG) equation, one gets

$$\left(\mu\frac{d}{d\mu} + \gamma_{\mathcal{O}_{ij}}(\mu)\right)\langle\mathcal{O}_j(\mu)\rangle = 0, \qquad \gamma_{\mathcal{O}}(\mu) = Z^{-1}\mu\frac{d}{d\mu}Z. \tag{3.31}$$

The product $C_i(\mu)\langle\mathcal{O}_i(\mu)\rangle$ must be also scale independent. Imposing this condition results in a Callan-Symanzik equation for the Wilson coefficients:

$$\left(\mu\frac{d}{d\mu} - \gamma_{\mathcal{O}_{ij}}(\mu)\right)C_j(\mu) = 0. \tag{3.32}$$

By integrating the RG equation, one can obtain the value of the Wilson coefficients at any energy scale within the validity range of that EFT. When the anomalous dimension matrix is not diagonal, the evolution produces the mixing of operators. Therefore, even if some Wilson coefficient is zero at a certain energy scale, it might be non-zero at other energies due to quantum loops effects.

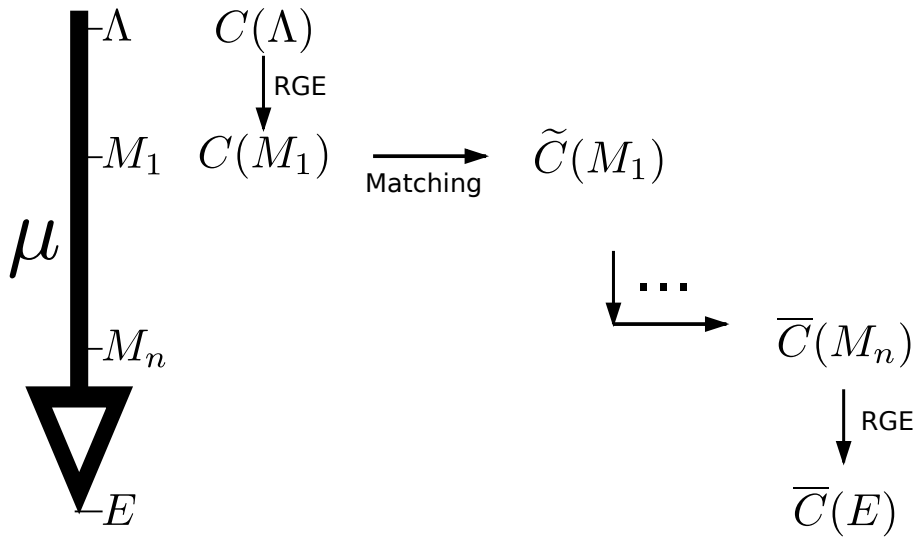

Figure 3.4: Stairway of EFTs from $\mu = \Lambda$ to $\mu = E$. Vertical arrows denote the running of the RG equations for a given theory. Horizontal arrows denote the matching between two theories, performed at the same scale, which is the mass of the heavy particle $M_1, \ldots, M_n$ integrated out.

As noted previously, Feynman diagrams with multiple insertions of operators are renormalized by operators of higher dimension, according to the power counting formula (3.18). This produces mixing of operators with different dimensions, and the RG equations are no longer lineal. For example [158],

$$\mu \frac{d}{d\mu} C_i^{(6)} = \gamma_{ij}^{(6)} C_j^{(6)} + \gamma_{ijk} C_j^{(5)} C_k^{(5)}, \tag{3.33}$$

where the notation $C_i^{(D)}$, $D = 5, 6, \cdots$ has been used to denote a Wilson coefficient for an effective operator $\mathcal{O}_i^{(D)}$ with dimension D.

If the theory also has mass terms, there is also mixing to operators of lower dimension,

$$\mu \frac{d}{d\mu} C_i^{(4)} = \gamma_{ij} C_j^{(4)} + m^2 \widetilde{\gamma}_{ij} C_j^{(6)} + \cdots. \tag{3.34}$$

Comparing the result of the differential equation in Eq. (3.31) with Eq. (3.29), we note that the RG evolution automatically sums large logarithms. In consequence, if one performs the matching procedure at the scale $\mu = \Lambda$, and then runs the RG equations down to the scale of interest $\mu = E$, the Wilson coefficients at the scale E are completely free from large logarithms that may invalidate the perturbative expansion.

To sum up, matching and running provides a workflow to use with theories with several energy scales, illustrated in Fig. 3.4:

1. Start with a theory at some high scale Λ.

2. Run the RG equations for the Wilson coefficients down to M_1, the mass of the heaviest particle.

3. At $\mu = M_1$, match with the EFT where the particle of mass M_1 is integrated out.

4. Repeat steps 1-3 for each particle that must be integrated out at $\mu = M_2, \ldots, M_n$.

5. Run the RG equations down to the energy scale $\mu = E$ of the physical process.

3.4 Standard Model Effective Field Theory

The Standard Model Effective Field Theory (SMEFT) is the EFT obtained when expanding the SM Lagrangian to operators with dimension $D > 4$, retaining all the SM fields and symmetries. The SMEFT is valid up to some energy scale Λ, usually taken to be of the order of a few TeV. Calculations in the SMEFT up to $D = 6$ are predominantly performed in the Warsaw basis, first introduced in [169]. Alternative bases were proposed in [179, 180] and [181]. The Warsaw basis has been extended to dimension 7 [182] and 8 [183].

In the Warsaw basis, the Wilson coefficients are defined to be dimensionless, with explicit prefactors of Λ^{4-D},

$$\mathscr{L}_{\text{SMEFT}} = \mathscr{L}_{\text{SM}} + \frac{1}{\Lambda}\sum_k C_k^{(5)} Q_k^{(5)} + \frac{1}{\Lambda^2}\sum_k C_k^{(6)} Q_k^{(6)} + \cdots, \tag{3.35}$$

where $Q_k^{(n)}$ denote dimension-n operators, and $C_k^{(n)}$ the corresponding Wilson coefficients.

The SMEFT does not contain any dimension 5 operator compatible with the full symmetry of the SM. However, there is one dimension 5 operator that violates the lepton number in $\Delta L = 2$, the Weinberg operator describing a Majorana mass for the neutrinos

$$Q_{\nu\nu} = (\widetilde{\varphi}\ell_p)^T C (\widetilde{\varphi}\ell_r), \tag{3.36}$$

where $C = i\gamma^2\gamma^0$ is the charge conjugation matrix and p, r are flavour indices. After EWSSB, this operator generates a mass term for the neutrinos, with $m_\nu \sim C_{\nu\nu} v^2/\Lambda_\nu$, where v is the Highs vacuum expectation value and Λ_ν the scale of the dimension 5 operator. The smallness of the neutrino masses, $m_\nu \sim 0.1$ eV, means that the Majorana scale must be $\Lambda_\nu \sim 10^{15}$ GeV. This scale is much higher than the scale Λ describing the NP integrated out in the dimension 6 operators. The separation of scales is consistent if the interactions at Λ conserve lepton number and therefore do not contribute to the Weinberg operator.

The dimension 6 operators are classified according to their field contents. The four fermion operators, that are the most numerous class, are further subdivided according to the chiral structure of their currents. In total, there are 2499 dimension 6 effective operators. Of these, 1350 operators are CP-even and 1149 are CP-odd. The SMEFT also contains dimension 6 operators that violate the baryon number in $\Delta B = \Delta L = \pm 1$, which

X^3		$X^2\varphi^2$	
Q_G	$f^{ABC}G^{A\nu}_{\mu}G^{B\rho}_{\nu}G^{C\mu}_{\rho}$	$Q_{\varphi G}$	$\varphi^\dagger\varphi G^A_{\mu\nu}G^{A\mu\nu}$
$Q_{\widetilde{G}}$	$f^{ABC}\widetilde{G}^{A\nu}_{\mu}G^{B\rho}_{\nu}G^{C\mu}_{\rho}$	$Q_{\varphi B}$	$\varphi^\dagger\varphi B_{\mu\nu}B^{\mu\nu}$
Q_W	$\epsilon^{IJK}W^{I\nu}_{\mu}W^{J\rho}_{\nu}W^{K\mu}_{\rho}$	$Q_{\varphi W}$	$\varphi^\dagger\varphi W^I_{\mu\nu}W^{I\mu\nu}$
$Q_{\widetilde{W}}$	$\epsilon^{IJK}\widetilde{W}^{I\nu}_{\mu}W^{J\rho}_{\nu}W^{K\mu}_{\rho}$	$Q_{\varphi WB}$	$\varphi^\dagger\tau^I\varphi W^I_{\mu\nu}B^{\mu\nu}$
φ^6		$Q_{\varphi\widetilde{G}}$	$\varphi^\dagger\varphi\widetilde{G}^A_{\mu\nu}G^{A\mu\nu}$
Q_φ	$(\varphi^\dagger\varphi)^3$	$Q_{\varphi\widetilde{B}}$	$\varphi^\dagger\varphi\widetilde{B}_{\mu\nu}B^{\mu\nu}$
φ^4D^2		$Q_{\varphi\widetilde{W}}$	$\varphi^\dagger\varphi\widetilde{W}^I_{\mu\nu}W^{I\mu\nu}$
$Q_{\varphi\Box}$	$(\varphi^\dagger\varphi)\Box(\varphi^\dagger\varphi)$	$Q_{\varphi\widetilde{W}B}$	$\varphi^\dagger\tau^I\varphi\widetilde{W}^I_{\mu\nu}B^{\mu\nu}$
$Q_{\varphi D}$	$(\varphi^\dagger D^\mu\varphi)^*(\varphi^\dagger D_\mu\varphi)$		

Table 3.1: SMEFT purely bosonic operators [169].

would describe proton decays. The full list of dimension 6 operators in the Warsaw basis is reproduced in Tables 3.1, 3.2, 3.3 and 3.4. In the tables, the flavour indices are omitted; there is an index for each fermion in the operator. For example, the expression for the operators $Q_{\varphi\ell(1)}$ and $Q_{\ell q(1)}$ with their explicit flavour indices become

$$\begin{aligned} Q^{ij}_{\varphi\ell(1)} &= \left(\varphi^\dagger i\overleftrightarrow{D}_\mu\varphi\right)(\bar{\ell}_i\gamma^\mu\ell_j)\,, \\ Q^{ijkl}_{\ell q(1)} &= (\bar{\ell}_i\gamma_\mu\ell_j)(\bar{q}_k\gamma^\mu q_l)\,. \end{aligned} \tag{3.37}$$

The notation $\overleftrightarrow{D}$ used to construct Hermitian derivative operators including the Higgs filed has the following meaning:

$$\begin{aligned} \varphi^\dagger i\overleftrightarrow{D}_\mu\varphi &\equiv i\varphi^\dagger(D_\mu - \overleftarrow{D}_\mu)\varphi \equiv i\varphi^\dagger(D_\mu\varphi) - i(D_\mu\varphi)^\dagger\varphi\,, \\ \varphi^\dagger i\overleftrightarrow{D}^I_\mu\varphi &\equiv i\varphi^\dagger(\tau^I D_\mu - \overleftarrow{D}_\mu\tau^I)\varphi \equiv i\varphi^\dagger\tau^I(D_\mu\varphi) - i(D_\mu\varphi)^\dagger\tau^I\varphi\,. \end{aligned} \tag{3.38}$$

One effect of the inclusion of dimension-6 SMEFT operators in the SM physics is the shift of the minimum of the Higgs potential from v to v_T [184] due to the additional term in the Higgs potential introduced by the effective operator Q_φ in Table 3.1. The new minimum of the potential is given by

$$v_T = v\left(1 + \frac{3C_\varphi v^2}{8\lambda}\right), \tag{3.39}$$

where λ is the quartic Higgs coupling and C_φ is the coefficient corresponding to the operator Q_φ.

The value of v in the SM is obtained from the measurement of G_F in μ decay. Several effective operators contribute to the muon decays of Eq. (3.28), modifying the definition

$\psi^2\varphi^3$		$\psi^2\varphi^2 D$	
$Q_{u\varphi}$	$(\varphi^\dagger\varphi)(\bar{q}u_R\widetilde{\varphi})$	$Q_{\varphi\ell(1)}$	$\left(\varphi^\dagger i\overleftrightarrow{D}_\mu\varphi\right)(\bar{\ell}\gamma^\mu\ell)$
$Q_{d\varphi}$	$(\varphi^\dagger\varphi)(\bar{q}d_R\varphi)$	$Q_{\varphi\ell(3)}$	$\left(\varphi^\dagger i\overleftrightarrow{D}^I_\mu\varphi\right)(\bar{\ell}\tau^I\gamma^\mu\ell)$
$Q_{e\varphi}$	$(\varphi^\dagger\varphi)(\bar{\ell}e_R\varphi)$	$Q_{\varphi e}$	$\left(\varphi^\dagger i\overleftrightarrow{D}_\mu\varphi\right)(\bar{e}_R\gamma^\mu e_R)$
$\psi^2 X\varphi$		$Q_{\varphi q(1)}$	$\left(\varphi^\dagger i\overleftrightarrow{D}_\mu\varphi\right)(\bar{q}\gamma^\mu q)$
Q_{eW}	$(\bar{\ell}\sigma^{\mu\nu}e_R)\tau^I\varphi W^I_{\mu\nu}$	$Q_{\varphi q(3)}$	$\left(\varphi^\dagger i\overleftrightarrow{D}^I_\mu\varphi\right)(\bar{q}\tau^I\gamma^\mu q)$
Q_{eB}	$(\bar{\ell}\sigma^{\mu\nu}e_R)\varphi B_{\mu\nu}$	$Q_{\varphi u}$	$\left(\varphi^\dagger i\overleftrightarrow{D}_\mu\varphi\right)(\bar{u}_R\gamma^\mu u_R)$
Q_{uG}	$(\bar{q}\sigma^{\mu\nu}T^A u_R)\widetilde{\varphi}G^A_{\mu\nu}$	$Q_{\varphi d}$	$\left(\varphi^\dagger i\overleftrightarrow{D}_\mu\varphi\right)(\bar{d}_R\gamma^\mu d_R)$
Q_{uW}	$(\bar{q}\sigma^{\mu\nu}u_R)\tau^I\widetilde{\varphi}W^I_{\mu\nu}$	$Q_{\varphi ud}$	$(\widetilde{\varphi}^\dagger iD_\mu\varphi)(\bar{u}_R\gamma^\mu d_R)+\text{h.c.}$
Q_{uB}	$(\bar{q}\sigma^{\mu\nu}u_R)\widetilde{\varphi}B_{\mu\nu}$		
Q_{dG}	$(\bar{q}\sigma^{\mu\nu}T^A d_R)\varphi G^A_{\mu\nu}$		
Q_{dW}	$(\bar{q}\sigma^{\mu\nu}d_R)\tau^I\varphi W^I_{\mu\nu}$		
Q_{dB}	$(\bar{q}\sigma^{\mu\nu}d_R)\varphi B_{\mu\nu}$		

Table 3.2: SMEFT mixed operators involving bosons and fermions [169].

of the Fermi constant [184, 185],

$$\frac{4G_F}{\sqrt{2}} = \frac{2}{v_T^2} - C_{\ell\ell}^{2112} - C_{\ell\ell}^{1221} + 2C_{\varphi\ell(3)}^{11} + 2C_{\varphi\ell(3)}^{22}. \tag{3.40}$$

Here $C_{\varphi\ell(3)}$ and $C_{\ell\ell}$ are the coefficients of the operators $Q_{\varphi q(3)}$ (Table 3.2) and $Q_{\ell\ell}$ (Table 3.3), respectively.

The mass matrix of the fermions is also modified by dimension-6 operators,

$$M_\psi = \frac{v_T}{\sqrt{2}}\left(y_\psi - \frac{v^2}{2}C^*_{\psi\varphi}\right), \tag{3.41}$$

where $\psi = u, d, e$. In general, the mass matrix is no longer proportional to the Yukawa matrix y_ψ, so it is not possible to simultaneously diagonalize them. As a consequence, the elements of the CKM matrix are also affected. The authors of Ref. [186] propose that the elements of the CKM matrix in the SMEFT context should determined from a set of four input observables, which must be accurately measured and theoretically clean, depending on few SMEFT Wilson coefficients. The observables chosen are:

- The ratio $\Gamma(K^- \to \mu^-\overline{\nu}_\mu)/\Gamma(\pi^- \to \mu^-\overline{\nu}_\mu)$ to determine $|V_{us}|^2/|V_{ud}|^2$. The ratio between these two decays is chosen in order to minimize the SM dependence on the lattice inputs of the form factors.

- The decay rate $\Gamma(B^- \to \tau^-\overline{\tau})$ is used to determine $|V_{ub}|^2$.

$(\bar{L}L)(\bar{L}L)$	
$Q_{\ell\ell}$	$(\bar{\ell}\gamma_\mu\ell)(\bar{\ell}\gamma^\mu\ell)$
$Q_{qq(1)}$	$(\bar{q}\gamma_\mu q)(\bar{q}\gamma^\mu q)$
$Q_{qq(3)}$	$(\bar{q}\gamma_\mu\tau^I q)(\bar{q}\gamma^\mu\tau^I q)$
$Q_{\ell q(1)}$	$(\bar{\ell}\gamma_\mu\ell)(\bar{q}\gamma^\mu q)$
$Q_{\ell q(3)}$	$(\bar{\ell}\gamma_\mu\tau^I\ell)(\bar{q}\gamma^\mu\tau^I q)$
$(\bar{R}R)(\bar{R}R)$	
Q_{ee}	$(\bar{e}_R\gamma_\mu e_R)(\bar{e}_R\gamma^\mu e_R)$
Q_{uu}	$(\bar{u}_R\gamma_\mu u_R)(\bar{u}_R\gamma^\mu u_R)$
Q_{dd}	$(\bar{d}_R\gamma_\mu d_R)(\bar{d}_R\gamma^\mu d_R)$
Q_{eu}	$(\bar{e}_R\gamma_\mu e_R)(\bar{u}_R\gamma^\mu u_R)$
Q_{ed}	$(\bar{e}_R\gamma_\mu e_R)(\bar{d}_R\gamma^\mu d_R)$
$Q_{ud(1)}$	$(\bar{u}_R\gamma_\mu u_R)(\bar{d}_R\gamma^\mu d_R)$
$Q_{ud(8)}$	$(\bar{u}_R\gamma_\mu T^A u_R)(\bar{d}_R\gamma^\mu T^A d_R)$

$(\bar{L}L)(\bar{R}R)$	
$Q_{\ell e}$	$(\bar{\ell}\gamma_\mu\ell)(\bar{e}_R\gamma^\mu e_R)$
$Q_{\ell u}$	$(\bar{\ell}\gamma_\mu\ell)(\bar{u}_R\gamma^\mu u_R)$
$Q_{\ell d}$	$(\bar{\ell}\gamma_\mu\ell)(\bar{d}_R\gamma^\mu d_R)$
Q_{qe}	$(\bar{q}\gamma_\mu q)(\bar{e}_R\gamma^\mu e_R)$
$Q_{qu(1)}$	$(\bar{q}\gamma_\mu q)(\bar{u}_R\gamma^\mu u_R)$
$Q_{qu(8)}$	$(\bar{q}\gamma_\mu T^A q)(\bar{u}_R\gamma^\mu T^A u_R)$
$Q_{qd(1)}$	$(\bar{q}\gamma_\mu q)(\bar{d}_R\gamma^\mu d_R)$
$Q_{qd(8)}$	$(\bar{q}\gamma_\mu T^A q)(\bar{d}_R\gamma^\mu T^A d_R)$
$(\bar{L}R)(\bar{R}L)$	
$Q_{\ell edq}$	$(\bar{\ell}^j e_R)(\bar{d}_R q^j)+\text{h.c.}$
$(\bar{L}R)(\bar{L}R)$	
$Q_{quqd(1)}$	$(\bar{q}^j u_R)\epsilon_{jk}(\bar{q}^k d_R)+\text{h.c.}$
$Q_{quqd(8)}$	$(\bar{q}^j T^A u_R)\epsilon_{jk}(\bar{q}^k T^A d_R)+\text{h.c.}$
$Q_{\ell equ(1)}$	$(\bar{\ell}^j e_R)\epsilon_{jk}(\bar{q}^k u_R)+\text{h.c.}$
$Q_{\ell equ(3)}$	$(\bar{\ell}^j\sigma_{\mu\nu}e_R)\epsilon_{jk}(\bar{q}^k\sigma^{\mu\nu}u_R)+\text{h.c.}$

Table 3.3: SMEFT purely fermionic operators which preserve Baryon number [169].

Baryon-number-violating	
$Q_{duq\ell}$	$(d_R^T C u_R)(q^T C\ell)+\text{h.c.}$
Q_{qque}	$(q^T C q)(u_R^T C e_R)+\text{h.c.}$
$Q_{qqq\ell}$	$\epsilon_{il}\epsilon_{jk}(q_i^T C q_j)(q_k^T C\ell_l)+\text{h.c.}$
Q_{duue}	$(d_R^T C u_R)(u_R^T C e_R)+\text{h.c.}$

Table 3.4: SMEFT Baryon-number-violating operators [169].

- The mass difference ΔM_d of the oscillation of the neutral mesons $B - \overline{B}$ is used to determine the product $|V_{tb}V_{td}|$.
- The mass difference ΔM_s of the oscillation of the neutral mesons $B_S - \overline{B}_S$ is used to determine the product $|V_{tb}V_{ts}|$.

The rest of the elements of the CKM matrix, or equivalently the Wolfenstein parameters defined in Eq. (2.20), can be extracted from this four quantities [186].

The one loop anomalous dimension matrices for the Warsaw basis were described in [184, 187–189]. These matrices include the renormalization of SM and SMEFT operators generated only by the dimension 6 operators. The effect of the Weinberg operator in (3.33) is usually considered negligible when assuming a separation of scales for lepton number violating and lepton number conserving NP.

3.5 Weak Effective Theory

The Weak Effective Theory (WET) is an EFT describing the physics below the electroweak scale $\Lambda_{\text{EW}} \sim M_W$. The WET contains the photon, gluon, all the leptons and all quarks except the top. This theory has operators obtained by the integration of the heavy SM particles, in addition to the new operators constructed from light fields in a bottom-up way. The symmetry group in this energy regime is $SU(3)_C \times U(1)_{em}$, that do not mix operators with different flavour quantum numbers.

Bases for the WET can be found in [185, 190–192], together with their RG evolution and matching conditions to the SMEFT. We will instead use a "traditional" basis (see e.g. [193, 194]), which is the same used internally by `flavio` [195], which is the routine that we use for the global fits, and fully characterized in [196].

The set of operators traditionally used in order to describe $|\Delta b| = |\Delta s| = 1$ decays is [193, 194, 197, 198]

$$\mathscr{L}_{\text{WET}_{bs}} = \frac{4G_F}{\sqrt{2}} V_{tb}V_{ts}^* \frac{\alpha_e}{4\pi} \left(\frac{m_b}{e} \sum_{j=7,8} (C_j O_j + C'_j O'_j) + \sum_{j=9,10,S,P,\nu} (C_j O_j + C'_j O'_j) \right), \tag{3.42}$$

with the effective operators

$$\begin{aligned}
O_7 &= (\bar{s}_L \sigma^{\mu\nu} b_R) F_{\mu\nu} & O'_7 &= (\bar{s}_R \sigma^{\mu\nu} b_L) F_{\mu\nu} \\
O_8 &= (\bar{s}_L \sigma^{\mu\nu} T^a b_R) G^a_{\mu\nu} & O'_8 &= (\bar{s}_R \sigma^{\mu\nu} T^a b_L) G^a_{\mu\nu} \\
O^\ell_9 &= (\bar{s}_L \gamma^\mu b_L)(\bar{e}_\ell \gamma_\mu e_\ell) & O'^\ell_9 &= (\bar{s}_R \gamma^\mu b_R)(\bar{e}_\ell \gamma_\mu e_\ell) \\
O^\ell_{10} &= (\bar{s}_L \gamma^\mu b_L)(\bar{e}_\ell \gamma_\mu \gamma_5 e_\ell) & O'^\ell_{10} &= (\bar{s}_R \gamma^\mu \gamma_5 b_R)(\bar{e}_\ell \gamma_\mu \gamma_5 e_\ell) \\
O^\ell_S &= (\bar{s}_L b_R)(\bar{e}_\ell e_\ell) & O'^\ell_S &= (\bar{s}_R b_L)(\bar{e}_\ell e_\ell) \\
O^\ell_P &= (\bar{s}_L b_R)(\bar{e}_\ell \gamma_5 e_\ell) & O'^\ell_P &= (\bar{s}_R b_L)(\bar{e}_\ell \gamma_5 e_\ell) \\
O^\ell_\nu &= 2(\bar{s}_L \gamma^\mu b_L)(\bar{\nu}_\ell \gamma_\mu P_L \nu_\ell) & O'^\ell_\nu &= 2(\bar{s}_R \gamma^\mu b_R)(\bar{\nu}_\ell \gamma_\mu P_L \nu_\ell)
\end{aligned} \tag{3.43}$$

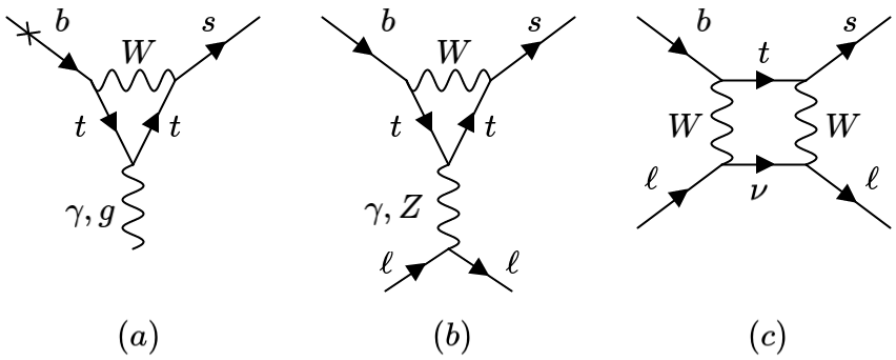

Figure 3.5: Example of SM Feynman diagrams contributing to WET operators: (a) penguin diagrams contributing to C_7 and C_8, (b) penguin diagrams contributing to C_9 and C_{10}, (c) box diagrams contributing to C_9, C_{10}.

The EFT scale has been factored out as $G_F \sim M_W^{-2}$, and therefore the Wilson coefficients are dimensionless. The primed operators O'_j are chirality-flipped version of the un-primed ones O_j.

The dimension-5 magnetic and chromomagnetic moment operators O_7 and O_8 receive contributions from SM penguin diagrams, as shown in Fig. 3.5(a). The dimension-6 operators O_9, O_{10} and O_ν also receive contributions from SM penguin and box diagrams, shown in Fig. 3.5(b) and Fig. 3.5(c) respectively. The chirality-flipped operators, as well as the scalar operator O_S and the pseudoscalar operator O_P, do not receive any contributions from the SM. For the operators with SM contributions, we can split their Wilson coefficients in a SM part, $C_i^{\rm SM}$, and a NP part, $C_i^{\rm NP}$:

$$C_i = C_i^{\rm SM} + C_i^{\rm NP}. \tag{3.44}$$

Operators that have an SM part tend to produce enhanced contributions to the physical observables, as compared to operators that are purely NP. This can be seen from the general dependence of the amplitude-squared for a process in the EFT,

$$|A|^2 \sim |C_i|^2 \sim (C_i^{\rm SM})^2 + 2C_i^{\rm SM}{\rm Re}C_i^{\rm NP} + |C_i^{\rm NP}|^2\,, \tag{3.45}$$

where the term $|C_i^{\rm NP}|^2$ is of order Λ^{-4} and therefore is suppressed compared to $2C_i^{\rm SM}{\rm Re}C_i^{\rm NP}$, which is of order Λ^{-2}.

The matching conditions from the SM to the WET at $\mu_b = 4.8$ GeV can be computed by using `flavio`. We have obtained the following results:

$$\begin{aligned} C_7^{\rm SM}(\mu_b) &= -0.318\,, & C_8^{\rm SM}(\mu_b) &= -0.173\,, \\ C_9^{\ell\ {\rm SM}}(\mu_b) &= 4.053\,, & C_{10}^{\ell\ {\rm SM}}(\mu_b) &= -4.189\,, \\ C_\nu^{\ell\ {\rm SM}}(\mu_b) &= -6.403\,. \end{aligned} \tag{3.46}$$

Notice that the matching is independent of the flavour ℓ of the charged leptons, and that $C_9^{\ell\,\mathrm{SM}}(\mu_b) \approx -C_{10}^{\ell\,\mathrm{SM}}(\mu_b)$. The first property is a consequence of the LFU in the SM, and the second property is due to the $V-A$ (vector minus axial) structure of the electroweak interactions.

For our studies using EFT of the B anomalies, we will need the expressions for the differential observables of $B \to K^{(*)}\ell^+\ell^-$ decays in the WET. Since the formulae are quite long, they have been included in Appendix A. We have analytically computed a numerical approximation to $R_{K^{*0}}$ as a function of $C_9^{\mu\,\mathrm{NP}}$, $C_{10}^{\mu\,\mathrm{NP}}$ in the region $1.1 \le q^2 \le 6.0\,\mathrm{GeV}^2$. After integration and some approximations regarding the scalar products of final state momenta, we obtain [1]:

$$R_{K^{*0}} \simeq \frac{0.9875 + 0.1759\,\mathrm{Re}\,C_9^{\mu\,\mathrm{NP}} - 0.2954\,\mathrm{Re}\,C_{10}^{\mu\,\mathrm{NP}} + 0.0212|C_9^{\mu\,\mathrm{NP}}|^2 + 0.0350|C_{10}^{\mu\,\mathrm{NP}}|^2}{1 \quad + 0.1760\,\mathrm{Re}\,C_9^{e\,\mathrm{NP}} - 0.3013\,\mathrm{Re}\,C_{10}^{e\,\mathrm{NP}} + 0.0212|C_9^{e\,\mathrm{NP}}|^2 + 0.0357|C_{10}^{e\,\mathrm{NP}}|^2} \qquad (1.1 \le q^2 \le 6.0\,\mathrm{GeV}^2) \tag{3.47}$$

We have checked that this approximation reproduces the `flavio`-computed value of $R_{K^{*0}}$ to better than 4% in a large region of the parameter space.

In the $|\Delta b| = |\Delta c| = 1$ sector, the WET Lagrangian reads [199, 200]

$$\mathscr{L}_{\mathrm{WET}\,bc} = -\frac{G_F}{\sqrt{2}} V_{cb} \left(C_T O_T + \sum_{j=V,S} (C_{jL} O_{jL} + C_{jR} O_{jR}) \right), \tag{3.48}$$

with the effective operators

$$\begin{aligned} O_{VL}^{\ell} &= (\bar{c}_L \gamma^\mu b_L)(\bar{e}_{\ell L} \gamma_\mu \nu_{\ell L}) & O_{VR}^{\ell} &= (\bar{c}_R \gamma^\mu b_R)(\bar{e}_{\ell L} \gamma_\mu \nu_{\ell L}) \\ O_{SL}^{\ell} &= (\bar{c}_R b_L)(\bar{e}_{\ell R} \nu_{\ell L}) & O_{SR}^{\ell} &= (\bar{c}_L b_R)(\bar{e}_{\ell R} \nu_{\ell L}) \\ O_T^{\ell} &= (\bar{c}_R \sigma^{\mu\nu} b_L)(\bar{e}_{\ell R} \sigma_{\mu\nu} \nu_{\ell L}). \end{aligned} \tag{3.49}$$

The only operator with a SM contribution is O_{VL}^{ℓ}. At tree level, the matching condition, from the integration of a W boson, is $C_{VL}^{\mathrm{SM}\,\ell} = 1$.

The expressions for the differential observables in the $B \to D^{(*)}\ell\nu$ decays can be found in Appendix A (section A.4). The dependence of the $R_{D^{(*)}}$ ratios on the Wilson coefficients is given by [201, 202]:

$$\begin{aligned} R_{D^{(*)}}^{\ell} &= R_{D^{(*)}}^{\ell,\mathrm{SM}} \frac{|1 + C_{VL}^{\tau\,\mathrm{NP}}|^2}{(|1 + C_{VL}^{e\,\mathrm{NP}}|^2 + |1 + C_{VL}^{\mu\,\mathrm{NP}}|^2)/2}, \\ R_{D^{(*)}}^{\mu} &= R_{D^{(*)}}^{\mu,\mathrm{SM}} \frac{|1 + C_{VL}^{\tau\,\mathrm{NP}}|^2}{|1 + C_{VL}^{\mu\,\mathrm{NP}}|^2}. \end{aligned} \tag{3.50}$$

Finally, we will also consider the $|\Delta b| = |\Delta s| = 2$ sector corresponding to the oscillations of the neutral mesons B_s. The WET Lagrangian in this sector is [194]:

$$\mathscr{L}_{\Delta B=2}^{\mathrm{NP}} = -\frac{4G_F}{\sqrt{2}} \left(V_{tb} V_{ts}^*\right)^2 \left[C_{bs}^{LL} O_{bs}^{LL} + \mathrm{h.c.}\right], \tag{3.51}$$

where C_{bs}^{LL} is the Wilson coefficient for the effective operator O_{bs}^{LL} defined as

$$O_{bs}^{LL} = \left(\bar{s}_L \gamma_\mu b_L\right)^2 . \tag{3.52}$$

This operator also receives a SM contribution in addition to the NP part. The SM contribution comes from the one-loop box diagram, and is calculated as [203]

$$C_{bs}^{LL\,\mathrm{SM}} = \frac{\sqrt{2} G_F M_W^2 \hat{\eta}_B S_0(x_t)}{16\pi^2} = 1.3397 \times 10^{-3}, \tag{3.53}$$

where $\hat{\eta}_B \approx 0.83798$ contains perturbative two-loop QCD corrections [204], $x_t = m_t^2/M_W^2$ and $S_0(x_t) = 2.36853$ is the Inami-Lim function for the box diagram [205].

Chapter 4

New Physics in Flavour

At the present time, there are discrepancies with the SM predictions in several observables involving B decays. In Chapter 2, some interesting experimental results concerning the semileptonic decays of the B mesons have been reviewed. These B anomalies show a disagreement with the SM at the level of statistical significance level of around $3\,\sigma$ in some cases. If confirmed by further measurements, these anomalies could radically change our paradigms about flavour-dependant interactions. In particular, FCNC constitute an exceptionally appropriate testground, since the SM suppressions can be easily dodged with NP, in consequence giving rise to sizeable contributions.

As discussed in Chapter 3, EFT can be used to describe the B anomalies and any other deviation from the SM in a model-independent way. But EFT are a descriptive tool, as the NP particles are integrated out and their nature can not be investigated. In order to go from the description to an explanation of NP, we need to consider specific models that are compatible with the EFT approach.

A complete revision of all theoretical proposals to explain the B decays is beyond the scope of this thesis. For a non-exhaustive list please check, for example, [206–233]. A recent review can be found on Ref. [234], and references therein. We will focus in this thesis on some of the simpler and most popular families of models, namely leptoquarks, W' and Z' bosons. This section provides some generalities of these models and few details needed for our analysis.

Apart from the B anomalies, we also will study the axions, proposed as a solution of the strong CP problem and also a possible component of Dark Matter, two of the open problems of the SM presented in Section 2.1.1. In particular, we will explore the possibility of pseudo-scalar particles with flavour-dependent couplings to the SM quarks and leptons. For completeness, a brief introduction to this issue is included in Section 4.3.

Finally, we discuss the Minimal Flavour Violation *ansatz* which proposes the flavour structure for any New Physics model. This *ansatz* will be an inspiration for our studies, although we do not follow it strictly.

4.1 Leptoquarks

Leptoquarks are hypothetical particles that can decay into a quark and a lepton. Leptoquarks appear naturally in many grand-unification scenarios [235–239]. Since leptoquarks couple to two fermions, they can be either scalars or vector bosons. Given that quarks are triplets of $SU(3)_C$ and leptons are singlets, leptoquarks must appear in a tridimensional representation of the colour group. Consequently, they cannot decay into a pair of leptons. Leptoquarks in the **3** representation of $SU(3)_C$ cannot decay into a pair of quarks either, and therefore they conserve both baryonic and leptonic numbers. According to their $SU(2)_L$, leptoquarks can belong to the **3** representation coupling two weak isospin doublets, to the **2** representation coupling one doublet and one singlet, or in the **1** representation coupling two singlets or two doublets. The scalar leptoquarks and vector leptoquarks that couple to the SM fermions (*i.e.* assuming no right-handed neutrinos) are summarized in Table 4.1 and 4.2 respectively [240]:

- The scalar leptoquarks in the $\overline{\mathbf{3}}$ representation of $SU(3)_C$ are denoted by the letter S, with their couplings to one lepton and one quark being y and their couplings to two quarks being z.

- The scalar leptoquarks in the **3** representation of $SU(3)_C$ are denoted by the letter R, and the letter y is used for their couplings to one quark and one lepton.

- The vector leptoquarks in the $\overline{\mathbf{3}}$ representation of $SU(3)_C$ are denoted by the letter V, with their couplings to one lepton and one quark being x and their couplings to two quarks being w.

- The vector leptoquarks in the **3** representation of $SU(3)_C$ are denoted by the letter U, and the letter x is used for their couplings to one quark and one lepton.

Each leptoquark, and their corresponding couplings, are labelled by a subscript indicating the $SU(2)_L$ representation. In the cases where two leptoquarks have the same $SU(3)_C$ and $SU(2)_L$ quantum numbers, one of them is indicated by a tilde. Finally, each coupling has a superscript corresponding to the chirality of the fermions.

Different leptoquark models have been proposed as solutions to the $R_{K^{(*)}}$ and $R_{D^{(*)}}$ anomalies. The leptoquarks that can mediate $b \to s\ell^+\ell^-$ transitions at tree level are S_3, R_2, $\widetilde{R}_2$, $\widetilde{S}_1$, U_3, V_2 and U_1 [241]. $b \to c\ell\nu$ transitions can be mediated by S_3, R_2, S_1, U_3, V_2 and U_1 [242, 243]. The most popular models to explain concurrently $R_{K^{(*)}}$ and $R_{D^{(*)}}$ are the vector leptoquark U_1 [244–249] and a combination of the scalar leptoquarks S_1 and S_3 [244, 250–258]. The Feynman diagrams of the U_1-mediated $b \to s\ell^+\ell^-$ and $b \to c\ell\nu$ transitions are depicted in Fig. 4.1.

The matching conditions for the leptoquarks to the SMEFT were obtained in [201, 259]. In particular, a leptoquark U_1 with mass M_U, is matched to the SMEFT at the scale

LQ	$SU(3)_C$	$SU(2)_L$	Y	Coupling to fermions
S_3	$\overline{\mathbf{3}}$	$\mathbf{3}$	$\frac{1}{3}$	$y_3^{LL}\overline{q}^C\epsilon(\tau S_3)\ell + z_3^{LL}\overline{q}^C\epsilon(\tau S_3)^\dagger q + \text{h.c.}$
R_2	$\mathbf{3}$	$\mathbf{2}$	$\frac{7}{6}$	$-y_2^{RL}\overline{u}_R R_2\epsilon\ell + y_2^{LR}\overline{e}_R R_2^* q + \text{h.c.}$
$\widetilde{R}_2$	$\mathbf{3}$	$\mathbf{2}$	$\frac{1}{6}$	$-\widetilde{y}_2^{RL}\overline{d}_R\widetilde{R}_2\epsilon\ell + \text{h.c.}$
$\widetilde{S}_1$	$\overline{\mathbf{3}}$	$\mathbf{1}$	$\frac{4}{3}$	$\widetilde{y}_1^{RR}\overline{d}_R^C\widetilde{S}_1 e_R + \widetilde{z}_1^{RR}\overline{u}_R^C\widetilde{S}_1^* u_R + \text{h.c.}$
S_1	$\overline{\mathbf{3}}$	$\mathbf{1}$	$\frac{1}{3}$	$y_1^{LL}\overline{q}^C S_1\epsilon\ell + y_1^{RR}\overline{u}_R^C S_1 e_R + z_1^{LL}\overline{q}^C S_1^*\epsilon q + z_1^{RR}\overline{u}_R^C S_1^* d_R + \text{h.c.}$

Table 4.1: Properties of the scalar leptoquarks. τ are the Pauli matrices and ϵ the antisymmetric dimension 2 tensor. Flavour and gauge indices have been omitted [240].

LQ	$SU(3)_C$	$SU(2)_L$	Y	Coupling to fermions
U_3	$\mathbf{3}$	$\mathbf{3}$	$\frac{2}{3}$	$x_3^{LL}\overline{q}\gamma^\mu(\tau U_{3\mu})\ell + \text{h.c.}$
V_2	$\overline{\mathbf{3}}$	$\mathbf{2}$	$\frac{5}{6}$	$x_2^{RL}\overline{d}_R^C\gamma^\mu V_{2\mu}\epsilon\ell + x_2^{LR}\overline{q}^C\gamma^\mu\epsilon V_{2\mu} e_R + w_2^{LR}\overline{q}^C\gamma^\mu V_{2\mu}^* u_R + \text{h.c.}$
$\widetilde{V}_2$	$\overline{\mathbf{3}}$	$\mathbf{2}$	$-\frac{1}{6}$	$\widetilde{x}_2^{RL}\overline{u}_R^C\gamma^\mu\widetilde{V}_{2\mu}\epsilon\ell + \widetilde{w}_2^{RL}\overline{d}_R^C\gamma^\mu\widetilde{V}_{2\mu}^* q + \text{h.c.}$
$\widetilde{U}_1$	$\mathbf{3}$	$\mathbf{1}$	$\frac{5}{3}$	$\widetilde{x}_1^{RR}\overline{u}_R\gamma^\mu\widetilde{U}_{1\mu} e_R + \text{h.c.}$
U_1	$\mathbf{3}$	$\mathbf{1}$	$\frac{2}{3}$	$x_1^{LL}\overline{q}\gamma^\mu U_{1\mu}\ell + x_1^{RR}\overline{d}_R\gamma_\mu U_{1\mu} e_R + \text{h.c.}$

Table 4.2: Properties of the vector leptoquarks. τ are the Pauli matrices and ϵ the antisymmetric dimension 2 tensor. Flavour and gauge indices have been omitted [240].

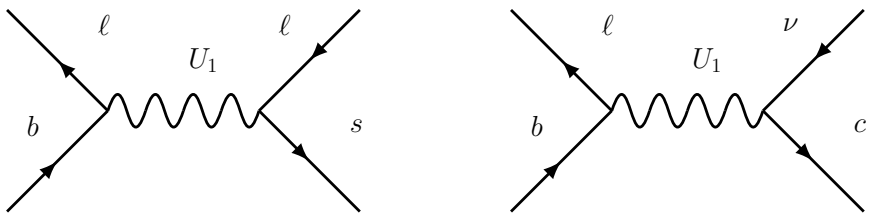

Figure 4.1: Vector leptoquark U_1 (a) mediating a $b \to s\ell^+\ell^-$ transition, (b) mediating a $b \to c\ell\nu$ transition.

Λ following the conditions

$$C_{\ell q(1)}^{ijkl} = C_{\ell q(3)}^{ijkl} = \frac{-\Lambda^2}{2M_U^2}(x_1^{LL})_{li}(x_1^{LL})_{kj}^*,$$
$$C_{ed}^{ijkl} = -\frac{1}{2}C_{ledq}^{ijkl} = \frac{-\Lambda^2}{M_U^2}(x_1^{RR})_{li}(x_1^{RR})_{kj}^*. \tag{4.1}$$

The matching has to be performed at an energy scale $\Lambda \sim M_U$, as indicated in the workflow of Fig. 3.4.

For the scalar leptoquark S_3 with mass M_{S_3}, we will be interested in the contribution to WET coefficients. The Wilson coefficients $C_{9,10}^{\mu\,\mathrm{NP}}$ arise at the tree level and are given by [260],

$$C_9^{\mu\,\mathrm{NP}} = -C_{10}^{\mu\,\mathrm{NP}} = \frac{\pi}{\sqrt{2}G_F M_{S_3}^2 \alpha}\left(\frac{(y_3^{LL})_{32}(y_3^{LL})_{22}^*}{V_{tb}V_{ts}^*}\right). \tag{4.2}$$

For $C_{bs}^{LL\,\mathrm{NP}}$ the contribution appears at the one loop level and can be written as [260, 261]:

$$C_{bs}^{LL\,\mathrm{NP}} = \frac{\eta^{LL}(M_{S_3})}{4\sqrt{2}G_F M_{S_3}^2}\frac{5}{64\pi^2}\left(\frac{\sum_\alpha (y_3^{LL})_{3\alpha}(y_3^{LL})_{2\alpha}^*}{V_{tb}V_{ts}^*}\right)^2, \tag{4.3}$$

where $\alpha = 1,2,3$ is a lepton family index, and $\eta^{LL}(M_{S_3}) > 0$ encodes the running down to the bottom mass scale.

The ATLAS and CMS experiments in LHC have performed direct searches of leptoquarks pair production from proton-proton collisions decaying into one quark and one neutrino. They have excluded at the 95% confidence level (C.L.) scalar leptoquarks with mass $M_{\mathrm{LQ}} \lesssim 1000$ GeV, and vector leptoquarks with mass $M_{\mathrm{LQ}} \lesssim 1500 \sim 1800$ GeV [262, 263].

In Chapter 5 we will analyze a NP scenario based on the leptoquark S_3. The leptoquark U_1 is considered in Chapter 6, and studied in Chapter 7, in the light of the results obtained in the analysis of SMEFT operators. In these two Chapters we also briefly discuss the compatibility with other leptoquarks, namely S_3, S_1 and U_3.

4.2 New gauge bosons

A colourless $SU(2)_L$ triplet of vector bosons with zero hypercharge contains charged bosons W' and a neutral boson Z' [264–266]. These bosons couple to left-handed fermions,

$$\mathscr{L}_{W'} = -\frac{1}{\sqrt{2}}\left(V_{ik}\lambda_{kj}^Q \overline{u}_{iL}\gamma^\mu d_j + \lambda_{ij}^L \overline{e}_{iL}\gamma^\mu \nu_j\right)W'^+_\mu + \mathrm{h.c.}, \tag{4.4}$$

$$\mathscr{L}_{Z'} = \frac{-1}{2}\left[\lambda_{ij}^Q(\overline{u}_{iL}\gamma^\mu u_{jL} - \overline{d}_{jL}\gamma^\mu d_{jL}) + \lambda_{ij}^L(\overline{\nu}_{iL}\gamma^\mu \nu_{jL} - \overline{e}_{iL}\gamma^\mu e_{jL})\right]Z'_\mu, \tag{4.5}$$

and the couplings can be non-universal and non-diagonal. The W' boson mediates new FCCC including $b \to c\ell\nu$ transition [267–269], while Z' generates tree-level FCNC, being

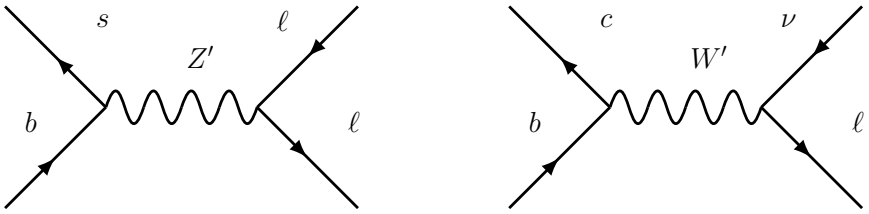

(a) (b)

Figure 4.2: New gauge bosons W' and Z' (a) mediating a $b \to s\ell^+\ell^-$ transition, (b) mediating a $b \to c\ell\nu$ transition.

a prime candidate to explain anomalies in $b \to s\ell^+\ell^-$ decays [270–273]. Fig. 4.2 includes the Feynman diagrams for these processes.

The integration of the Z' boson produces an effective Lagrangian relevant for $b \to s\mu^+\mu^-$ transitions and B_s-mixing, given by [260],

$$\begin{aligned} \mathscr{L}^{\text{eff}}_{Z'} &= -\frac{1}{2M^2_{Z'}}\left(\lambda^Q_{ij}\,\bar{d}_{i\,L}\gamma_\mu d_{j\,L} + \lambda^L_{\alpha\beta}\,\bar{e}_{\alpha\,L}\gamma_\mu e_{\beta\,L}\right)^2 \\ &\sim -\frac{1}{2M^2_{Z'}}\left[(\lambda^Q_{23})^2\left(\bar{s}_L\gamma_\mu b_L\right)^2 + 2\lambda^Q_{23}\lambda^L_{22}(\bar{s}_L\gamma_\mu b_L)(\bar{\mu}_L\gamma^\mu\mu_L) + \text{h.c.}\right] + \cdots, \end{aligned} \tag{4.6}$$

where λ^Q and λ^L are hermitian matrices in flavour space. When matching the above equation with Eqs. (3.42) and (3.51), one obtains the expressions for the Wilson coefficients at the tree level [260],

$$C_9^{\mu\,\text{NP}} = -C_{10}^{\mu\,\text{NP}} = -\frac{\pi}{\sqrt{2}G_F M^2_{Z'}\alpha}\left(\frac{\lambda^Q_{23}\lambda^L_{22}}{V_{tb}V^*_{ts}}\right), \tag{4.7}$$

and

$$C_{bs}^{LL\,\text{NP}} = \frac{\eta^{LL}(M_{Z'})}{4\sqrt{2}G_F M^2_{Z'}}\left(\frac{\lambda^Q_{23}}{V_{tb}V^*_{ts}}\right)^2, \tag{4.8}$$

where $\eta^{LL}(M_{Z'}) > 0$ encodes the running down to the bottom mass scale. The matching has to be performed at an energy scale $\Lambda \sim M_{Z'}$, as indicated in the workflow of Fig. 3.4.

Direct searches of heavy bosons decaying into a pair of fermions have ruled out at the 95% C.L. W' and Z' triplet bosons with masses up to $4.5 \sim 5$ TeV [274, 275].

In Chapter 5 we will study a model based on a heavy Z' boson with non-universal couplings to quarks and leptons. The viability of the W' and Z' bosons is briefly considered in Chapter 6 and Chapter 7.

4.3 Axions and Axion-like particles

As commented in Section 2.1.1, one of the open questions in the SM is the strong CP problem, that is, the lack of CP violation in the strong interactions. The Lagrangian of

the SM in Eq. (2.2) admits the addition of a new term $\mathscr{L}_\theta$ that has dimension 4 and is compatible with the gauge symmetries [276–280],

$$\mathscr{L}_\theta = \theta \frac{\alpha_s}{8\pi} G^a_{\mu\nu} \tilde{G}^{\mu\nu a}, \tag{4.9}$$

where $\tilde{G}^{\mu\nu a} = \epsilon^{\mu\nu\rho\sigma} G^a_{\rho\sigma}/2$ is the dual tensor of the gluon field strength tensor, and θ is an angular parameter $\theta \in [-\pi, \pi)$. A chiral transformation of any quark $q_L \to e^{i\alpha/2} q_L$, $q_R \to e^{-i\alpha/2} q_R$, which shifts the mass term to $m_q \to m_q e^{-i\alpha}$, transform the θ term as $\theta \to \theta + \alpha$. Therefore, the θ term can be rotated away if any of the quarks is massless [281] (which is not compatible with the current lattice predictions [282–286]). Otherwise, θ is a physical parameter of the Lagrangian that has the effect of acting as a new source of CP violation, in addition to the complex entries of the CKM matrix.

However, the θ term induces an electric dipole moment for hadrons. The neutron electric dipole moment has been found to be compatible with zero to an extraordinary accuracy [287], constraining the value of θ, $|\theta| < 8 \times 10^{-11}$ [280]. There is no known reason, at least within the SM, for the CP violations in the gluon sector to be that small or non-existent.

A possible solution to the strong CP problem was devised by Peccei and Quinn [288, 289]. They proposed the existence of a global axial $U(1)$ symmetry, classically exact and violated at the quantum level by the colour anomaly $G\tilde{G}$, and spontaneously broken at a high energy scale f_a. Weinberg and Wilczek noted that such a spontaneously broken global symmetry would imply the existence of a pseudo Nambu-Goldstone boson (pNG), the axion [290, 291]. The low-energy Lagrangian for the QCD-axion is

$$\mathscr{L}_a = \frac{1}{2}(\partial_\mu a)(\partial^\mu a) - \frac{\alpha_s}{8\pi} \frac{a}{f_a} G^a_{\mu\nu} \tilde{G}^{\mu\nu a}. \tag{4.10}$$

Compared to the Lagrangian in Eq. (4.9), the axion Lagrangian replaced the input parameter θ by a dynamical pseudoscalar field, the axion a. The QCD vacuum energy has its absolute minimum at $a = 0$ [292], and therefore, the axion would eventually reach its minimum and automatically solve the strong CP problem.

The axion, through the coupling to gluons, mixes into the η' meson and the neutral pion. Through this mixing, the axion acquires a mass [285, 293–295],

$$m_a f_a \approx m_\pi f_\pi \frac{\sqrt{m_u m_d}}{m_u + m_d} \sim m_\pi f_\pi, \tag{4.11}$$

where f_π is the decay constant of the pion. In the Peccei-Quinn model, the mass of the axion is uniquely determined by f_a.

The axion can be generalized to an Axion-Like Particle (ALP) by just assuming the existence of a pseudo-scalar a resulting from the spontaneous breaking of some $U(1)$ global symmetry, but removing the relation of Eq. (4.11). In this case, m_a and f_a are independent parameters, and the ALP does not fully (or at all) solve the strong CP problem. However,

ALPs are interesting on their own as they are predicted by several NP models [296, 297]. The simplest realization of the global $U(1)$ symmetry is [298]

$$a \to a + c\,, \qquad f' \to f'\,, \tag{4.12}$$

for all fermionic chiral fields $f' = \{q', u'_R, d'_R, \ell', e'_R\}$ defined as electroweak eigenstates. Under these transformations, it is clear that the effective operators

$$(\mathcal{O}_{f'})_{ij} = \frac{\partial_\mu a}{f_a}(\bar{f}'_i \gamma^\mu f'_j) \tag{4.13}$$

are invariant for any flavour indices i, j. The most general dimension-5 effective Lagrangian for the interaction between ALP and SM particles is [298]

$$\mathcal{L}_{\rm ALP} = c_G\mathcal{O}_G + c_W\mathcal{O}_W + c_B\mathcal{O}_B + c_\varphi\mathcal{O}_\varphi + \sum_{f'}(c_{f'})_{ij}(\mathcal{O}_{f'})_{ij}\,, \tag{4.14}$$

where $c_k (k \equiv G, W, B, \varphi, f')$ are the Wilson coefficients of each effective operator, and in particular $c_{f'}$ are general hermitian matrices (if the ALP-fermion interactions are assumed to not generate new sources of CP violation). The bosonic operators are defined as

$$\begin{aligned} \mathcal{O}_G &= \frac{\alpha_s}{4\pi}\frac{a}{f_a}G^a_{\mu\nu}\tilde{G}^{\mu\nu a}\,, & \mathcal{O}_W &= \frac{\alpha_2}{4\pi}\frac{a}{f_a}W^i_{\mu\nu}\tilde{W}^{\mu\nu i} \\ \mathcal{O}_B &= \frac{\alpha_1}{4\pi}\frac{a}{f_a}B_{\mu\nu}\tilde{B}^{\mu\nu}\,, & \mathcal{O}_\varphi &= \frac{\partial_\mu a}{f_a}(\varphi^\dagger i D^\mu \varphi + \text{h.c.})\,. \end{aligned} \tag{4.15}$$

However, the Lagrangian in Eq. (4.14) contains redundant operators:

- The O_φ operator can be eliminated redefining the Higgs and fermionic fields [298, 299],
$$\varphi \to e^{ic_\varphi a/f_a}\varphi\,, \qquad f' \to e^{-i\beta_{f'}c_\varphi a/f_a}f'\,, \qquad c_{f'} \to c_{f'} + \beta_{f'}c_\varphi\,. \tag{4.16}$$
- The derivative couplings are defined modulo generators of the global symmetries for the Baryon number and Lepton number generators [298]. The generator of the baryon number allows to eliminate one coupling to quarks, and the generators of lepton numbers allow to eliminate three couplings to leptons. The choice in [299] is to eliminate one diagonal element in $\mathcal{O}_{q'}$, and the three diagonal elements in $\mathcal{O}_{\ell'}$.

The total number of free parameters is 1 (mass) + 3 (boson couplings) + 5×9 (hermitian flavour couplings) - 4 (B and L generators) = 45.

Integrating by parts the derivative terms and using the SM equations of motion and axial anomaly [300] (or equivalently by using field redefinitions, see Appendix B of [299]), the operators $\mathcal{O}_{f'}$ can be written as a linear combination of bosonic operators and Yukawa-like operators $\mathcal{O}_{f'\varphi}$, given by

$$(\mathcal{O}_{u'\varphi})_{ij} = \frac{a}{f_a}\bar{q}'_i\tilde{\varphi}u'_{Rj}\,, \qquad (\mathcal{O}_{d'\varphi})_{ij} = \frac{a}{f_a}\bar{q}'_i\varphi d'_{Rj}\,, \qquad (\mathcal{O}_{e'\varphi})_{ij} = \frac{a}{f_a}\bar{\ell}'_i\varphi e'_{Rj}\,. \tag{4.17}$$

The Lagrangian in the new basis is [300, 301]

$$\mathscr{L}_{\text{ALP}} = C_G\mathscr{O}_G + C_W\mathscr{O}_W + C_B\mathscr{O}_B - \sum_{f'=u',d',e'}(C_{f'\varphi}\mathscr{O}_{f'\varphi} + \text{h.c.})\,. \tag{4.18}$$

The complex matrices $C_{f'\varphi}$ are not generic as in the usual Yukawa case (if they were, we would have $3\times 18 = 54$ free parameters). Instead, they are related to the $c_{f'}$ couplings by [300, 301]

$$C_{u'\varphi} = i(y_u c_{u'} - c_{q'} y_u)\,, \qquad C_{d'\varphi} = i(y_d c_{d'} - c_{q'} y_d)\,, \qquad C_{e'\varphi} = i(y_e c_{e'} - c_{\ell'} y_e)\,, \tag{4.19}$$

where y_f are the SM Yukawa matrices.

The bosonic couplings of the new basis $C_V (V \equiv G, W, B)$ receive contributions from the fermions [300, 301],

$$\begin{aligned} C_G &= c_G + \frac{1}{2}\text{Tr}(c_{d'} + c_{u'} - 2c_{q'})\,, \\ C_W &= c_W - \frac{1}{2}\text{Tr}(N_c c_{Q'} + c_{\ell'})\,, \\ C_B &= c_B + \text{Tr}[N_c(Y^2_{d'}c_{d'} + Y^2_{u'}c_{u'} - 2Y^2_{q'}c_{q'}) + Y^2_{e'}c_{e'} - 2Y^2_{\ell'}c_{\ell'}]\,, \end{aligned} \tag{4.20}$$

where $N_c = 3$ is the number of colours, and Y_F is the hypercharge of the chiral fields, defined as $Y = Q - T_3$.

Below the EWSSB, after rotating to the mass eigenbasis for the fermions, the interactions to the ALP are

$$\mathscr{L}_{f\,\text{ALP}} = -\frac{ia}{2f_a}\sum_{f=u,d,e}\sum_{i,j}\left[(m_{f_i} - m_{f_j})(k_{fR} + k_{fL})_{ij}\bar{f}_i f_j + (m_{f_i} + m_{f_j})(k_{fL} - k_{fR})_{ij}\bar{f}_i\gamma_5 f_j\right], \tag{4.21}$$

with the rotated couplings k_{fR} (k_{fL}) for the right-(left) handed fermions ($f = u, d, e$) given by

$$\begin{aligned} k_{uL} &= U_{uL}c_{q'}U^\dagger_{uL}, & k_{dL} &= U_{dL}c_{q'}U^\dagger_{dL} = V^\dagger k_U V, \\ k_{eL} &= U_{eL}c_{\ell'}U^\dagger_{eL}, & k_{fR} &= U_{fR}c_{f'}U^\dagger_{fR}. \end{aligned} \tag{4.22}$$

With the usual choice of rotation matrices $U_{uL} = U_{eL} = U_{dR} = U_{uR} = U_{eR} = \mathbb{1}$, $U_{dL} = V$, the conditions to have only flavour-conserving interactions are

$$\begin{aligned} &(c_{\ell'})_{ij} = (c_{d'})_{ij} = (c_{u'})_{ij} = (c_{e'})_{ij} = 0 && \text{for } i \neq j\,, \\ &c_{q'} = 0\,. \end{aligned} \tag{4.23}$$

If we also remove the redundant diagonal entries of $\mathscr{O}_{\ell'}$, the condition becomes clearer: in the derivative basis we only consider flavour-conserving couplings to right-handed fermions. Using this couplings, we arrive at the following Lagrangian [302]

$$\mathscr{L}_{f\,\text{ALP}} = -i\frac{a}{f_a}\sum_i c_{i'} m_i \bar{f}_i\gamma_5 f_i\,. \tag{4.24}$$

This Lagrangian will be our starting point for the studies performed in Chapter 8.

4.4 Minimal Flavour Violation

Minimal Flavour Violation (MFV) is a prescription for NP models in the flavour sector. The MFV ansatz [303] consists in the assumption that any source of flavour and CP violation in any NP models is the one in the SM, i.e. the Yukawa couplings. As explained in Section 2.1, the Yukawa interactions are the only terms of the renormalizable Lagrangian that are not invariant under the flavour symmetry, unless the Yukawa couplings are formally promoted to be fields, spurions, transforming non-trivially under this symmetries. NP models with MFV require that any new flavour structure should be analogous to the flavour structure of the SM. Formally, MFV requires that any term of the Lagrangian should be invariant under the flavour group $\mathscr{G}_F$ presented below, and flavour (and CP) violations can only appear through the spurions $\mathscr{Y}_u$, $\mathscr{Y}_d$ and $\mathscr{Y}_\ell$ [304, 305].

The largest group of unitary field transformations that commutes with the gauge group in the SM is $\mathscr{G}_F = U(5)^3$ [303]. The flavour group can be decomposed as

$$\begin{aligned} \mathscr{G}_F &= U(1)_Y \times U(1)_B \times U(1)_L \times U(1)_{\rm PQ} \times U(1)_{e_R} \times SU(3)_q^3 \times SU(3)_\ell^2, \\ SU(3)_q^3 &= SU(3)_q \times SU(3)_{u_R} \times SU(3)_{d_R}, \\ SU(3)_\ell^2 &= SU(3)_\ell \times SU(3)_{e_R}. \end{aligned} \tag{4.25}$$

The $U(1)$ charges correspond to the gauged hypercharge and the global baryon and lepton numbers, as well as the Peccei-Quinn symmetry, that affects right-handed d-type quarks and charged leptons, and a rotation in the e_R sector. The five $SU(3)$ groups rotate fermions of different generations for left-handed quarks, right-handed d-quarks, right-handed u-quarks, left-handed leptons and right-handed charged leptons. In the SM, only the $U(1)_Y \times U(1)_B \times U(1)_L$ symmetry survives at the classical level, and $SU(3)_q^3 \times SU(3)_\ell^2 \times U(1)_{\rm PQ} \times U(1)_{e_R}$ are explicitly broken by the Yukawa terms. However, it is possible to recover a *formal* flavour symmetry with the introduction of spurions [304], auxiliary (*i.e.* non-dynamical) fields that transform under the flavour group,

$$\mathscr{Y}_u \sim (\mathbf{3}, \overline{\mathbf{3}}, \mathbf{1})_{SU(3)_q^3}, \qquad \mathscr{Y}_d \sim (\mathbf{3}, \mathbf{1}, \overline{\mathbf{3}})_{SU(3)_q^3}, \qquad \mathscr{Y}_\ell \sim (\mathbf{3}, \overline{\mathbf{3}})_{SU(3)_\ell^2}. \tag{4.26}$$

The only renormalizable terms that can be written using the SM fields and these spurions, compatible with all the Lorentz and gauge symmetries, are

$$\mathscr{L}_{\mathscr{Y}} = \overline{q}'_L \mathscr{Y}_d \varphi d'_R + \overline{q}' \mathscr{Y}_u \widetilde{\varphi} u'_R + \overline{\ell} \mathscr{Y}_\ell \varphi e_R + \text{h.c.}, \tag{4.27}$$

which is precisely the Yukawa Lagrangian in Eq. (2.11), with the identification of the spurions with the Yukawa matrices. Particularizing to the leptonic sector, the consequence of the flavour symmetry is the LFU, since gauge bosons have the same couplings to all the leptons.

In NP models, the fact that flavour (and CP) violations can only appear through the spurions $\mathscr{Y}_u$, $\mathscr{Y}_d$ and $\mathscr{Y}_\ell$ imposes constraints for the combinations of flavour indices that

can appear. For example, the interaction for a Z' boson to a pair of quarks of Eq. (4.5), assuming MFV, would take the form

$$\mathscr{L} = Z'_\mu(\overline{u}_{iL}\gamma^\mu u_{jL} - \overline{d}_{iL}\gamma^\mu d_{jL})\left[a\delta_{ij} + b(\mathscr{Y}_u\mathscr{Y}_u^\dagger)_{ij} + \mathscr{O}(\mathscr{Y}^4)\right], \tag{4.28}$$

where a and b are flavour-universal coefficients expected to be of order $\mathscr{O}(1)$. The dominant source of flavour violation, in the basis where y_d is diagonal, comes from

$$(\mathscr{Y}_u\mathscr{Y}_u^\dagger)_{ij} = \sum_{k=u,c,t}\frac{m_k^2}{v^2}V_{ki}V_{kj}^* \approx \frac{m_t^2}{v^2}V_{ti}V_{tj}^*, \qquad i \neq j. \tag{4.29}$$

And consequently we can write the coupling as

$$\lambda_{ij}^Q \approx -2a\delta_{ij} - 2b\frac{m_t^2}{v^2}V_{ti}V_{tj}^*. \tag{4.30}$$

MFV is minimal in the sense that, even in the case where NP has a trivial flavour structure, radiative corrections from the SM interactions down to the electroweak scale will include new flavour terms that break $\mathscr{G}_F$ following the MFV principle [306].

MFV predicts correlations between NP effects in different observables [307–309], for example relating $B_s \to \mu^+\mu^-$ and $B \to \mu^+\mu^-$ decays. However, MFV is not capable of describing sizable violations of lepton flavour universality, as the ones seen in the $R_{K^{(*)}}$ and $R_{D^{(*)}}$ ratios, since the lepton flavour structure is determined solely by the small Yukawa couplings appearing in the spurion $\mathscr{Y}_e\mathscr{Y}_e^\dagger = \text{diag}(y_e^2, y_\mu^2, y_\tau^2)$.

Extensions of the MFV paradigm with more restricted flavour groups have been presented in [310, 311], where some of the $SU(3)$ subgroups are broken down to $SU(2)$ subgroups including only the light fermions. This allows, for example, to introduce some NP interactions that affect only the third generation quarks and leptons, and leave the light fermions unaffected. This is one of the proposals that we will study in our analysis, in Chapters 6 where NP only contributes to the third generation of quarks, and in Chapter 7, where it only contributes to the third generations of quarks and leptons.

Chapter 5

Fit to complex Wilson coefficients

This Chapter contains the first numerical analysis that we performed, using the framework of EFT, of the B anomalies. In particular, we studied the $R_{K^{(*)}}$ LFU ratios for the $b \to s\mu^+\mu^-$ FCNC transitions using the WET operators. We also considered the observable ΔM_s, the mass difference for the oscillation of the neutral mesons $M_s - \bar{M}_s$. At the time when we performed the analysis, there was a mild tension between the experimental measurements and theoretical prediction for ΔM_s; although this tension later disappeared with more precise theoretical inputs. Since the WET does not establish any relation between the effective operators affecting $R_{K^{(*)}}$ and ΔM_s, we turn our attention to two specific NP models, Z' and S_3 leptoquark models, that can provide the connection between the two types of observables, and in both cases complex Wilson coefficients are needed for a combined explanation. The introduction of complex parameters forces us to also consider the CP asymmetry.

This Chapter is based on the work published in [1]. The conclusions have been updated in order to reflect the new results published after the completion of this work. The code needed for the calculations of this work can be found in Appendix B.3.1.

5.1 Introduction

At present, many interesting measurements on flavour physics are performed at the LHC and B factories, as detailed in Section 2.4. Some of these decays allow us to build optimized observables, as ratios of these decays, that are theoretically clean observables and whose measurements are in tension with SM predictions. One example is the case of the $R_{K^{(*)}}$ observables in $b \to s\ell^+\ell^-$ transitions, defined in Eq. (2.41). For the analysis of this Chapter, we will consider only the experimental results that were available at the moment we have performed the computations presented in [1], that is, the values reported in Eq. (2.50) and (2.51); although the effects of newer measurements will be discussed in Section 5.5.1. In the SM $R_{K^+} = R_{K^{*0}} = 1$ with theoretical uncertainties of the order of 1% [93, 312], as a consequence of LFU. The compatibility of the above results with respect to the SM predictions is of 2.6σ deviation in the first case and for $R_{K^{*0}}$, in the low q^2 di-

lepton invariant mass region is of about 2.3 standard deviations; being in the central $-q^2$ of 2.4σ. A discrepancy of about 3σ is found when the measurements of R_{K^+} and $R_{K^{*0}}$ are combined [313]. Anomalous deviations were also observed in the angular distributions of the decay rate of $B \to K^* \mu^+ \mu^-$, being the most significant discrepancy for the $P_5^{'}$ observable shown in the first four rows of Table 2.2.

From the theoretical side, the ratios R_{K^+} and $R_{K^{*0}}$ are very clean observables; essentially free of hadronic uncertainties that cancel in the ratios [93]. The experimental data has been used to constrain NP models.

On the other hand, NP models are also severely constrained by other flavour observables, for example in B_s-mixing. An updated computation, performed in 2016 and 2017, for the B_s mesons mass difference in the SM was presented in [260, 314–317], showing a deviation with the experimental result [260, 318]:

$$\Delta M_s^{\text{exp}} = (17.757 \pm 0.021)\,\text{ps}^{-1}\,, \quad \Delta M_s^{\text{SM}} = (20.01 \pm 1.25)\,\text{ps}^{-1}\,, \tag{5.1}$$

such that $\Delta M_s^{\text{SM}} > \Delta M_s^{\text{exp}}$ at about 2σ. This fact imposes additional constraints over the NP parameter space. Therefore, a combined fit is mandatory when considering all updated flavour observables. A negative contribution to ΔM_s is needed to reconcile it with the experimental result, in the context of some NP models (like Z' or leptoquarks) it implies complex Wilson coefficients in the effective Lagrangian of $R_{K^{(*)}}$ [260] (see also below). To the best of our knowledge, most previous works have used only real Wilson coefficients in fits of $R_{K^{(*)}}$ observables together with ΔM_s, an exception being Ref. [319]. An effect of introducing complex couplings is the generation of CP asymmetries. The mixing-induced CP asymmetry in the B sector can be measured through $A_{CP}^{\text{mix}} \equiv A_{CP}^{\text{mix}}(B_s \to J/\psi\phi) \equiv \sin(\phi_s^{c\bar{c}s})$, experimentally it is measured to be [318]:

$$A_{CP}^{\text{mix exp}}(B_s \to J/\psi\phi) = -0.021 \pm 0.031\ . \tag{5.2}$$

In the SM it is given by $A_{CP}^{\text{mix SM}} = \sin(-2\beta_s)$ [55, 260, 320], with $\beta_s = 0.01852 \pm 0.00032$ [38] we obtain $A_{CP}^{\text{mix SM}} = -0.03703 \pm 0.00064$, which is consistent with the experimental result in Eq. (5.2) at the $\sim 0.5\sigma$ level. Here, β_s is one of the angles of the unitarity triangle $\sum V_{is}^* V_{ib} = 0$, given by [38]

$$\beta_s = \text{Arg}\left(-\frac{V_{ts}V_{tb}^*}{V_{cs}V_{cb}^*}\right). \tag{5.3}$$

Ref. [319] performed fits for the B decay physics observables using complex Wilson coefficients, in the model-independent and model dependent approaches. The analysis of Ref. [319] performs fits for the B decay observables using complex couplings, without including the ΔM_s or A_{CP}^{mix} observables, then Ref. [319] proceeds to provide predictions to CP-violation observables. Ref. [319] only includes ΔM_s and A_{CP}^{mix} in the Z'-model fit. Our results agree with the ones of Ref. [319] wherever comparable.

The aim of the present chapter is to investigate the effects of complex Wilson coefficients in the analyses of NP in B meson anomalies. We assume a model-independent effective Lagrangian approach and we study the region of NP parameter space compatible

with the experimental data, by considering the dependence of the results on the assumptions of imaginary or complex Wilson coefficients. We compare our results with the case of considering only real Wilson coefficients. A brief summary of the NP contributions to the effective Lagrangian relevant for $b \to s\ell^+\ell^-$ transitions and B_s-mixing is presented in Section 5.2, where we also recall the need to consider complex Wilson coefficients in the analysis. In Section 5.3 we discuss the effects of having imaginary or complex Wilson coefficients on $R_{K^{(*)}}$ observables. The impact of these complex Wilson coefficients in the analysis of B meson anomalies in two specific models, Z' and leptoquarks, is included in Section 5.4. We consider a combined fit of $R_{K^{(*)}}$ observables, together with ΔM_s and CP-violation observable $A_{CP}^{\rm mix}$ in this analysis. Finally, conclusions are given in Section 5.5.

5.2 Setting of the fits: Effective Lagrangian and New Physics models

The effective Lagrangian for $b \to s\ell^+\ell^-$ transitions has been introduced in Section 3.5. In order to analyze the anomalies in the $b \to s\ell^+\ell^-$ decays, we will use the operators of the WET $O_9^{(\prime)\ell}$ and $O_{10}^{(\prime)\ell}$ with $\ell = e, \mu$ defined in Eq. (3.43), and we analyze the NP contributions to the Wilson coefficients $C_i^{(\prime)\ell\,\rm NP}$. In most of our analysis we will consider the left-handed Wilson coefficients $C_i^{\ell\,\rm NP}$, the right-handed Wilson coefficients $C_i^{\prime\ell\,\rm NP}$ are treated briefly in the model-independent approach of Section 5.3 (see Table 5.1 below). The NP contributions to B_s-mixing are described by the effective Lagrangian of Eq. (3.51). In order to study the allowed NP parameter space we follow the same procedure as given in [260], comparing the experimental measurement of the mass difference with the prediction in the SM and NP. Therefore, the effects can be parameterized as [260],

$$\frac{\Delta M_s}{\Delta M_s^{\rm SM}} = \left| 1 + \frac{C_{bs}^{LL\,\rm NP}}{C_{bs}^{LL\,\rm SM}} \right| . \tag{5.4}$$

The NP prediction to the CP-asymmetry $A_{CP}^{\rm mix}$ is given by [55, 260, 320]

$$A_{CP}^{\rm mix} = \sin(\phi_\Delta - 2\beta_s) \quad , \quad \phi_\Delta = {\rm Arg}\left(1 + \frac{C_{bs}^{LL\,\rm NP}}{C_{bs}^{LL\,\rm SM}} \right) . \tag{5.5}$$

Since Eq. (5.1) establishes that $\Delta M_s^{\rm exp} < \Delta M_s^{\rm SM}$, Eq. (5.4) tells us that to obtain a prediction of ΔM_s closer to $\Delta M_s^{\rm exp}$ the NP Wilson coefficient $C_{bs}^{LL\,\rm NP}$ Eq. (3.51) must be negative ($C_{bs}^{LL\,\rm NP} < 0$). In a generic effective Lagrangian approach, each Wilson coefficient is independent, and setting $C_{bs}^{LL\,\rm NP} < 0$ has no effect on $C_9^{\mu\,\rm NP}$, $C_{10}^{\mu\,\rm NP}$, etc. However, explicit NP models give predictions on the Wilson coefficients which introduce correlations among them. We will concentrate on two specific models that have been proposed to solve the semi-leptonic B_s-decay anomalies: Z' and leptoquarks. The goal is to validate the compatibility of these models with the experimental data, and therefore the matching to the EFT is performed at the scale of the mass of the NP particle, as indicated in Fig. 3.4.

We start with the Z' model that contains a Z' boson with mass $M_{Z'}$ that may exhibit couplings to the SM fermions that are not diagonal. The interaction Lagrangian for a Z' can be found in Eq. (4.5). The part of the effective Lagrangian relevant for $b \to s\mu^+\mu^-$ transitions and B_s-mixing is given by Eq. (4.7).

When the new boson is integrated out, at the electroweak scale induces NP contributions to the $b \to s\ell^+\ell^-$ decays at tree level, and to the B_s mixing at one loop level, with the matching conditions of Eq. (4.7) and (4.8) respectively. From Eq. (4.8) it is clear that to obtain a negative $C_{bs}^{LL\,\mathrm{NP}}$ one needs an imaginary number inside the square ($\lambda_{23}^Q/(V_{tb}V_{ts}^*) \in \mathbb{I}$), but this is the same factor that appears in $C_9^{\mu\,\mathrm{NP}} = -C_{10}^{\mu\,\mathrm{NP}}$ in Eq. (4.7). $\lambda_{22}^L \in \mathbb{R}$, since λ is an hermitic matrix, then it follows that $C_{9,10}^{\mu\,\mathrm{NP}}$ would be imaginary ($C_{9,10}^{\mu\,\mathrm{NP}} \in \mathbb{I}$). Of course, a purely imaginary coupling (or Wilson coefficient) is just a particular and extreme case of having a generic complex coupling. Once one abandons the restriction of considering real couplings it seems more natural to consider the most generic case of complex couplings. There is, however, a motivation to try also the extreme case of imaginary couplings: an imaginary $\lambda_{23}^Q/(V_{tb}V_{ts}^*)$ provides a real $C_{bs}^{LL\,\mathrm{NP}}$ Eq. (4.8), which in turn provides no additional contributions to the CP-asymmetry A_{CP}^{mix} Eq. (5.5), so imaginary couplings might provide a way of improving the predictions on ΔM_s without introducing unwanted CP-asymmetries.

Now we focus on leptoquark models. Specifically, we consider the scalar leptoquark $S_3 \sim (\overline{\mathbf{3}},\mathbf{3},1/3)$ with mass M_{S_3}. The interaction Lagrangian can be found in first line of Table 4.1, assuming that the leptoquarks do not induce new quark-quark interactions, that is, $z_3^{LL} = 0$. To simplify the notation, in this Chapter we will use $y^{QL} \equiv y_3^{LL}$.

In this case, the matching of the leptoquark to the WET can be found in Eq. (4.2) and (4.3). Again, in order to obtain $C_{bs}^{LL\,\mathrm{NP}} < 0$ in Eq. (4.3), the couplings must comply the condition $\sum_{\alpha=1}^{3} y_{3\alpha}^{QL} y_{2\alpha}^{QL*}/(V_{tb}V_{ts}^*) \in \mathbb{I}$. If the combinations $y_{3\alpha}^{QL} y_{2\alpha}^{QL*}/(V_{tb}V_{ts}^*) \in \mathbb{I}$, then the expression in Eq. (4.2) suggests $C_{9,10}^{\mu\,\mathrm{NP}} \in \mathbb{I}$. Of course, the expression in Eq. (4.3) is a sum over all generations, so it is possible to set up a model with $y_{32}^{QL} y_{22}^{QL*}/(V_{tb}V_{ts}^*) \in \mathbb{R}$, and to have a cancellation such that the sum in Eq. (4.3) is imaginary, but this would be a highly fine-tuned scenario. If the sum in Eq. (4.3) has an imaginary part, it would be most natural if all its addends have some imaginary part.

Here we have shown two examples of new physics models which justify the choice of imaginary (or complex) values for the Wilson coefficients $C_{9,10}^{\mu\,\mathrm{NP}}$. In the next section we take an effective Lagrangian approach and explore whether an imaginary or complex NP Wilson coefficients can accommodate the experimental $R_{K^{(*)}}$ deviations.

5.3 Imaginary Wilson coefficients and $R_{K^{(*)}}$ observables

Several groups have analyzed the predictions for the ratios $R_{K^{(*)}}$ based on different global fits [313, 319, 321–328], extracting possible NP contributions or constraining it. As it is well known, an excellent fit to the experimental data is obtained when $C_9^{\ell\,\mathrm{NP}} = -C_{10}^{\ell\,\mathrm{NP}}$; corre-

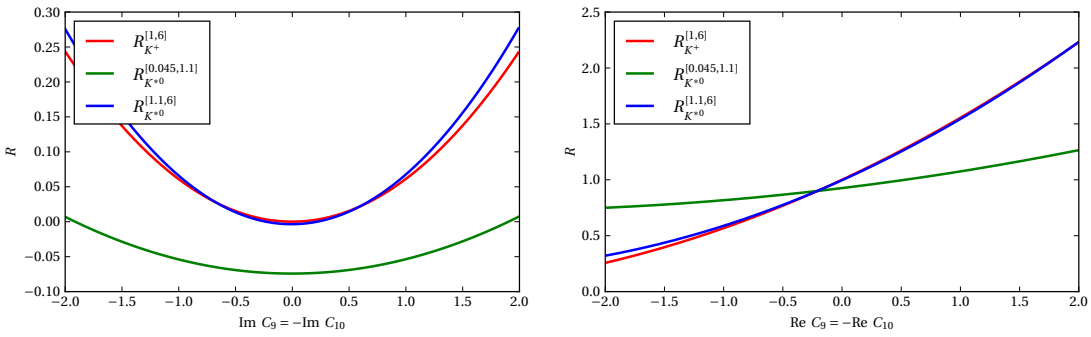

(a) (b)

Figure 5.1: Values of R_{K^+} and $R_{K^{*0}}$ with (a) imaginary and (b) real Wilson coefficients.

sponding to left-handed lepton currents. By considering this relation, we investigate the effects of having imaginary Wilson coefficients on $R_{K^{(*)}}$ observables. For the numerical evaluation we use inputs values as given in [329]. The SM input parameters most relevant for our computation are:

$$\begin{aligned}
&\alpha_s(M_Z) = 0.1181(11)\,, \; G_F = 1.1663787(6) \times 10^{-5}\,\text{GeV}^{-2}\,, \\
&M_W = 80.385(15)\,\text{GeV}\,, \; m_t = 173.1(0.6)\,\text{GeV}\,, \\
&M_{B_s} = 5.36689(19)\,\text{GeV}\,, \\
&V_{tb} = 0.9991022 \;\;, \;\; V_{ts} = -0.04137511 - 7.74823325 \times 10^{-4}\; i \;\;\;, \qquad (5.6)
\end{aligned}$$

note that the product $V_{tb}V_{ts}^*$, which appears in the computation of Wilson coefficients in NP models in Eqs. (4.7), (4.8), (4.2), (4.3) is approximately a negative real number ($V_{tb}V_{ts}^* \simeq -0.04$).

Figure 5.1 shows the values of the ratios $R_{K^{(*)}}$, in their respective q^2 ranges, when both Wilson coefficients $C_9^{\mu\,\text{NP}}$ and $C_{10}^{\mu\,\text{NP}}$ are imaginary (Figure 5.1a) and when they are real (Figure 5.1b), by assuming that $C_9^{\mu\,\text{NP}} = -C_{10}^{\mu\,\text{NP}}$. If these two coefficients are imaginary, in all cases the minimum value for the ratio is obtained at the corresponding SM point $C_9^{\mu\,\text{NP}} = -C_{10}^{\mu\,\text{NP}} = 0$. The addition of non-zero imaginary Wilson coefficients results in larger values of $R_{K^{(*)}}$, at odds with the experimental values $R_{K^{(*)}}^{\text{exp}} < R_{K^{(*)}}^{\text{SM}}$. This behaviour was already pointed out in Ref. [330], where it is shown that the interference of purely imaginary Wilson with the SM vanishes, and therefore they can not provide negative contributions to $R_{K^{(*)}}$ (see also below). In contrast, as shown in the right panel, values of $R_{K^{(*)}} \sim 0.7$ (as in the experimental measurements) are possible when the Wilson coefficients are real.

We have done a combined fit by including the ratios R_{K^+} and $R_{K^{*0}}$, and the angular observables P_4' and P_5' [133, 331, 332][1]. Results are shown in Figure 5.2. The allowed regions for imaginary values of $C_9^{\mu\,\text{NP}}$ and $C_{10}^{\mu\,\text{NP}}$ when fitting to measurements of a series

[1]For the P_4', P_5' observables we include all q^2 bins, except the ones around to the charm resonances $q^2 \in [8.7, 14]\,\text{GeV}^2$, where the theoretical computation is not reliable. In total we include 15 measurements for P_4' and 21 measurements for P_5' [133, 331, 332].

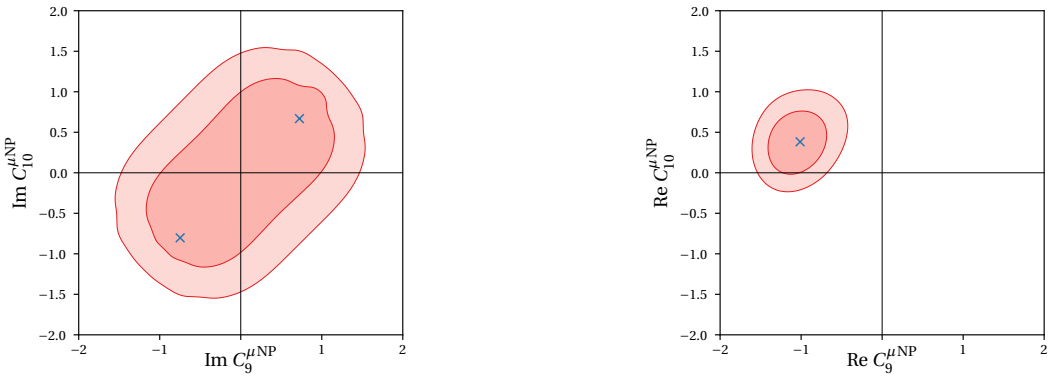

(a) (b)

Figure 5.2: Best fit and 1σ and 2σ contours to semi-leptonic B decays observables, R_{K^+}, $R_{K^{*0}}$, P_4' and P_5', using (a) imaginary and (b) real Wilson coefficients.

of $b \to s\mu^+\mu$ observables are presented in Figure 5.2a, by assuming all other Wilson coefficients to be SM-like. The numerical analysis has been done by using the open source code `flavio 0.28` [195], which computes the χ^2 function with each $(C_9^{\mu\mathrm{NP}}, C_{10}^{\mu\mathrm{NP}})$ pair. The χ^2 difference is evaluated with respect to the SM point, $\Delta\chi^2_{\mathrm{SM}} = \chi^2_{\mathrm{SM}} - \chi^2_{\mathrm{min}}$. Then, the pull in σ is defined as $\sqrt{\Delta\chi^2_{\mathrm{SM}}}$, in the case of only one Wilson coefficient, and for the two-dimensional case it can be evaluated by using the inverse cumulative distribution function of a χ^2 distribution having two degrees of freedom (d.o.f.); for instance, $\Delta\chi^2 = 2.29$ for 1σ. The darker red shaded regions in Fig. 5.2 correspond to the points with $\Delta\chi^2 = \chi^2 - \chi^2_{\mathrm{min}} \leq 2.29$, that is, they are less than 1σ away from the best fit point, whereas the lighter red shaded regions correspond to $\Delta\chi^2 \leq 6.18$ ($\equiv 2\sigma$). The crosses mark the position of the best fit points. In Fig. 5.2a the χ^2 function has a broad flat region centered around the origin, with two nearly symmetric minima found at ($C_9^{\mu\mathrm{NP}} = 0.72\,i$, $C_{10}^{\mu\mathrm{NP}} = 0.74\ i$) and ($C_9^{\mu\mathrm{NP}} = -0.75\,i$, $C_{10}^{\mu\mathrm{NP}} = -0.74\,i$). The pull of the SM, defined as the probability that the SM scenario can describe the best fit assuming that $\Delta\chi^2_{\mathrm{SM}}$ follows a χ^2 distribution with 2 d.o.f., is of just $\sqrt{\Delta\chi^2_{\mathrm{SM}}} = 1.42$ ($\equiv 0.91\sigma$) and $\sqrt{\Delta\chi^2_{\mathrm{SM}}} = 1.38$ ($\equiv 0.87\sigma$) respectively, and both of them have the same $\chi^2_{\mathrm{min}}/\text{d.o.f.} = 2.25$, that is, purely complex couplings do not provide a good description of the data. For completeness, the fit to real values of the Wilson coefficients are included in Figure 5.2b. Now the confidence regions are much tighter and do not include the SM point. In fact, the best fit point ($C_9^{\mu\mathrm{NP}} = -1.09$, $C_{10}^{\mu\mathrm{NP}} = 0.481$) improves the SM by $\sqrt{\Delta\chi^2_{\mathrm{SM}}} = 6.28$ ($\equiv 5.95\sigma$), and a much lower $\chi^2_{\mathrm{min}}/\text{d.o.f.} = 1.24$.

Ref. [330] showed that imaginary Wilson coefficients do not interfere with the SM amplitude, an therefore imaginary $C_{9,10}^{\mu\mathrm{NP}}$ can not decrease the prediction for $R_{K^{(*)}}$. This is numerically shown in the above analysis, where imaginary Wilson coefficients $C_{9,10}^{\mu\mathrm{NP}}$ are not able to reduce significantly the prediction for $R_{K^{(*)}}$. To further investigate this question, we can examine the approximate expression for $R_{K^{*0}}$ that we have obtained in Eq. (3.47).

	Best fit(s)	Pull ($\sqrt{\Delta\chi^2_{\rm SM}}$)	Pull (σ)	$\chi^2_{\rm min}$/d.o.f.
$C_9^{\mu\,\rm NP}$	$-1.11-0.02\,i$	5.94	$5.60\,\sigma$	1.35
$C_{10}^{\mu\,\rm NP}$	$1.66+1.99\,i$ $1.67-2.01\,i$	5.02	$4.65\,\sigma$	1.62
$C_9^{\mu\,\rm NP}=-C_{10}^{\mu\,\rm NP}$	$-1.16+1.14\,i$ $-1.18-1.18\,i$	6.06	$5.72\,\sigma$	1.31
$C_9^{\prime\,\mu\,\rm NP}$	$-0.24-0.003\,i$	1.07	$0.57\,\sigma$	2.27
$C_{10}^{\prime\,\mu\,\rm NP}$	$0.33-0.014\,i$	2.22	$1.72\,\sigma$	2.17
$C_9^{e\,\rm NP}$	$-3.29+5.02\,i$ $-3.35-5.04\,i$	4.85	$4.47\,\sigma$	1.67
$C_{10}^{e\,\rm NP}$	$-0.27+3.48\,i$ $-0.27-3.48\,i$	4.72	$4.34\,\sigma$	1.70
$C_9^{e\,\rm NP}=-C_{10}^{e\,\rm NP}$	$-3.29+4.58\,i$ $-3.35-4.59\,i$	4.85	$4.47\,\sigma$	1.67
$C_9^{\prime\,e\,\rm NP}$	$-0.59+3.89\,i$ $-0.59-3.89\,i$	4.81	$4.43\,\sigma$	1.68
$C_{10}^{\prime\,e\,\rm NP}$	$0.52+3.88\,i$ $0.53-3.88\,i$	4.81	$4.43\,\sigma$	1.68

Table 5.1: Best fit Wilson coefficients complex values to semi-leptonic decay observables R_{K^+}, $R_{K^{*0}}$, P_4' and P_5', allowing only one free coefficient at a time. Shown are also the corresponding pulls, and $\chi^2_{\rm min}$/d.o.f..

Now, if we assume that NP does not affect the electron channel ($C_9^{e\,\rm NP}=C_{10}^{e\,\rm NP}=0$), it is clear that to obtain $R_{K^{*0}}<R_{K^{*0}}^{\rm SM}$ one needs to introduce $C_9^{\mu\,\rm NP}$ and $C_{10}^{\mu\,\rm NP}$ with a non-zero real part: the only possible negative contributions come from the $\mathrm{Re}\,C_9^{\mu\,\rm NP}$, $\mathrm{Re}\,C_{10}^{\mu\,\rm NP}$ terms, whereas the $|C_9^{\mu\,\rm NP}|^2$, $|C_{10}^{\mu\,\rm NP}|^2$ terms have a positive-defined sign, and can not reduce the value of $R_{K^{*0}}$. Thus, purely imaginary values of $C_{9,10}^{\mu\,\rm NP}$ contribute only to the modulus (positive-definite) and not to the real part, and can not bring the prediction of $R_{K^{*0}}$ closer to the experimental value. In addition, this expression tells us that the better option to reduce the prediction of $R_{K^{*0}}$ is using a real negative $C_9^{\mu\,\rm NP}$, and a real positive $C_{10}^{\mu\,\rm NP}$. This is actually the result that we have obtained in our numerical analysis. Fig. 5.1b shows that, for real Wilson coefficients, the lowest prediction for $R_{K^{*0}}$ is obtained for $C_9^{\mu\,\rm NP}=-C_{10}^{\mu\,\rm NP}<0$, and Fig. 5.2b shows that the best fit is obtained for negative $C_9^{\mu\,\rm NP}$ and positive $C_{10}^{\mu\,\rm NP}$. Fig. 5.1a shows that, in general, imaginary Wilson coefficients give positive contributions to $R_{K^{(*)}}$, in accordance with Eq. (3.47). Of course, the full expression is richer than Eq. (3.47), and we expect some deviations, Fig. 5.2a shows that the best fit point is not the SM ($C_9^{\mu\,\rm NP}=C_{10}^{\mu\,\rm NP}=0$), but the best fit regions are centered around it, and the SM pull with respect the best fit points is small.

We conclude that, actually, a NP explanation for R_{K^+}, $R_{K^{*0}}$ requires that $C_9^{\mu\,\rm NP}$, $C_{10}^{\mu\,\rm NP}$

	R_{K^+}	$R_{K^{*0}}^{[0.045,1.1]}$	$R_{K^{*0}}^{[1.1,6]}$
$C_9^{\mu\,\mathrm{NP}}$	0.77 ± 0.03	0.887 ± 0.009	0.82 ± 0.04
$C_{10}^{\mu\,\mathrm{NP}}$	0.78 ± 0.05	0.87 ± 0.03	0.80 ± 0.10
$C_9^{\mu\,\mathrm{NP}} = -C_{10}^{\mu\,\mathrm{NP}}$	0.59 ± 0.08	0.83 ± 0.03	0.63 ± 0.09
$C_9^{'\mu\,\mathrm{NP}}$	0.95 ± 0.05	0.96 ± 0.03	1.09 ± 0.09
$C_{10}^{'\mu\,\mathrm{NP}}$	0.92 ± 0.07	0.95 ± 0.03	1.07 ± 0.09
$C_9^{e\,\mathrm{NP}}$	0.76 ± 0.09	0.69 ± 0.12	0.52 ± 0.17
$C_{10}^{e\,\mathrm{NP}}$	0.69 ± 0.06	0.77 ± 0.06	0.59 ± 0.13
$C_9^{e\,\mathrm{NP}} = -C_{10}^{e\,\mathrm{NP}}$	0.76 ± 0.09	0.70 ± 0.10	0.52 ± 0.17
$C_9^{'e\,\mathrm{NP}}$	0.75 ± 0.09	0.71 ± 0.10	0.52 ± 0.18
$C_{10}^{'e\,\mathrm{NP}}$	0.75 ± 0.09	0.80 ± 0.09	0.66 ± 0.14

Table 5.2: R_{K^+}, $R_{K^{*0}}$ predictions with $1\,\sigma$ uncertainties corresponding to the best fit Wilson coefficients of Table 5.1.

have a non-zero real part, whereas we saw above that NP explanation for ΔM_s requires that $C_9^{\mu\,\mathrm{NP}}$, $C_{10}^{\mu\,\mathrm{NP}}$ have a non-zero imaginary part. Then, to have a NP explanation for both observables $C_9^{\mu\,\mathrm{NP}}$, $C_{10}^{\mu\,\mathrm{NP}}$ should be general complex numbers. Following this reasoning we have performed a combined fit to the semi-leptonic decay observables R_{K^+}, $R_{K^{*0}}$, P_4' and P_5' using generic complex Wilson coefficients allowing only one free Wilson coefficient at a time. Table 5.1 shows the best fit values, pulls (defined as $\sqrt{\Delta\chi^2_{\mathrm{SM}}}$) and $\chi^2_{\mathrm{min}}/\mathrm{d.o.f.}$, for scenarios with NP in one individual complex Wilson coefficient, and Table 5.2 shows the prediction for $R_{K^{(*)}}$ for the corresponding central values of each fit, together with the $1\,\sigma$ uncertainties. The primed Wilson coefficients are also included. We found that the best fit of R_{K^+} and $R_{K^{*0}}$ and the angular distributions is obtained for $C_9^{\mu\,\mathrm{NP}} = -1.11 - 0.02\,i$, for $C_{10}^{\mu\,\mathrm{NP}}$ we find two points with similar minimum value for χ^2 with opposite signs of the imaginary part, $C_{10}^{\mu\,\mathrm{NP}} = 1.66 + 1.99\,i$ and $C_{10}^{\mu\,\mathrm{NP}} = 1.65 - 2.10\,i$. Assuming $C_9^{\mu\,\mathrm{NP}} = -C_{10}^{\mu\,\mathrm{NP}}$ we also obtain a double minimum $C_9^{\mu\,\mathrm{NP}} = -C_{10}^{\mu\,\mathrm{NP}} = -1.16 + 1.14\,i$ and $C_9^{\mu\,\mathrm{NP}} = -C_{10}^{\mu\,\mathrm{NP}} = -1.18 - 1.18\,i$ with a pull of $\sqrt{\Delta\chi^2_{\mathrm{SM}}} = 6.06$ ($\equiv 5.72\,\sigma$) and a $\chi^2_{\mathrm{min}}/\mathrm{d.o.f.} = 1.31$. By looking at $\chi^2_{\mathrm{min}}/\mathrm{d.o.f.}$ we see that the scenarios with only $C_9^{\mu\,\mathrm{NP}}$ or $C_9^{\mu\,\mathrm{NP}} = -C_{10}^{\mu\,\mathrm{NP}}$ provide the best description of experimental data, whereas the scenarios with $C_9^{'\mu\,\mathrm{NP}}$ and $C_{10}^{'\mu\,\mathrm{NP}}$ provide the worst description. If only real Wilson coefficients are chosen the best fit of R_{K^+} and $R_{K^{*0}}$ yields $C_9^{\mu\,\mathrm{NP}} = -1.59$, $C_{10}^{\mu\,\mathrm{NP}} = 1.23$ or $C_9^{\mu\,\mathrm{NP}} = -C_{10}^{\mu\,\mathrm{NP}} = -0.64$, with a pull around $4.2\,\sigma$ [324].

Ref. [319] also provides fits for complex generic Wilson coefficients. Their *scenario I* corresponds to our first line in Table 5.1, our best fit value agrees with their result ($C_9^{\mu\,\mathrm{NP}} = (-1.1 \pm 0.2) + (0 \pm 0.9\,i)$), within the large uncertainties they give for the imaginary part, but we obtain larger pulls ($5.6\,\sigma$ vs. $4.2\,\sigma$ of Ref. [319]). Their *scenario II* corresponds to our third line in Table 5.1 ($C_9^{\mu\,\mathrm{NP}} = -C_{10}^{\mu\,\mathrm{NP}}$), we agree with the main features of their fit, for the real part they obtain $\mathrm{Re}(C_9^{\mu\,\mathrm{NP}}) = \mathrm{Re}(C_{10}^{\mu\,\mathrm{NP}}) = -0.8 \pm 0.3$, we obtain a slightly smaller

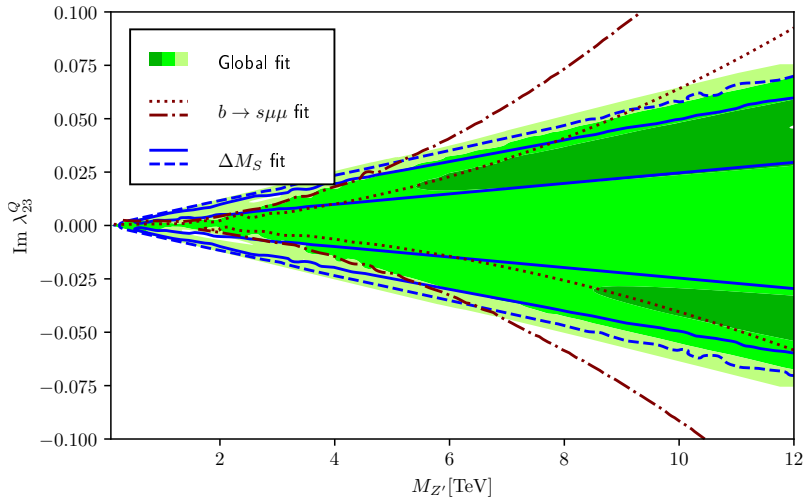

Figure 5.3: Fit on Z' parameter space in the $M_{Z'}$-Im λ_{23}^Q plane (see text).

real part, but they agree within uncertainties, both of us obtain a double minimum for the imaginary part $\sim \pm(1.1-1.2)\,i$, again, we obtain a slightly larger pull ($5.72\,\sigma$ vs. 4.0, $4.2\,\sigma$ of Ref. [319]).

Choosing complex Wilson coefficients also implies additional constraints from CP-violating observables. This fact has not been considered in the previous analysis. In the next section we study the consequences of having these coefficients in the analysis of B meson anomalies on some NP models and we consider a combined fit of both the ratios R_{K^+} and $R_{K^{*0}}$ and the angular observables P_4' and P_5', and also the CP-mixing asymmetry.

5.4 B_s-mixing and NP models

Several NP models that are able to explain the lepton flavour universality violation effects are constrained by other flavour observables like B_s-mixing. In particular the parameter space of Z' and leptoquark models are severely constrained by the present experimental results of ΔM_s [260]. Besides, as already mentioned, additional constraints emerge from CP-violating observables when considering complex couplings. Ref. [260] argues that nearly imaginary Wilson coefficients could explain the discrepancies with the ΔM_s experimental measurement, but a combined fit of R_{K^+} and $R_{K^{*0}}$ observables, together with ΔM_s and CP-violation observable A_{CP}^{mix} in $B_s \to J/\psi\phi$ decays should be performed. In the next subsections we investigate these issues for the case of Z' and leptoquark models.

5.4.1 Z' fit

From now on, a combined fit of R_{K^+} and $R_{K^{*0}}$ observables, ΔM_s and the CP-violation observable A_{CP}^{mix} is included in our analysis.

Best fits	Real	Imaginary	Complex
λ_{23}^{Q}	-0.002	$\pm 0.047\, i$	$-0.0020 - 0.0021\, i$
$M_{Z'}$	1.31 TeV	12 TeV	1.08 TeV
Pull $(\sqrt{\Delta\chi^2_{\rm SM}})$	5.70	1.61	6.05
Pull (σ)	$5.39\,\sigma$	$1.09\,\sigma$	$5.43\,\sigma$
$\chi^2_{\rm min}$/d.o.f.	1.41	2.12	1.34
R_{K^+}	0.66 ± 0.05	1.00 ± 0.01	0.65 ± 0.07
$R_{K^{*0}}^{[0.045,1.1]}$	0.849 ± 0.013	0.93 ± 0.02	0.84 ± 0.02
$R_{K^{*0}}^{[1.1,6]}$	0.68 ± 0.05	1.00 ± 0.01	0.68 ± 0.07
ΔM_s	$20.41 \pm 1.26\ \text{ps}^{-1}$	$18.0 \pm 1.7\ \text{ps}^{-1}$	$19.95 \pm 1.27\ \text{ps}^{-1}$
$A_{CP}^{\rm mix}$	-0.0369 ± 0.0002	-0.041 ± 0.002	-0.035 ± 0.003

Table 5.3: Best fits, and corresponding pulls, to R_{K^+}, $R_{K^{*0}}$, ΔM_s and $A_{CP}^{\rm mix}$; considering real, imaginary and complex couplings on the Z' model. Shown are also the corresponding pulls, $\chi^2_{\rm min}$/d.o.f., and the predictions for semi-leptonic decay observables R_{K^+}, $R_{K^{*0}}$; ΔM_s and $A_{CP}^{\rm mix}$ with $1\,\sigma$ uncertainties.

Figure 5.3 shows the fits on the Z' mass $M_{Z'}$ and the imaginary coupling λ_{23}^{Q} (setting $\lambda_{22}^{L} = 1$) imposed by $b \to s\mu^+\mu^-$ decays and B_s-mixing. The red lines (dotted, dash-dotted) correspond to the fit using only semi-leptonic B meson decays, i.e. $b \to s\mu^+\mu^-$ as in Figure 5.2 plus the branching ratios BR$(B_s \to \mu^+\mu^-)$ and BR$(B^0 \to \mu^+\mu^-)$. The best fit region is the one between the curves; dotted lines: $\Delta\chi^2 = 1$, dash-dotted lines: $\Delta\chi^2 = 4$. Blue lines (solid, dashed) correspond to the fit to B_s-mixing observables ΔM_s and $A_{CP}^{\rm mix}$. The best fit region is the one between the lines; solid lines $\Delta\chi^2 = 1$, dashed lines $\Delta\chi^2 = 4$, there are two regions with $\Delta\chi^2 < 1$, but between them $\Delta\chi^2$ is always smaller than 4. The green regions are the combined fit: dark region $\Delta\chi^2 \leq 1$, medium $\Delta\chi^2 \leq 4$ and light $\Delta\chi^2 \leq 9$.

The best fit for the $b \to s\mu^+\mu^-$ observables in the region under study is $M_{Z'} = 11\,\text{TeV}$, $\lambda_{23}^{Q} = 0.015\, i$, with a tiny $\sqrt{\Delta\chi^2_{\rm SM}} = 0.23$, which makes it statistically indistinguishable from the SM, and a large $\chi^2_{\rm min}$/d.o.f. $= 2.92$ which indicates that it does not provide a good fit to the data. For the B_s-mixing observables, the best fit is found at the maximum allowed mass $M_{Z'} = 12\,\text{TeV}$, $\lambda_{23}^{Q} = \pm 0.05\, i$, which corresponds to $C_{bs}^{LL\,\rm NP} = -1.54 \times 10^{-4}$. The SM has a pull of $\sqrt{\Delta\chi^2_{\rm SM}} = 1.73$ $(\equiv 1.21\,\sigma)$, and the minimum has a $\chi^2_{\rm min}$/d.o.f. $= 0.52$. The best fit when all observables are considered, in the $M_{Z'}$ region of our analysis, and λ_{23}^{Q} being a pure imaginary coupling, is found at $M_{Z'} = 12\,\text{TeV}$, $\lambda_{23}^{Q} = \pm 0.047\, i$, and the pull of the SM is $\sqrt{\Delta\chi^2_{\rm SM}} = 1.61 (\equiv 1.09\,\sigma)$ and $\chi^2_{\rm min}$/d.o.f. $= 2.12$. Larger values of $M_{Z'}$ do not improve the pull of the SM. Actually, if one allows larger values for $M_{Z'}$ the best fit point has a linear relation between the coupling and the maximal allowed mass: $\lambda_{23}^{Q} \simeq i\,(3.95 \times M_{Z'}^{\rm max}/\,\text{TeV}) \times 10^{-3}$. This linear relation produces a (approximately) constant $C_{bs}^{LL\,\rm NP}$ Eq. (4.8), with a ΔM_s prediction close to the experimental value in Eq. (5.1), while the contributions to $|C_{9,10}^{\mu\,\rm NP}|$ decrease as $M_{Z'}^{-1}$ Eq. (4.7). Since imaginary couplings worsen the $R_{K^{(*)}}$

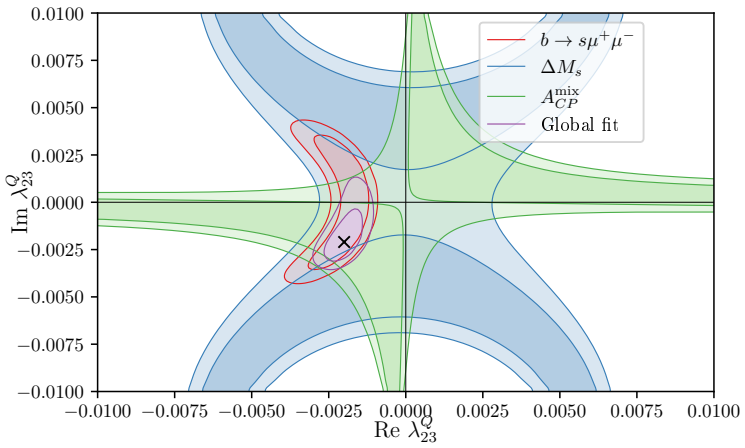

Figure 5.4: Fit on Z' parameter space in the λ_{23}^Q complex plane for the best fit Z' mass $M_{Z'} = 1.08\,\text{TeV}$ (see text).

prediction, the larger $M_{Z'}$ provides better predictions for them, bringing them closer to the SM value. The best fit $\Delta\chi^2_{\rm SM}$ grows very slowly with growing allowed $M_{Z'}$. Table 5.3 summarizes the best fit values for λ_{23}^Q and $M_{Z'}$, and corresponding pulls, to R_{K^+} and $R_{K^{*0}}$ observables, ΔM_s and $A_{CP}^{\rm mix}$; considering real, imaginary and complex Wilson coefficients. Results for the above observables in each scenario are included in this table. It is clear that $R_{K^{(*)}}$ observables prefer real Wilson coefficients, as expected. For real couplings the description is better than the SM, with a pull of $5.39\,\sigma$ but it does not improve the prediction for ΔM_s. Contrary, to improve the prediction for ΔM_s imaginary couplings are required in the Z' model, however the pull with respect the SM is small, and it has a large $\chi^2_{\rm min}$/d.o.f.. When allowing generic complex couplings (third column in Table 5.3) we find that the best fit point is close to the best fit point using only real couplings (first column in Table 5.3), and the pull with respect the SM improves slightly ($5.43\,\sigma$ versus $5.39\,\sigma$), and the predictions for the observables are also close to the pure real couplings case, showing a slight improvement in the prediction for ΔM_s.

Fig. 5.4 shows the best fit regions in the complex λ_{23}^Q plane for the best fit mass value $M_{Z'} = 1.08\,\text{TeV}$ (Table 5.3). The red region shows the 2-dimensional 1 and $2\,\sigma$ allowed values ($\Delta\chi^2 = 2.29, 6.18$) including only the $b \to s\mu^+\mu^-$ observables, the blue region shows the 1 and $2\,\sigma$ allowed values including only ΔM_s, and the green region show the 1 and $2\,\sigma$ allowed values including only $A_{CP}^{\rm mix}$, the violet region shows the combined fit. Here we see the tension between the $b \to s\mu^+\mu^-$ and ΔM_s fits. $b \to s\mu^+\mu^-$ selects a region around the real axis of the coupling, whereas ΔM_s selects regions away from it. There are two small intersection regions for the $1\,\sigma$ allowed values of both fits. The $A_{CP}^{\rm mix}$ fit selects one of these regions, and breaks the degeneracy. Actually, the $b \to s\mu^+\mu^-$ fit selects fixed values of $C_9^{\mu\,\rm NP} = -C_{10}^{\mu\,\rm NP}$, Eq. (4.7), since $C_9^{\mu\,\rm NP} = -C_{10}^{\mu\,\rm NP}$ scale as $\sim \lambda_{23}^Q / M_{Z'}^2$, for fixed $C_9^{\mu\,\rm NP} = -C_{10}^{\mu\,\rm NP}$ the allowed values of λ_{23}^Q (red region in Fig. 5.4) around the real axis will grow as $M_{Z'}^2$, but, at the same time, the allowed region will move away from the imaginary axis as $M_{Z'}^2$.

On the other hand, the fit on ΔM_s selects fixed values of $C_{bs}^{LL\,\mathrm{NP}}$, Eq. (4.8), since $C_{bs}^{LL\,\mathrm{NP}} \sim (\lambda_{23}^Q)^2/M_{Z'}^2$, for fixed $C_{bs}^{LL\,\mathrm{NP}}$ the $1\,\sigma$ unfavored region around the origin (light blue region in Fig. 5.4) will grow as $\lambda_{23}^Q \sim M_{Z'}$. As $M_{Z'}$ grows, the red region moves away from the origin as $M_{Z'}^2$, but the blue region expands only as $M_{Z'}$, so that at some $M_{Z'}$ value their $1\,\sigma$ regions do not longer intersect. This is the reason why we obtain a relatively low $M_{Z'}$ in the fits of Table 5.3.

Ref. [319] provides also a fit for the Z' model, using a fixed $M_{Z'} = 1\,\mathrm{TeV}$, this value is close to our best fit value of Table 5.3. For $\lambda_{22}^L = 1$ they obtain the best fit coupling $\lambda_{23}^Q = (-0.8 \pm 0.3) \times 10^{-3} + (-0.4 \pm 3.1) \times 10^{-3}\, i$ with a pull of $4.0\,\sigma$. Our best fit values agree with them within uncertainties. Note that we do not provide uncertainties for the best fit values, the reason being that the parameters are not independent, the 2-dimensional best fit regions in Fig. 5.4 are not ellipses, and the best fit points are not on the center of the figures, so that giving a central value with 1-dimensional uncertainties overestimates the uncertainty and leads to confusion about the meaning and position of the best fit point.

We conclude that, in the framework of Z' models, $R_{K^{(*)}}$ observables are better described than in the SM, with a pull $\gtrsim 5.39\,\sigma$ for $M_{Z'} \simeq 1 - 1.3\,\mathrm{TeV}$, and a coupling with a real part $\mathrm{Re}(\lambda_{23}^Q) \simeq -0.002$. The presence of a similar imaginary part for the coupling $\mathrm{Im}(\lambda_{23}^Q) \simeq -0.0021$ improves slightly the fit, as well as the ΔM_s prediction.

5.4.2 Leptoquark fit

The leptoquark model has three independent couplings contributing to ΔM_s Eq. (4.3). For the combined fits we will assume that the dominant coupling is the muon coupling $y_{32}^{QL} y_{22}^{QL*}$, which is the one contributing to $R_{K^{(*)}}$ Eq. (4.2). The fits on the S_3 leptoquark mass M_{S_3} and the imaginary coupling $y_{32}^{QL} y_{22}^{QL*}$ imposed by $b \to s\mu^+\mu^-$ decays and B_s-mixing are presented in Figure 5.5. The observables used in the respective fits are the same as in Figure 5.3. The red lines (dotted, dash-dotted) correspond to the fit using only semi-leptonic B meson decays, i.e. $b \to s\mu^+\mu^-$ plus the branching ratios $\mathrm{BR}(B_s \to \mu^+\mu^-)$ and $\mathrm{BR}(B^0 \to \mu^+\mu^-)$, the best fit region is the one between the curves; dotted lines: $\Delta\chi^2 = 1$, dash-dotted lines: $\Delta\chi^2 = 4$. Blue lines (solid, dashed) correspond to the fit to B_s-mixing observables ΔM_s and A_{CP}^{mix}. The best fit region is the one between the lines; solid lines $\Delta\chi^2 = 1$, dashed lines $\Delta\chi^2 = 4$, there are two regions with $\Delta\chi^2 < 1$, but between them $\Delta\chi^2$ is always smaller than 4. The green regions are the combined fit: dark region $\Delta\chi^2 \leq 1$, medium $\Delta\chi^2 \leq 4$ and light $\Delta\chi^2 \leq 9$. In the $b \to s\mu^+\mu^-$ fit the best fit parameters for imaginary couplings is $y_{32}^{QL} y_{22}^{QL*} = -0.2\, i$, $M_{S_3} = 40.8\,\mathrm{TeV}$. The leptoquark fit to B_s-mixing observables has a double minimum, located at $M_{S_3} = 44.9\,\mathrm{TeV}$, $y_{32}^{QL} y_{22}^{QL*} = \pm 2\, i$, with a SM pull of $\sqrt{\Delta\chi^2_{\mathrm{SM}}} = 1.74$ ($\equiv 1.22\,\sigma$) and $\chi^2_{\mathrm{min}}/\mathrm{d.o.f.} = 0.51$. These points correspond to a value for the Wilson coefficient of $C_{bs}^{LL\,\mathrm{NP}} = -1.39 \times 10^{-4}$. The combined fit, including all observables, and considering only imaginary $y_{32}^{QL} y_{22}^{QL*}$ couplings, is located at $M_{S_3} = 50\,\mathrm{TeV}$, $y_{32}^{QL} y_{22}^{QL*} = -1.67\, i$; with a SM pull of only $\sqrt{\Delta\chi^2_{\mathrm{SM}}} = 1.1 (\equiv 0.6\,\sigma)$ and a

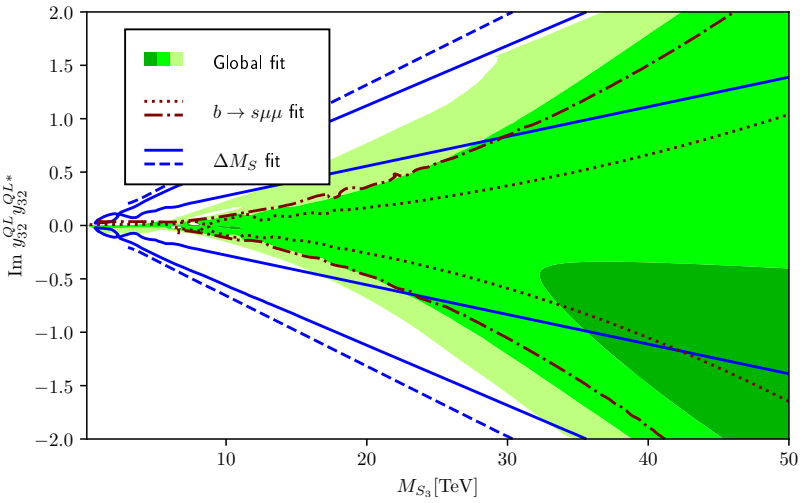

Figure 5.5: Fit on S_3 leptoquark parameter space in the M_{S_3}-Im $y_{32}^{QL} y_{22}^{QL*}$ plane (see text).

large χ^2_{min}/d.o.f. = 2.16. Larger M_{S_3} masses provide similar values for the best fit couplings, and observable predictions, and the pulls improve slowly. The situation is similar than in the Z' case: by allowing larger M_{S_3} masses the best fit coupling reaches an asymptotic straight line, where the contribution to ΔM_s is constant Eq. (4.3), whereas the contribution to $|C_{9,10}^{\mu\text{NP}}|$ Eq. (4.2) decreases as $M_{S_3}^{-1}$, the best fit coupling behaves as $y_{32}^{QL} y_{22}^{QL*} \simeq i\,(4.43 \times 10^{-2} \times M_{S_3}/\,\text{TeV})$. Table 5.4 shows the best fit parameters for the leptoquark model considered in this work, corresponding pulls, predictions to the observables R_{K^+}, $R_{K^{*0}}$, ΔM_s and A_{CP}^{mix} and χ^2_{min}/d.o.f., considering real, imaginary and complex Wilson coefficients. Table 5.4 shows that only imaginary couplings do not improve the results, they cannot explain the $R_{K^{(*)}}$ anomaly. However, when complex couplings are considered, we found a better fit of $R_{K^{(*)}}$ observables, the best fit parameters emerge at $M_{S_3} = 4.1\,\text{TeV}$ and $y_{32}^{QL} y_{22}^{QL*} = 0.033 + 0.034\,i$, with $\sqrt{\Delta\chi^2_{\text{SM}}} = 5.90$ ($\equiv 5.27\,\sigma$). The best fit point M_{S_3} and the coupling real part are similar to the real couplings case. The imaginary part of the coupling is similar to the real part. The pull with respect the SM is marginally better in the case of complex couplings ($\sqrt{\Delta\chi^2_{\text{SM}}} = 5.9$ versus 5.82), but it actually worsens in units of σ, since the complex coupling fit has one more free parameter. The χ^2_{min}/d.o.f. is similar in both scenarios. The predictions for the B meson physics observables are similar than in the real couplings case.

Fig. 5.6 shows the best fit regions in the complex $y_{32}^{QL} y_{22}^{QL*}$ plane, for the best fit mass parameter $M_{S_3} = 4.1\,\text{TeV}$, Table 5.4. The meaning of each region is as in Fig. 5.4. In this model there is no intersection between the $1\,\sigma$ best fit regions of the $b \to s\mu^+\mu^-$ and the ΔM_s fits. Here we also find the tension between the $b \to s\mu^+\mu^-$ and ΔM_s observables, and the different evolution of the best fit regions with the leptoquark mass M_{S_3}. The ΔM_s fit moves the best fit point away from the real axis, and the A_{CP}^{mix} fit selects of the of the signs for the imaginary part, however the combined best fit region lies outside the $1\,\sigma$ region for ΔM_s, and the ΔM_s prediction does not improve with respect the SM.

Ref. [319] also provides a fit for the leptoquark scenario, our model corresponds to

Best fits	Real	Imaginary	Complex
$y_{32}^{QL}\, y_{22}^{QL*}$	0.04	$-1.67\, i$	$0.033 + 0.034\, i$
M_{S_3}	5.19 TeV	50 TeV	4.10 TeV
Pull $(\sqrt{\Delta\chi^2_{\rm SM}})$	5.82	1.10	5.90
Pull (σ)	$5.47\,\sigma$	$0.60\,\sigma$	$5.27\,\sigma$
$\chi^2_{\rm min}$/d.o.f.	1.38	2.16	1.39
R_{K^+}	0.64 ± 0.06	1.00 ± 0.01	0.62 ± 0.14
$R_{K^{*0}}^{[0.045,1.1]}$	0.835 ± 0.015	0.93 ± 0.02	0.84 ± 0.04
$R_{K^{*0}}^{[1.1,6]}$	0.66 ± 0.06	1.00 ± 0.01	0.66 ± 0.14
ΔM_s	$20.07 \pm 1.27\ \text{ps}^{-1}$	$18.8 \pm 1.7\ \text{ps}^{-1}$	$20.0 \pm 1.2\ \text{ps}^{-1}$
$A_{CP}^{\rm mix}$	-0.0374 ± 0.0006	-0.039 ± 0.002	-0.032 ± 0.003

Table 5.4: Best fits, and corresponding pulls, to R_{K^+}, $R_{K^{*0}}$, ΔM_s and $A_{CP}^{\rm mix}$; considering real, imaginary and complex couplings on the S_3 leptoquark. Shown are also the corresponding pulls, $\chi^2_{\rm min}$/d.o.f. and the predictions for semi-leptonic decay observables R_{K^+}, $R_{K^{*0}}$; ΔM_s and $A_{CP}^{\rm mix}$ with $1\,\sigma$ uncertainties.

their $\vec{\Delta}_{1/3}[S3]$ model. Ref. [319] performs a fit fixing the leptoquark mass to $M_{S_3} = 1\,\text{TeV}$, and they obtain a two nearly degenerate minimums with positive and negative imaginary parts. The reason for that is that they do not include the $A_{CP}^{\rm mix}$ observable in the fit. Since the $C_9^{\mu\,\rm NP} = -C_{10}^{\mu\,\rm NP}$ Wilson coefficient scales like $\sim y_{32}^{QL}\, y_{22}^{QL*}/M_{S_3}^2$ Eq. (4.2) we can compare both results by scaling the best fit coupling with the mass squared, by taking their central value for the positive imaginary part, we obtain $y_{32}^{QL}\, y_{22}^{QL*} = (1.4 + 1.7\, i) \times 10^{-3} \times (4.1)^2 = 0.023 + 0.029\, i$, which is similar to our third column in Table 5.4, and is inside the best fit region of Fig. 5.6. Again, we obtain a larger pull $(\sqrt{\Delta\chi^2_{\rm SM}} = 5.9$ versus $4.0)$.

If one relaxes the condition $y_{33}^{QL}\, y_{23}^{QL*} \simeq y_{31}^{QL}\, y_{21}^{QL*} \simeq 0$ then the leptoquark contributions to ΔM_s Eq. (4.3) and $C_{9,10}^{\mu\,\rm NP}$ Eq. (4.2) are no longer correlated, it would be possible to choose: a purely real coupling to muons, such that it fulfills the first column of Table 5.4; a vanishing coupling for electrons, such that it does not contribute to $R_{K^{(*)}}$; and a complex coupling for taus, such that $y_{33}^{QL}\, y_{23}^{QL*} + y_{32}^{QL}\, y_{22}^{QL*}$ is purely imaginary, and provides a good prediction for ΔM_s like in the second column of Table 5.4. Of course, this would be a quite strange arrangement for leptoquark couplings! Another option would be to take an specific model construction for the relations among the leptoquark couplings, and make a fit on these parameters. This analysis is beyond the scope of the present work.

To end the discussion of this chapter, we study the impact of considering complex Wilson coefficients in the analysis of B meson anomalies in the two specific models discussed previously, Z' and S_3 leptoquark. We have performed a fit of the R_{K^+} and $R_{K^{*0}}$ observables, together with ΔM_s and CP-violation observable $A_{CP}^{\rm mix}$ when these complex couplings are included in the analysis. Results are presented in Fig. 5.7. Predictions for the Z' model are represented in blue, and for the S_3 leptoquark model in red. The central

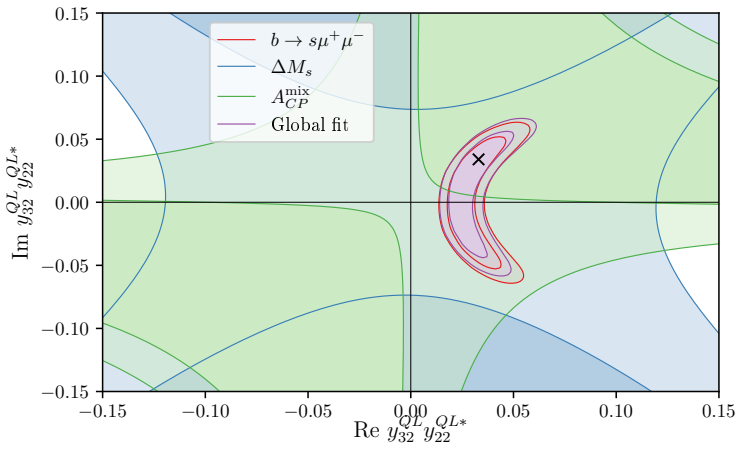

Figure 5.6: Fit on S_3 leptoquark parameter space in the complex $y_{32}^{QL} y_{22}^{QL*}$ plane for the best fit leptoquark mass $M_{S_3} = 4.1\,\text{TeV}$ (see text).

values are marked with a circle in the real fits, with a triangle in the imaginary fits and with a square in the complex fit. The length of the error bars corresponds to the $1\,\sigma$ confidence interval. Our predictions are compared to the SM predictions (yellow rectangles) and experimental values (green rectangles), with the height of the rectangles corresponding to the $1\,\sigma$ values. The obtained results confirm that real Wilson coefficients cannot explain the B_s-mixing anomaly; but also only imaginary Wilson coefficients cannot explain the $R_{K^{(*)}}$ anomaly. For complex couplings, the predictions for R_{K^+}, $R_{K^{*0}}$ and ΔM_s are similar to those of real couplings (Tables 5.3, 5.4), although the tension in ΔM_s slightly decreases.

5.5 Conclusions

We have updated the analysis of NP violating LFU, by using the effective Lagrangian approach and also in the Z' and leptoquark models [1]. By considering generic complex Wilson coefficients we found that purely imaginary coefficients do not improve significantly B meson physics observable predictions, whereas complex coefficients (Table 5.1) do improve the predictions, with a slightly improved pull than using only real coefficients [324]. We have analyzed the impact of considering complex Wilson coefficients in the analysis of B meson anomalies in two specific models: Z' and leptoquarks, and we have presented a combined fit of R_{K^+} and $R_{K^{*0}}$ observables, together with ΔM_s and CP-violation observable $A_{CP}^{\rm mix}$ when these complex couplings are included in the analysis, Fig. 5.7. We confirm that real Wilson coefficients cannot explain the B_s-mixing anomaly; but also only imaginary Wilson coefficients cannot explain the $R_{K^{(*)}}$ anomaly. Contrary, complex couplings offer a slightly better fit. For complex couplings the predictions for R_{K^+}, $R_{K^{*0}}$ and ΔM_s are similar than for real couplings (Tables 5.3, 5.4). For Z' models the best fit in both cases is obtained for $M_{Z'} \simeq 1 - 1.3\,\text{TeV}$, a negative real part of the coupling $\text{Re}(\lambda_{23}^{Q}) \simeq -0.002$, with

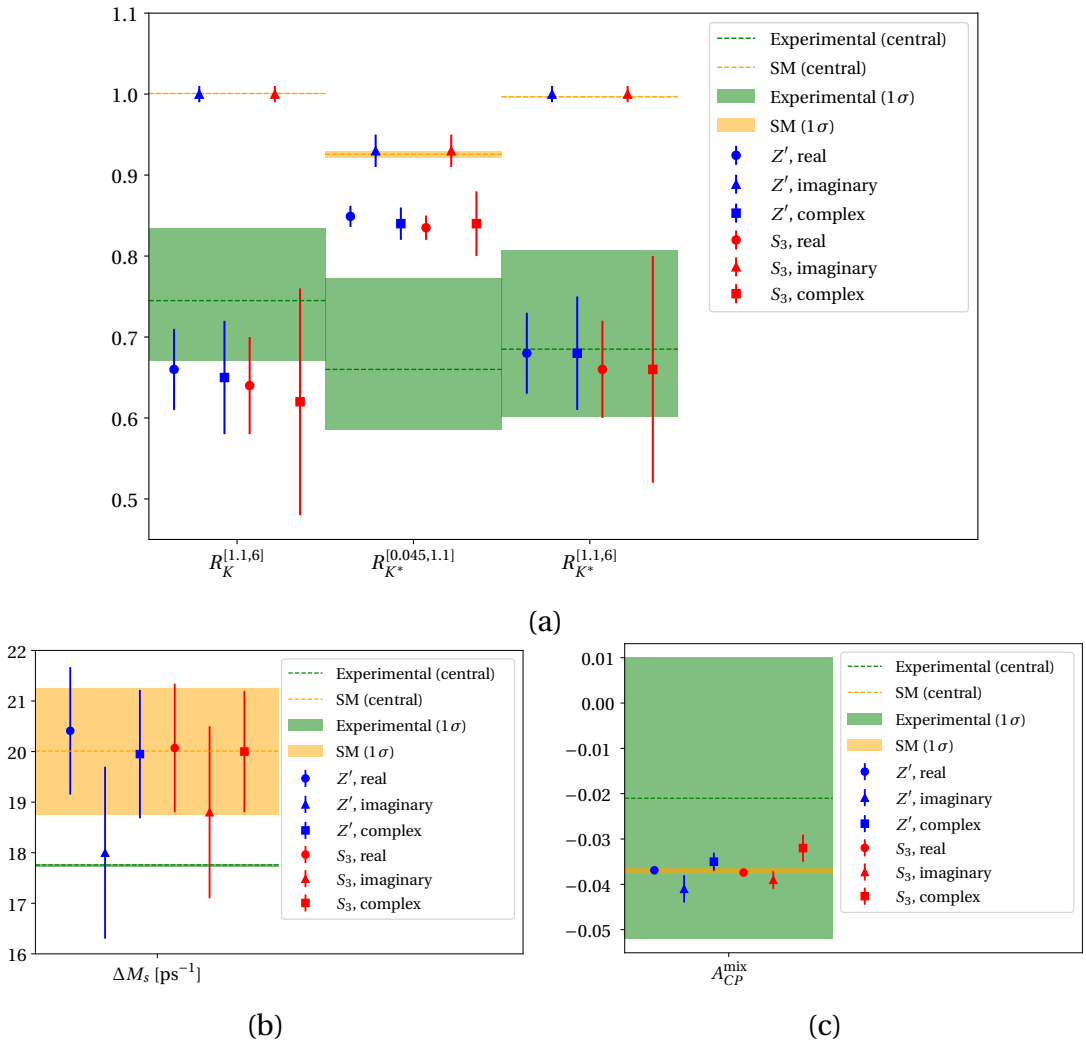

Figure 5.7: Predictions for the observables included in the fit: (a) R_{K^+} and $R_{K^{*0}}$, (b) ΔM_s and (c) $A_{\mathrm{CP}}^{\mathrm{mix}}$. Predictions for the Z' models are represented in blue, and for the S_3 leptoquark model in red. Central values are marked with a circle in the real fits, with a triangle in the imaginary fits and with a square in the complex fit. The length of the error bars corresponds to the 1σ confidence interval. Our predictions are compared to the SM predictions (yellow rectangles) and experimental values (green rectangles), with the height of the rectangles corresponding to the 1σ values.

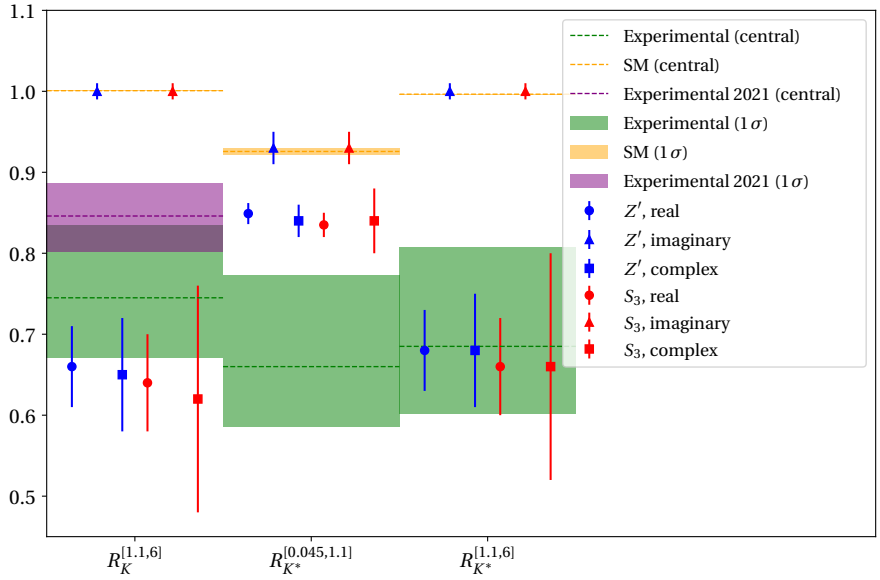

Figure 5.8: Updated version of Fig. 5.7(a), with the experimental value of $R_{K^{(*)}}$ obtained by LHCb in [123] (purple rectangle). Model predictions are unchanged.

possibly a similar imaginary coupling part $\mathrm{Im}(\lambda^Q_{23}) \simeq -0.0021$. For leptoquark models the situation is similar, with a best fit mass of $M_{S_3} = 4-5\,\mathrm{TeV}$ and a coupling with a positive real part $y^{QL}_{32} y^{QL*}_{22} \simeq 0.03-0.04$, the presence of a similar imaginary part does not improve significantly the fit. One can obtain better fits in the leptoquark models by relaxing the assumption on the leptoquark couplings, or providing specific models for leptoquark couplings, this analysis is beyond the scope of the present work. In summary, new physics Z' or leptoquark models with complex couplings provide a slightly improved fit to B meson physics observables as compared with models with real couplings.

5.5.1 Updated conclusions

After the completion of this work, Ref. [203] appeared also analyzing the presence of complex couplings in the B system. Our results agree with Ref. [203] wherever comparable.

After the publication of [1], the SM predictions of the B_s mass difference has been updated to $\Delta M_s^{\mathrm{SM}} = (18.4^{+0.7}_{-1.2})\ \mathrm{ps}^{-1}$ [317, 333–337]. In consequence, the theoretical values now lies just within $1\,\sigma$ of the experimental measurement, dispelling for now any hint of anomaly concerning this particular observable. While ΔM_s will be considered in the rest of the global analyses, we will focus on real Wilson coefficients.

The 2019 and 2021 measurement of R_K in LHCb [123, 129] increased the experimental value of this observable. The predictions obtained with our models are no longer compatible at the $1\,\sigma$ level, as shown in Fig. 5.8.

Chapter 6

Fit to SMEFT coefficients and future prospects

This Chapter is devoted to an analysis of the B anomalies using the SMEFT formalism. In order to guarantee the internal consistency of the results when the mixing induced by the RG equations is considered, the analysis also includes observables from several physical sectors. We will focus on eleven scenarios containing various combinations of effective operators that include two leptons and two third generation quarks. After comparing all the scenarios, the most descriptive scenario is studied in more detail, in order to understand how each Wilson coefficient is affected by the observables. In the last Section, the analysis is generalized in order to see how the expected improvement of the electroweak experimental measurements could impact the results of the global fit.

This chapter is based on [2], and Section 6.4 is also based on [3, 5]. Some of the results have been updated and extended with respect to the published versions, comparisons between old and new results are included.

6.1 Introduction

As detailed in Section 2.4, several experimental collaborations observed LFUV processes in B meson decays that would be a clear sign for NP. Besides the $R_{K^{(*)}}$ ratios discussed in the previous section, another example is the case of the $R_{D^{(*)}}$ ratios defined in Eq. (2.43). In the $b \to c\ell\nu$ transitions, signs of violation of lepton universality have been observed only in the $e-\tau$ and $\mu-\tau$ cases, while the universality has been tested to great precision in the $e-\mu$ case [102–104]. As a consequence, both $R^{\ell}_{D^{(*)}}$ and $R^{\mu}_{D^{(*)}}$ should have similar predictions and measurements. We will consider for the present analysis all the experimental measurements available for the $R_{D^{(*)}}$ ratios, that have been described in Section 2.4.2. For the purposes of this analysis we also consider all the available experimental data for the $R_{K^{(*)}}$ ratios and related $b \to s\ell^+\ell^-$ observables, namely the optimized angular observable P'_5 [84], that can be found in Section 2.4.1.

The compatibility of the individual measurements with respect to the SM predictions is of 3.1σ for the R_{K^+} ratio, 2.3σ for the $R_{K^{*0}}$ ratio in the low-q^2 region and 2.4σ in the central-q^2 region, taking into account the 2019 and 2021 experimental results.

In this chapter we investigate the effects of the global fits to the Wilson coefficients assuming a model-independent effective Lagrangian approach and including a discussion of the consequences of our analysis in leptoquark models. We define different scenarios for the phenomenological study by considering the NP contributions to the Wilson coefficients in such a way that NP is present in one, two or three of the Wilson coefficients simultaneously. These scenarios are used to study the impact of the global fits on the Wilson coefficients and, therefore, to exhibit more clearly which combinations of Wilson coefficients are preferred and/or constrained by experimental data.

We begin in section 6.2 by presenting a brief summary of the EFT used to describe possible NP contributions to B decays observables. Then, section 6.3 is devoted to the global fits to the Wilson coefficients, presenting the set of scenarios that we are going to analyze. As already explained, we will work in different scenarios that arise by considering the presence of NP contributions in one, two or three of the Wilson coefficients. We will compare the results of the global fit in each scenario with respect to two cases: the SM and the best fit point of the three independent Wilson coefficients scenario (the most general case). This particular choice of the Wilson coefficients that will enter our analysis is the main difference with respect to previous global fits analysis in the literature. Section 6.3.1 is devoted to discuss in more detail the most general proposed scenario, scenario VII, in which the prediction of the $R_{D^{(*)}}$ and $R_{K^{(*)}}$ observables is improved. In section 6.4 we include a discussion of the impact that future e^+e^- linear colliders will have in the B anomalies. Finally, the phenomenological implications of our analysis in leptoquark models is included in section 6.5. Conclusions are presented in section 6.6. Appendix C.1 contains the list of observables that contribute to the global fit with their prediction in the most general scenario: the global fit to three independent Wilson coefficients receiving NP contributions.

6.2 Setting of the fit

The SMEFT presented in Section 3.4 is formulated at an energy scale $\mu_{\text{SMEFT}} = \Lambda$ higher that the electroweak scale, and the degrees of freedom are all the SM fields. The WET presented in section 3.5 is formulated at an energy scale below the electroweak scale, for example $\mu_{\text{WET}} = m_b$, and the top quark, Higgs, W and Z bosons are integrated out. All the numerical analyses of this chapter will be performed using only the SMEFT operators, while the WET Lagrangian will be useful for the discussion of the results.

We consider NP contributions at an energy scale Λ ($\Lambda \sim \mathcal{O}(\text{TeV})$) described by the SMEFT Lagrangian in Eq. (3.35). Since we are interested in the B anomalies, we only study the SMEFT operators containing two left-handed quarks and two left-handed leptons,

that is,

$$\mathscr{L}_{\text{SMEFT}} = \frac{1}{\Lambda^2}\left(C^{ijkl}_{\ell q(1)}\, Q^{ijkl}_{\ell q(1)} + C^{ijkl}_{\ell q(3)}\, Q^{ijkl}_{\ell q(3)}\right), \tag{6.1}$$

where the dimension six operators are defined as

$$Q^{ijkl}_{\ell q(1)} = (\bar{\ell}_i \gamma_\mu \ell_j)(\bar{q}_k \gamma^\mu q_l), \qquad Q^{ijkl}_{\ell q(3)} = (\bar{\ell}_i \gamma_\mu \tau^I \ell_j)(\bar{q}_k \gamma^\mu \tau^I q_l), \tag{6.2}$$

ℓ and q are the lepton and quark $SU(2)_L$ doublets defined in the mass basis[1], τ^I the Pauli matrices, and i, j, k, l denote generation indices. The $Q_{\ell q(1)}$ operator couples two $SU(2)_L$-singlet currents, while the $Q_{\ell q(3)}$ operator couples two $SU(2)_L$-triplet currents. Consequently, $Q_{\ell q(1)}$ only mediates FCNC processes, and $Q_{\ell q(3)}$ mediates both FCNC and FCCC processes. We will restrict our analysis to operators including only third generation quarks and same-generation leptons, and we will use the following notation for their Wilson coefficients:

$$C^e_{\ell q} \equiv C^{1133}_{\ell q}, \qquad C^\mu_{\ell q} \equiv C^{2233}_{\ell q}, \qquad C^\tau_{\ell q} \equiv C^{3333}_{\ell q}. \tag{6.3}$$

This particular choice of the Wilson coefficients that will enter our analysis is motivated by the fact that the most prominent discrepancies between SM predictions and experimental measurements, namely $R_{K^{(*)}}$ and $R_{D^{(*)}}$, affect the third quark generation. From a symmetry point of view, this would amount to imposing an $U(2)^3 = U(2)_q \times U(2)_u \times U(2)_d$ symmetry between the first and second quark generations [310, 338, 339], that remain SM-like. No restriction is imposed on the third quark generation. In the lepton sector we only consider diagonal entries in order to avoid LFV decays. This flavour structure for NP contributions has been presented in [339] as a minimal working setup. An analysis that studies NP contributions to $C^e_{\ell q}$ and $C^\mu_{\ell q}$, although not simultaneously, can be found at [340].

These operators contribute to the NP part of the C^ℓ_{VL} operators in Eqs. (3.48), C^ℓ_9 and C^ℓ_{10} operators in Eqs. (3.42) of the WET when matched at the electroweak scale μ_{EW}. Using the package `wilson` [341], we define the $C_{\ell q}$ operators at $\Lambda = 1\,\text{TeV}$, we calculate their running down to $\mu_{\text{EW}} = M_Z$, then match them with the WET operators and finally run the down to $\mu = m_b$, where the B physics observables are computed. We found the following relations between the Wilson coefficients at high and low energies:

$$\begin{aligned} C_9^{e,\mu\,\text{NP}}(m_b) &= -0.583\, C^{e,\mu}_{\ell q(1)} - 0.596\, C^{e,\mu}_{\ell q(3)}, & C_{10}^{e,\mu\,\text{NP}}(m_b) &= 0.588\, C^{e,\mu}_{\ell q(1)} + 0.591\, C^{e,\mu}_{\ell q(3)}, \\ C_{VL}^{e,\mu\,\text{NP}}(m_b) &= 0.0012\, C^{e,\mu}_{\ell q(1)} - 0.0644\, C^{e,\mu}_{\ell q(3)}, & C_{VL}^{\tau\,\text{NP}}(m_b) &= -0.0598\, C^{\tau}_{\ell q(3)}. \end{aligned} \tag{6.4}$$

The $R_{D^{(*)}}$ ratios obey the expressions of Eq. (3.50). The dependence of the $R_{K^{(*)}}$ ratios on the Wilson coefficients has been obtained in Appendix A, and an analytic computation of $R_{K^{*0}}$ as a function of $C_9^{\mu\,\text{NP}}$, $C_{10}^{\mu\,\text{NP}}$ in the region $1.1 \le q^2 \le 6.0\,\text{GeV}^2$ can be found in Eq. (3.47).

[1] In both the "Warsaw" and in the "Warsaw-down" basis, the lepton and d-quark fields are defined so that their mass matrices are diagonal. Consequently, translating from one to another does not modify the Lagrangian in Eq. (6.1). The relation between the two basis is shown in Eq. (7.3) of the next chapter.

It is important to note that the RG-induced SMEFT operators shift the Fermi constant [185] according to Eq. 3.40 and the elements of the CKM matrix [186] from their SM values. These shifts are already included in the matching conditions of Eq. (6.4).

The $\mathcal{O}_{\ell q}$ operators (6.2) also produce unwanted contributions to the $B \to K^{(*)}\nu\bar{\nu}$ decays [202, 342]. In order to obey these constraints, we will fix the relation at the scale $\Lambda = 1\,\text{TeV}$

$$C^i_{\ell q(1)} = C^i_{\ell q(3)} \equiv C^i_{\ell q}\,. \tag{6.5}$$

While Eq. (6.5) eliminates the tree-level contribution to the $B \to K^{(*)}\nu\bar{\nu}$ decays, the RG generates a one-loop contribution proportional to the $C_{\ell q(3)}$ coefficients. However, we have checked that this term is only a correction of 0.1% of the SM prediction. Eq. (6.5) also has the positive consequence of a partial cancellation of loop-induced effects in Z-pole and LFV observables.

6.3 Global fits

The effective operators affect a large range of observables. Therefore, any NP prediction based on Wilson coefficients has to be confronted not only with the $R_{K^{(*)}}$ an $R_{D^{(*)}}$ measurements, but also with several additional measurements involving the decays of B mesons. In the case of the SMEFT, the evolution of the RG produces a mix of the low-energy effective operators. For example, the $Q_{\ell q}$ operators mix under RG evolution with [184, 188]

$$\begin{aligned} Q^{jk}_{\varphi\ell(1)} &= (\varphi^\dagger i\overleftrightarrow{D}_\mu\varphi)(\bar{\ell}_j\gamma^\mu\ell_k)\,, \qquad Q^{jk}_{\varphi\ell(3)} = (\varphi^\dagger i\overleftrightarrow{D}^I_\mu\varphi)(\bar{\ell}_j\gamma^\mu\tau^I\ell_k)\,, \\ Q^{jk}_{\varphi e} &= (\varphi^\dagger i\overleftrightarrow{D}_\mu\varphi)(\bar{e}_j\gamma^\mu e_k)\,, \end{aligned} \tag{6.6}$$

that modify the W and Z couplings to leptons. In consequence, NP in the semileptonic couplings of third generation quarks will indirectly affect electroweak (EW) observables, such as the mass of the W boson, the hadronic cross-section of the Z boson σ^0_{had} or the branching ratios of the Z to different leptons. In order to keep the predictions consistent with this range of experimental test, global fits have proven to be a valuable tool [225, 343–345].

We have performed global fits to the $C_{\ell q}$ Wilson coefficients using the package `smelli` v2.3 [342]. The global fit includes the $R_{K^{(*)}}$ and $R_{D^{(*)}}$ observables, the electroweak precision observables, W and Z decay widths and branching ratios to leptons, superallowed nuclear β decays, the $b \to s\mu^+\mu^-$ observables (including P'_5 and the branching ratio of $B_s \to \mu^+\mu^-$) and the $b \to s\nu\bar{\nu}$ observables. The SM input parameters are presented in Table 6.1. These values are taken from open source code `flavio` v2.3 [195], sources used by the program are quoted when available. Note that the experimental measurements used to determine the SM input parameters, such as the $\mu \to e\bar{\nu}\nu$ decay, are not included in the fit in order to ensure the consistency of the procedure. This code assumes unitarity of the CKM matrix.

G_F^0	$1.1663787(6) \times 10^{-5}$ GeV^{-2}	PDG 2014 [346]
$\alpha_e(M_Z)$	0.00781616(86)	[195]
$\alpha_s(M_Z)$	0.1182(8)	FLAG 2019 [333]
$\sin^2\hat{\theta}_W(M_Z)$, $\overline{\text{MS}}$	0.23129(5)	PDG 2017 [329]
V_{us}^0	0.2248(8)	FLAG 2017 $N_f = 2+1+1$ [347]
$\lvert V_{ub}^0\rvert$	$3.73(14) \times 10^{-3}$	FLAG 2017 $N_f = 2+1$ $B \to \pi\ell\nu$ [347]
V_{cb}^0	$4.221(78) \times 10^{-2}$	[195]
δ_{KM}^0	1.27(12)	[195]
$m_u(2\text{ GeV})$, $\overline{\text{MS}}$	2.130(41) MeV	[348]
$m_d(2\text{ GeV})$, $\overline{\text{MS}}$	4.675(56) MeV	[348]
$m_s(2\text{ GeV})$, $\overline{\text{MS}}$	92.47(69) MeV	[348]
$m_c(m_c)$, $\overline{\text{MS}}$	1.273(10) GeV	[348]
$m_b(m_b)$, $\overline{\text{MS}}$	4.195(14) GeV	[348]

Table 6.1: SM input parameters.

We proceed to study observables by defining some specific scenarios for combinations of the $C_{\ell q}^i$ operators such that NP contributions to the Wilson coefficients emerge in one, two or three of the Wilson coefficients simultaneously: in Scenarios I-III NP only modifies the $C_{\ell q}$ operators in one lepton flavour at a time; in Scenarios IV-VI and X NP is present in two of the Wilson coefficients simultaneously; and finally in Scenarios VII-IX and XI we consider the more general case in which three of the $C_{\ell q}^i$ operators receive NP contributions. The more general one of these last three scenarios is Scenario VII, in which we consider three independent Wilson coefficients. This scenario is discussed in more detail in section 6.3.1.

The goodness of each fit is evaluated with its difference of χ^2 with respect to the SM, $\Delta\chi^2_{\text{SM}} = \chi^2_{\text{SM}} - \chi^2_{\text{fit}}$. The package `smelli` actually computes the differences of the logarithms of the likelihood function $\Delta\log L = -\frac{1}{2}\Delta\chi^2$. In order to compare two fits A and B, we use the pull between them in units of σ, defined as [349, 350]

$$\text{Pull}_{A\to B} = \sqrt{2}\text{Erf}^{-1}[F(\Delta\chi^2_A - \Delta\chi^2_B; n_B - n_A)]\,, \tag{6.7}$$

where Erf^{-1} is the inverse of the error function, F is the cumulative distribution function of the χ^2 distribution and n is the number of degrees of freedom of each fit. We will compare each scenario against two cases: the SM ($C_{\ell q} = 0$, $n = 0$) and the fit to three independent Wilson coefficients (scenario VII), which is the more general and descriptive case. The pull from the SM quantifies how much each scenario is preferred over the SM to describe the data. The larger the pull, the better description of the data of the pre-

ferred scenario. The pull of scenario VII quantifies how much the fit over the whole space of parameters is preferred over the simpler and more constrained fits. From the analysis of this pull we are able to discuss the relevance of the proposed scenarios, the larger the pull means that the more restricted scenario represents a worser description of the experimental data.

The results of the fits are summarized in Table 6.2 for several combinations of $C^i_{\ell q}$ operators, with one, two or three lepton flavour present simultaneously in the Wilson coefficients as defined below. The best fit values at 1σ and pulls from the SM and to scenario VII for all scenarios are included in this table.

- **Scenarios I, II and III:** In these scenarios, NP only modifies the $C^i_{\ell q}$ operators in one lepton flavour at a time, i.e $C^e_{\ell q}$, $C^\mu_{\ell q}$ or $C^\tau_{\ell q}$. The largest pull from the SM prediction, more than 4σ, is found in scenario II when the coupling to muons is added. This result is in line with the common wisdom about the anomalies, explaining them through NP in the muon sector [323–325, 328, 349], as well as the importance of the superallowed nuclear β decays in the fit. The worst pull is obtained in the fit to the tau coefficient, with 1.96σ, as it does not modify the value of the $R_{K^{(*)}}$ ratios. Scenarios I and II both produce SM-like predictions for the observables R_D and R_{D^*}: $R^\ell_D = 0.3006$ and $R^\ell_{D^*} = 0.2528$ for Scenario I and $R^\ell_D = 0.3048$ and $R^\ell_{D^*} = 0.2563$ for Scenario II. Scenario III, with a larger value of its Wilson coefficient, produces values closer to the average of the experimental measurements; i.e $R^\ell_D = 0.318$ and $R^\ell_{D^*} = 0.268$. In order to fully address the anomaly in these observables, a larger deviation from the SM would be needed; however such a deviation would be in conflict with the electroweak precision data, as we will see later in section 6.3.1, and in agreement with [351].

- **Scenarios IV, V and VI:** In these scenarios NP is present in two of the Wilson coefficients. The best fit corresponds to scenario IV, where the contributions to $C^e_{\ell q}$ and $C^\mu_{\ell q}$ are favoured with a pull of 4.73σ with respect to the SM. Figure 6.1a-c shows the allowed regions for these fits at 1 and 2σ levels. In the fit to Scenario IV, the $R_{K^{(*)}}$ and $R_{D^{(*)}}$ observables constrain the $C^e_{\ell q} - C^\mu_{\ell q}$ combination; while the LFU-conserving electroweak precision observables tightly constrain the combination $C^e_{\ell q} + C^\mu_{\ell q}$, and the nuclear $beta$ decays only affect $C^\mu_{\ell q}$. It is clear that EW precision observables play an important role in the global fit and the preferred values for the Wilson coefficients. The reason for this behaviour is justified by deviations in Z-couplings to leptons, the τ-leptonic decays and the Z and W decays widths, as shown in [352]. The values of the $R_{K^{(*)}}$ and $R_{D^{(*)}}$ observables in this scenario are given in Table 6.3. Together, these sets of observables constrain the fit to a narrow ellipse around the best fit point. In Scenarios V and VI, the $C^\tau_{\ell q}$ coefficient is determined by the electroweak precision observables, that are compatible with a SM-like coefficient, and by $R_{D^{(*)}}$ observables, that prefer a large negative value. All the experimental con-

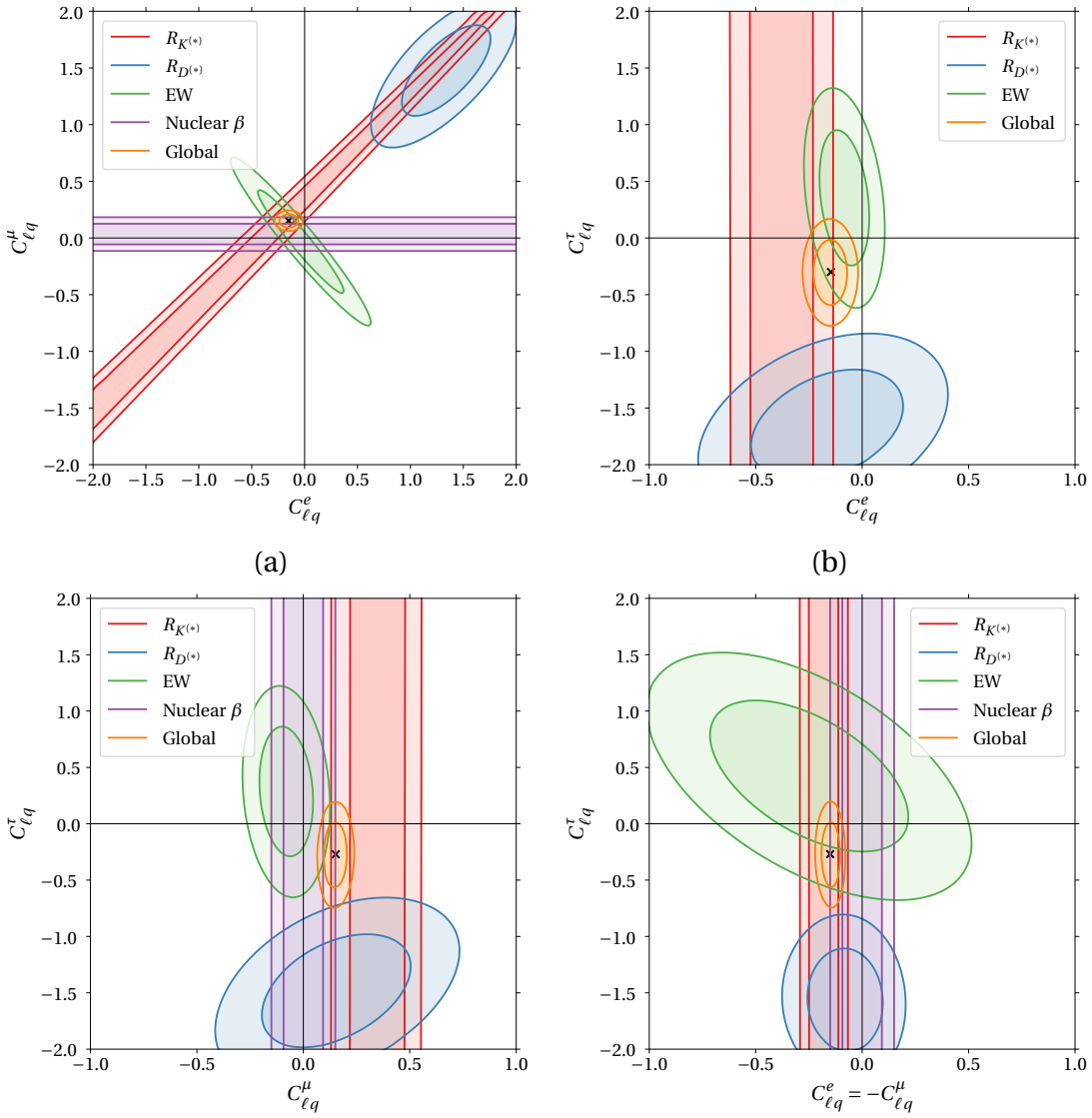

Figure 6.1: 1σ and 2σ contours for scenarios with two lepton flavours present in the Wilson coefficients: (a) Scenario IV, (b) Scenario V, (c) Scenario VI and (d) Scenario XI. All available data is considered. The likelihood associated with the nuclear β decays is not displayed in scenario V because it does not depend on the Wilson coefficients $C^{e}_{\ell q}$ and $C^{\tau}_{\ell q}$.

Scenario		$C^e_{\ell q}$	$C^\mu_{\ell q}$	$C^\tau_{\ell q}$	$\Delta\chi^2_{\text{SM}}$	Pull from SM	Pull to VII
I	e	-0.15 ± 0.04			8.19	$2.86\,\sigma$	$4.07\,\sigma$
II	μ		0.15 ± 0.03		17.89	$4.23\,\sigma$	$2.75\,\sigma$
III	τ			-0.30 ± 0.19	2.55	$1.60\,\sigma$	$4.68\,\sigma$
IV	e and μ	-0.15 ± 0.09	0.15 ± 0.06		26.10	$4.73\,\sigma$	$1.42\,\sigma$
V	e and τ	-0.15 ± 0.06		-0.3 ± 0.3	10.68	$2.82\,\sigma$	$4.18\,\sigma$
VI	μ and τ		0.15 ± 0.05	-0.3 ± 0.3	19.96	$4.07\,\sigma$	$2.86\,\sigma$
VII	e, μ and τ	-0.15 ± 0.11	0.15 ± 0.07	-0.3 ± 0.3	28.12	$4.64\,\sigma$	
VIII	$e = \mu = \tau$	0.04 ± 0.03	0.04 ± 0.03	0.04 ± 0.03	1.98	$1.40\,\sigma$	$4.74\,\sigma$
IX	$e = -\mu = \tau$	-0.152 ± 0.005	0.152 ± 0.005	-0.152 ± 0.005	27.73	$5.27\,\sigma$	$0.62\,\sigma$
X	$e = -\mu$	-0.15 ± 0.03	0.15 ± 0.03		26.10	$4.94\,\sigma$	$1.42\,\sigma$
XI	$e = -\mu, \tau$	-0.15 ± 0.05	0.15 ± 0.05	-0.3 ± 0.3	28.12	$4.94\,\sigma$	$0\,\sigma$

Table 6.2: Best fit values and pulls from the SM and of scenario VII for several combinations of the $C^i_{\ell q}$ operators; with one, two and three of the $C_{\ell q}$ operators receiving NP contributions.

Observable	Scenario IV	Scenario VII	Scenario IX	Scenario X	Scenario XI	Measurement
$R^{[1.1,6]}_{K^+}$	0.862 ± 0.015	0.864 ± 0.016	0.861 ± 0.004	0.862 ± 0.016	0.863 ± 0.015	0.85 ± 0.03
$R^{[0.045,\,1.1]}_{K^{*0}}$	0.889 ± 0.006	0.890 ± 0.006	0.889 ± 0.004	0.889 ± 0.006	0.889 ± 0.006	0.65 ± 0.09
$R^{[1.1,\,6]}_{K^{*0}}$	0.862 ± 0.016	0.864 ± 0.016	0.861 ± 0.006	0.862 ± 0.016	0.864 ± 0.015	0.68 ± 0.10
R^ℓ_D	0.297 ± 0.015	0.306 ± 0.007	0.302 ± 0.007	0.297 ± 0.008	0.306 ± 0.008	0.35 ± 0.03
$R^\ell_{D^*}$	0.244 ± 0.008	0.252 ± 0.008	0.249 ± 0.007	0.244 ± 0.008	0.252 ± 0.009	0.296 ± 0.016
$R^\mu_{D^*}$	0.249 ± 0.009	0.257 ± 0.009	0.254 ± 0.007	0.249 ± 0.009	0.257 ± 0.009	0.31 ± 0.03

Table 6.3: Values of the $R_{K^{(*)}}$ and $R_{D^{(*)}}$ observables in the scenarios with best pulls.

straints for $C^{\tau}_{\ell q}$ show large uncertainties, which result in less statistical significance of these fits and $C^{\tau}_{\ell q}$ still being compatible with zero at 2σ level. The central values with 1σ uncertainties of the $R_{K^{(*)}}$ and $R_{D^{(*)}}$ observables for Scenario IV (the best fit scenario in this subset) are shown in Table 6.3 and Figure 6.2. Below we compare these results in various scenarios.

- **Scenario VII:** In this fit, the three $C_{\ell q}$ operators receive independent NP contribution. The pull from the SM, 4.64σ, is similar to that of scenario IV, and the values of $C^{e}_{\ell q}$ and $C^{\mu}_{\ell q}$ are similar too, therefore the predictions for the $R_{K^{(*)}}$ observables are very similar, as shown in Figure 6.2a. The value of $C^{\tau}_{\ell q}$ is close to that of Scenarios III, V and VI, which allows a better fit to the $R_{D^{(*)}}$ observables, and especially to R^{ℓ}_{D}, that is compatible at 1σ with its experimental value, as shown in Figure 6.2b. Therefore, we conclude that the prediction of the $R_{D^{(*)}}$ and $R_{K^{(*)}}$ observables is improved in scenario VII. We will discuss this scenario in more detail in Section 6.3.1.

- **Scenario VIII:** This scenario has *universal* couplings; the three Wilson coefficients have the same *universal* contribution, and does not violate LFU. It has the smallest pull with respect to the SM (1.40σ). This shows that LFU NP can not explain experimental data, and LFU violation is needed to accommodate it.

- **Scenario IX, X and XI:** In these scenarios we impose the condition $C^{e}_{\ell q} = -C^{\mu}_{\ell q}$ taking inspiration from Scenario VII. The allowed region for Scenario XI is depicted in Figure 6.1d The treatment of $C^{\tau}_{\ell q}$ is what differentiates each scenario: In Scenario IX the three Wilson coefficients have the same absolute value, but $C^{\mu}_{\ell q}$ has the opposite sign; in Scenario X there is no NP contribution to $C^{\tau}_{\ell q}$; and in Scenario XI $C^{\tau}_{\ell q}$ enters the fit independently from the other two coefficients. All three scenarios produce a similar $\Delta\chi^2_{\text{SM}}$, with Scenario X slightly lower because it does not describe the $R_{D^{(*)}}$ anomalies, as we shall see. Scenario IX produces a better pull value, 5.27σ since it requires less degrees of freedom. Scenarios IX and XI are able to reproduce Scenario VII in a more parsimonious way.

The results for the $R_{K^{(*)}}$ and $R_{D^{(*)}}$ observables in the scenarios with best pulls, Scenarios IV, VII, IX, X and XI are presented in Table 6.3. Figure 6.2 shows the results for the central value and 1σ uncertainty of these two observables in the three scenarios, compared to the SM prediction (yellow area) and experimental measurements (green area). These three scenarios have similar fits for the Wilson coefficients $C^{e}_{\ell q}$ and $C^{\mu}_{\ell q}$, and therefore reproduce the experimental value of $R_K^{[1.1,6]}$ and reduce the tension in $R_{K^*}^{[1.1,6]}$. The main difference between these Scenarios is the fit for $C^{\tau}_{\ell q}$: Scenario IV and X have no NP contribution in the τ sector and consequently predicts SM-like $R_{D^{(*)}}$ ratios; Scenarios VII and XI have a large contribution to $C^{\tau}_{\ell q}$ and is able to produce a prediction for R^{ℓ}_{D} compatible with the experimental results at the 1σ level, and significantly improve the predictions for $R^{\ell}_{D^*}$ and $R^{\mu}_{D^*}$; Scenario IX has an intermediate value of $C^{\tau}_{\ell q}$, and consequently its

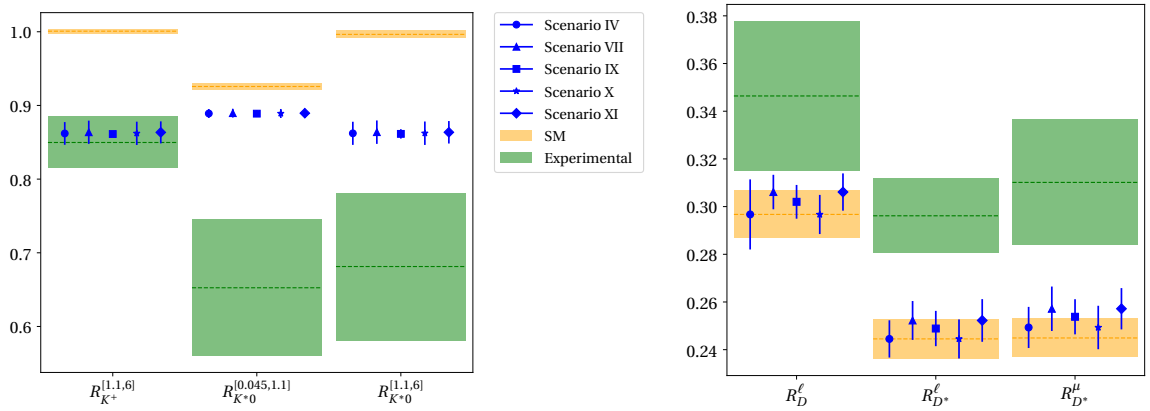

(a) (b)

Figure 6.2: Central value and 1σ uncertainty of the (a) $R_{K^{(*)}}$ observables, and (b) $R_{D^{(*)}}$ observables (blue lines) in scenarios IV, VII, IX, X and XI compared to the SM prediction (yellow) and experimental measurements (green).

predictions for the $R_{D^{(*)}}$ ratios are not as good as in Scenario VII and XI.

In addition to the observables included in our global fits, it is also possible to constrain the NP contributions to Wilson coefficients using high-energy collision data from LHC. In particular, it is known that high p_T tails in proton-proton collisions producing tau leptons provide bounds that are competitive to those from the $R_{D^{(*)}}$ ratios in B physics [353]. Ref. [353] finds the bound $|C^\tau_{\ell q(3)}|/\Lambda^2 < 2.6\ \text{TeV}^{-2}$ by recasting the $pp \to \tau^+\tau^-$ searches in ATLAS 13 TeV with 3.2 fb^{-1}. The constraint $|C^\tau_{VL}| < 0.32$ is established [354] for mono-τ searches $pp \to \tau X + \not{E}_T$, by combining the results from ATLAS with 36.1 fb^{-1} and CMS with 35.9 fb^{-1}, at 13 TeV. In order to compare this constraint in the WET with our fits in the SMEFT basis, we use the matching condition in Eq. (6.4), obtaining that $|C^\tau_{\ell q(3)}| < 5.35$. Therefore, we can conclude that all the results of our fits are clearly compatible with the limits imposed by the high-p_T phenomena.

6.3.1 Scenario VII

Since the scenario VII is the more general one and we found that the prediction of the $R_{D^{(*)}}$ and $R_{K^{(*)}}$ observables is improved in this case, we discuss in this section this scenario in more detail.

The χ^2 of the fit can be expressed as a series expansion around its minimum [350],

$$\chi^2(C^k_{\ell q}) = \chi^2_{\text{fit}} + \delta C^i_{\ell q}\, \mathbb{H}_{ij}\, \delta C^j_{\ell q} + \mathcal{O}((\delta C^k_{\ell q})^3)\,, \tag{6.8}$$

where $\delta C^i_{\ell q} = C^i_{\ell q} - C^i_{\ell q}|_{\text{BF}}$ represent the deviation with respect to the best fit (BF) and $\mathbb{H}$ is the Hessian matrix evaluated at the best fit. In scenario VII, the Hessian matrix takes the

value:

$$\mathbb{H} = \begin{pmatrix} 307.34 & 56.741 & -0.16755 \\ 56.741 & 669.62 & -6.3921 \\ -0.16755 & -6.3921 & 28.466 \end{pmatrix}. \tag{6.9}$$

Within the quadratic approximation, the points with constant $\Delta\chi^2$ (e.g. all the points that are $1\,\sigma$ away from the best fit) are located in the surface of an ellipsoid. The length and orientation of the ellipsoid can be found with the Singular Value Decomposition (SVD) of the Hessian,

$$\mathbb{H} = U\Sigma U^T, \tag{6.10}$$

where U is an orthogonal matrix whose columns are the directions of the principal axes, and Σ is a diagonal matrix. The lengths of the semi-axes for a given value of $\Delta\chi^2$ are

$$a_j = \sqrt{\frac{\Delta\chi^2}{\Sigma_{jj}}}. \tag{6.11}$$

In a χ^2 distribution with 3 degrees of freedom, the $1\,\sigma$ confidence region corresponds to $\Delta\chi^2 = 3.527$. The lengths of the semi-axes, in decreasing order, are

$$a_1 = 0.352, \qquad a_2 = 0.109, \qquad a_3 = 0.0721\,. \tag{6.12}$$

The orientation of the axes, also in decreasing order of a_i, are given by

$$U = \begin{pmatrix} 0.001453 & 0.9885 & -0.1512 \\ -0.01010 & -0.1512 & -0.9885 \\ -0.9999 & 0.002963 & 0.009761 \end{pmatrix}. \tag{6.13}$$

The first direction (i.e. the one that is less constrained by the fit) corresponds to the τ coefficient, while the second and third directions contain a mix of the two other Wilson coefficients, with a mixing angle $\theta_{e\mu} = 8.7°$,

$$C_1 \sim -C^{\tau}_{\ell q}, \tag{6.14}$$

$$C_2 \sim \cos\theta_{e\mu} C^{e}_{\ell q} - \sin\theta_{e\mu} C^{\mu}_{\ell q}, \qquad C_3 \sim -\sin\theta_{e\mu} C^{e}_{\ell q} - \cos\theta_{e\mu} C^{\mu}_{\ell q},$$

$$C^{e}_{\ell q} \sim \cos\theta_{e\mu} C_2 - \sin\theta_{e\mu} C_3, \qquad C^{\mu}_{\ell q} \sim -\sin\theta_{e\mu} C_2 - \cos\theta_{e\mu} C_3\,. \tag{6.15}$$

In the previous fit presented in [4], the mixing angle was $\theta_{e\mu} \approx 45°$. The physical interpretation of the orientation of the axes in that case was pretty clear from our analysis. We concluded that the NP effects in τ (axis 1) are mostly uncorrelated with those of the lighter leptons, and NP in e and μ are better described as a combination of LFU effects (axis 2) and LFUV effects (axis 3). The value obtained for the coordinate 3 implies a simultaneous decrease in the electronic part and an increase in the muonic part to describe the LFUV observables; and the value of coordinate 2 so close to 0 indicates that the LFU processes are not changed with respect to the SM. However, the current fit is greatly affected by the inclusion of the superallowed nuclear β decays, which constrain the possible values of

$C^{\mu}_{\ell q}$ while leaving $C^{e}_{\ell q}$ and $C^{\tau}_{\ell q}$ unaffected. As a result, the mixing between the first and second lepton generations is less important than before.

The extrema of the 1σ confidence ellipsoid are located at

$$C^{i}_{\ell q}\Big|_{js} = C^{i}_{\ell q}\Big|_{\rm BF} + sU_{ik}A_{kj}\,, \tag{6.16}$$

where $j = 1,2,3$, $s = \pm 1$ and $A_{kj} = a_j\delta_{kj}$.

Other notable points on the ellipsoid are found moving from the best fit point in the direction of the $C^{e}_{\ell q}$, $C^{\mu}_{\ell q}$ and $C^{\tau}_{\ell q}$ axes ($j = e,\mu,\tau$). The distance from the best fit to the ellipsoid when changing only one Wilson coefficient j is

$$a_j = \sqrt{\frac{\Delta\chi^2}{\mathbb{H}_{jj}}}, \qquad\qquad j = e,\,\mu,\,\tau\,, \tag{6.17}$$

and the points of the ellipsoid obtained when only one Wilson coefficient is changed from its best fit value are given by

$$C^{i}_{\ell q}\Big|_{js} = C^{i}_{\ell q}\Big|_{\rm BF} + sa_j\delta^{i}_{j}, \qquad\qquad j = e,\,\mu,\,\tau\,. \tag{6.18}$$

Finally, the points on the 1σ ellipsoid closest and furthest in the direction connecting the best fit point and the SM benchmark are given by

$$C^{i}_{\ell q}\Big|_{{\rm SM}\,s} = C^{i}_{\ell q}\Big|_{\rm BF}(1 + sa_{\rm SM})\,, \tag{6.19}$$

where the distance $a_{\rm SM}$ is given by

$$a_{\rm SM} = \sqrt{\frac{\Delta\chi^2}{C^{i}_{\ell q}|_{\rm BF}\,\mathbb{H}_{ij}\,C^{j}_{\ell q}|_{\rm BF}}}\,. \tag{6.20}$$

The Wilson coefficients at these points of the ellipse, from the corresponding best fit point to the ellipsoid, at 1σ confidence level, are given in Table 6.4.

The pull for a single observable is defined as

$$\text{Pull}_{\mathscr{O}}(C_{\ell q}) = \frac{\mathscr{O}(C_{\ell q}) - \mathscr{O}_{\rm exp}}{\sqrt{\sigma^2_{\rm exp} + \sigma^2_{\rm th}(C_{\ell q})}}\,. \tag{6.21}$$

The theoretical uncertainties of the observables in general depend on the SMEFT coefficients. The package `smelli` treats the theoretical uncertainties in two different ways: in some observables, such as the EW precision tests, the theoretical uncertainty is considered negligible compared to the experimental uncertainty. In other cases, like the B physics observables, both theoretical and experimental uncertainties are included, but they are assumed to be Gaussian. The list of observables that contribute to the global fit with their prediction in scenario VII as well as the pulls that compare the predictions against experimental measurements for NP models (NP pull) and in the SM (SM pull) is presented in Appendix C.1. Notice that the values of these pulls are approximate, as they

j	s	$C^e_{\ell q}$	$C^\mu_{\ell q}$	$C^\tau_{\ell q}$	$\Delta\chi^2$
BF		-0.150	0.150	-0.269	
1	+	-0.149	0.146	-0.622	3.35
1	−	-0.150	0.153	0.0829	3.39
2	+	-0.0423	0.133	-0.269	4.29
2	−	-0.257	0.166	-0.270	4.44
3	+	-0.161	0.0784	-0.269	3.71
3	−	-0.139	0.221	-0.270	3.70
e	+	-0.0426	0.150	-0.269	4.07
e	−	-0.257	0.150	-0.269	4.17
μ	+	-0.150	0.222	-0.269	4.08
μ	−	-0.150	0.0771	-0.269	3.78
τ	+	-0.150	0.150	0.0824	3.39
τ	−	-0.150	0.150	-0.621	3.35
SM	+	-0.210	0.210	-0.378	4.69
SM	−	-0.0897	0.0897	-0.161	4.29

Table 6.4: Values of the Wilson coefficients at some points located at 1σ confidence ellipsoid around the best fit point in Scenario VII.

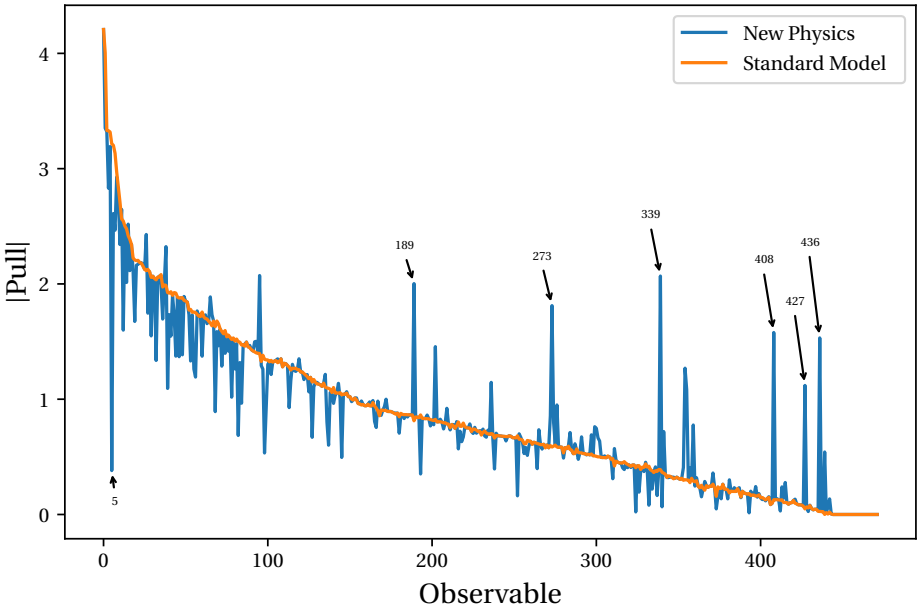

Figure 6.3: Pulls in the Standard Model (orange) and scenario VII (blue) of the observables included in the global fit. The observables with a difference of pulls between the SM and Scenario VII of more than 1σ are highlighted: $R^{[1,1,6]}_{K^+}$ (obs. 5), BR($\tau^- \to e^- \nu\bar{\nu}$) (obs. 189), $\mathcal{F}t(^{54}\text{Co})$ (obs. 273), $\mathcal{F}t(^{34}\text{Cl})$ (obs. 339), $\mathcal{F}t(^{50}\text{Mn})$ (obs. 408), $\mathcal{F}t(^{14}\text{O})$ (obs. 427) and $\mathcal{F}t(^{38m}\text{K})$ (obs. 436).

do not take in account the correlation between observables and the uncertainty of the fit is not considered in the reported values.

Figure 6.3 shows the pull of the observables included in the global fit for scenario VII with respect to their experimental measurement (blue line), compared to the same pull in the SM (orange line). It is clear that, for most of the observables, the NP either improves their prediction, especially for R_{K^+}, $R_{K^{*0}}$ (observables 5, 12 and 16 in the table presented in Appendix C.1), as well as the differential branching ratios of $b \to s\mu^+\mu^-$ processes in several low-q^2 bins [2]; or leave the prediction mostly unchanged. Nevertheless, in the case of the following observables, the pull of the scenario VII is significantly worse than that of the SM:

$$R_{e\mu}(K^+ \to \ell^+\nu) = \frac{\mathrm{BR}(K^+ \to e^+\nu)}{\mathrm{BR}(K^+ \to \mu^+\nu)}\,, \qquad \mathrm{BR}(\tau^- \to e^-\nu\bar{\nu})\,,$$
$$R_{D^*}^{\mu/e} = R_{\mu e}(B \to D^*\ell^+\nu) = \frac{\mathrm{BR}(B \to D^*\mu^+\nu)}{\mathrm{BR}(B \to D^*e^+\nu)}\,, \qquad \mathrm{BR}(\pi^+ \to e^+\nu)\,. \tag{6.22}$$

Those observables corresponds to observables 95, 189, 276 and 299 respectively in the table given in Appendix C.1. Scenario VII also produces worse predictions of the $R_{K^{(*)}}$ ratios in the low-recoil bins $q^2 > 14\ \mathrm{GeV}^2$ (observables 154 and 197 in Appendix C.1), and the corrected half-lives $\mathscr{F}t$ parameters of various superallowed nuclear β decays [355, 356] (observables 202, 236, 273, 339, 355, 408, 427, 439).

In order to identify which operators are constraining the fit in each direction we use the difference of the pulls, defined as [350]:

$$\delta'_{js}(\mathscr{O}) = \mathrm{Pull}_{\mathscr{O}}(C_{\ell q}|_{\mathrm{BF}}) - \mathrm{Pull}_{\mathscr{O}}(C_{\ell q}|_{js})\,, \tag{6.23}$$

where js represents the direction of the corresponding axis, as described in Eqs. (6.16), (6.18). The observables with the largest values of the square of δ' for each extreme of the ellipse are shown in Table 6.5. We can see that the values of $C^e_{\ell q}$ are constrained mostly by the R_{K^+} ratio and the electroweak precision tests: the electron asymmetry in the Z decay A_e, the $W-$mass, the forward-backward asymmetry $A_{\mathrm{FB}}(Z \to \bar{b}b)$ and the Z-decay width Γ_Z (corresponding to observable 18-A_e, observable 58-m_W, observable 15-A_{FB} and observable 272-Γ_Z as presented in Appendix C.1). The coefficient $C^\mu_{\ell q}$ is constrained mostly by the $\mathscr{F}t$ values for superallowed nuclear decays (observable 202-^{26m}Al, observable 339-^{34}Cl, observable 436-^{38m}K, observable 145-^{46}V), as well as R_{K^+}. Finally, the coefficient $C^\tau_{\ell q}$ is constrained by τ observables: the branching ratios of $\tau \to e\bar{\nu}\nu$ and $\tau \to \mu\bar{\nu}\nu$ (observables 189 and 38) and the ratios $R^\ell_{D^*}$ and $R^\mu_{D^*}$ (observables 3 and 72). This result is in agreement with [357].

If we focus instead in the principal directions of the uncertainty ellipsoid, the picture is similar: axis 1 is still dominated by τ observables. Axis 2, which is aligned predominantly with $C^e_{\ell q}$, is constrained by the LFU tests R_{K^+} and $R^{\mu/e}_{D^*}$ (observables 5 and 284) and the

[2] See for example observables 1, 6, 7, 10, 29, 39, 41, 43, 46, 48, 53, 55, 56, 60, 78, 80, 84, 99, 127, 137, 140, 216, 238, 310, 324 in Appendix C.1

$C_{\ell q}^{e}$			$C_{\ell q}^{\mu}$			$C_{\ell q}^{\tau}$		
No.	Observable	δ'^2	No.	Observable	δ'^2	No.	Observable	δ'^2
5	$R_{K^+}^{[1.1,6]}$	1.05	202	$\mathscr{F}t(^{26m}\mathrm{Al})$	1.22	189	$\mathrm{BR}(\tau^- \to e^- \nu\overline{\nu})$	0.99
18	A_e	0.47	399	$\mathscr{F}t(^{34}\mathrm{Cl})$	0.67	38	$\mathrm{BR}(\tau^- \to \mu^- \nu\overline{\nu})$	0.97
58	m_W	0.41	436	$\mathscr{F}t(^{38m}\mathrm{K})$	0.57	354	σ_{had}^0	0.68
15	A_{FB}	0.34	145	$\mathscr{F}t(^{46}\mathrm{V})$	0.55	3	$R_{D^*}^{\ell}$	0.43
272	Γ_Z	0.27	5	$R_{K^+}^{[1.1,6]}$	0.53	72	R_D^{ℓ}	0.16

Axis 1			Axis 2			Axis 3		
No.	Observable	δ'^2	No.	Observable	δ'^2	No.	Observable	δ'^2
189	$\mathrm{BR}(\tau^- \to e^- \nu\overline{\nu})$	0.98	5	$R_{K^+}^{[1.1,6]}$	1.42	202	$\mathscr{F}t(^{26m}\mathrm{Al})$	1.17
38	$\mathrm{BR}(\tau^- \to \mu^- \nu\overline{\nu})$	0.97	18	A_e	0.35	339	$\mathscr{F}t(^{34}\mathrm{Cl})$	0.65
354	σ_{had}^0	0.69	58	m_W	0.30	436	$\mathscr{F}t(^{38m}\mathrm{K})$	0.55
3	$R_{D^*}^{\ell}$	0.43	180	$\mathrm{BR}(\pi^+ \to e^+ \nu)$	0.27	145	$\mathscr{F}t(^{46}\mathrm{V})$	0.53
72	R_D^{ℓ}	0.16	284	$R_{D^*}^{\mu/e}$	0.26	408	$\mathscr{F}t(^{50}\mathrm{Mn})$	0.47

SM direction		
No.	Observable	δ'^2
5	$R_{K^+}^{[1.1,6]}$	1.40
202	$\mathscr{F}t(^{26m}\mathrm{Al})$	0.83
339	$\mathscr{F}t(^{34}\mathrm{Cl})$	0.46
436	$\mathscr{F}t(^{38m}\mathrm{K})$	0.39
145	$\mathscr{F}t(^{46}\mathrm{V})$	0.38

Table 6.5: Observables with the largest difference of pulls between the best fit and the extreme of the 1σ confidence ellipsoid. Number of the observables corresponds to the ones given in Appendix C.1.

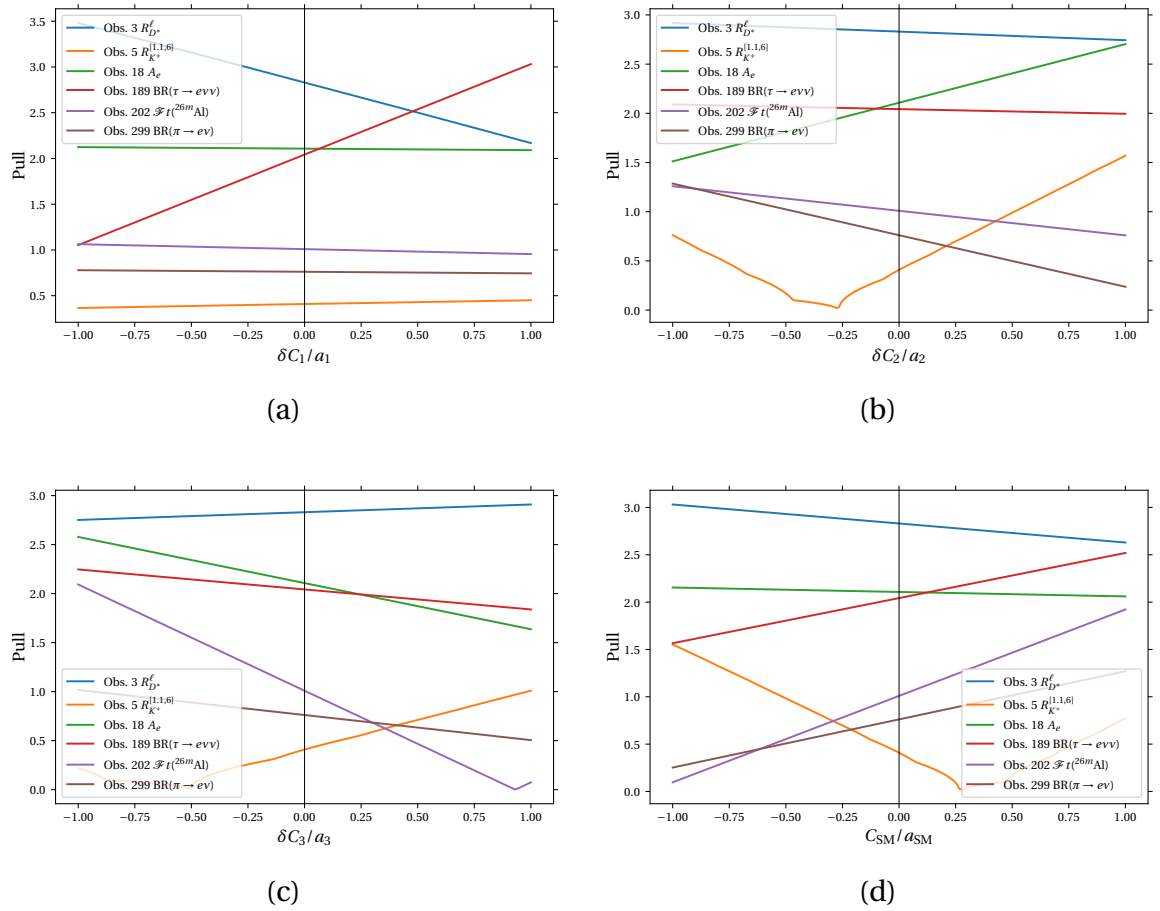

Figure 6.4: Evolution of the pull of the observables in Table 6.5 along each axis of the ellipsoid (a)-(c) and the SM direction (d).

electroweak precision tests A_e, m_W (observables 18 and 58). Axis 3, on the other hand, is constrained by the $\mathcal{F}t$ values.

Figure 6.4 represents the evolution of some selected observables from various sectors (the B anomalies $R_{D^{(*)}}$ and $R_{K^{(*)}}$, electroweak tests, τ and π decays and superallowed nuclear β decays) along the axes of the ellipsoid (see eq. (6.14) for definitions of C_1, C_2, C_3). In the case of the first axis, $\delta C_1/a_1 = -1$ corresponds to a suppression of NP in the τ sector, which is preferred by the τ decays, while $\delta C_1/a_1 = 1$ is an increase of τ effects with respect to the best fit, that accommodates better the $R_{D^{(*)}}$ anomalies, as was previously pointed out in [351]. In the second axis, $\delta C_2/a_2 = 1$ decreases the deviation of $C^e_{\ell q}$, and to a lesser extent also of $C^{\mu}_{\ell q}$ from their SM values, which would improve the pull for the π decay into an electron and the $\mathcal{F}t$ parameters, and to a lesser extent, also for the $\tau \to e\nu\bar{\nu}$ decay and the $R^{\ell}_{D^*}$ ratio. On the other hand, a decrease in C_2 would be favored by the electroweak observables, and R_{K^+} for moderate decreases. In the case of axis 3, $\delta C_3/a_3 = -1$ favours NP effects in muons and slightly reduce the impact of NP in electrons, resulting in improved pulls for R_{K^+} and $R^{\ell}_{D^*}$, and worse pulls for the $\mathcal{F}t$ parameters, electroweak observables and the τ and π leptonic decays into electrons.

The last columns of Table 6.5 and Figure 6.4d show the observables that constrain the fit along the direction connecting the SM and best fit point, that is in the points with Wilson coefficients of the form $C^i_{\ell q} = C^i_{\ell q}|_{\rm BF}\,(1+\delta C_{\rm SM})$. We observe that this direction is determined mostly by the LFUV observables $R^{[1.1,6]}_{K^+}$ and the $\mathscr{F}t$ values from superallowed nuclear β decays. These are the observables whose pulls change the most when comparing the best fit and SM, and therefore the ones more relevant to constrain the fit. In particular, the fit shows a tension between these observables, with R_{K^+}, together with $R_{D^{(*)}}$ and the electroweak precision tests, preferring larger NP contributions, and $\mathscr{F}t$ and the leptonic decays preferring the Wilson coefficients to be more SM-like.

6.4 Prospects from future colliders

A new generation of particle colliders, complementary to the LHC and its future upgrade HL-LHC, will be ready in the coming decades. The International Linear Collider (ILC) will be a linear e^+e^- collider in Japan, operating at center-of-mass energies ranging from $\sqrt{s}$ =250 GeV at the first stages up to $\sqrt{s}$ =1 TeV [358]. The Compact Linear Collider (CLIC) at CERN will also be a linear e^+e^- collider, operating from $\sqrt{s}$ = 380 GeV up to $\sqrt{s}$ = 3 TeV [359]. The Future Circular Collider (FCC), also at CERN, will be a circular collider first using electrons (FCC-ee) from $\sqrt{s}$ =90 GeV (Z pole) up to $\sqrt{s}$ =365 GeV, and then using hadrons (FCC-hh) reaching $\sqrt{s}$ =100 TeV [360]. These colliders are conceived primarily as Higgs factories, exploring the origin of the EWSSB mechanism and the hierarchy problem. But they can also supplement the flavour programs of the LHCb and Belle in different ways: by producing B flavoured hadrons in $e^+e^- \to Z \to b\bar{b}$ events (ILC operating at the Z pole is expected to produce around 10^9 Zs ("GigaZ") [361], and the FCC-ee is expected to deliver 10^{12} Zs ("TeraZ") [362]); by searching for new particles responsible for the deviations, such as leptoquarks or Z' bosons; by probing the effects of Wilson coefficients in the kinematical distributions sensible to virtual effects; and by improving the precision of the observables that enter our global fits. Due to the high number of Z bosons produced, EW observables are a prime example of the advantages of e^+e^- colliders.

In what follows, we will focus on the prospects of indirect discovery using Wilson coefficients and EW observables. The increased center-of-mass energy of the future colliders improves the sensitivity to the effects of any dimension-6 Wilson coefficient. This is evident from the energy scaling of the $2 \to 2$ scattering amplitudes mediated by a dimension-6 effective operator, $A_6 \propto \frac{E^2}{\Lambda^2}$ [363].

The study of neutral-current benefits greatly from the clean signatures and small theoretical uncertainties provided by lepton colliders. The use of polarized beams allows for the study of the different helicity structures of the Wilson coefficients. The constraints from lepton colliders for the four-fermion contact operators are the result of a variety of final states. For example, the $e^+e^- \to t\bar{t}$ events can constrain $C_{\ell q(1)} - C_{\ell q(3)}$, while $e^+e^- \to b\bar{b}$ events can constrain $C_{\ell q(1)} + C_{\ell q(3)}$ [365]. Also the leading higher-derivative

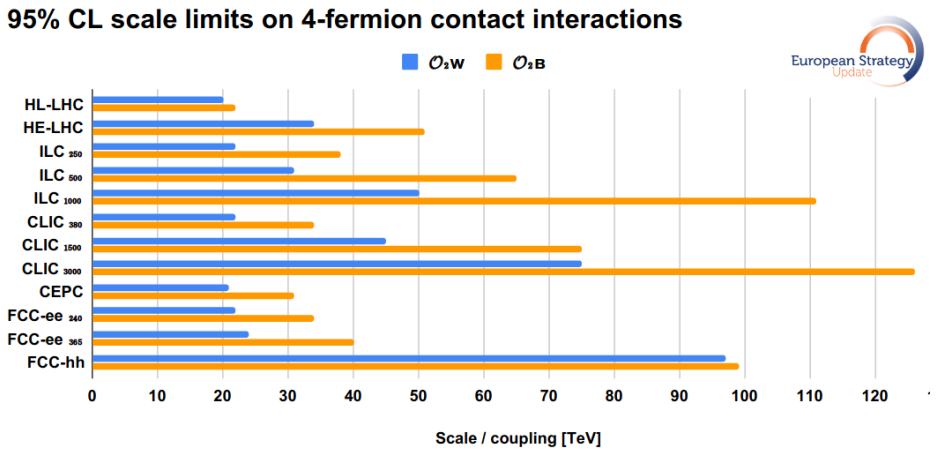

Figure 6.5: 95% exclusion reach in future colliders from the operators $\mathcal{O}_{2W}$ (blue) and $\mathcal{O}_{2B}$ (orange). The effective scale is given by $\Lambda/(g'^2\sqrt{C_{2W}})$ for the blue bars, and $\Lambda/(g^2\sqrt{C_{2B}})$ for the orange bars. Taken from [364].

corrections to the W and Z bosons propagators from the $\mathcal{O}_{2W}$ and $\mathcal{O}_{2B}$ operators,

$$\mathcal{O}_{2W} = (D^\mu W_{\mu\nu})^i (D_\rho W^{\rho\nu})^i, \qquad \mathcal{O}_{2B} = (\partial^\mu B_{\mu\nu})(\partial_\rho B^{\rho\nu}) \tag{6.24}$$

from the Strongly Interacting Light Higgs (SILH) basis [179] can be recast into flavour-universal four-fermion operators using the equations of motion

$$\mathcal{O}_{2W} = -\frac{g^2}{4}\sum_{i,j} O^{iijj}_{\ell q(3)} + \cdots, \qquad \mathcal{O}_{2B} = -\frac{g'^2}{6}\sum_{i,j} O^{iijj}_{\ell q(1)} + \cdots, \tag{6.25}$$

where g and g' are the gauge couplings for the $SU(2)_L$ and $U(1)_Y$ SM groups.

The exclusion reach for the operators $\mathcal{O}_{2W}$ and $\mathcal{O}_{2B}$ in the different colliders are depicted in Figure 6.5, taken from [364]. Lepton colliders provide better sensitivity for singlet operators ($\mathcal{O}_{2B}$) than for triplet operators ($\mathcal{O}_{2W}$), while the sensitivity of hadron colliders is similar in both cases. In its initial stage at $\sqrt{s}$ =250 GeV, ILC is expected to provide a better sensitivity than the HL-LHC.

Since in our global fit, we found that NP couplings to electrons have roughly similar values to the couplings to muons (see Table 6.2), this opens a window of possible observation in an e^+e^- machine, specially using $e^+e^- \to bs$ production. This process has a very clean SM background due to it is only generated at one loop and CKM-suppressed by V_{ts} [366].

The lepton linear colliders running at their initial stages will generate a great number of W and Z bosons (about 10^8 in ILC at $\sqrt{s} = 250$ GeV and 10^7 in CLIC at $\sqrt{s} = 380$ GeV [364]). This will allow to improve the precision of the EW observables: the mass of the W boson m_W, and the decay asymmetries (A) and rates of the Z boson (R). A dedicated program running at the Z pole would increase the number of bosons by an order of magnitude, improving accordingly the precision of the measurements. Circular e^+e^- colliders using transversely polarized beams will achieve even better results.

Obs	Central value							Error
	IV	V	VI	VII	IX	X	XI	
m_W [GeV]	80.359	80.369	80.348	80.359	80.359	80.359	80.359	0.002
A_e	0.14724	0.14884	0.14537	0.14725	0.14726	0.14725	0.14725	0.00015
A_μ	0.1479	0.1486	0.1451	0.1468	0.1467	0.1468	0.1468	0.0008
A_τ	0.1470	0.1491	0.1458	0.1474	0.1472	0.1470	0.1474	0.0008
A_c	0.6675	0.6682	0.6668	0.6675	0.6675	0.6675	0.6675	0.0014
A_b	0.9347	0.9348	0.9346	0.9347	0.9347	0.9347	0.9347	0.0006
R_e	20.73	20.73	20.73	20.73	20.73	20.73	20.73	0.02
R_μ	20.74	20.74	20.74	20.74	20.74	20.74	20.74	0.02
R_τ	20.78	20.77	20.77	20.77	20.78	20.78	20.77	0.02
R_c	0.1722	0.1722	0.1722	0.1722	0.1722	0.1722	0.1722	0.0008
R_b	0.2158	0.2158	0.2158	0.2158	0.2158	0.2158	0.2158	0.0002

Table 6.6: Assumed central values for the EW observables and their uncertainties in the ILC global fits for several scenarios.

It is important to stress that, since the EW precision observables play an important role in the global fit and the preferred values for the Wilson coefficients, a significant improvement in the precision of EW observables would have consequently a great impact on our results and, in general, on the analysis of flavour anomalies. In order to study the impact of the improved precision on our analysis, we have performed a new global fit.

Our projections for the EW observables to be included in our new fit are constructed as follows: the central values correspond to the predictions in each of our scenarios, and the uncertainties are taken from the ILC at $\sqrt{s} = 250$ GeV projections from [364]. The central values and uncertainties for the EW observables are shown on Table 6.6 for Scenarios IV, V, VI, VII, IX, X and XI. The largest tensions between our inputs and the SM predictions are found in the observables A_e and m_W (as a matter of example, being 5.6σ and 2.9σ respectively in scenario VII). This choice for the projections guarantees us that the best fit points are the same as in the previous section, so we can do a direct comparison between the allowed regions between both fits.

The results for the fits to scenarios IV, V, VI and XI, the ones with NP contributions present in two Wilson coefficients simultaneously are displayed in Figure 6.6. Both the predictions obtained by the analysis of present colliders and by using the projected ILC values are included. Solid lines correspond to the current fits, and dash-dotted lines to the fits including the ILC projections. For clarification, a detailed region in which the ILC prediction appears is displayed. The results confirm that EW precision observables are relevant in the global fit. The reason for this behaviour is justified by deviations in Z-couplings to leptons, the τ-leptonic decays and the Z and W decays widths, as shown in [352]. Notice that in the scenarios where NP is present on the $C^\tau_{\ell q}$ coefficient (Scenarios

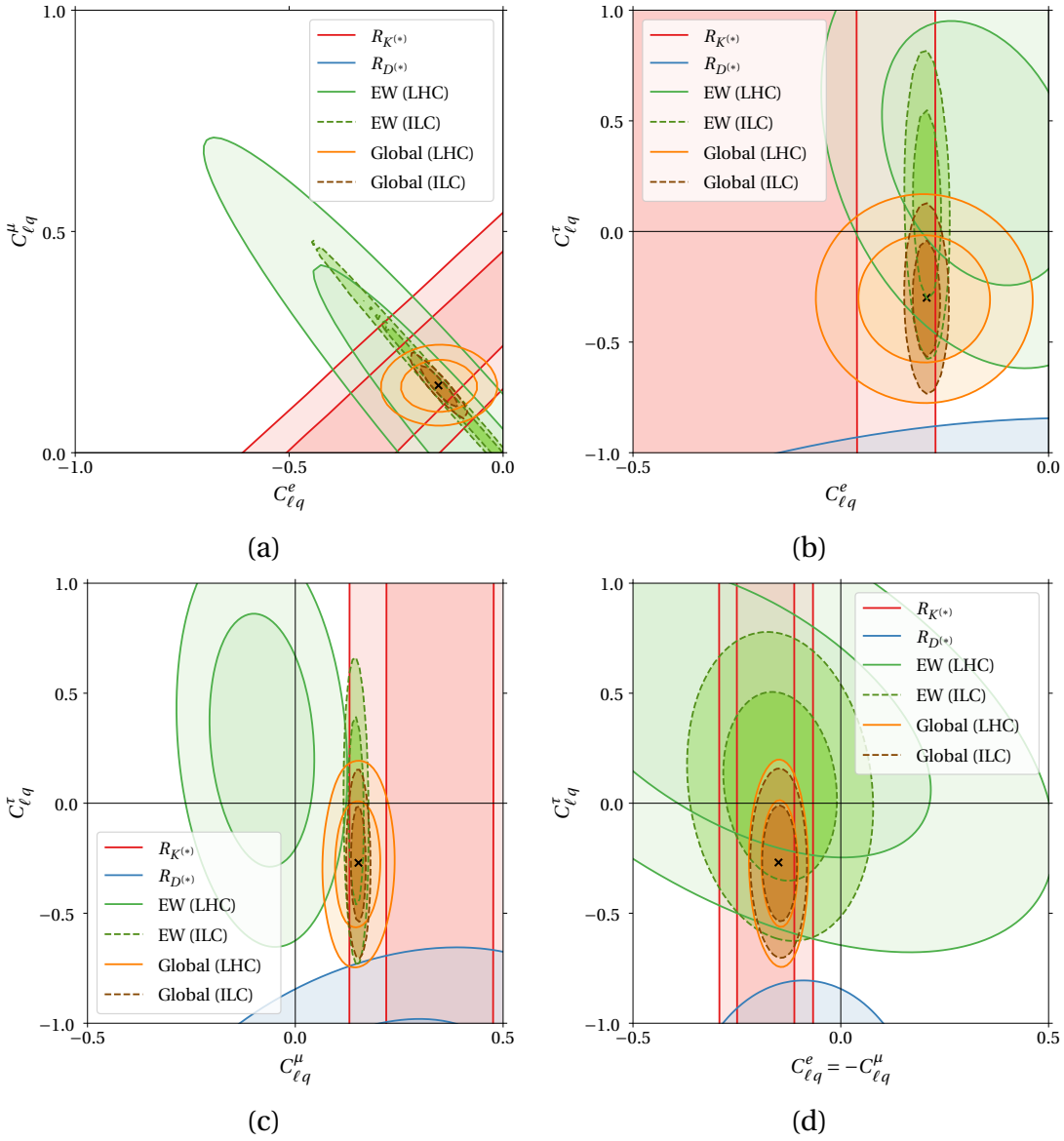

Figure 6.6: 1σ and 2σ contours for scenarios with two lepton flavours present in the Wilson coefficients: (a) Scenario IV, (b) Scenario V, (c) Scenario VI and (d) Scenario XI. Solid lines correspond to the current fits, and dash-dotted lines to the fits including the ILC projections. All available data are considered.

Observable	Scenario IV	Scenario VII	Scenario IX	Scenario X	Scenario XI
$R_{K^+}^{[1.1,6]}$	0.862 ± 0.013	0.864 ± 0.013	0.861 ± 0.003	0.862 ± 0.016	0.864 ± 0.013
$R_{K^{*0}}^{[0.045,\ 1.1]}$	0.889 ± 0.006	0.890 ± 0.006	0.888 ± 0.003	0.889 ± 0.006	0.890 ± 0.005
$R_{K^{*0}}^{[1.1,\ 6]}$	0.862 ± 0.013	0.864 ± 0.014	0.861 ± 0.005	0.862 ± 0.016	0.864 ± 0.014
R_D^ℓ	0.297 ± 0.007	0.306 ± 0.007	0.302 ± 0.007	0.297 ± 0.008	0.306 ± 0.007
$R_{D^*}^\ell$	0.245 ± 0.007	0.252 ± 0.008	0.249 ± 0.007	0.244 ± 0.008	0.252 ± 0.008
$R_{D^*}^\mu$	0.249 ± 0.008	0.257 ± 0.010	0.254 ± 0.008	0.249 ± 0.009	0.257 ± 0.010

Table 6.7: Values of the $R_{K^{(*)}}$ and $R_{D^{(*)}}$ observables in the scenarios with better pulls for the fit with the upgraded ILC precision.

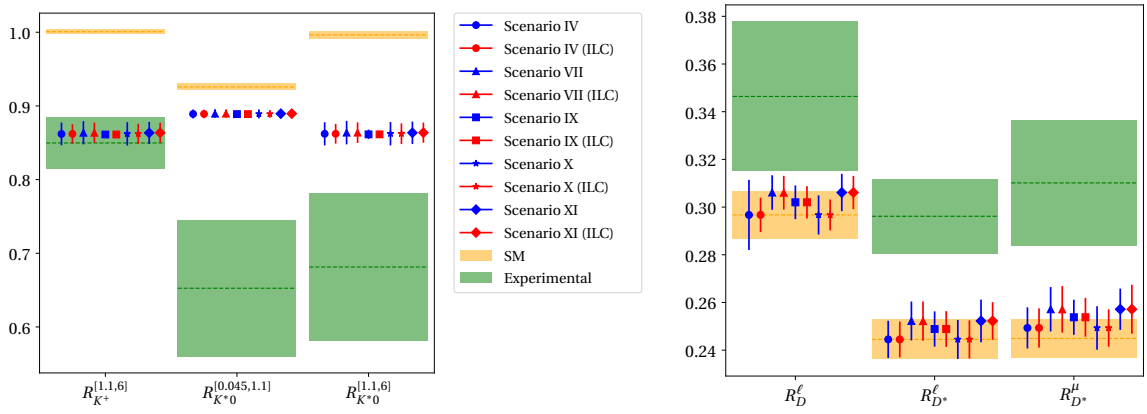

(a) (b)

Figure 6.7: Central value and 1σ uncertainty of the (a) $R_{K^{(*)}}$ observables, and (b) $R_{D^{(*)}}$ observables in scenarios IV, VII and IX (blue lines for current predictions, red lines for ILC-based predictions), compared to the SM prediction (yellow) and experimental measurements (green).

V and VI), $C_{\ell q}^\tau$ is determined by the EW precision observables and by $R_{D^{(*)}}$ observables, that prefer a large negative value. The experimental constraints for $C_{\ell q}^\tau$ show large uncertainties, then less statistical significance of these fits is expected.

The effects of the improved sensitivity to electroweak observables is most evident in the $C_{\ell q}^e - C_{\ell q}^\mu$ plane, as can be seen in Figure 6.6(a). The mixing angle in Scenario VII is now $\theta_{e\mu}^{\rm ILC} = 47°$, indicating a clearly marked separation between the LFUV physics, described by $C_2^{\rm ILC} = \cos\theta_{e\mu}^{\rm ILC} C_{\ell q}^e - \sin\theta_{e\mu}^{\rm ILC} \approx \frac{1}{\sqrt{2}}(C_{\ell q}^e - C_{\ell q}^\mu)$, and the LFU physics, described by $C_3^{\rm ILC} = \sin\theta_{e\mu}^{\rm ILC} C_{\ell q}^e + \cos\theta_{e\mu}^{\rm ILC} \approx \frac{1}{\sqrt{2}}(C_{\ell q}^e + C_{\ell q}^\mu)$. The LFUV direction is constrained mostly by the $R_{K^{(*)}}$ ratios, and the LFUV is tightly constrained by the ILC projections around $C_{\ell q}^e + C_{\ell q}^\mu \approx 0$. Consequently, the scenarios that assume no LFU contribution to $C_{\ell q}^e$ and $C_{\ell q}^\mu$, that is Scenarios IX, X and XI, are barely affected by the changes to the electroweak observables. A similar demarcation between LFUV contributions and LFU contributions to the effective operators, in this case in the WET, was previously found in Ref. [367, 368].

The predictions for the $R_{K^{(*)}}$ and $R_{D^{(*)}}$ observables in the best fit points for scenarios

IV, VII, IX, X and XI with the upgraded ILC precision can be found in Table 6.7. Figure 6.7 displays the central value and 1σ uncertainty of the $R_{K^{(*)}}$ and $R_{D^{(*)}}$ observables in the three scenarios, compared to the SM prediction (yellow area) and experimental measurements (green area). Both the current predictions (blue lines) and the ILC predictions (red lines) are included in this figure. By the construction of Table 6.6, the central values are the same as the ones in Table 6.3. The uncertainties in the predictions for the $R_{K^{(*)}}$ ratios are controlled by C_2^{ILC}, and for the $R_{D^{(*)}}$ ratios by $C^{\tau}_{\ell q}$, in both cases with little affection from the ILC prospects. The exception is $R_{D^{(*)}}$ in Scenario IV, since these ratios are also sensitive to LFU contributions and $C^{\tau}_{\ell q}$ is not included in this scenario.

6.5 Connection to leptoquark models

For completeness, we discuss in this section the phenomenological implications of our assumptions in the leptoquark models, concretely in the vector leptoquark model $U_1 \sim (\bar{\mathbf{3}}, \mathbf{1}, 2/3)$. The goal is to check the compatibility of the leptoquarks with our assumptions and the experimental data, but we do not seek to impose new bounds on their scale.

The U_1 leptoquark couples to left-handed and right-handed fermions according to the Lagrangian in Table 4.2. The matching conditions of an vector leptoquark U_1 of mass M_U to the SMEFT Wilson coefficients can be found in Eq. (4.1). This matching is performed at the scale of M_U, as indicated in Figure 3.4.

If we only allow couplings to the left-handed fermions, the leptoquark only affects $C_{\ell q}$, as we used in our assumptions. The coefficients used in scenarios I through XI in terms of the leptoquarks couplings are

$$C^{e}_{\ell q} = -\frac{\Lambda^2}{2M_U^2}|(x_1^{LL})_{be}|^2 \qquad C^{\mu}_{\ell q} = -\frac{\Lambda^2}{2M_U^2}|(x_1^{LL})_{b\mu}|^2 \qquad C^{\tau}_{\ell q} = -\frac{\Lambda^2}{2M_U^2}|(x_1^{LL})_{b\tau}|^2\,, \tag{6.26}$$

which obviously must be negative real numbers.

According to the results of the fits in Table 6.2, the scenarios that include NP contributions in the electronic or tau sectors show preference for negative values of $C^{e}_{\ell q}$ and $C^{\tau}_{\ell q}$, and thus can be described by a U_1 leptoquark. On the contrary, all the fits to scenarios affecting the muon coupling show clear preference for positive values of the Wilson coefficient $C^{\mu}_{\ell q}$. In consequence, with our assumptions, the leptoquark U_1 can not describe the anomalies in the muon sector and therefore, does not play an important role in describing the LFUV, as shown by the fact that the scenarios with a greater pull from the SM, scenarios IV, VII and IX, are not compatible. These results confirm previous results which have shown that the U_1 leptoquark models with couplings only to the third generation quarks can not describe the anomalies on $R_{K^{(*)}}$ and can only address the deficit in this observable when it has both couplings to $b\mu$ and $s\mu$ (see, for example [369]).

Other leptoquark models do not retain the $C_{\ell q(1)} = C_{\ell q(3)}$ condition [201, 259], and therefore produce large contributions to the $B \to K^{(*)}\nu\bar{\nu}$ decays. That is the case of the

scalar $S_3 = (\bar{\mathbf{3}},\mathbf{3})_{1/3}$, that predicts $C_{\ell q(1)} = 3C_{\ell q(3)}$, and the vector $U_3 = (\bar{\mathbf{3}},\mathbf{3})_{2/3}$, where $C_{\ell q(1)} = -3C_{\ell q(3)}$. The scalar $S_1 = (\bar{\mathbf{3}},\mathbf{1})_{1/3}$ is even less suited, as it predicts $C_{\ell q(1)} = -C_{\ell q(3)}$, which would result in no NP contributing to $b \to s\ell^+\ell^-$ at all. New vector bosons W' and Z' would also be in conflict with the $B \to K^{(*)}\nu\bar{\nu}$ decays, as they predict $C_{\ell q(1)} = 0$ while $C_{\ell q(3)}$ has a non-zero value.

6.6 Conclusions

In this chapter we provide an analysis of the effects of the global fits to the Wilson coefficients assuming a model-independent effective Lagrangian approach and including a discussion of the consequences of our assumptions on the analysis in leptoquark models. The global fit includes $b \to s\mu^+\mu^-$ observables (including the Lepton Flavour Universality ratios $R_{K^{(*)}}$, the angular observables P_5' and the branching ratio of $B_s \to \mu^+\mu^-$), as well as the $R_{D^{(*)}}$, $b \to s\nu\bar{\nu}$ and electroweak precision observables (W and Z decay widths and branching ratios to leptons).

We consider different scenarios for the phenomenological analysis such that NP is present in one, two or three of the Wilson coefficients at a time (Table 6.2), with the choice of the effective operators motivated by a $U(2)^3$ symmetry between light quarks. Our results are relevant for model-independent analysis, clarifying which combinations of the Wilson coefficients are constrained by the data. For all scenarios we compare the results of the global fit with respect to both the SM and the more general and descriptive scenario: the best fit point of the three independent Wilson coefficients scenario in which NP modifies each of the operators independently.

We conclude that, when NP contributes to only one lepton flavour operator at a time, the largest pull from the Standard Model prediction, almost 4σ (Table 6.2), appears when the coupling to muons is added independently, corresponding to our scenario II. In those scenarios in which NP is present in two of the Wilson coefficients simultaneously, the best fit corresponds to the case of scenario IV, where the contributions to $C^e_{\ell q}$ and $C^\mu_{\ell q}$ are favoured with a pull of 4.73σ with respect to the SM (Table 6.2).

If we focus on the more general and descriptive scenario of three independent Wilson coefficients, we found that the prediction of the $R_{D^{(*)}}$ and $R_{K^{(*)}}$ observables is improved in the scenario in which the three $C_{\ell q}$ operators receive independent NP contributions: Scenario VII. In this case, the pull from the Standard Model is 4.64σ (Table 6.2) and the predictions for the $R_{K^{(*)}}$ observables are very similar to the case of Scenario IV. A better fit to $R_{D^{(*)}}$ observables, and specially to R^ℓ_D, is obtained in this scenario. From our analysis, we also conclude that the more relevant observables in the global fit are the LFUV observable $R^{[1.1,6]}_{K^+}$ and the $\mathscr{F}t$ parameters of the superallowed β decays; given that these observables exhibit the larger change in their pulls along the direction connecting the SM and best fit point, that is $C^i_{\ell q} = C^i_{\ell q}|_{\rm BF}\,(1+\delta C_{\rm SM})$. These observables are also the more relevant when constraining the $C^\mu_{\ell q}$ Wilson coefficient, while electroweak observables constrain

$C^e_{\ell q}$, and leptonic τ decays and the $R_{D^{(*)}}$ ratios constrain $C^\tau_{\ell q}$.

Scenario IX (Table 6.2) represents a much more restricted scenario with only one free Wilson coefficient, nevertheless it provides a good fit to experimental data, with a pull of $5.27\,\sigma$ with respect to the SM, and it is compatible with Scenario VII at $0.62\,\sigma$, therefore it provides a similar description to experimental data with less free parameters. Scenario XI, with two degrees of freedom, provides a similar fit and a pull of $4.94\,\sigma$.

Summarizing, Scenario VII (three independent Wilson coefficients) is the favoured one for explaining the tension between SM predictions and B physics anomalies, with Scenario IX and XI providing a similar fit goodness with a smaller set of free parameters.

We have also discussed that the future particle colliders, and in particular the linear lepton colliders ILC and CLIC, will provide valuable new information to cast light on the B anomalies.

Finally, we compare our setting to the U_1 leptoquark model. We conclude that, with our assumptions, this model can not describe the anomalies in the muon sector, and therefore, does not play an important role in describing the LFUV. Other leptoquark models do not contribute to the effective operators that we consider in this chapter.

6.6.1 Updated conclusions

The results presented in this chapter have been obtained using the version 2.3 of `flavio` and `smelli`, in contrast to version 1.3 that was used in [2, 3, 5]. The update has altered some of our previous conclusions:

- Our previous analysis combined the 2014 and 2021 R_{K^+} measurements as if they were statistically independent. However, the 2021 LHCb data included the $9\,\text{fb}^{-1}$ of data from 2014 plus $4\,\text{fb}^{-1}$ additional data, so the new result supersedes the old one. This problem has been fixed in the present chapter, that includes only the newest measurement for R_{K^+}. The consequence is a slightly smaller experimental uncertainty for this observable, and therefore a larger SM pull (from $2.3\,\sigma$ to $3.2\,\sigma$).

- The new version uses a different set of $B \to D^* \ell \bar{\nu}$ form factors [370]. The previous implementation produced smaller SM predictions for the $R_{D^{(*)}}$ ratios and also underestimated the theoretical uncertainties; both effects combined approximately compensated when calculating the statistical significance. Since the NP predictions are proportional to the SM values (see Eq. (3.50)), the consequence of the new form factors is that the predictions of our analysis for $R_{D^{(*)}}$ are less compatible with the experimental results.

- The number of observables included in the `flavio` database and present in the fit has increased dramatically, from 251 to 476. The most impactful inclusion are the $\mathscr{F}t$ values of the superallowed nuclear β decays. These experiments are very sensitive to the RG-induced modifications of the Fermi constant caused by the Wilson

coefficient $C^{\mu}_{\ell q}$ (which mixes with $C^{22}_{\varphi\ell(3)}$ and $C^{1221}_{\ell\ell}$ appearing in Eq. (3.40)). While our previous results showed a marked separation between the LFU ($C^{e}_{\ell q} + C^{\mu}_{\ell q}$) and LFUV ($C^{e}_{\ell q} - C^{\mu}_{\ell q}$) phenomenology, the new observables blurred this separation. We were only able to recover it when we studied the impact of the ILC by adding to the fit very precise LFU observables.

Chapter 7

Using Machine Learning techniques in flavour physics

This Chapter is devoted to another global fit to the SMEFT operators, with the ultimate goal of finding a common description for the $R_{K^{(*)}}$ and $R_{D^{(*)}}$ anomalies in B meson decays. The difference with respect to the previous Chapter is a more complicated flavour arrangement for the Wilson coefficients of the effective operators. This arrangement is based on the idea that a NP interaction could affect only to one generation of fermions, in a basis of eigenstates not aligned with the mass basis.

Due to the complicated geometry of the likelihood function, inherited from the non-linear constraints between Wilson coefficients imposed by the flavour arrangement considered, an analysis of the best-fit point and the surrounding region requires the generation of samples of points using the Montecarlo algorithm. And to ease the time of computation, a Machine Learning algorithm based on regression trees is trained in order to approximate the likelihood function. This allows for a determination of the importance of each fit parameter in the approximation, and the analysis of correlations between operators and between observables. Finally, the results of the fit are interpreted in terms of a vector leptoquark.

This Chapter is based on [4]. Some of the results have been updated compared to the published version, although the conclusions remain unchanged.

7.1 Introduction

In the previous two chapters we have presented the results of analyzing LFUV processes in B meson decays, in tension with the SM predictions. Concretely, we include in our study the ratios of branching fractions $R_{K^{(*)}}$ (Eq. (2.41)), and $R^{\ell}_{D^{(*)}}$ and $R^{\mu}_{D^{(*)}}$ (Eq. (2.43)), by performing a global fit to the experimental results available when the corresponding works have been done [1–3, 5].

It is also known that there exist other observables displaying some discrepancies with

SM predictions even when larger theoretical uncertainties are taken into account [71, 137, 371, 372]. It is clear than when investigating the implications of the experimental measurements in flavour physics observables, a global fit should be considered. Several global fits can be found in the literature (see, for example [1–3, 209, 225, 323, 343–345, 373, 374] and references therein).

In this chapter, we consider the SMEFT Lagrangian as before and we perform a global fit by including the $b \to s\mu^+\mu^-$ observables; i.e. the Lepton Flavour Universality ratios $R_{K^{(*)}}$, the angular observables P_5' and the branching ratio of $B_s \to \mu^+\mu^-$, as well as the $R_{D^{(*)}}$, $b \to s\nu\bar{\nu}$ and electroweak precision observables (W and Z decay widths and branching ratios to leptons). Because of the Gaussian approximation to characterize the fit is not successful, we will use for the first time in this context a Montecarlo analysis to extract the confidence intervals and other relevant statistics, and we explicitly show that machine learning, taking jointly with the SHapley Additive exPlanation (SHAP) values, constitute a suitable strategy to use in this analysis.

This chapter is organized as follows: Section 7.2 presents some details, not previously included, of the EFT used to describe possible NP contributions to B decays observables. For completeness, we then discuss in section 7.3 few details of the global fits performed, introducing the phenomenological scenarios that we used in the analysis and presenting our results. We found that the Gaussian approximation is not suitable to characterize the fit and, therefore, in order to extract the confidence intervals and other relevant statistics, we use a Montecarlo analysis that is described in section 7.4. The agreement of the results obtained by the Maching Learning Montecarlo algorithm that we have proposed and the ones obtained by using the Renormalization Group equations is also included in this section. Section 7.5 includes a discussion of the phenomenological implications of our analysis in leptoquark models. The conclusions are presented in section 7.6. Appendix C.2 contains the list of observables that contribute to the global fit, as well as their prediction in the most general scenario considered in this work.

7.2 Setting of the fit

This section presents some issues of the EFT formalism used in our analysis that have not been explained previously. First, at energy scales relevant for flavour processes it is convenient to work at an energy scale below the electroweak scale, for example $\mu_{\rm WET} = m_b$, with the top quark, Higgs, W and Z bosons being integrated out. This theory has been reviewed in Section 3.5, and the relevant operators for our analysis are O_{VL}^{ℓ} in Eq. (3.48) for the $R_{D^{(*)}}$ anomalies, O_9^{ℓ} and O_{10}^{ℓ} in Eq. (3.42) for the $R_{K^{(*)}}$ anomalies, and O_{ν}^{ℓ}, also in Eq. (3.42) for the $B \to K^{(*)}\nu\bar{\nu}$ decays. The dependence of the $R_{K^{(*)}}$ ratios on the Wilson coefficients has been obtained in Appendix A, and an analytic computation of $R_{K^{*0}}$ as a function of $C_9^{\mu\,\rm NP}$, $C_{10}^{\mu\,\rm NP}$ in the region $1.1 \le q^2 \le 6.0\,\text{GeV}^2$ can be found in Eq. (3.47). For the $R_{D^{(*)}}$ ratios, their expressions in the WET are included in Eq. (3.50).

Second, the NP contributions at an energy scale Λ ($\Lambda \sim \mathcal{O}$(TeV)) is defined via the SMEFT Lagrangian of Eq. (3.35). We note that we will use the SMEFT operators for our numerical analysis, and will refer to the WET operators only f or discussion and comparison with other previous results in the literature. We focus on only a subset of operators that affect the semileptonic B decays, as given in Eq. (6.1), but where the dimension six operators are defined as

$$Q^{ijkl}_{\ell q(1)} = (\bar{\ell}'_i \gamma_\mu \ell'_j)(\bar{q}'_k \gamma^\mu q'_l), \qquad Q^{ijkl}_{\ell q(3)} = (\bar{\ell}'_i \gamma_\mu \tau^I \ell'_j)(\bar{q}'_k \gamma^\mu \tau^I q'_l), \tag{7.1}$$

being τ^I the Pauli matrices, ℓ' and q' the lepton and quark $SU(2)_L$ doublets in the basis of electroweak eigenstates, and i, j, k, l denoting generation indices. As was established in Section 6.2, translating from the mass basis to the electroweak basis not modify the Lagrangian in Eq. (6.1). The translation between the SMEFT Lagrangian in the electroweak basis and in the mass basis was obtained in [200]. The SMEFT Lagrangian in the mass basis is

$$\begin{aligned}
\mathscr{L}_{\text{mass}} = &\frac{\widetilde{C}^{ijkl}_{\ell q(1)}}{\Lambda^2}\Big(\bar{\nu}_{iL}\gamma_\mu \nu_{jL} + \bar{e}_{iL}\gamma_\mu e_{jL}\Big)\Big(V_{mk}V^*_{nl}\bar{u}_{mL}\gamma^\mu u_{nL} + \bar{d}_{kL}\gamma^\mu d_{lL}\Big) \\
&+ \frac{\widetilde{C}^{ijkl}_{\ell q(3)}}{\Lambda^2}\Big(\bar{\nu}_{iL}\gamma_\mu \nu_{jL} - \bar{e}_{iL}\gamma_\mu e_{jL}\Big)\Big(V_{mk}V^*_{nl}\bar{u}_{mL}\gamma^\mu u_{nL} - \bar{d}_{kL}\gamma^\mu d_{lL}\Big) \\
&+ 2\frac{\widetilde{C}^{ijkl}_{\ell q(3)}}{\Lambda^2}\Big[(\bar{\nu}_{iL}\gamma_\mu e_{jL})(V_{mk}\bar{u}_{mL}\gamma^\mu d_{lL}) + (\bar{e}_{iL}\gamma_\mu \nu_{jL})(V^*_{nl}\bar{d}_{kL}\gamma^\mu d_{nL})\Big].
\end{aligned} \tag{7.2}$$

The relation between the $C_{\ell q}$ coefficients in the electroweak basis and the $\widetilde{C}_{\ell q}$ coefficients in the mass basis is given by [200]

$$\widetilde{C}^{ijkl}_{\ell q(1)} = C^{ijmn}_{\ell q(1)}(U^*_{dL})_{km}(U_{dL})_{ln}, \qquad \widetilde{C}^{ijkl}_{\ell q(3)} = C^{ijmn}_{\ell q(3)}(U^*_{dL})_{km}(U_{dL})_{ln}, \tag{7.3}$$

where U_{dL} and U_{uL} are the SM rotation matrices for the left-handed quarks, defined in Eq. (2.13). The only constraint for these matrices is given by the CKM matrix, $V = U_{uL}U^\dagger_{dL}$. The choice $U_{dL} = 1$, $U_{uL} = V$ defines the "Warsaw-down" basis of the SMEFT [196], where $C_{\ell q(1)} = \widetilde{C}_{\ell q(1)}$ and $C_{\ell q(3)} = \widetilde{C}_{\ell q(3)}$.

Finally, there is a recent proposal that links the B meson anomalies with NP in the top sector [202, 352, 375]. In the interaction basis, denoted by double-primed fermions, only the third generation particles exhibit NP couplings,

$$\mathscr{L}_{\text{NP}} = \frac{1}{\Lambda^2}[C_1(\bar{\ell}''_3\gamma_\mu \ell''_3)(\bar{q}''_3\gamma^\mu q''_3) + C_3(\bar{\ell}''_3\gamma_\mu \tau^I \ell''_3)(\bar{q}''_3\gamma^\mu \tau^I q''_3)], \tag{7.4}$$

where $C_1 = C^{3333}_{\ell q(1)}$ and $C_3 = C^{3333}_{\ell q(3)}$. The interaction basis is related to the basis where the mass matrices are diagonal via the unitary transformations,

$$u_L = \hat{U}_u u''_L, \qquad d_L = \hat{U}_d d''_L, \qquad \nu_L = \hat{U}_\ell \nu''_L, \qquad e_L = \hat{U}_\ell e''_L, \tag{7.5}$$

where $\psi_L = P_L\psi$ ($\psi = u,\ d,\ \nu,\ e$), $\hat{U}_\psi$ are generic unitary matrices, and the quark unitary matrices are related to the CKM matrix as $\hat{U}_u\hat{U}_d^\dagger = V$. The fermionic bilinears are transformed as follows,

$$\begin{aligned}
&\bar{u}_3''\gamma_\mu u_3'' = \lambda^u_{ij}\bar{u}_i\gamma_\mu u_j\,, && \bar{d}_3''\gamma_\mu d_3'' = \lambda^q_{ij}\bar{d}_i\gamma_\mu d_j\,, && \bar{u}_3''\gamma_\mu d_3'' = \lambda^{ud}_{ij}\bar{u}_i\gamma_\mu d_j\\
&\bar{e}_3''\gamma_\mu e_3'' = \lambda^\ell_{ij}\bar{e}_i\gamma_\mu e_j\,, && \bar{\nu}_3''\gamma_\mu \nu_3'' = \lambda^\ell_{ij}\bar{\nu}_i\gamma_\mu \nu_j\,, && \bar{e}_3''\gamma_\mu \nu_3'' = \lambda^\ell_{ij}\bar{e}_i\gamma_\mu \nu_j\,,
\end{aligned} \tag{7.6}$$

with the flavour matrices λ given by

$$\begin{aligned}
\lambda^u_{ij} &= (\hat{U}_u)_{3i}(\hat{U}_u)^*_{3j}\,, & \lambda^q_{ij} &= (\hat{U}_d)_{3i}(\hat{U}_d)^*_{3j}\,,\\
\lambda^{ud}_{ij} &= (\hat{U}_u)_{3i}(\hat{U}_d)^*_{3j}\,, & \lambda^\ell_{ij} &= (\hat{U}_\ell)_{3i}(\hat{U}_\ell)^*_{3j}\,.
\end{aligned} \tag{7.7}$$

We can write all the quark matrices in terms of λ^q,

$$\lambda^u = V\lambda^q V^\dagger\,, \qquad \lambda^{ud} = V\lambda^q\,, \tag{7.8}$$

so every u-type quark picks an additional CKM matrix, which are exactly the same factors appearing in the Lagrangian for the mass basis in Eq. (7.2). For example, if we expand the first term in Eq. (7.4), we obtain

$$\begin{aligned}
&\frac{C_1}{\Lambda^2}(\bar{\ell}_3''\gamma_\mu\ell_3'')(\bar{q}_3''\gamma^\mu q_3'')\\
=&\frac{C_1}{\Lambda^2}\Big(\bar{\nu}_3''\gamma_\mu\nu_3'' + \bar{e}_3''\gamma_\mu e_3''\Big)\Big(\bar{u}_3''\gamma^\mu u_3'' + \bar{d}_3''\gamma^\mu d_3''\Big)\\
=&\frac{C_1}{\Lambda^2}\lambda^\ell_{ij}\lambda^q_{kl}\Big(\bar{\nu}_{i\,L}\gamma_\mu\nu_{j\,L} + \bar{e}_{i\,L}\gamma_\mu e_{j\,L}\Big)\Big(V_{mk}V^*_{nl}\bar{u}_{m\,L}\gamma^\mu u_{n\,L} + \bar{d}_{k\,L}\gamma^\mu d_{l\,L}\Big),
\end{aligned} \tag{7.9}$$

which agrees with Eq. (7.2) with the identification $C^{ijkl}_{\ell q(1)} = \widetilde{C}^{ijkl}_{\ell q(1)} = C_1\lambda^\ell_{ij}\lambda^q_{kl}$. Repeating the same steps with the other term in Eq. (7.4), we arrive to $C^{ijkl}_{\ell q(3)} = \widetilde{C}^{ijkl}_{\ell q(3)} = C_3\lambda^\ell_{ij}\lambda^q_{kl}$.

In conclusion, the Lagrangian of Eq. (7.4) in the "Warsaw-down" basis becomes

$$\mathscr{L}_{\rm NP} = \frac{\lambda^\ell_{ij}\lambda^q_{kl}}{\Lambda^2}\left(C_1(\bar{\ell}_i\gamma_\mu\ell_j)(\bar{q}_k\gamma^\mu q_l) + C_3(\bar{\ell}_i\gamma_\mu\tau^I\ell_j)(\bar{q}_k\gamma^\mu\tau^I q_l)\right). \tag{7.10}$$

We perform the RG running of the SMEFT Wilson coefficients from $\Lambda = 1\,$TeV down to $\mu_{\rm EW}$ [376], where we match the SMEFT and WET operators [185], and finally we perform the RG running of the WET coefficients down to $\mu = m_b$ [190]. We check that the analytical expressions are in agreement with the numerical results obtained by the package `Wilson` [341]. This operation is performed for all the effective operators in the WET that receive contributions from the Lagrangian in Eq. (7.10). Here we reproduce the matching conditions for the Wilson coefficients with the largest impact on the semileptonic B meson decays, that is, $C_9^{i\,\rm NP}$ and $C_{10}^{i\,\rm NP}$ for the $B\to K^{(*)}\ell^+\ell^-$ decays, $C_{VL}^{i\,\rm NP}$ for the $B\to D^{(*)}\ell\nu$

decays, and C_ν^i for the $B \to K^{(*)}\nu\bar{\nu}$ decays:

$$
\begin{aligned}
C_9^{i\,\mathrm{NP}} &\approx \frac{2\sqrt{2}\pi^2}{e^2 V_{tb}V_{ts}^*}\frac{1}{G_F\Lambda^2}(C_1+C_3)\lambda_{23}^q\lambda_{ii}^\ell + \frac{\sqrt{2}}{3V_{tb}V_{ts}^*}\frac{1}{G_F\Lambda^2}(C_1+C_3)\lambda_{23}^q \log\frac{m_b}{\Lambda}\,,\\
C_{10}^{i\,\mathrm{NP}} &\approx -\frac{2\sqrt{2}\pi^2}{e^2 V_{tb}V_{ts}^*}\frac{1}{G_F\Lambda^2}(C_1+C_3)\lambda_{23}^q\lambda_{ii}^\ell\,,\\
C_{VL}^{i\,\mathrm{NP}} &\approx -\frac{1}{\sqrt{2}G_F\Lambda^2}C_3\lambda_{ii}^\ell\left(\frac{V_{cs}}{V_{cb}}\lambda_{23}^q+\lambda_{33}^q\right),\\
C_\nu^i &\approx \frac{2\sqrt{2}\pi^2}{e^2 V_{tb}V_{ts}^*}\frac{1}{G_F\Lambda^2}(C_1-C_3)\lambda_{23}^q\lambda_{ii}^\ell + \frac{3\sqrt{2}g'^2}{2e^2 V_{tb}V_{ts}^*}\frac{1}{G_F\Lambda^2}C_3\lambda_{23}^q\lambda_{ii}^\ell\log\frac{m_b}{\Lambda}\,.
\end{aligned}
\tag{7.11}
$$

We find out that there is a sizeable subleading term that affects $C_9^{i\,\mathrm{NP}}$ and not $C_{10}^{i\,\mathrm{NP}}$, thus breaking the leading-order relation $C_9^{i\,\mathrm{NP}} = -C_{10}^{i\,\mathrm{NP}}$. However, this subleading term is LFU, since it does not depend on the leptonic flavour matrix λ^ℓ, and consequently this term alone can not explain the anomalies observed in the universality ratios $R_{K^{(*)}}$. Any explanation will inevitably include some LFUV effects appearing at tree level. The interplay between the tree-level and loop-induced terms is well-known and was also previously discussed by [377].

In order to describe the rotation between the two bases, the flavour matrices λ introduced in Eq. (7.7) must be hermitian, idempotent $\lambda^2 = \lambda$, and $\mathrm{tr}\lambda = 1$. These properties are consequences of the fact that, in the interaction basis, NP only affects one generation, and follow immediately from the definitions:

$$
\begin{aligned}
\lambda_{ji} &= \hat{U}_{3j}\hat{U}_{3i}^* = (\hat{U}_{3i}\hat{U}_{3j}^*)^* = \lambda_{ij}^*\,,\\
\lambda_{ij}\lambda_{jk} &= \hat{U}_{3i}\hat{U}_{3j}^*\hat{U}_{3j}\hat{U}_{3k}^* = \hat{U}_{3i}\hat{U}_{3k}^* = \lambda_{ik}\,,\\
\mathrm{tr}\lambda &= \sum_i \lambda_{ii} = \sum_i \hat{U}_{3i}\hat{U}_{3i}^* = (\hat{U}\hat{U}^\dagger)_{33} = 1\,.
\end{aligned}
\tag{7.12}
$$

A 3×3 hermitian idempotent matrix with trace one has 4 free real parameters, or equivalently, 2 free complex parameters. Without loss of generality, we can use the parameterization [202]

$$
\lambda^{\ell,q} = \frac{1}{1+|\alpha^{\ell,q}|^2+|\beta^{\ell,q}|^2}\begin{pmatrix} |\alpha^{\ell,q}|^2 & \alpha^{\ell,q}\bar{\beta}^{\ell,q} & \alpha^{\ell,q} \\ \bar{\alpha}^{\ell,q}\beta^{\ell,q} & |\beta^{\ell,q}|^2 & \beta^{\ell,q} \\ \bar{\alpha}^{\ell,q} & \bar{\beta}^{\ell,q} & 1 \end{pmatrix},
\tag{7.13}
$$

where $\alpha^{\ell,q}$ and $\beta^{\ell,q}$ are complex numbers, which are related to the unitary rotation matrices as

$$
\begin{aligned}
(\hat{U}_{\ell,q})_{31} &= \frac{\alpha^{\ell,q}}{\sqrt{1+|\alpha^{\ell,q}|^2+|\beta^{\ell,q}|^2}}\,,\\
(\hat{U}_{\ell,q})_{32} &= \frac{\beta^{\ell,q}}{\sqrt{1+|\alpha^{\ell,q}|^2+|\beta^{\ell,q}|^2}}\,,
\end{aligned}
$$

$$(\hat{U}_{\ell,q})_{33} = \frac{1}{\sqrt{1+|\alpha^{\ell,q}|^2+|\beta^{\ell,q}|^2}},$$
$$\alpha^{\ell,q} = \frac{(\hat{U}_{\ell,q})_{31}}{(\hat{U}_{\ell,q})_{33}}, \qquad \beta^{\ell,q} = \frac{(\hat{U}_{\ell,q})_{32}}{(\hat{U}_{\ell,q})_{33}}. \tag{7.14}$$

We can therefore understand the parameters α^ℓ and β^ℓ as the relative degree of mixing to the first and second generations of leptons, respectively, produced by the rotation from the interaction basis to the mass basis. Analogously, the parameters α^q and β^q represent the relative degree of mixing to the first and second generations of d-type quarks (remember that the u-type quarks pick additional CKM factors).

The conditions in Eq. (7.13) impose several relations between the LFUV operators, which are proportional to the diagonal entries of λ^ℓ, and the LFV operators, proportional to the off-diagonal entries:

$$C_{\ell q}^{11ij} = \frac{|C_{\ell q}^{13ij}|^2}{C_{\ell q}^{33ij}}, \qquad C_{\ell q}^{22ij} = \frac{|C_{\ell q}^{23ij}|^2}{C_{\ell q}^{33ij}}. \tag{7.15}$$

On the other hand, the $O_{\ell q}$ operators also produce unwanted contributions to the $B \to K^{(*)}\nu\bar{\nu}$ decays [202]. In order to obey these constraints, we will fix at the scale $\mu = \Lambda$ the relation

$$C_{\ell q(1)}^{ijkl} = C_{\ell q(3)}^{ijkl} \equiv C_{\ell q}^{ijkl}. \tag{7.16}$$

This relation cancels the tree-level contribution to the $B \to K^{(*)}\nu\bar{\nu}$, but there is still a loop-induced contribution, proportional to the $C_{\ell q(3)}$ coefficients. However, we have checked that in our scenarios, this is only a 0.1% correction of the SM predictions.

7.3 Global fits

As previously mentioned and discussed in details, the effective operators affect a large number of observables, connected between them via the Wilson coefficients, and therefore, global fits are mandatory in order to keep the predictions consistent with experimental measurements. As in chapter 6, the global fits to the $C_{\ell q}$ Wilson coefficients have been performed by using the packages `flavio` v2.3 [195] and `smelli` v2.3 [342]. As before, the goodness of each fit is evaluated with its difference of χ^2 with respect to the SM, and in order to compare two fits we use the pull between them in units of σ, as defined in Eq. (6.7). The SM input parameter used for these fits are also the same as in the previous chapter (Table 6.1). The Renormalization Group effects of the SMEFT operators that shift the Fermi constant G_F [185] from its SM value G_F^0, as described by Eq. (3.40), are considered. The effects on the CKM matrix [186] are also considered by `smelli`. In particular, for the best fit point of Scenario II (see below), we find a correction of 8% for V_{ub}, while V_{us}, V_{cb} and $\delta_{\rm KM}$ remain unchanged.

	Scenario I	Scenario II
C	-0.13 ± 0.05	-0.13 ± 0.08
α^ℓ		$\pm(0.07^{+0.04}_{-0.07})$
β^ℓ	0 ± 0.025	0 ± 0.025
α^q		$-0.05^{+0.12}_{-0.07}$
β^q	$0.8^{+2.0}_{-0.5}$	$0.73^{+2.8}_{-0.6}$
$\Delta\chi^2_{\rm SM}$	40.32	57.06
SM Pull	$5.75\,\sigma$	$6.57\,\sigma$

Table 7.1: Best fits to the flavour parameters and the coefficient C in Scenarios I and II.

Now we proceed to fit the set of flavour observables to the parameters $C_1 = C_3 \equiv C$, $\alpha^{\ell,q}$ and $\beta^{\ell,q}$ of Eqs. (7.10) and (7.13). In this setting, we consider two Scenarios:

- **Scenario I:** $\lambda^{\ell,q}_{11} = \lambda^{\ell,q}_{12} = \lambda^{\ell,q}_{13} = 0$, that is, $\alpha^\ell = \alpha^q = 0$, and $C_1 = C_3$.

- **Scenario II:** The only assumption is $C_1 = C_3$.

In both scenarios $C_1 = C_3$ in order to implement the constraints from the $B \to K^{(*)}\bar{\nu}\nu$ observables, as previously mentioned (see Eq. (7.16)). In Scenario I we also set $\lambda^{\ell,q}_{11} = \lambda^{\ell,q}_{12} = \lambda^{\ell,q}_{13} = 0$, i.e. $\alpha^\ell = \alpha^q = 0$, assuming that the mixing affecting the first generation are negligible; this is the same assumption used in [202]. Scenario II is more general, including non-negligible mixings to the first generation, allowing us to check the validity of the above assumption and to discuss the results in a more general situation; focusing in the relevance of the mixing in the first generation. In both scenarios, we only consider real values for the parameters of the fit.

The best fits to the flavour parameters α and β for leptons and quarks and to the Wilson coefficient $C \equiv C_1 = C_3$ in these two Scenarios are summarized in Table 7.1. The better fit is found for Scenario II, with a pull of $6.57\,\sigma$ with respect to the Standard Model, $3.68\,\sigma$ with respect to Scenario I. We note that the β^ℓ parameter, which mix the second and third generations of leptons at tree level, is negligible in both fits. Figure 7.1 shows the two-dimensional sections of the likelihood function $\Delta\chi^2_{\rm SM}$ for the α^ℓ-β^ℓ and α^q-β^q parameters in Scenario II, at $1\,\sigma$ and $2\,\sigma$. The rest of parameters are given as in the best fit point of this Scenario. Results for the $R_{K^{(*)}}$ and $R_{D^{(*)}}$ observables and for the LFV observables, as well as for the global fit are included. We can observe that, due to the non-linear relations imposed by Eq. (7.13), the regions of equal probability are highly non-ellipsoidal. Therefore, we cannot use the Gaussian approximation to characterize the fit. Instead, we will use a Montecarlo analysis, described in section 7.4, in order to extract the confidence intervals and correlations between observables. The values of the parameters of the La-

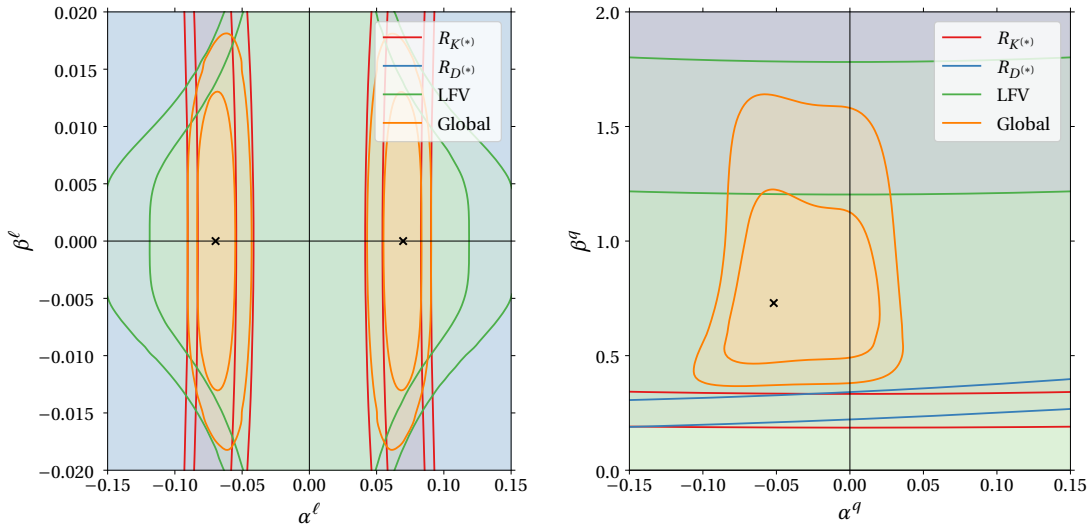

(a) (b)

Figure 7.1: 1σ and 2σ contours for the (a) α^ℓ and β^ℓ and (b) α^q and β^q parameters, with the rest of parameters as in the best fit point of Scenario II.

grangian (7.10) in Scenario II are $C = C_1 = C_3 = -0.126 \pm 0.010$, and

$$\lambda^\ell = \begin{pmatrix} (5\pm3)\times10^{-3} & (0\pm1)\times10^{-3} & (6\pm3)\times10^{-2} \\ (0\pm1)\times10^{-3} & (0\pm2)\times10^{-4} & (0\pm1.5)\times10^{-2} \\ (6\pm3)\times10^{-2} & (0\pm1.5)\times10^{-2} & 0.995\pm0.003 \end{pmatrix}, \tag{7.17}$$

$$\lambda^q = \begin{pmatrix} (1.7\pm1.5)\times10^{-3} & (-2\pm2)\times10^{-2} & (-3\pm2)\times10^{-2} \\ (-2\pm2)\times10^{-2} & 0.35\pm0.2 & 0.47\pm0.08 \\ (-3\pm2)\times10^{-2} & 0.47\pm0.08 & 0.65\pm0.2 \end{pmatrix}. \tag{7.18}$$

The most notable effect of the mass rotation is the mixing of the second and third generation quarks, and there is also some mixing between the first and third generation leptons.

In order to better understand and discuss the results obtained in Scenario II, we present the matching of the parameters in Table 7.1 to the more relevant WET Wilson coefficients,

$$\begin{aligned} C_9^{\mu\,\mathrm{NP}} &= -0.67\pm0.21, & C_{10}^{\mu\,\mathrm{NP}} &= -0.002\pm0.012, & C_{VL}^{\tau\,\mathrm{NP}} &= 0.098\pm0.03, \\ C_9^{e\,\mathrm{NP}} &= -0.32\pm0.25, & C_{10}^{e\,\mathrm{NP}} &= -0.36\pm0.25. \end{aligned} \tag{7.19}$$

As established in Eq. (7.11), subleading RG effects cause a notable deviation from the leading-order relation $C_9^{\mu\,\mathrm{NP}} = -C_{10}^{\mu\,\mathrm{NP}}$. This is in agreement with the fits performed in [1, 313, 321, 323–325, 327, 328, 349, 378–383], where the Wilson coefficient $C_9^{\mu\,\mathrm{NP}}$ receives a greater NP contribution than $C_{10}^{\mu\,\mathrm{NP}}$. According to our fit, $C_{10}^{\mu\,\mathrm{NP}} \approx 0$: from the matching conditions, this operator is generated at tree level and is proportional to $\lambda^\ell_{22} \sim |\beta^\ell|^2$. From the plot in Fig. 7.1 we learn that the parameter β^ℓ is severely constrained by the LFV observables, in green lines. Consequently, $C_9^{\mu\,\mathrm{NP}} = -C_{10}^{\mu\,\mathrm{NP}} + C_9^{\mathrm{loop}} \approx C_9^{\mathrm{loop}}$ is dominated

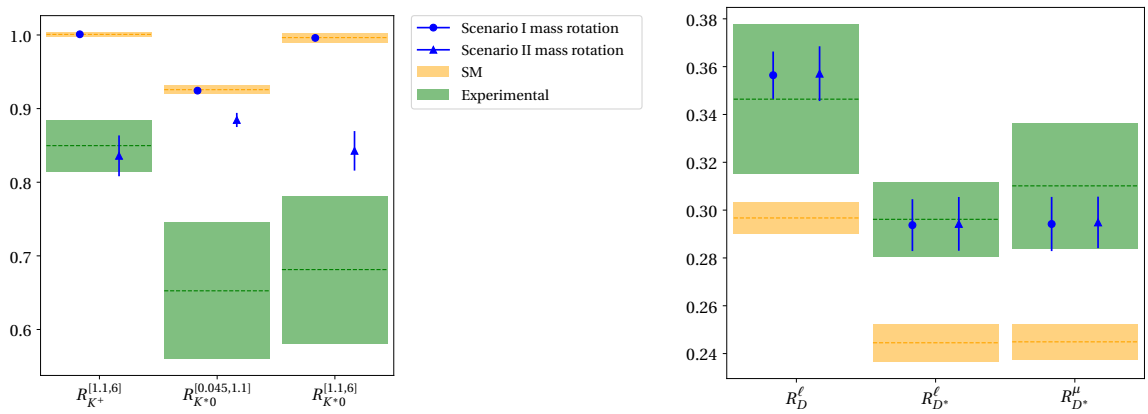

(a) (b)

Figure 7.2: Central value and $1\,\sigma$ uncertainty (blue lines) of the (a) $R_{K^{(*)}}$ observables and (b) $R_{D^{(*)}}$ observables in Scenarios I and II, compared to the Standard Model prediction (yellow area) and experimental measurements (green area).

by the loop-generated term in Eq. (7.11). Clearly, the logarithmic term that appear in the first equation of (7.11) is relevant in the phenomenological analysis. In the electron sector, the mixing parameter α^ℓ does not suffer large constraints from the LFV sector. In this case, the tree-level and loop-level terms are similar, and therefore $C_9^{e\,\mathrm{NP}} = -C_{10}^{e\,\mathrm{NP}} + C_9^{\mathrm{loop}} \approx -C_{10}^{e\,\mathrm{NP}} + C_9^{\mu\,\mathrm{NP}}$, which is of the same order of magnitude as $C_{10}^{e\,\mathrm{NP}}$. In Section 7.5, we assess an specific model of leptoquarks where these relations are met.

The predictions for $R_{K^{(*)}}$ and $R_{D^{(*)}}$ observables in the best fit points for both scenarios are displayed in Figure 7.2, where the central value and $1\,\sigma$ uncertainty of the observables is included. The yellow area corresponds with the SM prediction, and the green area with the experimental measurements for each observable. Table 7.2 summarizes the results for the $R_{K^{(*)}}$ and $R_{D^{(*)}}$ observables in Scenarios I and II for the corresponding best fit points. For comparison, an statistical combination of all the available measurements of each observable, performed by `flavio` is included in the last column of this table.

From the above results, it is clear that the assumptions of Scenario I do not allow for a simultaneous explanation of the $R_{K^{(*)}}$ and $R_{D^{(*)}}$ anomalies, as already pointed out in [202]. In particular, a value of the mixing between the second and third generation leptons β^ℓ is large enough to describe $R_{K^{(*)}}$ through the tree-level $C_9^{\mu\,\mathrm{NP}} = -C_{10}^{\mu\,\mathrm{NP}}$ coefficients, but implies that $R_{D^{(*)}} < R_{D^{(*)}}^{\mathrm{SM}}$. Instead, our fit shows a preference for a negligible β^ℓ, and therefore the $R_{D^{(*)}}$ anomalies are explained only through NP in C_{VL}^τ. The predictions for the branching ratios and angular observables of the $B \to K^{(*)}\mu^+\mu^-$ decays are improved thanks to the flavour-universal loop-induced contribution to $C_9^{\mu\,\mathrm{NP}} = C_9^{\mathrm{loop}}$, while the $R_{K^{(*)}}$ ratios are not sensitive to the universal contribution and remain SM-like.

The parameters in the fit of Scenario II, on the other hand, are able to describe the $R_{K^{(*)}}$ and $R_{D^{(*)}}$ anomalies at the same time, as it is shown in Figure 7.2 and Table 7.2. To consider the mixing between the first and third lepton generation does not notably alter

Observable	Scenario I	Scenario II	Measurement
$R_{K^+}^{[1.1,6]}$	1.0009 ± 0.0011	0.84 ± 0.03	0.85 ± 0.03
$R_{K^{*0}}^{[0.045,\ 1.1]}$	0.924 ± 0.004	0.885 ± 0.010	0.65 ± 0.09
$R_{K^{*0}}^{[1.1,\ 6]}$	0.9960 ± 0.0010	0.84 ± 0.03	0.68 ± 0.10
R_D^ℓ	0.356 ± 0.010	0.357 ± 0.011	0.35 ± 0.03
$R_{D^*}^\ell$	0.294 ± 0.011	0.294 ± 0.011	0.296 ± 0.016
$R_{D^*}^\mu$	0.294 ± 0.011	0.295 ± 0.011	0.31 ± 0.03

Table 7.2: Values of the $R_{K^{(*)}}$ and $R_{D^{(*)}}$ observables in Scenarios I and II for the best fit points.

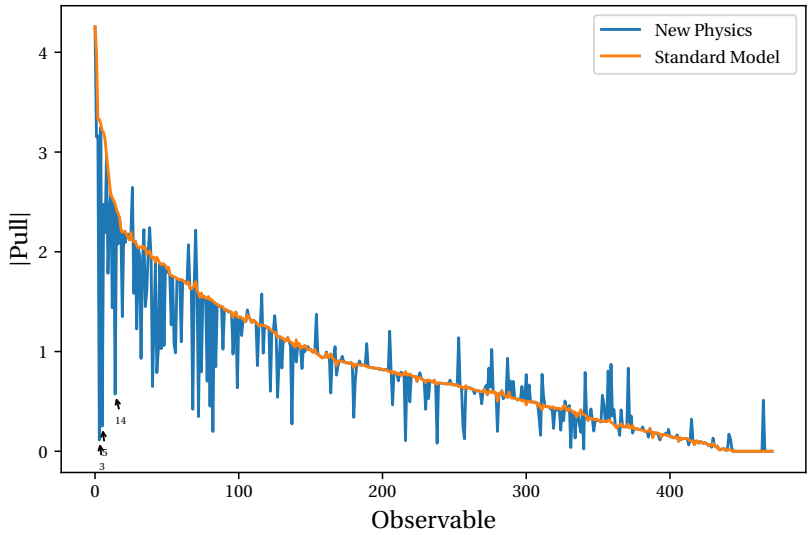

Figure 7.3: Pulls in the Standard Model (orange) and Scenario II (blue) of the observables included in the global fit. The observables whose pull changes in more than 1.5σ between the SM and Scenario II are specially marked in the plot: $R_{D^*}^\ell$ (observable 3), $R_{K^+}^{[1.1,6]}$ (observable 5) and $R_{D^*}^\mu$ (observable 14).

the prediction for $R_{D^{(*)}}$. At the same time, it originates a tree-level contribution to $C_9^{e\,\mathrm{NP}} = -C_{10}^{e\,\mathrm{NP}}$, that breaks the universality between the electron and muon Wilson coefficients, allowing for $R_{K^{(*)}} \neq 1$.

The comparison of the pull of each observable for this scenario with respect to their experimental measurement (blue line), compared to the same pull in the SM (orange line) is presented in Figure 7.3. The observables whose pull changes in more than 1.5σ between the SM and Scenario II are specially marked in the plot, i.e. R_{K^+}, $R_{D^{(*)}}^l$ and $R_{D^{(*)}}^\mu$ (observables 5, 3 and 14 in the table presented in Appendix C.2). It is clear that for these observables NP improves their prediction. For completeness, the full list of predictions and pulls is also included in Appendix C.2. We have checked that all the observables in the appendix, with the only exception of $|\epsilon_K|$ (observable 20), can receive a contribution from the Wilson coefficients in Scenario II when considering the full RG equations. It is

also important to note that the muon lifetime is not included in the above list of observables because it is used to determine the SM value of G_F; an input parameter.

Finally, we also investigate which class of observables constraint each parameter of the fit. For this purpose we modify the flavour parameters α and β for leptons and quarks and the Wilson coefficient $C \equiv C_1 = C_3$ independently, and we compare the results with respect to the likelihood for $R_{K^{(*)}}$, $R_{D^{(*)}}$ and LFV observables, and to the global likelihood. Figure 7.4 shows the evolution of the likelihood for $R_{K^{(*)}}$ and $R_{D^{(*)}}$ observables and LFV observables, as well as the global likelihood, when one parameter is modified from its best fit value. The interplay between all observables is clearly established when the Wilson coefficient C is modified (Figure 7.4 (a)). In the case of the lepton mixing, it is clear that the $R_{K^{(*)}}$ observables determine the best values of α^ℓ (Figure 7.4 (b)), while the LFV observables limit the allowed values of β^ℓ to a narrow region around zero; being the observables that determine the behaviour of the global fit in this case (Figure 7.4 (c)). In the quark mixing (Figure 7.4 (d) and (e)), we found that α^q is constrained by the observable BR($K^+ \to \pi^+ \nu\bar{\nu}$), while β^q is determined by the interplay of $R_{K^{(*)}}$ and $R_{D^{(*)}}$, that prefer larger values, and the LFV observables, that disallow $\beta^q > 1$.

Clearly, the above results show the interplay between all parameters and confirm the relevance of considering all observables when performing phenomenological studies in the context of B anomalies and the discussion of possible explanation of these anomalies through NP models.

7.4 Montecarlo analysis using Machine Learning

In this section we study the parameter points in the neighborhood of the best fit point. We will generate samples of parameter points following the χ^2 distribution given by the likelihood of the fit. The Montecarlo algorithm is the standard procedure to generate samples that follow a known distribution. In our case, the computation time needed to calculate the likelihood of each candidate point is a huge drawback. Instead, we opted to use a Machine Learning algorithm to construct an approximation to the likelihood function and that can be evaluated in a much shorter time. As far as we know, this is the first time that these procedure is used in the analysis of flavour anomalies. There exist a previous article that address the problem of NP model in $b \to c\tau\nu_\tau$ decays by using a specific machine learning algorithm [384], but the techniques used in this work are different to the ones we used here.

7.4.1 Methodology

The first Machine Learning tool that we will use for our analysis is a model able to approximate any arbitrary function $f : \mathbb{R}^n \to \mathbb{R}$, that we will use to create an approximation of the log-likelihood function of our fit. We have chosen an ensemble method based on

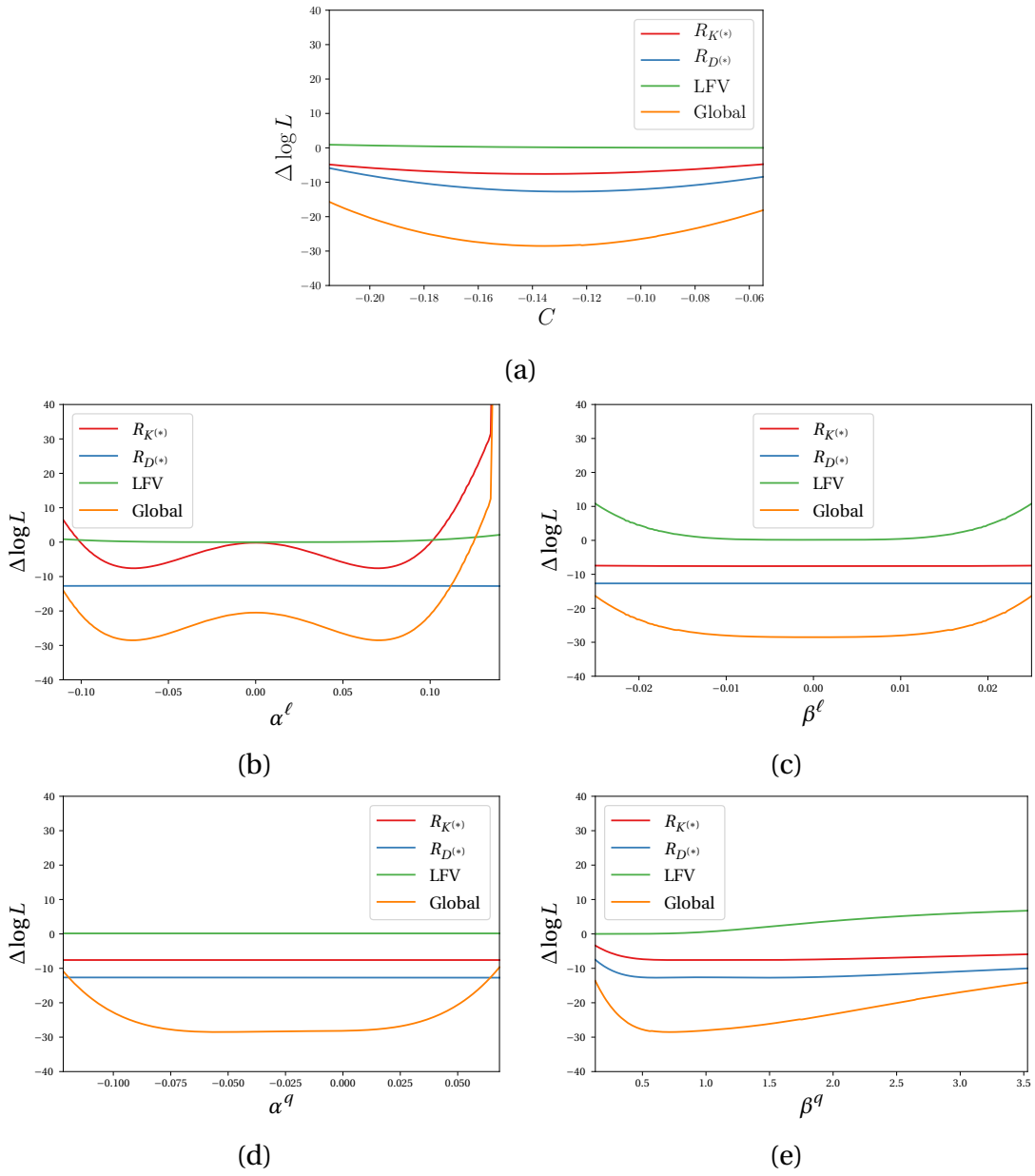

Figure 7.4: Likelihood of the fit when one coefficient is modified: (a) C, (b) α^ℓ, (c) β^ℓ, (d) α^q, (e) β^q.

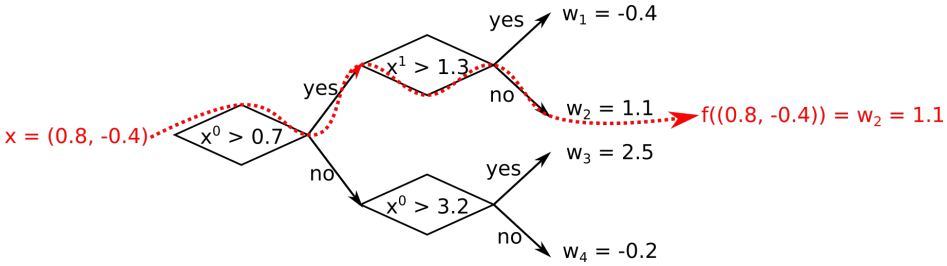

Figure 7.5: Example of regression tree with four leaves. In red, application of the function $f(x)$ associated with the tree to an input x.

regression trees, which is implemented by `xgboost` [385].

Regression trees are a type of decision tree. A decision tree is a diagram that recursively partitions data into subsets, based on the binary (true/false) conditions located at the nodes of the tree. The final subsets in which the data are classified are called "leaves". A decision tree with T leaves is formally a function $q : \mathbb{R}^n \to \{1, 2, \ldots, T\}$ which associates to each data point $x \in \mathbb{R}^n$ its leaf $q(x)$. A regression tree assigns to each leaf i a real number $w_i \in \mathbb{R}$. The regression tree therefore defines a function $f : \mathbb{R}^n \to \mathbb{R}$, given by

$$f(x) = w_{q(x)}\,. \tag{7.20}$$

An example of a regression tree with four leaves is depicted in Fig. 7.5. In practice, a single tree is not general enough to reproduce an arbitrary function. For this reason, we consider instead an ensemble of K regression trees $\mathscr{F} = \{f^{(1)}, f^{(2)}, \ldots, f^{(K)}\}$. The ensemble defines a function $\phi : \mathbb{R}^n \to \mathbb{R}$,

$$\phi(x) = \sum_{i=1}^{K} f^{(i)}(x) = \sum_{i=1}^{K} w^{(i)}_{q(x)}\,. \tag{7.21}$$

The function $\phi(x)$ will represent the approximation for the log-likelihood function. It will be calculated using supervised learning, that is, the trees are obtained from a dataset $\mathscr{D} = \{(x_i, y_i)\}$ where $x_1, \ldots x_N \in \mathbb{R}^n$ are the inputs and $y_1, \ldots y_N \in \mathbb{R}$ are the pre-computed outputs for each input. In our case, the input data will be of the form $x_i = (C_i, \alpha_i^\ell, \beta_i^\ell, \alpha_i^q, \beta_i^q)$, and the outputs will be $y_i = \log L(x_i)$.

In order to train the model from the dataset, we need to define an objective function $\mathscr{L}[\phi]$ that measures how well the model fits the data,

$$\mathscr{L}[\phi] = \sum_i l(\phi(x_i), y_i) + \sum_k \Omega(f^{(k)})\,, \tag{7.22}$$

which has two components:

- The loss function $l(\phi(x_i), y_i)$ is a differentiable function that measures the similarity between the true output y_i and its approximation $\phi(x_i)$. We use as loss function the mean absolute error, $l(\phi(x_i), y_i) = |\phi(x_i) - y_i|$.

- The function Ω is the regularization term, that penalizes the complexity of trees, that is, trees with many leaves or with large $||w||$. The purpose of the regularization

is to prevent over-fitting, that is, the model learning "by heart" the training data and being unable to extrapolate from them.

The ensemble is constructed in an iterative way, starting from one single tree $f^{(0)}$ that contains just one leaf. At the step t of the iteration, the tree $f^{(t)}$ is obtained by splitting one of the leaves of the tree $f^{(t-1)}$ into two leaves; the splitting is determined by the optimization of the objective function. In order to prevent over-fitting, the shrinkage technique is used, that scales newly added weights by a factor $\eta < 1$, similar to the learning rate in other Machine Learning algorithms.

Once we have an approximation of the log-likelihood function, we put it to use new samples of datapoints $x_i = (C_i, \alpha_i^\ell, \beta_i^\ell, \alpha_i^q, \beta_i^q)$. We use a Montecarlo algorithm to produce the data distributed according to the χ^2 distribution of the fit. At each step of the Montecarlo algorithm, a new tentative x_i is proposed, which is accepted if the ratio of its probability divided by the probability of the best fit point is greater than a random number u distributed uniformly in the interval $[0,1]$, and rejected otherwise. Expressed in terms of the logarithms of the likelihood function instead,

$$\log L(x_i) > \log L_{\rm bf} + \log u\,. \tag{7.23}$$

This algorithm requires many calls to the likelihood function, which are computationally very tasking, and most of the proposed points are rejected. As a way to ease the burden, we use the approximated log-likelihood $\phi(x_i)$ instead of the true function.

We can asses the importance of each parameter in the Machine Learning approximation at any point of the generated samples by using SHAP values [386, 387]. SHAP values are based in Lloyd Shapley's work on game theory [388], who won the Nobel Prize in Economics for it in 2012.

The SHAP values are designed with three properties in mind:

- **Local accuracy:** The sum of the SHAP values is equal to the model prediction.
- **Missingness:** If any feature is missing, its SHAP value is zero.
- **Consistency:** If the model is changed so any feature has larger impact, its SHAP value will increase.

Given a model $\phi(x)$, the SHAP trains 2^n new models $\phi_z(x)$ for $z \in \{0,1\}^n$ binary vectors. The model $\phi_z(x)$ contains the feature $x^{(i)}$ only if $z^{(\alpha)} = 1$, while that feature is ignored when training if $z^{(\alpha)} = 0$. The marginal contribution $\phi_{z'}(x_i) - \phi_z(x_i)$ for two models differing only in the presence of one feature (i.e. $z^{(\alpha)} = 0$, $z'^{(\alpha)} = 1$ and $z^{(\beta)} = z'^{(\beta)}\ \forall\ \beta \neq \alpha$), gives the importance of adding the feature α to the model z. The SHAP value for the feature α in the point x_i is just the weighted average of all marginal contributions, with the weight given by a combinatorial factor. An example is depicted in Fig. 7.6. The prediction without any features $\phi_{0\cdots0}$ is simply the average of the values y_i in the dataset, and acts as a base value common for all x_i.

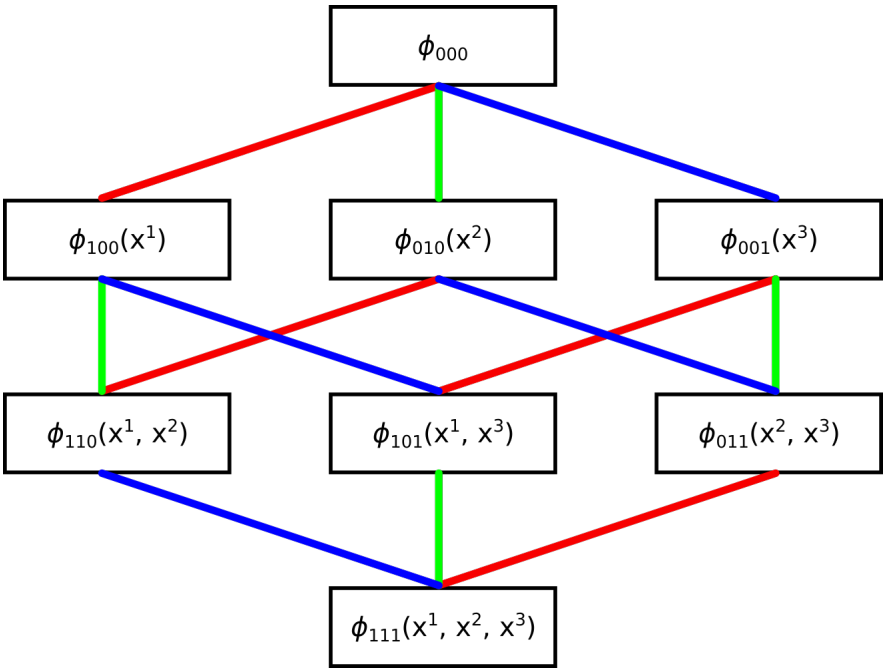

Figure 7.6: Prediction models that would we necessary to train for three features in order to calculate the SHAP values. The edges represent the marginal contributions for each feature: in red for x^1, green for x^2 and blue for x^3.

Finally, we will analyze the correlations between the points in the generated samples, in order to understand the physical relations caused by the NP.

7.4.2 Procedure and results

In the first place we create a sample of 10000 parameter points (5000 re-used from the calculation of Fig. 7.1 and 5000 randomly generated) and their likelihood. We discard the points with $\Delta\chi^2_{\text{SM}} < 20$, retaining 5763 points.

We train a Machine Learning predictor using the pre-computed sample. We used the eXtreme Gradient Boosting (XGBoost) algorithm. We split the sample in two parts, 75% of the points for the training and 25% points for the validation of the model. The algorithm uses a learning rate of 0.05 and 1000 estimators, allowing early stopping at 5 rounds. The performance of the Machine Learning predictor can be seen in Figure 7.7 (a). The horizontal axis represents the actual value of the $\Delta\chi^2_{\text{SM}}$ for each point of the validation dataset, computed using the full `flavio` and `smelli` code, with the best fit point found in Section 7.3 corresponding to the maximum value. The vertical axis represents the predicted value for the same points obtained using the Machine Learning approximation. The predicted values for the $\Delta\chi^2_{\text{SM}}$ reproduce their actual values, with a Pearson regression coefficient $r = 0.971$ and Mean Absolute Error of 0.655 in the validation dataset. The agreement between the predicted and actual values is specially good for parameters near the best fit point ($\Delta\chi^2_{\text{SM}} > 45$).

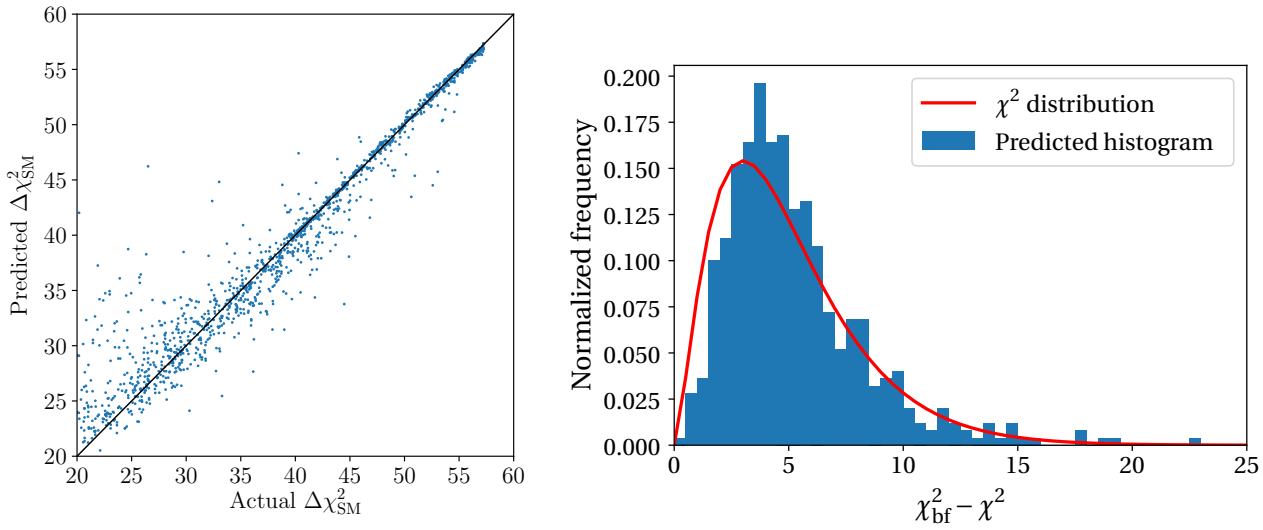

(a) (b)

Figure 7.7: Predictor performance: (a) Regression of the predicted values of $\Delta\chi^2$ compared to the real ones in the validation dataset. (b) Histogram of the predictions for the Montecarlo points generated using the Machine Learning algorithm.

Base value	SHAP value for C	α^ℓ	β^ℓ	α^q	β^q	Final prediction	Actual $\log L$
39.43	3.293	4.056	1.993	2.671	4.086	55.537	57.06

Table 7.3: SHAP values and Machine Learning prediction for the best fit point.

Next we implement the Montecarlo algorithm. To check if the Machine Learning Montecarlo algorithm can actually reproduce the χ^2 distribution, we generate a sample of 500 points. The histogram for the predicted values of the χ^2 are plotted in Figure 7.7 (b). The histogram follow the general shape of the χ^2 distribution, although there is an excess of points near the best fit and a deficit of points in the region of low likelihood.

In order to understand how each parameter affects the prediction of the likelihood, we use the SHAP values. Table 7.3 contains an example of the SHAP values for $\log L$ at the best fit point. According to the Machine Learning model, the values of C and α^ℓ and β^q have the larger impact in the Machine Learning prediction.

Figure 7.8 shows the impact of each parameter to the final prediction, measured as the mean of the absolute values of their SHAP values across a sample of 1000 Montecarlo points.The SHAP values allow us to quantify the relative importance of each parameter in the fit. The parameters β^q and α^ℓ have the largest contribution and β^ℓ and C contribute the less. This results is in disagreement with the assumption of Scenario I. Therefore, the obtained result is in agreement with the previous section, where we already concluded that the mixing with the first generation were necessary in order to describe both anoma-

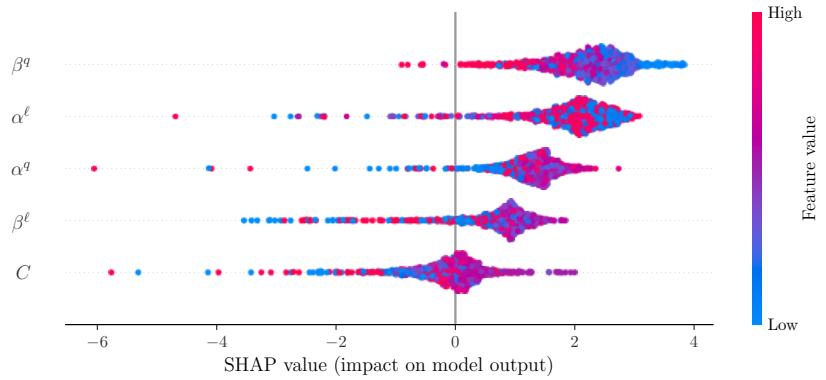

Figure 7.8: Distribution of the SHAP values for each parameter in a sample of 1000 generated points.

lies simultaneously.

We calculate the SHAP values for the logarithm of the likelihood at each point of the Montecarlo sample. In this way, we can determine how each parameter contributes to the fit, as shown in Figure 7.9. We can compare these SHAP values with Figure 7.4, where only one parameter was changed at a time. We can conclude that the SHAP values reproduce correctly the general features of the fit.

The above results show that the Machine Learning Montecarlo algorithm can be very useful in this kind of analysis, being able to reproduce the results obtained in the previous section in a shorter time. We can conclude that the machine learning, made jointly with the SHAP values, constitute a suitable strategy to use in complex fitting problems with large dimensionalities and complicated constraints, where a direct evaluation is too time-consuming.

In order to check our Machine Learning procedure, we now discuss on the agreement of the results obtained by the Machine Learning Montecarlo algorithm that we have proposed and the ones obtained by using the RG equations defined as given in Section 7.2.

The Lagrangian in Eq. (7.10) exhibit a flavour structure, given by the λ matrices, relating the different entries of the tensor of Wilson coefficients $C_{\ell q}^{ijkl}$. Under the RG evolution and matching, this flavour structure is imprinted in the WET Lagrangian in Eq. (3.42) and (3.48), and therefore in the related observables. Using the Machine Learning Montecarlo algorithm described in the previous section, we generate a sample of 1000 points in parameter space around the best fit point. In each point we run the RG equations down to the electroweak scale, perform the matching with the WET, and run the RG equations again down to $\mu = m_b$. We compute the correlations between the semileptonic $b \to s$ and $b \to c$ coefficients $C_9^{\ell\,\mathrm{NP}}$, $C_{10}^{\ell\,\mathrm{NP}}$, $C_{VL}^{\ell\,\mathrm{NP}}$ and C_ν^ℓ for the different lepton generations. Figure 7.10 shows the matrix of Pearson coefficients describing linear correlations between the WET Wilson Coefficients. In the electron sector, $C_{10}^{e\mathrm{NP}}$, $C_{VL}^{e\mathrm{NP}}$ and C_ν^e show strong correlations close to ± 1. In the muon sector, $C_{10}^{\mu\mathrm{NP}}$, $C_{VL}^{\mu\mathrm{NP}}$ and C_ν^μ are also correlated between

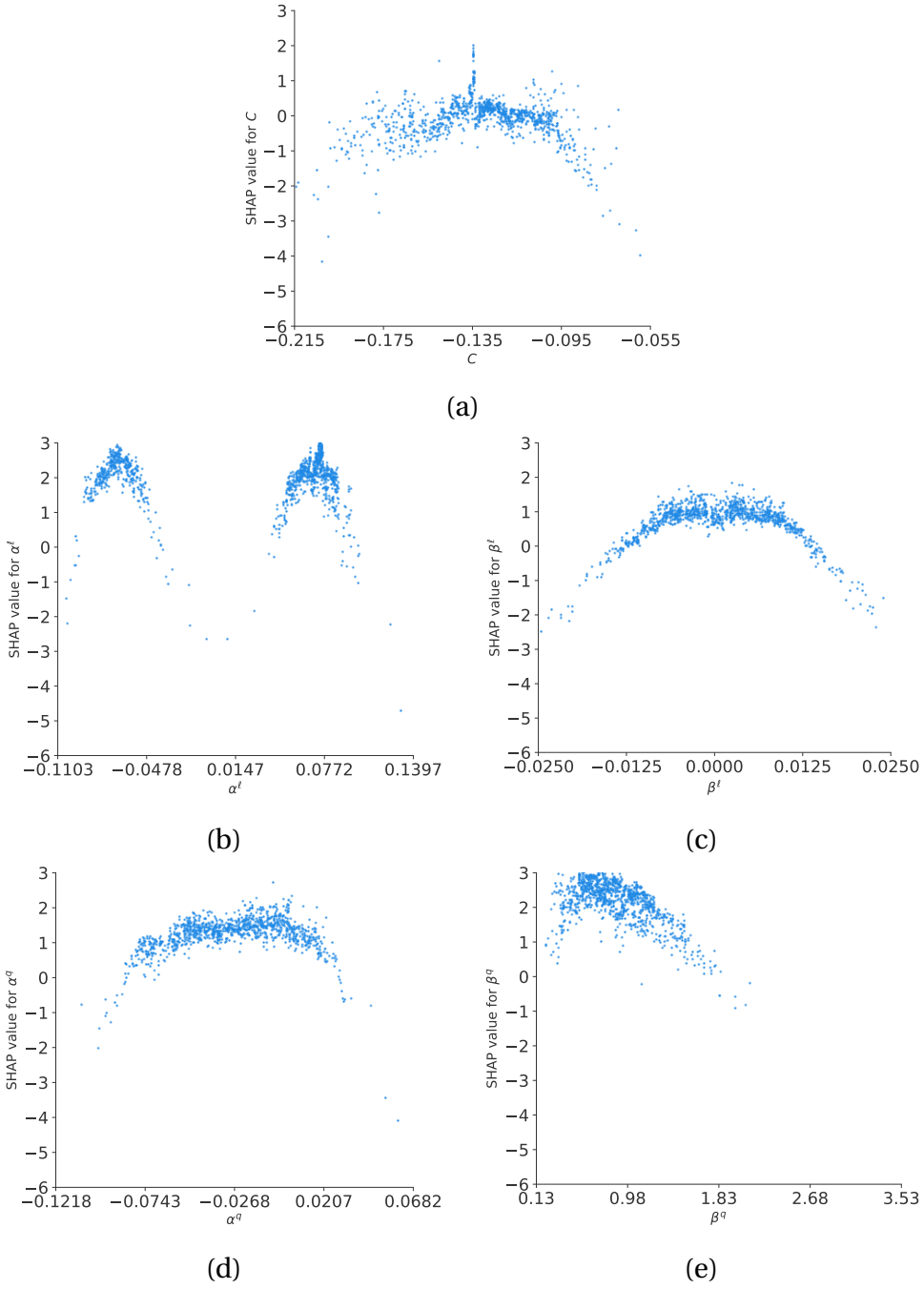

Figure 7.9: SHAP values for the parameters of the fit at the sample of 1000 generated points.

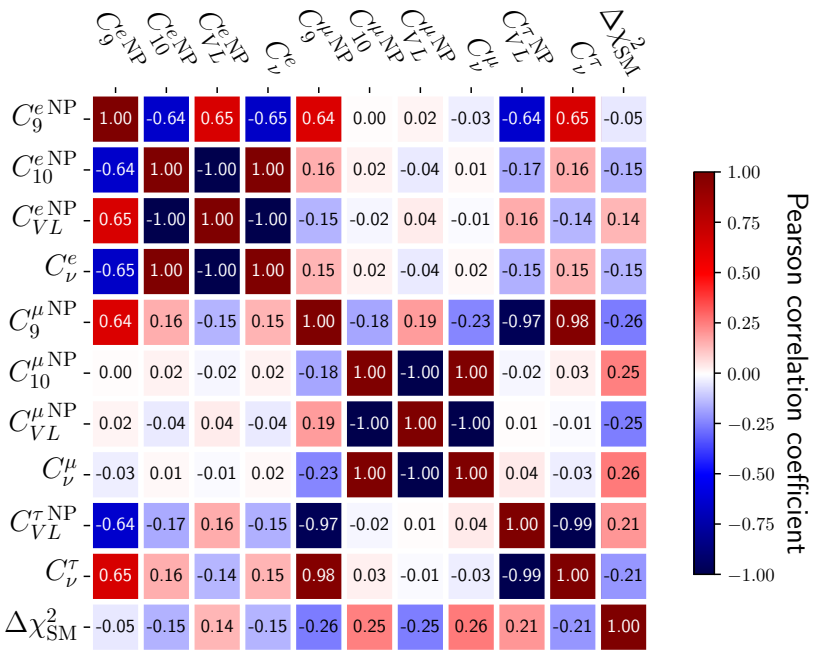

Figure 7.10: Matrix of Pearson correlation coefficients between semileptonic WET Wilson Coefficients in the sample of 1000 points in parameter space.

them, however they are linearly independent of $C_9^{\mu\mathrm{NP}}$. Instead, $C_9^{\mu\mathrm{NP}}$ is correlated with the tau coefficients $C_{VL}^{\tau\mathrm{NP}}$ and C_ν^τ, and to a lesser extent to $C_9^{e\mathrm{NP}}$.

The correlations that we have found are consistent with the results of RG evolution and matching in Eq. (7.11). In the case of the electron sector, the $C_{10}^{e\mathrm{NP}}$, $C_{VL}^{e\mathrm{NP}}$ and C_ν^e coefficients are all proportional to the product $C\lambda_{23}^q\lambda_{11}^\ell$ appearing in the tree-level contribution. Analogously in the muon sector $C_{10}^{\mu\mathrm{NP}}$, $C_{VL}^{\mu\mathrm{NP}}$ and C_ν^μ, depend on $C\lambda_{23}^q\lambda_{22}^\ell$ and in the tau sector $C_{VL}^{\tau\mathrm{NP}}$ and C_ν^τ depend on $C\lambda_{23}^q\lambda_{33}^\ell$. The coefficient $C_9^{\mu\mathrm{NP}}$ is not correlated to the rest of the muonic coefficients because it is dominated by the loop-level contribution C_9^{loop}, which depend on the product $C\lambda_{23}^q$. The coefficient $C_9^{e\mathrm{NP}}$ receives sizeable contributions both from the tree-level and the one-loop terms, and consequently shows a mild correlation with $C_9^{\mu\mathrm{NP}}$ and a total correlation with the combination $C_9^{\mu\mathrm{NP}} - C_{10}^{e\mathrm{NP}}$. Lastly, there is a perfect correlation of ± 1 between $C_9^{\mu\mathrm{NP}}$ and the tau coefficients, which is caused by the fact that $\lambda_{33}^l = 0.994 \pm 0.001$ is almost constant, so $C\lambda_{23}^q\lambda_{33}^l \approx C\lambda_{23}^q$. We can therefore conclude that the obtained data is in agreement with the arrangement of Wilson coefficients presented in Eq. (7.11).

Besides, in the same sample of 1000 points, we determine the predictions of our model for several selected observables of various flavour sectors, with large pull differences between the SM and Scenario II predictions: $R_{K^{*0}}^{[1.1,6]}$ (observable 12 in the table presented in Appendix C.2)), $\mathrm{BR}(B^+ \to K^+\nu\bar{\nu})$ (observable 89) and $\mathrm{BR}(B_s \to \mu^+\mu^-)$ (observable 39) from $b \to s$ decays, R_D^ℓ (observable 72) from $b \to c$ decays, $\mathrm{BR}(B^0 \to \mu^+\mu^-)$ (observable 258) from $b \to d$ decays, $\mathrm{BR}(K^+ \to \pi^+\mu^+\mu^-)$ (observable 394) from $s \to d$ decays that has a

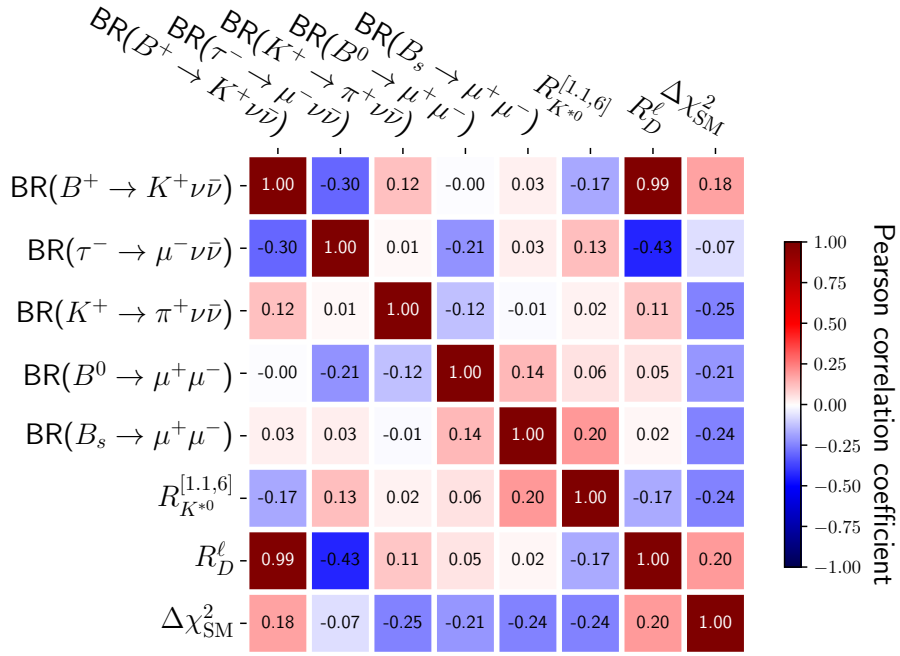

Figure 7.11: Matrix of Pearson correlation coefficients for selected observables in the 1000 points sample.

great impact in the fit value of α^q, and the tau decay BR($\tau^- \to \mu^-\nu\bar{\nu}$) (observable 38). The correlation matrices are depicted in Figure 7.11.

From the above results, it is clear that the observables $R^{\ell}_{D^*}$ and BR($B^+ \to K^+\nu\bar{\nu}$) show an almost-perfect correlation. Then, predictions for these two observables in the generated sample are shown in Figure 7.12. The green vertical band in this figure corresponds to the $R^{\ell}_{D^*}$ measurement [148], the red horizontal band to the 90% C.L. excluded region for BR($B \to K^*\nu\bar{\nu}$) [389] and the gray band to the 2021 world average obtained by Belle II [390]. The yellow horizontal band summarizes the SM prediction. The obtained values of Montecarlo points and the best fit prediction of our computations are also included. It is important to stress that $R^{\ell}_{D^*}$ depends on the Wilson coefficient $C^{\tau\,\mathrm{NP}}_{VL}$, and BR($B^+ \to K^+\nu\bar{\nu}$) on C^{τ}_{ν}, and both of them are proportional to the product $C\lambda^q_{23}\lambda^{\ell}_{33}$. This is in contrast with the conclusions of [391], where several leptoquark scenarios coupling to right-handed neutrinos did not find a significant correlation between both observables. Even if the correlation is strong, the prediction for the $B^+ \to K^+\nu\nu$ decay remains compatible with the 90% C.L., BR($B \to K^+\nu\nu$) $< 1.6 \times 10^{-5}$ [389], for the whole range of experimentally-compatible values of $R^{\ell}_{D^*}$. The world average for the branching ratio obtained by Belle II [390] (not included in our numerical analysis) shows an enhancement of a factor of 2.4 ± 0.9 compared to the SM prediction [391]. While our data is in tension with this world average, it is an encouraging sign of a possible interplay between $R_{D^{(*)}}$ and BR($B^+ \to K^+\nu\bar{\nu}$). Future experimental results from Belle II will further clarify the situation.

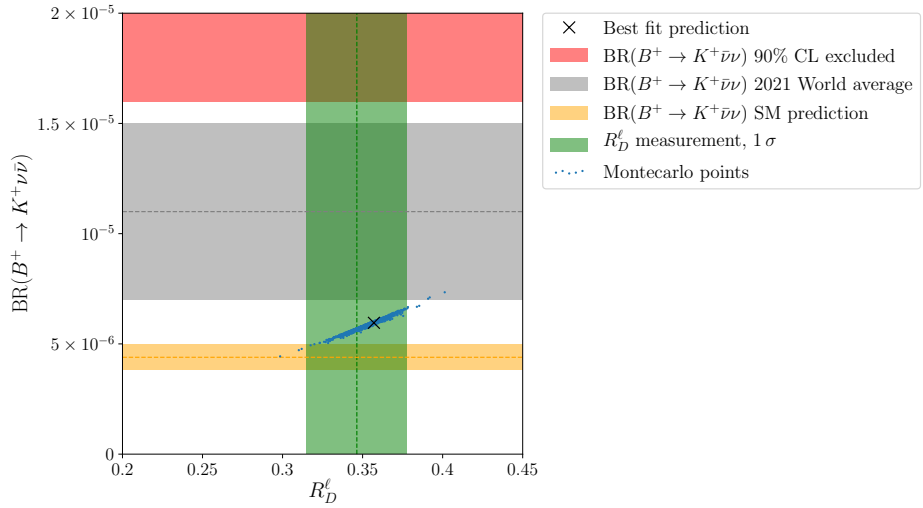

Figure 7.12: Predictions for the observables $R^\ell_{D^*}$ and BR($B^+ \to K^+\nu\bar{\nu}$) in the generated sample. The green vertical band corresponds to the $R^\ell_{D^*}$ [148] measurement, the red horizontal band to the 90% C.L. excluded region for BR($B \to K^*\nu\bar{\nu}$) [389], the grey band to the 2021 world average obtained by Belle II [390] and the yellow horizontal band to its SM prediction.

It is worth stressing that the observable $R_{K^{*0}}$ displays a moderate correlation with $R^\ell_{D^*}$ and BR($B^+ \to K^+\nu\bar{\nu}$), caused by the relation of the Wilson coefficient $C_9^{\mu\,\mathrm{NP}}$ with C^τ_{VL} and C^τ_ν. On the other hand, $R_{K^{*0}}$ shows a mild correlation to BR($B_s \to \mu^+\mu^-$), even though both observables depend on $C_{10}^{\mu\,\mathrm{NP}}$. This is a result that sets us apart from many NP models that impose the relation $C_9^{\mu\,\mathrm{NP}} = -C_{10}^{\mu\,\mathrm{NP}}$, in which case the correlation would be stronger.

Finally, none of the selected observables display a large correlation to the goodness of fit measured by $\Delta\chi^2$. This is a sign that there is not a single observable dominating the fit, and reaffirms that global fits are in fact a necessity on the analysis of flavour anomalies.

7.5 Connection to leptoquark models

In this section we discuss the phenomenological implications of our assumptions in the vector leptoquark model. The goal is to check the compatibility of the leptoquarks with our assumptions and the experimental data, but we do not seek to impose new bounds on their scale.

The vector leptoquark $U_1 \sim (\bar{\mathbf{3}}, \mathbf{1}, 2/3)$ couples to left-handed and right-handed fermions, with an interaction Lagrangian included in Table 4.2. An U_1 leptoquark with mass M_U, when matched with the SMEFT at the scale Λ, contributes to the Wilson coefficients $C_{\ell q(1)}$, $C_{\ell q(3)}$, C_{ed}^{ijkl} and C_{ledq}^{ijkl}. The matching conditions to these operators are indicated in Eq. (4.1). This matching is performed at the scale of M_U, as indicated in Fig. 3.4.

Our model does not include couplings to right-handed leptons in the interaction Lagrangian, and therefore all the x_R couplings are set to zero. The left-handed couplings x_L

are related to the parameters of the Lagrangian in Eq. (7.10) according to

$$|(x_1^{LL})_{ji}|^2 = -\frac{2M_U^2}{\Lambda^2} C \lambda^{\ell}_{ii} \lambda^{q}_{jj}\,,$$
$$\mathrm{Arg}((x_1^{LL})_{ji}) = \mathrm{Arg}(\lambda^{q}_{j3}) - \mathrm{Arg}(\lambda^{\ell}_{i3}) + \theta\,, \tag{7.24}$$

where θ is a free global complex phase. Since the flavour matrices λ are hermitian (λ^{ℓ}_{ii} and λ^{q}_{jj} are real and positive), we need $C_1 = C_3$ to be a real negative number. This condition is fulfilled in both Scenarios I and II.

Without loss of generality we set $\theta = 0$. The mass of the leptoquark is chosen to be $M_U = 1.5$ TeV, the lowest mass not excluded by direct searches [392]. The RG evolution from the scale of the matching $\mu = M_U = 1.5\,\mathrm{TeV}$ down to the scale $\mu = \Lambda = 1\,\mathrm{TeV}$ of the Wilson coefficients in the previous sections is negligible. Taking this into account, Eq. (7.24) provides a one to one correspondence between the flavour parameters in the Lagrangian of Eq. (7.10) and the leptoquark couplings to left-handed fermions. In the context of this work, the leptoquark only couples to the third generation fermions in its interaction basis, and the expression in Eq. (7.24) is the result of the rotation to the mass basis of quarks and leptons.

In particular, if we apply Eq. (7.24) to the results of the fit in Scenario I in Table 7.1, corresponding to an U_1 leptoquark interacting with the second and third generations of fermions in the mass basis, we obtain

$$x_1^{LL} = \begin{pmatrix} 0 & 0 & 0 \\ 0 & 1\times 10^{-14} & 0.495 \\ 0 & 1\times 10^{-14} & 0.586 \end{pmatrix}. \tag{7.25}$$

And if we apply Eq. (7.24) to the results of the fit in Scenario II in Table 7.1, corresponding to an U_1 leptoquark interacting with all three generations of fermions in the mass basis, we obtain

$$x_1^{LL} = \begin{pmatrix} -2.27\times 10^{-3} & -3.76\times 10^{-10} & -0.0325 \\ 0.0319 & 5.29\times 10^{-9} & 0.458 \\ 0.0437 & 7.25\times 10^{-9} & 0.627 \end{pmatrix}. \tag{7.26}$$

In both scenarios, the most important couplings are $(x_1^{LL})_{23}$ to second generation quarks and third generation leptons, and $(x_1^{LL})_{33}$ to third generation quarks and leptons. A similar leptoquark model has been proposed previously, as scenario RD2A in [393] as a solution for the $R_{D^{(*)}}$ anomaly. The advantage of our proposal is that the inclusion of small non-zero values of the couplings $(x_1^{LL})_{21}$ and $(x_1^{LL})_{31}$ is able to explain the $R_{K^{(*)}}$ anomalies at the same time. The values of $(x_1^{LL})_{23}$ and $(x_1^{LL})_{33}$ are compatible with the exclusion limits set in [393].

Other leptoquark models do not retain the $C_{\ell q(1)} = C_{\ell q(3)}$ condition [201, 259], and therefore produce large contributions to the $B \to K^{(*)}\nu\bar{\nu}$ decays. That is the case of the

scalar $S_3 = (\overline{\mathbf{3}}, \mathbf{3}, 1/3)$, that predicts $C_{\ell q(1)} = 3C_{\ell q(3)}$, and the vector $U_3 = (\overline{\mathbf{3}}, \mathbf{3}, 2/3)$, where $C_{\ell q(1)} = -3C_{\ell q(3)}$. The scalar $S_1 = (\overline{\mathbf{3}}, \mathbf{1}, 1/3)$ is even less suited, as it predicts $C_{\ell q(1)} = -C_{\ell q(3)}$, which would result in no NP contributing to $b \to s\ell^+\ell^-$ at all. New vector bosons W' and Z' would also be in conflict with the $B \to K^{(*)}\nu\bar{\nu}$ decays, as they predict $C_{\ell q(1)} = 0$ while $C_{\ell q(3)}$ has a non-zero value.

7.6 Conclusions

In this chapter, we present the results of the global fit to the flavour physics observables that exhibit some discrepancies with respect to the SM values, by considering the NP effects on the Wilson coefficients of the SMEFT Lagrangian. The global fit includes the $b \to s\mu^+\mu^-$ observables; i.e. the Lepton Flavour Universality ratios $R_{K^{(*)}}$, the angular observables P_5' and the branching ratio of $B_s \to \mu^+\mu^-$, as well as the $R_{D^{(*)}}$, $b \to s\nu\bar{\nu}$ and electroweak precision observables (W and Z decay widths and branching ratios to leptons). We choose two scenarios in which the condition $C_1 = C_3$ is imposed in order to avoid unwanted contributions to the $B \to K^{(*)}\nu\bar{\nu}$ decays. In Scenario I we fix parameters by assuming that the mixing in the first generation are negligible, as already considered in [202]. Scenario II includes non-negligible mixings to the first generation, allowing us to check the validity of the above assumption. We found that the better fit is obtained for Scenario II, with a pull of 7.08σ with respect to the Standard Model, 2.92σ with respect to Scenario I (Table 7.1). Simultaneous explanation of the $R_{K^{(*)}}$ and $R_{D^{(*)}}$ anomalies have been also found in Scenario II (Figure 7.2 and Table 7.2).

We show that the Gaussian approximation to characterize the fit is not successful (see Figure 7.1) and therefore, we use for the first time in the context of the so-called B anomalies a Machine-Learning Montecarlo analysis to extract the confidence intervals and correlations between observables. We found that our procedure reproduce the results obtained in Section 7.3 for both the $\Delta\chi^2$ distribution and the analysis of the impact of each parameter on the global fit. We also have checked the agreement between the results obtained by the Machine Learning Montecarlo algorithm proposed in this work and the ones obtained by following the RG equations. Therefore, we conclude that machine learning, jointly with the SHAP values, constitute a suitable strategy to use in this kind of analysis.

This is a promising area of study even if present uncertainties do not allow us to conclusively establish the presence of physics beyond the SM, and further analyses are needed. An observation of the $B^+ \to K^+\nu\bar{\nu}$ decay in the near future at Belle II could provide further insight in the $R_{K^{(*)}}$ and $R_{D^{(*)}}$ anomalies, especially if the excess in the current world average is confirmed. This, together with the expected improved measurements of the electroweak observables in the future linear colliders that we previously studied in [2, 3], underlines the fundamental role of global analyses and experimental precision in the quest for an explanation of the B anomalies.

Chapter 8

Leptonic Meson Decays into Invisible ALP

This Chapter is devoted to a phenomenological study of ALP models with generic flavour couplings to fermions. We only consider "invisible" ALP, that is, particles that evade direct detection because of either a long half-life or preferential decays into other "invisible" particles. The processes that we study are leptonic decays of mesons $M \to \ell \nu_\ell$, with $M = K, D, D_s, B$, that are expected to be sensitive to invisible particles with masses of hundreds of MeV, or even a few GeV. The analytical expressions for leptonic meson decays with the production of a massive ALP are derived and compared with the literature for the massless case. The expressions are used, together with experimental data, to obtain bounds for the couplings to the different flavours of quarks and leptons. Two methods to obtain the bounds are compared, one of them uses the full branching ratio and the other exploits the kinematical structure of a three-body decay by analyzing the differential decay rate.

This chapter is based on [6]. The work of this chapter was carried out during the stay at Università degli Studi di Padova, Italy.

8.1 Introduction

Light pseudo–scalar particles naturally arise in many extensions of NP, as they are a common feature of any model endowed with a global $U(1)_{PQ}$ symmetry spontaneously broken at a scale $f_a \gg v$. Small breaking terms of the global $U(1)_{PQ}$ symmetry are needed for providing a mass term, $m_a \ll f_a$, to the pNG. Sharing a common nature with the QCD axion [289–291], these class of pNGBs are generically dubbed as ALP. The key difference between the QCD axion and a generic ALP can be summarized in the fact that ALPs do not need to satisfy the well-known constraint [290], $m_a f_a \approx m_\pi f_\pi$, that bounds the QCD axion mass and the $U(1)_{PQ}$ symmetry breaking scale via QCD instanton effects. Therefore, in a generic ALP framework, one can assume the ALP mass being determined by some unspecified UV physics, and, consequently, m_a and f_a can be taken as independent pa-

rameters.

The ALP parameter space has been intensively explored in several terrestrial facilities, covering a wide energy range [394–403], as well as by many astrophysical and cosmological probes [404–408]. The synergy of these experimental searches allows to access several orders of magnitude in ALP masses and couplings, cf. e.g. Ref. [279] and references therein. While astrophysics and cosmology impose severe constraints on very light ALPs, the most efficient probes of weakly-coupled particles in the MeV-GeV range come from experiments acting on the precision frontier [409]. Fixed-target facilities such as E949 [410–412], NA62 [413, 414] and KOTO [415] and the proposed SHiP [416] and DUNE [417] experiments can be very efficient to constrain long-lived particles. Furthermore, the rich ongoing research program in the B physics experiments at LHCb [418, 419] and the B factories [420–428] offers several possibilities to probe ALP couplings in ALP mass regions not completely explored yet.

The main goal of this chapter is the detailed analysis of pseudo–scalar meson leptonic decays, $M \to \ell\, \nu_\ell\, a$, with an ALP escaping the detector or decaying into an "invisible" sector. These decay channels were previously analyzed in [302] for a massless ALP and for a universal ALP–fermion coupling. Here, a generic ALP mass and generic, yet flavour–conserving, ALP couplings are going to be considered. Moreover, a factor 2 misprint in Eq. (15) of [302] (and equivalently a factor 4 misprint in the hadronic contribution of Eq. (17) of [302]) is going to be corrected.

8.2 Leptonic Meson Decays in ALP

The most general effective Lagrangian describing ALP interactions with SM fermions, including operators up to dimension five and assuming flavor conserving couplings reads:

$$\delta\mathscr{L}^{a}_{\text{eff}} = -\frac{\partial_\mu a}{2f_a}\sum_i c_i\,\overline{f}_i\gamma^\mu\gamma_5 f_i = i\frac{a}{f_a}\sum_{i=fer} c_i\, m_i\,\overline{f}_i\gamma_5 f_i\,. \tag{8.1}$$

The Lagrangian in Eq. (8.1) depends only on nine independent flavor diagonal couplings, c_i, one for each massive fermion $f_i = \{u,d,c,s,t,b,e,\mu,\tau\}$, once fermionic vector–current conservation and massless neutrinos are implied. It might be useful, for simplifying intermediate calculations, and explicitly showing the mass dependence of ALP-fermion couplings, to write the effective Lagrangian in the "Yukawa" basis instead of the "derivative" one. The two versions of the effective Lagrangian in Eq. (8.1) are equivalent up to operators of $O(1/f_a^2)$.

Using the effective Lagrangian of Eq. (8.1) one can calculate the leptonic decay rates of pseudo–scalar mesons, $M \to \ell\, \nu_\ell\, a$, with the ALP sufficiently long-lived to escape the detector without decaying (or decaying into invisible channels). In such a case the only possible ALP signature is its missing energy/momentum. In the following, M_M and P_M will denote the mass and 4–momentum of the decaying meson, while leptons and ALP

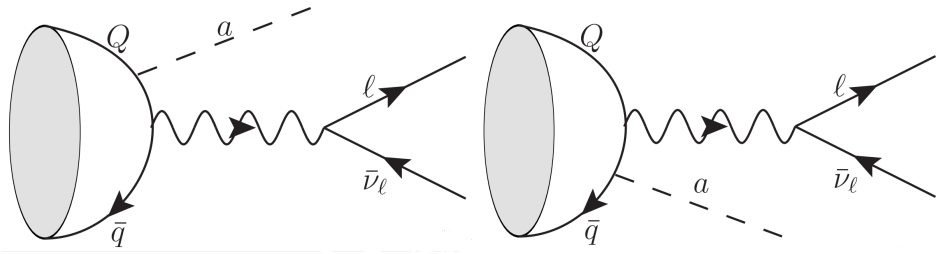

Figure 8.1: Tree level contributions to the $M \to \ell\, \nu_\ell\, a$ amplitude, with the ALP emitted from the M meson. The diagram where the ALP is emitted from the charged lepton is straightforward.

masses and 4–momenta will be indicated with m_ℓ, m_a, p_ℓ, p_ν and p_a respectively. Neutrinos will be assumed massless.

Charged pseudo-scalar meson decays proceed through the s–channel tree-level diagrams of Fig. 8.1, where only the diagrams where the ALP is emitted from the M–meson are shown. The diagram where the ALP is emitted from the charged lepton follow straightforwardly, while the one with the ALP emitted from the W^+ internal line automatically vanishes, being the W^+W^-–ALP coupling proportional to the fully antisymmetric 4D tensor. In the following, the derivation of the decay amplitude for the channel in which the ALP is emitted from the initial quarks or from the final charged lepton are discussed separately, as they need two different hadronization treatments.

8.2.1 Hadronic ALP Emission

The two diagrams depicted in Fig. 8.1 represent the contributions to the $M \to \ell\, \nu_\ell\, a$ decay in which the parent meson constituent quarks emit the ALP and then annihilate into a virtual W boson, producing the final leptons. One refers to this case as hadronic ALP emission. The corresponding amplitude [1] can be written as:

$$\mathcal{M}_h = \langle 0|\, \bar{q}\Gamma_h^\mu Q\, |M\rangle \left(\bar{\ell}\gamma_\mu P_L \nu_\ell\right), \tag{8.2}$$

with Γ_h^μ given by

$$\Gamma_h^\mu = -\frac{4G_F}{\sqrt{2}} V_{qQ} \left(\frac{c_q m_q}{f_a} \gamma^\mu P_L \frac{\not{p}_a - \not{p}_q + m_q}{m_a^2 - 2p_a\cdot p_q}\gamma_5 - \frac{c_Q m_Q}{f_a}\gamma_5 \frac{\not{p}_a - \not{p}_q - m_Q}{m_a^2 - 2p_a\cdot p_Q}\gamma^\mu P_L \right). \tag{8.3}$$

In Eq. (8.3) p_q and p_Q are the initial quarks momenta, with c_q and c_Q the corresponding ALP-fermion couplings.

The calculation of the $\langle 0|\, \bar{Q}\Gamma_h^\mu q\, |M\rangle$ hadronic matrix element in Eq. (8.2) is complicated by the fact that the meson is a bound state of quarks and one must assume a model to describe the effective quark-antiquark momenta distribution. This can be done following the Lepage–Brodsky technique [429, 430]. In the case of a massless ALP and universal ALP-fermion couplings this amplitude have been firstly derived in [302].

[1] For definiteness, the leptonic current is written assuming a negative charged meson $M = \bar{q}Q$ state, being q a light up-type quark and Q an heavy down-type one.

Following [302, 429, 430], the ground state of a meson M is parameterized with the wave–function

$$\Psi_M(x) = \frac{1}{4}\phi_M(x)\gamma^5(\not{P}_M + g_M(x)M_M). \tag{8.4}$$

In Eq. (8.4), with x one typically denotes the fraction of the momentum carried by the heaviest quark in the meson. The function $\phi_M(x)$ describes the meson's quark momenta distribution, that for heavy and light mesons reads, respectively:

$$\phi_H(x) \propto \left[\frac{\xi^2}{1-x} + \frac{1}{x} - 1\right]^{-2}, \qquad \phi_L(x) \propto x(1-x), \tag{8.5}$$

with the normalization fixed such that:

$$\int_0^1 dx\,\phi_M(x) = 1. \tag{8.6}$$

The parameter ξ in $\phi_H(x)$ is a small parameter typically of $O(m_q/m_Q)$, being q and Q the light and heavy quark in the meson. The mass function $g_M(x)$ is usually taken to be a constant varying from $g_H(x) \approx 1$ and $g_L(x) \ll 1$ for a heavy or a light meson. The hadronic matrix element can then be obtained by integrating, over the momentum fraction x, the trace of the Γ^μ amplitude multiplied by the meson wave–function $\Psi_M(x)$:

$$\langle 0|\,\bar{q}\Gamma^\mu Q\,|M\rangle \equiv i f_M \int_0^1 dx\,\mathrm{Tr}\left[\Gamma^\mu \Psi_M(x)\right], \tag{8.7}$$

with the meson decay constants f_M defined as:

$$\langle 0|\,\bar{q}\gamma^\mu\gamma_5 Q\,|M\rangle = i f_M P_M^\mu. \tag{8.8}$$

In Eqs. (8.4–8.7), a slightly different notation with respect to the referred literature is used. In particular the functions $\phi_M(x)$ have been normalized to one, in such a way that in Eq. (8.7) the mesonic form factor can be explicitly factorized.

Inserting Eq. (8.3) and Eq. (8.4) into Eq. (8.7), and defining the initial quark momenta as:

$$p_q = (1-x)P_M, \qquad p_Q = xP_M, \tag{8.9}$$

one obtains the following decay amplitudes for the meson ALP–emission process:

$$\mathscr{M}_h = \frac{4iG_F V_{qQ}}{\sqrt{2}}\frac{f_M}{f_a}\frac{M_M^2}{2p_a\cdot P_M}\left[c_Q\frac{m_Q}{M_M}\Phi_M^{(Q)}(m_a^2) - c_q\frac{m_q}{M_M}\Phi_M^{(q)}(m_a^2)\right](\bar{\ell}\,\not{p}_a P_L \nu_\ell), \tag{8.10}$$

where the functions $\Phi_M^{(q,Q)}(m_a^2)$ contain the integrals over the quark momentum fraction and are defined respectively as:

$$\begin{aligned}\Phi_M^{(q)}(m_a^2) &= \int_0^{1-\delta_M} \frac{p_a\cdot P_M}{m_a^2 - 2(1-x)p_a\cdot P_M}\phi_M(x)g_M(x)\,dx,\\ \Phi_M^{(Q)}(m_a^2) &= \int_{\delta_M}^1 \frac{p_a\cdot P_M}{m_a^2 - 2x\,p_a\cdot P_M}\phi_M(x)g_M(x)\,dx.\end{aligned} \tag{8.11}$$

The presence of the kinematical cutoff $\delta_M = m_a/(2M_M)$ prevents the appearance of unphysical bare singularities.

One can check the calculation done in Ref. [302] by taking the $m_a = 0$ limit in Eq. (8.10) and by setting $c_q = c_Q = 2$, as demanded by the different normalization of the corresponding ALP-fermion couplings introduced in the effective Lagrangians. Notice that

$$\left[\frac{m_b}{M_B}\Phi_B^{(b)}(0) - \frac{m_u}{M_B}\Phi_B^{(u)}(0)\right] = 2\sqrt{6}\Phi(m_b, M_B)\,, \tag{8.12}$$

with $\Phi(m_b, M_B)$ the integral defined in Ref. [302]. Doing all these replacements one realizes that Eq. (15) of Ref. [302] is wrong and 1/2 of the result obtained from Eq. (8.10).

8.2.2 Leptonic ALP Emission

The leptonic decay amplitude for the lepton ALP–emission process can be easily obtained by using the definition of the meson form factors of Eq. (8.8), giving

$$\mathscr{M}_\ell = \langle 0|\,\bar{q}\gamma_\mu P_L Q\,|M\rangle\left(\bar{\ell}\Gamma_\ell^\mu \nu_\ell\right), \tag{8.13}$$

with

$$\Gamma_\ell^\mu = -\frac{4G_F}{\sqrt{2}}V_{qQ}\left(\frac{c_\ell m_\ell}{f_a}\gamma_5\frac{\not{p}_a + \not{p}_\ell + m_\ell}{m_a^2 + 2p_a\cdot p_\ell}\gamma^\mu P_L\right). \tag{8.14}$$

In Eq. (8.14) p_ℓ dubs the momentum of the final charged lepton. By making use of all the Dirac matrices relations one obtains:

$$\mathscr{M}_\ell = -\frac{4iG_F}{\sqrt{2}}V_{qQ}\frac{f_M}{f_a}\left[c_\ell m_\ell\left(\bar{\ell}P_L\nu_\ell\right) - \frac{c_\ell m_\ell^2}{m_a^2 + 2\,p_a\cdot p_\ell}\left(\bar{\ell}\,\not{p}_a P_L\nu_\ell\right)\right]. \tag{8.15}$$

From Eq. (8.15), by setting $m_a = 0$ and $c_\ell = 2$ one recovers correctly the result in Eq. (7) of Ref. [302].

8.2.3 Differential Decay Rate

For the 3-body decay at hand, and assuming a massless neutrino, one can define the following Mandelstam variables:

$$\begin{aligned} s &= (P_M - p_\ell)^2 = (p_\nu + p_a)^2 = M_M^2 + m_\ell^2 - 2M_M\omega_\ell\,,\\ t &= (P_M - p_\nu)^2 = (p_\ell + p_a)^2 = M_M^2 - 2M_M\omega_\nu\,,\\ u &= (P_M - p_a)^2 = (p_\ell + p_\nu)^2 = M_M^2 + m_a^2 - 2M_M\omega_a\,, \end{aligned} \tag{8.16}$$

with the energy conservation providing the identity:

$$s + t + u = M_M^2 + m_\ell^2 + m_a^2\,. \tag{8.17}$$

The differential 3-body decay rate of any scalar particle in its rest frame can be simply written as function of two independent final energies ω_i, or equivalently of the two independent Mandelstam variables, as

$$(d\Gamma_M)_{RF} = \frac{1}{(2\pi)^3}\frac{1}{8M_M}|\overline{\mathscr{M}_M}|^2\,d\omega_e\,d\omega_a = \frac{1}{(2\pi)^3}\frac{1}{32M_M^3}|\overline{\mathscr{M}_M}|^2\,ds\,du\,, \tag{8.18}$$

with $\mathscr{M}_M = \mathscr{M}_\ell + \mathscr{M}_h$. The Feynman amplitude squared reads:

$$|\overline{\mathscr{M}_\ell}|^2 = C_M c_\ell^2 \frac{m_\ell^2}{M_M^2}\left\{\frac{p_\ell\cdot p_\nu}{M_M^2} + \frac{m_\ell^2}{M_M^2}\left(\frac{p_a\cdot p_\nu}{m_a^2+2\,p_a\cdot p_\ell} + m_a^2\frac{p_\ell\cdot(p_a+p_\nu)}{(m_a^2+2p_a\cdot p_\ell)^2}\right)\right\}, \tag{8.19}$$

$$|\overline{\mathscr{M}_h}|^2 = C_M\left[c_Q\frac{m_Q}{M_M}\Phi_M^{(Q)}(m_a^2) - c_q\frac{m_q}{M_M}\Phi_M^{(q)}(m_a^2)\right]^2\frac{2(p_a\cdot p_\ell)(p_a\cdot p_\nu) - m_a^2 p_\ell\cdot p_\nu}{(p_a\cdot P_M)^2}, \tag{8.20}$$

$$\overline{\mathscr{M}_h\mathscr{M}_\ell^*} = C_M c_\ell\frac{m_\ell^2}{M_M^2}\left[c_Q\frac{m_Q}{M_M}\Phi_M^{(Q)}(m_a^2) - c_q\frac{m_q}{M_M}\Phi_M^{(q)}(m_a^2)\right]\frac{m_a^2(p_a\cdot p_\nu + p_\ell\cdot p_\nu)}{(m_a^2+2p_a\cdot p_\ell)(p_a\cdot P_M)}, \tag{8.21}$$

with the overall constant factor defined as:

$$C_M = 4G_F^2|V_{qQ}|^2 M_M^4\frac{f_M^2}{f_a^2}. \tag{8.22}$$

One can notice from Eq. (8.21), that the mixed product is proportional both to the ALP and the charged lepton masses and, consequently, can be neglected either for a massless ALP or for meson decays to a light charged lepton.

The total decay rate, for a general ALP mass, can be obtained by numerically integrating the differential decay rate of Eq. (8.18) in the kinematically allowed region. On the other hand, the massless ALP limit can be easily integrated analytically. By setting $m_a = 0$ one obtains:

$$\begin{aligned}\Gamma_{M\to\ell\nu_\ell a} = \frac{G_F^2|V_{qQ}|^2 M_M^5}{384\pi^2}\frac{f_M^2}{f_a^2}\Big\{&c_\ell^2\left(2\rho^2+3\rho^4+12\rho^4\log\rho-6\rho^6+\rho^8\right)+\\ &+\left[\frac{c_Q m_Q}{M_M}\Phi_M^{(Q)}(0) - \frac{c_q m_q}{M_M}\Phi_M^{(q)}(0)\right]^2\left(1-6\rho^2-12\rho^4\log\rho+3\rho^4+2\rho^6\right)\Big\}.\end{aligned} \tag{8.23}$$

For $c_\ell = c_q = c_Q = 2$ one recovers an agreement with the leptonic part of the decay rate in Eq. (17) of Ref. [302], while the hadronic part is wrong and 1/4 of the result in Eq. (8.23), consistently with what obtained from the Feynman amplitude check.

8.3 Bounds on ALP-fermion couplings

Pseudo–scalar leptonic decay experiments can be used to constraint flavour–diagonal ALP-fermion couplings of Eq. (8.1) via the ALP (invisible) decay rate derived in the previous section. Leptonic B decays have been measured at B factories, latest Belle data for electron, muon and tau channel can be found in [431–433], respectively. Charmed meson decays have been measured at BESS (see [434–436] for D and [437, 438] for D_s decays respectively) and at Belle [439]. Leptonic kaon decays have been measured by KLOE and NA62 [37, 440, 441]. In Tab. 8.1 available experimental determinations for the leptonic pseudo–scalar decay branching ratios are summarized and the lowest order SM predictions are shown for comparison.

The main assumption underlying the following phenomenological analysis is that the ALP lifetime is sufficiently long to escape the detector (i.e. $\tau_a \gtrsim 100$ ps) or alternatively that the ALP is mainly decaying into a, not better specified, invisible sector. In both cases,

Channel	SM Branching Ratio	Experiment	Ref.
$B^\pm \to e^\pm \bar{\nu}_e$	8.37×10^{-12}	$< 9.8 \times 10^{-7}$	[431]
$B^\pm \to \mu^\pm \bar{\nu}_\mu$	3.57×10^{-7}	$(5.3 \pm 2 \pm 0.9) \times 10^{-7}$	[432]
$B^\pm \to \tau^\pm \bar{\nu}_\tau$	7.95×10^{-5}	$(7.2 \pm 2.7 \pm 1.1) \times 10^{-5}$	[433]
$D^\pm \to e^\pm \bar{\nu}_e$	9.51×10^{-9}	$< 8.8 \times 10^{-6}$	[434]
$D^\pm \to \mu^\pm \bar{\nu}_\mu$	4.04×10^{-4}	$(3.71 \pm 0.19 \pm 0.06) \times 10^{-4}$	[435]
$D^\pm \to \tau^\pm \bar{\nu}_\tau$	1.08×10^{-3}	$(1.2 \pm 0.24 \pm 0.12) \times 10^{-3}$	[438]
$D_s^\pm \to e^\pm \bar{\nu}_e$	1.24×10^{-7}	$< 8.3 \times 10^{-5}$	[439]
$D_s^\pm \to \mu^\pm \bar{\nu}_\mu$	5.28×10^{-3}	$(5.49 \pm 0.17) \times 10^{-3}$	[436]
$D_s^\pm \to \tau^\pm \bar{\nu}_\tau$	5.15×10^{-2}	$(4.83 \pm 0.65 \pm 0.26) \times 10^{-2}$	[437]
$K^\pm \to e^\pm \bar{\nu}_e$	1.62×10^{-5}	$(1.582 \pm 0.007) \times 10^{-5}$	[37]
$K^\pm \to \mu^\pm \bar{\nu}_\mu$	0.629	0.6356 ± 0.0011	[37]

Table 8.1: Lowest order SM predictions and experimental constraints on the considered $M \to \ell\nu$ decay branching ratios.

the ALP signature is a missing energy/momentum, just as for neutrinos. In this scenario, the simplest way to constrain ALP–fermion couplings is then to saturate the 1σ experimental limits on the corresponding leptonic branching ratio adding the leptonic ALP decay to the leptonic SM amplitude. No kinematical constraint (2-body vs 3-body decay) is used in the analysis at this stage.

The derived bounds on the $U(1)_{PQ}$ breaking scale f_a are shown in Tab. 8.2. These values have been obtained by setting the relevant ALP-fermion coupling to one, with all the others vanishing. The results are provided for two reference values of the ALP mass $m_a = 0$ GeV and $m_a = M_M/2$ GeV, showing the variability range that should be expected for a massive vs (almost) massless ALP. As an example, the first row in Tab. 8.2 should be read as follows: the "up–quark" columns represent the f_a limits obtained by setting $c_u = 1$ and $c_b = c_e = 0$ for the two reference values of m_a, the "down–quark" columns represent the limits obtained by setting $c_b = 1$ and $c_u = c_e = 0$, and finally the values in the "lepton" columns are obtained by setting $c_e = 1$ and $c_u = c_b = 0$.

For heavy pseudo–scalar mesons, such as B, D and D_s, the formulas described in Section 8.2 are straightforward. These mesons are very well described by the heavy wave function $\phi_H(x)$ in Eq. (8.5), with $g_M = 1$. Constituent quark masses should be used for partons, instead of bare masses, i.e. $M_M = \hat{m}_Q + \hat{m}_q$ (being $\hat{m}_Q \approx m_Q$) with Q and q the heavy and light quark in the meson, respectively. The kaon sector is more delicate as kaons cannot be treated fully consistently neither as heavy or as light mesons [442]. Therefore, as the Kaon mass is not too far from Λ_{QCD}, the Brodsky–Lepage method introduces larger hadronic uncertainties compared to the heavy mesons case. Here, conservatively, the

Channel	f_a [MeV] up-quark		f_a [MeV] down-quark		f_a [MeV] lepton	
	$m_a = 0$	$m_a = M_M/2$	$m_a = 0$	$m_a = M_M/2$	$m_a = 0$	$m_a = M_M/2$
$B^\pm \to e^\pm \bar{\nu}_e$	2849	79	3918	1294	0.50	0.13
$B^\pm \to \mu^\pm \bar{\nu}_\mu$	6016	167	8274	2723	218	59
$B^\pm \to \tau^\pm \bar{\nu}_\tau$	380	6	522	65	200	55
$D^\pm \to e^\pm \bar{\nu}_e$	5960	2130	5688	858	1.99	0.53
$D^\pm \to \mu^\pm \bar{\nu}_\mu$	3923	1370	3744	559	267	70
$D^\pm \to \tau^\pm \bar{\nu}_\tau$	7		7		6	
$D_s^\pm \to e^\pm \bar{\nu}_e$	7921	2939	8236	1870	2.47	0.66
$D_s^\pm \to \mu^\pm \bar{\nu}_\mu$	5487	1995	5706	1284	349	92
$D_s^\pm \to \tau^\pm \bar{\nu}_\tau$	21		12		17	
$K^\pm \to e^\pm \bar{\nu}_e$	249144	87087	169804	10176	243	65
$K^\pm \to \mu^\pm \bar{\nu}_\mu$	1744	497	1188	47	321	60

Table 8.2: Limits on the $U(1)_{PQ}$ scale f_a derived from leptonic pseudo–scalar meson decays, setting the relevant ALP-fermion coupling equal to one, with all the other couplings vanishing.

heavy meson wave–function is used [2], with $g_K = 1$ and the partonic masses defined as $\hat{m}_u = m_u + \Lambda$ and $\hat{m}_s = m_s + \Lambda$ with $\Lambda = (M_K - m_u - m_s)/2$ a parameter of order Λ_{QCD}. Different choices for g_K, lead to different limits on f_a that can obtained by a simple rescaling of the ones shown in the last two rows of Tab. 8.2, i.e. $f_a' = g_K f_a$. Therefore, smaller values for g_K result in less stringent bounds for the $U(1)_{PQ}$ scale.

One can immediately realize that the f_a bounds shown in Tab. 8.2 from up-type and down-type ALP-quark sectors are far from being competitive with the ones derived from FCNC processes, like $K \to \pi\, a$ or $B \to K\, a$. For example, from [427], one can infer a limit $f_a \gtrsim 10^9$ MeV stemming from the top-enhanced penguin contribution, assuming $c_t = 1$. Tree–level diagram contributions to FCNC processes can provide constraints on lighter quark sectors [403], giving limits on f_a in the range $f_a \gtrsim 10^6 - 10^7$ MeV. From $Y(ns)$ decays on can obtain a constraint of the same order for the bottom sector [428]. The only pseudo–scalar meson leptonic channel that provide almost comparable bounds on the quark sector is the $K^\pm \to e^\pm \bar{\nu}_e$ decay, while most the other pseudo–scalar leptonic decays provide limits in the ballpark $f_a \gtrsim 10^3 - 10^4$ MeV for the light lepton decays and $f_a \gtrsim 10^1 - 10^2$ MeV for the τ ones.

Nonetheless, pseudo–scalar meson leptonic decays can be still very useful, as they provide the best present limits on the ALP–lepton sector for an ALP with m_a in the (sub)–GeV range, bounding $f_a \gtrsim 10^2 - 10^3$ MeV for most of the available channels. Typically,

[2] Using the heavy meson wave–function $\phi_H(x)$ one obtains a decay amplitude roughly 2/3 of one obtained using the light meson wave–function, $\phi_L(x)$. A detailed analysis of the hadronic uncertainties for K decays can be found in [403].

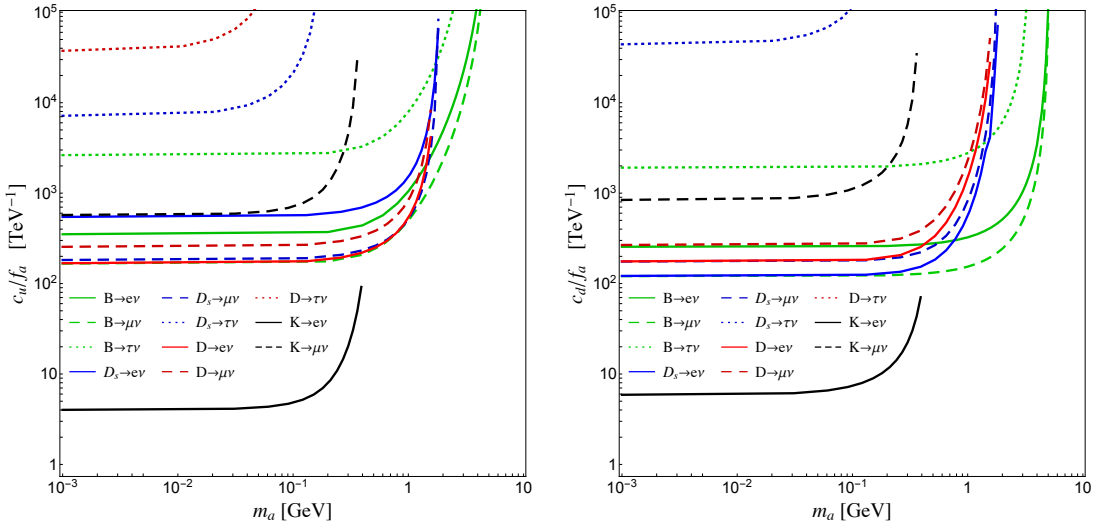

(a) (b)

Figure 8.2: Limits on the coupling (a) c_u/f_a and (b) c_d/f_a derived from the leptonic meson decay indicated in the legend, as function of the ALP mass m_a.

the muon sector gives better limits on f_a as it combines experimental data with relatively smaller errors and a not too large lepton mass suppression of the amplitude in Eq. (8.19). The electron sector suffers from a larger mass suppression and typically provides bounds on $f_a \gtrsim 10^5 - 10^6$ MeV, with the only exception of the $K^\pm \to e^\pm \bar{\nu}_e$ channel benefiting from its highly precise determination [3]. Furthermore, in this ALP mass range, the results presented here on the electron coupling c_e can be complementary with present and future ALP-Dark Matter searches like EDELWEISS [443] and LDMX [444] and reactor searches at CONNIE, CONUS, MINE, and ν-cleus [445].

The same information can be visually obtained from the plots in Fig. 8.2 and Fig. 8.3, where the dependence of the c_i/f_a bounds on the ALP mass is shown for the ALP couplings to up-type and down-type quarks (Fig. 8.2 (a) and Fig. 8.2 (b) respectively) and for the ALP couplings to charged leptons (Fig. 8.3 (a)). As previously noticed, the $K^\pm \to e^\pm \bar{\nu}_e$ channel is the most promising one, putting bounds on $c_{u,s}/f_a \lesssim 5$ TeV^{-1}, while most of the other channels are providing limits $c_{u,c,s,b}/f_a \lesssim 10^2 - 10^3$ TeV^{-1}, still far from the perturbativity region for $f_a = 1$ TeV. Concerning the ALP-charged lepton coupling notice that the best limits come form μ decay channels, bounding $c_\mu/f_a \lesssim 10^3 - 10^4$ TeV^{-1}. Measures of c_τ are still limited by worse experimental resolution providing bounds $c_\tau/f_a \lesssim 10^5$ TeV^{-1}. Sensitivity to the ALP-electron coupling c_e is obviously suppressed by the tiny electron mass giving $c_e/f_a \lesssim 10^6 - 10^7$ TeV^{-1}.

The results presented here represent an improvement of at least one order of magnitude compared with limits obtained in Tab. III of [302]. Three main reasons can be

[3] Recall, however, that caution should be used when handling K data as a larger hadronic uncertainty has to be accounted for, unavoidably.

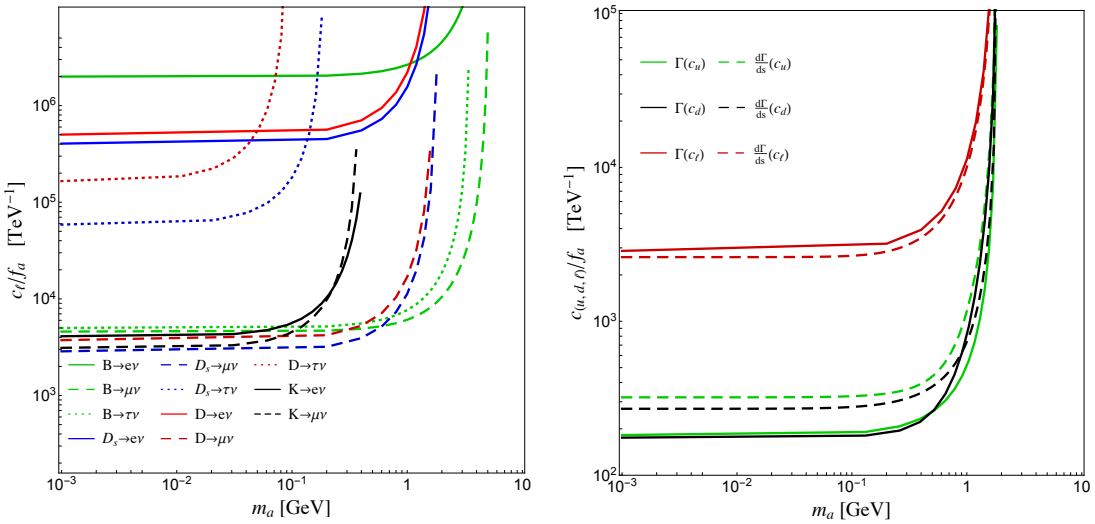

(a) (b)

Figure 8.3: Limits on the coupling c_ℓ/f_a (a) derived from the leptonic meson decays indicated in the legend, as function of the ALP mass m_a. Figure (b) shows the limits obtained on all the couplings from the analysis of the $D_s \to \mu\nu_\mu a$ decay using the experimental BR (full lined) and the missing mass distribution (dashed line).

advocated:

1. First of all, since the publishing of [302], experimental determination of pseudo–scalar leptonic decays has typically improved by roughly a factor ten, leading to more stringent bounds on f_a.

2. Moreover, one has to recall that the leading hadronic contribution in Eq. (17) of [302] underestimates by 1/4 the ALP branching ratio, resulting again in lower f_a bounds.

3. Finally, assuming a universal ALP-fermion coupling results in a parametric cancellation, clearly shown in Eq. (8.10) and Eq. (8.12) once $c_q = c_Q$ is assumed, causing a lost in sensitivity that numerically can be estimated in the 50%–70% range [4].

All the bounds shown up to now have been extracted using only information inferred from the total decay rate. One may think that stronger constraints should be derived from the differential decay rate $d\Gamma/d\omega_e$ (or equivalently $d\Gamma/ds$) obtained integrating Eq. (8.18) over the ALP energy ω_a (or over the Mandelstam variable u), thus exploiting the different leptonic energy distribution characterizing two–body vs three–body decays. The SM two-body decay distribution is peaked around vanishing missing mass $s = m_\nu^2 \approx 0$, and therefore any excess of events with $s > 0$ could be an indication of a three-body decay. Unfortunately this analysis cannot be performed for most of the decays under considerations as available public results lack of the needed information regarding signal and background differential distributions. However, as an example, in Fig. 8.3(b), the limit on

[4] A detailed and more qualitative discussion of this effect can be found in [403].

the c_i/f_a coefficients obtained from the differential decay rate analysis for the $D_s \to \mu\nu_\mu$ decay observed by BESIII [436] is shown. BESSIII collaboration provides data on missing mass distribution (i.e. s in our notation) only for $s < 0.2$ GeV^2, thus all limits for $m_a > 0.44$ have been obtained assuming a flat background distribution up to the kinematical allowed bound. For comparison, in the same plot, also the bounds from the branching ratio (solid lines) are reported. The analysis reported in Fig. 8.3(b) should be considered as a theoretical exercise, offering nevertheless an order of magnitude comparison between the two approaches, showing that at the moment no clear improvement is obtained adding spectral information. Having said that, a more serious effort could be done only having full access to all the experimental data of signal and background distributions, and is beyond the scope of this work.

8.4 Conclusions

A detailed analysis of the pseudo–scalar meson leptonic ALP decays, $M \to \ell\,\nu_\ell\,a$ has been presented. These decay channels were previously analyzed in Ref. [302] but only for a massless ALP and for a universal ALP–fermion coupling. Moreover, a factor 2 misprint in Eq. (15) of Ref. [302] (and equivalently a factor 4 misprint in the hadronic contribution of Eq. (17) of Ref. [302]) has been addressed.

Bounds on flavor diagonal ALP–fermion couplings are derived from the latest experimental limits on the corresponding leptonic decays. The stringent bounds on ALP-quarks couplings can be derived from the $K \to e\,\bar{\nu}_e\,a$ decay, with $c_{s,u}/f_a$ around 5 TeV^{-1}, barring large hadronic uncertainties. This bound is, however, still quite far from being competitive with the ones derived from the $K \to \pi\,a$ process (see for example [403] for a recent analysis). From heavier pseudo–scalar meson decay channels with a final electron o muon, one can derive bounds on ALP-quarks couplings, $c_q/f_a \gtrsim 10^2$ TeV^{-1}. Typically, less stringent bounds can be obtained from the tau channels, mainly due to larger experimental uncertainties.

Nevertheless, pseudo–scalars leptonic decays can provide the most stringent independent upper bounds on ALP–leptons couplings, for and ALP mass, m_a, in the (sub)–GeV range. From D_s and B muon and tau decays one derives limits on $c_{\mu,\tau}/f_a$ around 5×10^3 TeV^{-1}, in all the kinematically allowed m_a range. The most stringent limit on the ALP–electron coupling can be derived from the $K \to e\,\nu_e\,a$ decay, $c_e/f_a \lesssim 4 \times 10^3$ TeV^{-1}, for $m_a \lesssim 0.3$ GeV. For heavier ALP, D_s and B pseudo–scalar meson decays provide much softer bounds with $c_e/f_a \lesssim 10^6$ TeV^{-1}. Present bounds on ALP–electron couplings can be complementary to those obtained from ALP–Dark Matter searches [446].

Chapter 9

Conclusions

Along the pages of this thesis, we have studied different physical processes related to the phenomenology of Flavour Physics for quarks and leptons. A common thread is the idea to account for the possible deviations of experimental results compared to the theoretical predictions from a point of view free of prejudices from specific models of New Physics. The way to do this is by extending the Standard Model in the most general way, but without losing predictive power, with the use of Effective Field Theory. For the most part, our studies have focused on the anomalies observed in the semileptonic decays of B mesons. We have also analyzed the leptonic decays of several mesons and their compatibility with ALPs.

The Standard Model offers an excellent prediction for most of the phenomena that are observed in the high energy experiments, and these predictions must not be spoilt just to find an explanation for a few puzzling observables. Therefore, it is mandatory to perform global studies comprising all available experimental data from diverse physical sectors.

We saw a first example of this when the introduction of imaginary or complex couplings and Wilson coefficients forced us to consider the implications on the CP asymmetry. An even clearer example were the fits to the Standard Model Effective Field Theory at the energy scale of $\Lambda = 1\,\text{TeV}$, where we discussed how our results were limited by observables coming from superallowed nuclear β decays, electroweak precision tests and Leptonic Flavour Violation. Finally, in the case of the invisible ALP production, we have seen the importance of different leptonic meson decay channels, and their comparison with other decays analyzed previously.

Phenomenology is an area of physics that lives in the balance between theory and experiment, and therefore, any new development in either can have a large impact in our results. This is specially true in the phenomenology of Flavour Physics, which is in rapid evolution caused by the plethora of experimental measurements and the renewed theoretical interest. We have experienced this evolution during the elaboration of the thesis, forcing us to redo some of our analyses and even re-evaluate previous conclusions. An example is our initial interest in a possible anomaly affecting the observable ΔM_s, included with other flavour observables in the analysis of [1]. However, improved theoretical cal-

culations within the SM solved the anomaly, making obsolete our results in this regard. On the contrary, the anomalies that have centered most of our work, $R_{K^{(*)}}$ and $R_{D^{(*)}}$, have maintained their interest with new experimental measurements, and in the case of $R_{K^{(*)}}$, its significance has even increased slightly. In fact, in our works [2, 4] we have updated our global fits taking into account experimental measurements with improved precision which have been published after the completion of our works. Additionally, we have studied the possible impact on our analysis of the future measurements of the electroweak precision tests in the next generation of linear electron colliders. A final example of the evolution in Flavour Physics is present in the study of [6], where the new experimental measurements in the leptonic decays of several mesons have been an important factor in the results that we have obtained.

A last general point of discussion is that, as we study more complete theories or models and include more observables, the required calculations become more involved. At first this means the jump from analytical to numerical calculations, and when even the traditional numerical approaches become too complicated and slow, as is the case of our fit in Chapter 7, we need to look for alternative methods. We have resorted to a Machine Learning algorithm based on decision trees in order to approximate the likelihood function and speed up the calculations [4]. It is important to note that, although Machine Learning methods are useful in physics to help in the computations, they will never substitute physical theories as our guide to understand reality.

In the aforementioned works, which have been included in this thesis, we have performed a series of numerical analyses, including global fits, which have produced some novel results:

- In the analysis of the impact of complex Wilson coefficients for the B anomalies within the Z' and S_3 leptoquark models, we have considered a combined fit of the observables R_{K^+}, $R_{K^{*0}}$, ΔM_s and A_{CP}^{mix}. We have concluded that purely imaginary couplings allow us to reproduce the tension in ΔM_s while obeying the constraints imposed by the CP asymmetry, but not achieving compatibility with the $R_{K^{(*)}}$ anomalies.
  The introduction of complex couplings in the leptoquark and Z' models results in a slightly improved fit, compatible with the observed values of $R_{K^{(*)}}$, while slightly improving the prediction for ΔM_s.

- Taking into account the new theoretical determinations of ΔM_s and the limited impact of imaginary parts in the Wilson coefficients for the B anomalies, it is safe to assume for the rest of our work that all Wilson coefficients are real.

- In the global fit to the SMEFT Wilson coefficients $C_{\ell q(1)}$ and $C_{\ell q(3)}$, which included the $b \to s\mu^+\mu^-$ observables, as well as $R_{D^{(*)}}$, $\text{BR}(B \to K^{(*)}\nu\bar{\nu})$ and the precision tests in electroweak and nuclear β decays, we found that the favored scenarios are those with maximal violation of Lepton Universality between the first and second

generations, that is needed to explain the $R_{K^{(*)}}$ anomalies. Additionally, scenarios where NP also contributes to the τ sector provide improved predictions for the $R_{D^{(*)}}$ anomalies.
The value of the best fit can be understood as the interplay between three different sectors: the B anomalies are sensitive to violations of lepton flavour universality, electroweak observables that are sensitive to universal NP contributions, and the superallowed nuclear β decays that are sensitive to physics in the muonic part. It is therefore evident the relevance of the inclusion of all physical sectors in a phenomenological analysis.

- We have shown that future measurements in the linear electron colliders will significantly improve the constrains to lepton-universal NP contributions.

- A mechanism for the simultaneous generation of the $R_{K^{(*)}}$ and $R_{D^{(*)}}$ anomalies has been proposed, where the Effective Theory reflects an interaction that, at the high scale, affects only the third generation fermions before the corresponding rotation to the mass basis of the physical quarks and leptons. In this picture, the $R_{D^{(*)}}$ ratios are tree level phenomena, while the $R_{K^{(*)}}$ ratios are the result of the interplay between tree level affecting only the $B \to K^{(*)} e^+ e^-$ decays, and loop level affecting universally the electron and muon decay modes. Tree level contributions to the muon decay modes are severly limited by Lepton Flavour-violating observables.
An interesting prediction of our proposal is the correlation between the $R_{D^{(*)}}$ anomalies and an excess in the $B \to K^{(*)} \nu \bar{\nu}$ decays. A similar an excess has been independently reported by the Belle II experiment.

- A possible realization of this mechanism has been proposed in the form of a vector leptoquark U_1 that interacts with the second and third generations of quarks and the first and third generations of leptons. This leptoquark model extends a previous proposal to explain only the $R_{D^{(*)}}$ anomalies, and is compatible with all the experimental searches.

- Our work marks a novel approach to the study of the flavour anomalies, with a Machine Learning analysis being used to extract confidence intervals and correlations between observables. We have shown that the Machine Learning techniques constitute a suitable and useful tool for this kind of analyses.

- Finally, we have presented a detailed analysis of leptonic decays of mesons that could produce pseudoescalar ALPs, $M \to \ell \nu_\ell a$. We have found that leptonic kaon decays can impose bounds to the couplings of invisible ALPs to quarks which are comparable, although not competitive, with bounds coming from hadronic decays. The bounds derived from other leptonic meson decays are less stringent by several orders of magnitude. On the other hand, the bounds on ALP-leptons couplings

coming from leptonic meson decays, and specially from $K \to e\nu_e a$, are the most stringent in the GeV and sub-GeV range.

9.1 Conclusiones

A lo largo de las páginas de esta tesis, hemos estudiado diferentes procesos físicos relacionados con la fenomenología de la Física del Sabor. El hilo conductor ha sido la idea de investigar posibles desviaciones en resultados experimentales de los últimos años con respecto a las predicciones del Modelo Estándar, y además, hacerlo desde un punto de vista *libre de prejuicios* de adopción de modelos específicos de Nueva Física. Con esta intención, debemos extender el Modelo Estándar de la manera más general posible, pero sin perder poder predictivo, mediante el uso de Teorías de Campos Efectivas. La mayoría de nuestros estudios se han centrado en las anomalías en las desintegraciones semileptónicas de mesones B. Posteriormente también hemos analizado las desintegraciones leptónicas de varios mesones y su compatibilidad con ALPs.

El Modelo Estándar describe con una extraordinaria precisión la gran mayoría de los fenómenos que se observan en los experimentos de altas energías. Sus predicciones no deben ponerse en entredicho solo para buscar una explicación a unos pocos observables de interés en los que hemos observado posibles desviaciones, como es el caso de las anomalías en la física de sabor. Para tenerlo en cuenta es necesario realizar estudios globales incluyendo todos los datos experimentales disponibles de los diversos sectores físicos del modelo.

En nuestro trabajo hemos visto un ejemplo de la necesidad de estos estudios globales desde sus inicios, cuando introducir los acoplamientos y coeficientes de Wilson complejos nos forzó a considerar las implicaciones en la asimetría CP. Un ejemplo aún más claro han sido los ajustes estadísticos globales a la Teoría Efectiva del Modelo Estándar en la escala de energía $\Lambda = 1\,\text{TeV}$, donde hemos discutido cómo nuestros resultados estaban limitados tanto por los observables de las desintegraciones β nucleares como por los tests de precisión electrodébiles y los observables de violación del sabor leptónico. Finalmente, en el caso de la producción de ALPs invisibles, hemos comprobado la relevancia de los diferentes modos de desintegración leptónicos de los mesones, así como su comparación con otras desintegraciones analizadas previamente.

La fenomenología es un área de la física que vive en el equilibrio entre la teoría y el experimento, y por lo tanto, cualquier avance en una u otra dirección puede tener un gran impacto en nuestros resultados y conclusiones. En el presente, la fenomenología de la Física del Sabor está marcada por una rápida evolución debido a la multitud de resultados experimentales y el renovado interés teórico en el campo. En el transcurso de los trabajos que se incluyen en esta tesis, esta evolución nos ha llevado a rehacer algunos de nuestros análisis e incluso re-evaluar conclusiones previas. Un ejemplo de ello es que inicialmente nos interesamos en una posible anomalía que afectaba al observable ΔM_s, realizando

nuestro análisis de este observable, conjuntamente a otros asociados a la física del sabor, en [1]. Sin embargo, la precisión en los cálculos teóricos en el seno del Modelo Estándar resolvió la anomalía, haciendo que nuestros resultados en ese respecto quedaran obsoletos. Por el contrario, dos anomalías que han centrado la mayor parte de esta tesis, $R_{K^{(*)}}$ y $R_{D^{(*)}}$, han corroborado su interés a medida que se publicaban nuevas medidas experimentales, y en el caso de $R_{K^{(*)}}$, su significancia incluso ha aumentado ligeramente. En nuestros trabajos [2, 4], de hecho, hemos ido actualizando los análisis globales teniendo en cuenta medidas experimentales más precisas posteriores a la publicación de los mismos. Además, hemos abordado el posible impacto en nuestro análisis de las futuras mediciones de los tests de precisión electrodébiles en la próxima generación de colisionadores lineales [3, 5]. Otro ejemplo de la evolución en la Física del Sabor lo constituye el estudio realizado en [6], donde la aparición de nuevas mediciones experimentales en las desintegraciones leptónicas de varios mesones ha sido uno de los factores que han conrtibuido a los resultados obtenidos.

Un último punto de discusión general es el hecho de que, a medida que estudiamos teorías más completas e incluimos más observables, los cálculos necesarios pasan a ser más complejos. Al principio esto significa el salto de cálculos analíticos a numéricos, y cuando incluso los enfoques numéricos tradicionales se vuelven demasiado complicados y lentos, como es el caso de nuestro ajuste del Capítulo 7, hay que buscar métodos alternativos. Hemos recurrido a un algoritmo de "Machine Learning" basado en árboles de decisión con el objetivo de hacer una aproximación de la función de verosimilitud y acelerar los cálculos [4]. Es importante notar que los métodos de "Machine Learning", aunque resulten útiles en física para ayudar en los cálculos, nunca reemplazarán a las teorías físicas como nuestra guía para comprender la realidad.

En los trabajos antes mencionados, e incluídos en esa tesis doctoral, hemos desarrollado una serie de análisis numéricos, incluyendo ajustes estadísticos globales con el propósito de investigar las anomalías en la Física de Sabor. Resumimos a continuación los resultados más relevantes obtenidos:

- En el análisis del impacto de los coeficientes de Wilson complejos en el estudio de las anomalías de mesones B en los modelos Z' y leptoquark S_3, hemos considerando un ajuste combinado de los observables R_{K^+}, $R_{K^{*0}}$, ΔM_s y A_{CP}^{mix}. Hemos concluido que los acoplamientos imaginarios puros nos permiten reproducir la tensión en el observable ΔM_s, obedeciendo las restricciones impuestas por la asimetría CP, pero no siendo compatibles con las anomalías en $R_{K^{(*)}}$.
  La introducción de acoplamientos complejos para los modelos de leptoquarks o Z' conlleva un ajuste ligeramente mejor que puede ser compatible con los valores observados de $R_{K^{(*)}}$, y mejorar ligeramente la predicción para ΔM_s.

- Teniendo en cuenta la nueva determinación teórica de ΔM_s, que resolvió la anomalía en este observable, y el impacto limitado que tienen las partes imaginarias de

los coeficientes de Wilson sobre las anomalías B, podemos afirmar que es plausible considerar que todos los coeficientes de Wilson sean reales.

- En el ajuste estadístico a los coeficientes de Wilson del SMEFT $C_{\ell q(1)}$ y $C_{\ell q(3)}$, incluyendo tanto los observables asociados de $b \to s\mu^+\mu^-$, así como $R_{D^{(*)}}$, BR($B \to K^{(*)}\nu\bar{\nu}$) y los observables de precisión electrodébiles y nucleares β, encontramos que los escenarios más favorables son aquellos que muestran una violación máxima de la universalidad de los leptones, que es necesaria para explicar las anomalías $R_{K^{(*)}}$. Además, los escenarios donde la Nueva Física también contribuye al sector del τ proporcionan predicciones mejoradas para las anomalías $R_{D^{(*)}}$.
  El valor que ofrece el mejor ajuste se puede entender como el resultado de los efectos combinados de tres sectores: las anomalías B detectan las violaciones de la universalidad del sabor leptónico, los observables electrodébiles detectan las contribuciones universales de Nueva Física, y las desintegraciones nucleares β detectan la física en el sector muónico. Esta interpretación es una evidencia de la relevancia de considerar todos los sectores físicos en una análisis fenomenológico.

- Hemos mostrado que las mediciones futuras en los colisionadores lineales de electrones mejorarán significativamente los límites a las contribuciones universales de Nueva Física.

- Se ha propuesto un mecanismo para la generación simultánea de las anomalías de $R_{K^{(*)}}$ y $R_{D^{(*)}}$, donde la teoría efectiva refleja una interacción que, a escalas altas de energía, afecta solamente a la tercera generación de fermiones, antes de la correspondiente rotación a la base de masa de los quarks y leptones físicos. En esta situación, las anomalías de $R_{D^{(*)}}$ se generan a nivel de diagramas a nivel árbol, mientras que $R_{K^{(*)}}$ es el resultado combinado de diagramas a nivel árbol que afectan solamente a la desintegración $B \to K^{(*)}e^+e^-$ y efectos a un *bucle* que afectan de modo universal a los modos de desintegración tanto en electrones como en muones. Las contribuciones a nivel árbol a los modos de desintegración en muones están muy limitadas por los observables de violación del sabor leptónico.
  Una predicción interesante de nuestra propuesta es la correlación entre la anomalía $R_{D^{(*)}}$ y un exceso en las desintegraciones $B \to K^{(*)}\nu\bar{\nu}$. El experimento Belle II ha reportado un exceso similar.

- En este marco de trabajo, hemos propuesto una posible implementación de este mecanismo en forma de un leptoquark vectorial U_1 que interacciona con la segunda y tercera generaciones de quarks, y la primera y tercera generaciones de leptones. Este modelo de leptoquarks extiende una propuesta previa que explicaba solamente la anomalía $R_{D^{(*)}}$, y es compatible con todas las búsquedas experimentales.

- Una novedad relevante de nuestro trabajo es que utilizamos por primera vez en el contexto de las llamadas anomalías de sabor un análisis de Machine-Learning para

extraer los intervalos de confianza y las correlaciones entre observables, demostrando que es una herramienta útil y adecuada en este tipo de análisis.

- Finalmente, hemos presentado un análisis detallado de las desintegraciones leptónicas de mesones que podrían producir ALPs pseudoescalares, $M \to \ell \nu_\ell a$. Encontramos que las desintegraciones leptónicas de kaones pueden imponer límites para los acoplamientos de ALPs invisibles a quarks que son comparables, aunque no competitivos, con los límites provenientes de las desintegraciones hadrónicas. Los límites derivados de las desintegraciones leptónicas de otros mesones son varios órdenes de magnitud menos restrictivos. Por otra parte, los límites a los acoplamientos ALP-leptones provenientes de desintegraciones leptónicas, y en especial de $K \to e\nu_e a$, son los más restrictivos en el ámbito de los ALP de masas del orden del GeV o sub-GeV.

Appendix A

Differential observables for B decays in the Weak Effective Theory

A.1 $B \to K\ell^+\ell^-$ decay

In the limit of vanishing lepton masses, the differential decay rate for the $B \to K\ell^+\ell^-$ decay is given by [447]

$$\frac{d\Gamma(B \to K\ell^+\ell^-)}{dq^2} = \frac{G_F^2 \alpha_{\rm em}^2 |V_{tb}V_{ts}^*|^2}{2^{10}\pi^5 M_B^5} \lambda^{3/2}(M_B^2, M_K^2, q^2)\Big(|F_V|^2 + |F_A|^2\Big), \tag{A.1}$$

where λ is the Källén function,

$$\lambda(x,y,z) = x^2 + y^2 + z^2 - 2(xy + xz + yz), \tag{A.2}$$

and the vector and axial structures are

$$\begin{aligned} F_V(q^2) &= (C_9 + C_9')f_+(q^2) + \frac{2m_b}{M_B + M_K}(C_7 + C_7')f_T(q^2) + h_K(q^2) \\ F_A(q^2) &= (C_{10} + C_{10}')f_+(q^2). \end{aligned} \tag{A.3}$$

The function $h_K(q^2)$ contains non-factorizable contributions, including the charm loop effects. The functions $f_+(q^2)$ and $f_T(q^2)$ are the form factors introduced in Eq. (2.38).

A.2 $B \to K^*\ell^+\ell^-$ decay

The transversity amplitudes are the projections of the total amplitude into the basis of chirality of the quark current and polarization of the virtual boson decaying into the pair of leptons. The transversity amplitudes for the $B \to K^*\ell^+\ell^-$ decay in the WET are [83,

448]

$$
\begin{aligned}
A_\perp^{L,R} &= \sqrt{2}N\lambda^{1/2}(M_B^2, M_{K^*}^2, q^2)\left[(C_9^\ell + C_9^{'\ell}) \mp (C_{10}^\ell + C_{10}^{'\ell})\frac{V(q^2)}{M_B + M_{K^*}} + \frac{2m_b}{q^2}(C_7 + C_7')T_1(q^2)\right],\\
A_\parallel^{L,R} &= -\sqrt{2}N(M_B^2 - M_{K^*}^2)\left[(C_9^\ell - C_9^{'\ell}) \mp (C_{10}^\ell - C_{10}^{'\ell})\frac{A_1(q^2)}{M_B - M_{K^*}} + \frac{2m_b}{q^2}(C_7 - C_7')T_2(q^2)\right],\\
A_0^{L,R} &= -\frac{N}{2M_{K^*}\sqrt{q^2}}\left[(C_9^\ell - C_9^{'\ell}) \mp (C_{10}^\ell - C_{10}^{'\ell})\frac{A_{12}(q^2)}{M_B - M_{K^*}} + \frac{2m_b}{q^2}(C_7 - C_7')T_{23}(q^2)\right],\\
A_t &= \frac{N}{\sqrt{q^2}}\lambda^{1/2}(M_B^2, M_{K^*}^2, q^2)\left[2(C_{10}^\ell - C_{10}^{'\ell} + \frac{q^2}{m_\ell}(C_P^\ell - C_P^{'\ell})\right]A_0(q^2),\\
A_S &= -2N\lambda^{1/2}(M_B^2, M_{K^*}^2, q^2)(C_S^\ell - C_S^{'\ell})A_0(q^2),
\end{aligned}
\tag{A.4}
$$

where $V(q^2)$, $A_0(q^2)$, $A_1(q^2)$, $T_1(q^2)$, $T_2(q^2)$ and $T_3(q^2)$ are the form factors in Eq. (2.39), and the combinations of form factors A_{12} and T_{23} are defined as

$$
\begin{aligned}
A_{12}(q^2) &= (M_B^2 - M_{K^*}^2)(M_B^2 - M_{K^*}^2 - q^2)A_1(q^2) - \lambda(M_B^2, M_{K^*}^2, q^2)\frac{M_B - M_{K^*}}{M_B + M_{K^*}}A_2(q^2),\\
T_{23}(q^2) &= q^2(M_B^2 + 3M_{K^*}^2 - q^2)T_2(q^2) - \lambda(M_B^2, M_{K^*}^2, q^2)\frac{q^2}{M_B^2 - M_{K^*}^2}T_3(q^2),
\end{aligned}
\tag{A.5}
$$

and the overall normalization is defined as

$$
N = V_{tb}V_{ts}^*\left(\frac{G_F^2\alpha_{\rm em}^2}{3072\pi^5 M_B^3}q^2\sqrt{1 - \frac{4m_\ell^2}{q^2}}\lambda^{1/2}(M_B^2, M_{K^*}^2, q^2)\right)^{1/2}. \tag{A.6}
$$

The angular observables are given in terms of the transversity amplitudes by

$$
\begin{aligned}
I_1^s &= \frac{3 - 4m_\ell^2/q^2}{4}(|A_\perp^L|^2 + |A_\parallel^L|^2 + |A_\perp^R|^2 + |A_\parallel^R|^2) + \frac{4m_\ell^2}{q^2}\mathrm{Re}(A_\perp^L A_\perp^{R*} + A_\parallel^L A_\parallel^{R*}),\\
I_1^c &= |A_0^L|^2 + |A_0^R|^2 + \frac{4m_\ell^2}{q^2}[|A_t|^2 + 2\mathrm{Re}(A_0^L A_0^{R*})] + \left(1 - \frac{4m_\ell^2}{q^2}\right)|A_S|^2,\\
I_2^s &= \frac{1}{4}\left(1 - \frac{4m_\ell^2}{q^2}\right)(|A_\perp^L|^2 + |A_\parallel^L|^2 + |A_\perp^R|^2 + |A_\parallel^R|^2),\\
I_2^c &= -\left(1 - \frac{4m_\ell^2}{q^2}\right)(|A_0^L|^2 + |A_0^R|^2),\\
I_3 &= \frac{1}{2}\left(1 - \frac{4m_\ell^2}{q^2}\right)(|A_\perp^L|^2 - |A_\parallel^L|^2 + |A_\perp^R|^2 - |A_\parallel^R|^2),\\
I_4 &= \frac{1}{\sqrt{2}}\left(1 - \frac{4m_\ell^2}{q^2}\right)\mathrm{Re}(A_0^L A_\parallel^{L*} + A_0^R A_\parallel^{R*}),\\
I_5 &= \sqrt{2}\left(1 - \frac{4m_\ell^2}{q^2}\right)\left[\mathrm{Re}(A_0^L A_\perp^{L*} - A_0^R A_\perp^{R*}) - \frac{m_\ell}{\sqrt{2}}\mathrm{Re}(A_\parallel^L A_S^* + A_\parallel^R A_S^*)\right],\\
I_6^s &= 2\left(1 - \frac{4m_\ell^2}{q^2}\right)\mathrm{Re}(A_\parallel^L A_\perp^{L*} - A_\parallel^R A_\perp^{R*}),
\end{aligned}
$$

$$
\begin{aligned}
I_6^c &= \frac{4m_\ell}{\sqrt{q^2}}\left(1-\frac{4m_\ell^2}{q^2}\right)\mathrm{Re}(A_0^L A_S^* + A_0^R A_S^*),\\
I_7 &= \sqrt{2}\left(1-\frac{4m_\ell^2}{q^2}\right)\left[\mathrm{Im}(A_0^L A_\parallel^{L*} - A_0^R A_\parallel^{R*}) + \frac{m_\ell}{\sqrt{q^2}}\mathrm{Im}(A_\perp^L A_S^* + A_\perp^R A_S^*)\right],\\
I_8 &= \frac{1}{\sqrt{2}}\left(1-\frac{4m_\ell^2}{q^2}\right)\mathrm{Im}(A_0^L A_\perp^{L*} + A_0^R A_\perp^{R*}),\\
I_9 &= \left(1-\frac{4m_\ell^2}{q^2}\right)\mathrm{Im}(A_\parallel^{L*} A_\perp^L + A_\parallel^{R*} A_\perp^R).
\end{aligned}
\tag{A.7}
$$

A.3 $B \to D\ell\nu$ decay

The expression for the differential decay rate is [96]

$$
\begin{aligned}
\frac{d\Gamma(B\to D\ell\nu)}{dq^2} &= \frac{G_F^2 V_{cb}^2}{192 M_B^3 \pi^3} q^2 \lambda^{1/2}(M_B^2, M_D^2, q^2)\left(1-\frac{m_\ell^2}{q^2}\right)^2\\
&\times\left\{|C_{VL}^\ell + C_{VR}^\ell|^2\left[(H_{V0}^s)^2\left(\frac{m_\ell^2}{q^2}+1\right)+\frac{3m_\ell^2}{2q^2}(H_{Vt}^s)^2\right]\right.\\
&+\frac{3}{2}(H_S^s)^2|C_{SL}^\ell + C_{SR}^\ell|^2 + 8(H_T^s)^2|C_T^\ell|^2\left(1+\frac{2m_\ell^2}{q^2}\right)\\
&+3\mathrm{Re}[(C_{VL}^\ell + C_{VR}^\ell)(C_{SL}^\ell + C_{SR}^\ell)^*]\frac{m_\ell}{\sqrt{q^2}}H_S^s H_{Vt}^s\\
&\left.-12\mathrm{Re}[(C_{VL}^\ell + C_{VR}^\ell)(C_T^\ell)^*]\frac{m_\ell}{\sqrt{q^2}}H_T^s H_{V0}^s\right\},
\end{aligned}
\tag{A.8}
$$

where the helicity amplitudes are given by

$$
\begin{aligned}
H_{V0}^s(q^2) &= \sqrt{\frac{\lambda(M_B^2, M_D^2, q^2)}{q^2}} f_+(q^2),\\
H_{Vt}^s(q^2) &= \frac{M_B^2 - M_D^2}{\sqrt{q^2}} f_0(q^2),\\
H_S^s(q^2) &= \frac{M_B^2 - M_D^2}{m_b - m_c} f_0(q^2)\\
H_T^s(q^2) &= -\frac{\sqrt{\lambda(M_B^2, M_D^2, q^2)}}{M_B + M_D} f_T(q^2).
\end{aligned}
\tag{A.9}
$$

A.4 $B \to D^*\ell\nu$ decay

The transversity amplitudes in this decay are [96]

$$
\begin{aligned}
A_0 &= N\frac{M_B + M_{D^*}}{2M_{D^*}\sqrt{q^2}}\left[-(M_B^2 - M_{D^*}^2 - q^2)A_1(q^2) + \frac{\lambda(M_B^2, M_{D^*}^2, q^2)}{(M_B + M_{D^*})^2}A_2(q^2)\right](C_{VL}^\ell - C_{VR}^\ell),\\
A_\parallel &= \sqrt{2}N(M_B + M_{D^*})A_1(q^2)(C_{VL}^\ell - C_{VR}^\ell),
\end{aligned}
$$

$$
\begin{aligned}
A_\perp &= -\sqrt{2}N\frac{\lambda^{1/2}(M_B^2,M_{D^*}^2,q^2)}{M_B+M_{D^*}}V(q^2)(C_{VL}^\ell+C_{VR}^\ell),\\
A_t &= -N\sqrt{\frac{\lambda(M_B^2,M_{D^*}^2,q^2)}{q^2}}A_0(q^2)(C_{VL}^\ell-C_{VR}^\ell),\\
A_P &= -N\frac{\lambda^{1/2}(M_B^2,M_{D^*}^2,q^2)}{m_b+m_c}A_0(q^2)(C_{SL}^\ell-C_{SR}^\ell),\\
A_{T0} &= \frac{N}{M_{D^*}}\left[-(M_B^2+3M_{D^*}^2-q^2)T_2(q^2)+\frac{\lambda(M_B^2,M_{D^*}^2,q^2)}{M_B^2-M_{D^*}^2}T_3(q^2)\right]C_T^\ell,\\
A_{T\parallel} &= 2N\sqrt{\frac{2}{q^2}}(M_B^2-M_{D^*}^2)T_2(q^2)C_T^\ell,\\
A_{T\perp} &= 2N\sqrt{\frac{2}{q^2}}\lambda(M_B^2,M_{D^*}^2,q^2)T_1(q^2)C_T^\ell.
\end{aligned}
\tag{A.10}
$$

The normalization of the amplitudes is

$$
N=\left[\frac{G_F^2|V_{cb}|^2}{384\pi^3M_B^3}q^2\lambda^{1/2}(M_B^2,M_{D^*}^2,q^2)\left(1-\frac{m_\ell^2}{q^2}\right)^2\mathrm{BR}(D^*\to D\pi)\right]^{1/2}. \tag{A.11}
$$

The angular observables in terms of the transversity amplitudes are

$$
\begin{aligned}
I_1^c &= 2\left[\left(1+\frac{m_\ell^2}{q^2}\right)(|A_0|^2+4|A_{T0}|^2)-\frac{8m_\ell^2}{\sqrt{q^2}}\mathrm{Re}(A_0A_{T0}^*)+\frac{2m_\ell^2}{q^2}\left|A_t+\frac{\sqrt{q^2}}{m_\ell}A_P\right|^2\right],\\
I_1^s &= \frac{}{2}\left[\left(3+\frac{m_\ell^2}{q^2}\right)(|A_\perp|^2+|A_\parallel|^2)+4\left(1+\frac{3m_\ell^2}{q^2}\right)(|A_{T\perp}|^2+|A_{T\parallel}|^2)-8\frac{m_\ell}{\sqrt{q^2}}\mathrm{Re}(A_\perp A_{T\perp}^*+A_\parallel A_{T\parallel}^*)\right],\\
I_2^c &= -2\left(1-\frac{m_\ell^2}{q^2}\right)(|A_0|^2-4|A_{T0}|^2),\\
I_2^s &= \frac{}{2}\left(1-\frac{m_\ell^2}{q^2}\right)(|A_\perp|^2+|A_\parallel|^2-4|A_{T\perp}|^2-4|A_{T\parallel}|^2),\\
I_3 &= \left(1-\frac{m_\ell^2}{q^2}\right)(|A_\perp|^2-|A_\parallel|^2-4|A_{T\perp}|^2+4|A_{T\parallel}|^2),\\
I_4 &= \sqrt{2}\left(1-\frac{m_\ell^2}{q^2}\right)\mathrm{Re}(A_0A_\parallel^*-4A_{T0}A_{T\parallel}^*),\\
I_5 &= 2\sqrt{2}\left[\mathrm{Re}[(A_0-\frac{2m_\ell}{\sqrt{q^2}}A_{T0})(A_\perp^*-\frac{2m_\ell}{\sqrt{q^2}}A_{T\perp}^*)]-\frac{m_\ell^2}{q^2}\mathrm{Re}[(A_t^*+\frac{\sqrt{q^2}}{m_\ell}A_P^*)(A_\parallel-2\frac{\sqrt{q^2}}{m_\ell}A_{T\parallel})]\right],\\
I_6^c &= \frac{8m_\ell^2}{q^2}\mathrm{Re}[(A_t^*+\frac{\sqrt{q^2}}{m_\ell}A_P^*)(A_0-2\frac{\sqrt{q^2}}{m_\ell}A_{T0})],\\
I_6^s &= 4\mathrm{Re}[(A_\parallel-2\frac{\sqrt{q^2}}{m_\ell}A_{T\parallel})(A_\perp^*-2\frac{\sqrt{q^2}}{m_\ell}A_{T\perp}^*)],\\
I_7 &= -2\sqrt{2}\left[\mathrm{Im}[(A_0-\frac{2m_\ell}{\sqrt{q^2}}A_{T0})(A_\perp^*-\frac{2m_\ell}{\sqrt{q^2}}A_{T\perp}^*)]+\frac{m_\ell^2}{q^2}\mathrm{Re}[(A_t^*+\frac{\sqrt{q^2}}{m_\ell}A_P^*)(A_\parallel-2\frac{\sqrt{q^2}}{m_\ell}A_{T\parallel})]\right],\\
I_8 &= \sqrt{2}\left(1-\frac{m_\ell^2}{q^2}\right)\mathrm{Im}(A_0A_\perp^*-4A_{T0}A_{T\perp}^*),
\end{aligned}
$$

$$I_9 = 2\left(1 - \frac{m_\ell^2}{q^2}\right) \mathrm{Im}(A_\parallel A_\perp^* - 4 A_{T\parallel} A_{T\perp}^*). \tag{A.12}$$

Appendix B

Codes

In order to calculate predictions for observables in the SM and EFT and their uncertainties, perform fits of the Wilson coefficients to several observables and plot the results, I needed a combination of code publicly available complemented with code I wrote. All the code is written in `python3`, with the code in Appendix B.3.2 requiring at least `python3.8`.

My code relies on the following common packages:

- `matplotlib` [449]: plotting.
- `numpy` [450] and `scipy` [451]: mathematics and array handling.
- `pandas` [452]: large datasets.
- `iminuit` [453] v1.x: function minimization, based on MINUIT [454].

B.1 Public codes for Flavour Physics

In this section I will comment the principal characteristics of the public codes designed specifically for computations in the field of Flavour Physics, `wilson`, `flavio` and `smelli`.

B.1.1 `wilson`

The package `wilson` [341] is used for matching and running Wilson coefficients of dimension six effective operators. `wilson` works in both the SMEFT and WET, as well as effective theories at lower energies where the b and c quarks are integrated out. The bases available, and the notation for the effective operators in each basis, follow the Wilson Coefficient eXchange Format (wcxf) [196].

The RG evolution of the Wilson coefficient is performed, by default, by numerical integration of the RG equations in [184, 187–189] for the SMEFT and [190] for the WET, although the package also offers the option of the leading-log approximation.

The matching between the SMEFT and WET is performed at tree level at the scale $\mu_{\text{EW}} = M_Z = 91.1876$ GeV, implementing the equations from [185].

The method `match_run` solves the complete task of running down the SMEFT Wilson coefficients from the NP scale Λ to the electroweak scale, matching them to the WET coefficients and running from the electroweak scale down to the m_b scale.

As an example of `wilson`, the following code defines the SMEFT Wilson coefficients $C^{2233}_{\ell q(1)} = C^{2233}_{\ell q(3)} = 1$ at the scale $\Lambda = 1$ TeV and obtains the value of $C_9^{\mu\,\mathrm{NP}}$ and $C_{10}^{\mu\,\mathrm{NP}}$ at the scale m_b.

```
from wilson import Wilson

Lambda_SMEFT = 1000 #All dimensionful quantities are in powers of GeV
m_b = 4.2

wc_SMEFT = Wilson({'lq1_2233': 1/Lambda_SMEFT**2,
                   'lq3_2233': 1/Lambda_SMEFT**2},
                  scale = Lambda_SMEFT, eft = 'SMEFT', basis = 'Warsaw')
wc_WET = wc_SMEFT.match_run(scale = m_b, eft = 'WET', basis = 'flavio')

C9mu = wc_WET.values['C9_bsmumu']['Re']
C10mu = wc_WET.values['C10_bsmumu']['Re']
print('C9mu = ' + str(C9mu) + '\tC10mu = ' + str(C10mu))
```

Obtaining the output:

```
C9mu = -1.1781396204511558    C10mu = 1.1791467325619762.
```

An alternative to `wilson` is provided by the `Mathematica` package `DSixTools` [455]. `DSixTools` also implements the RG evolution of the Wilson coefficients (available methods are numerical integration, leading log and evolution matrix), and matching with the WET at the electroweak scale. The main drawback of `DSixTools` is that it only implements the basis defined in [185] for the WET, that is not widely used in the literature. The results of `wilson` have been tested against those of `DSixTools`.

B.1.2 `flavio`

The code `flavio` [195] is used to calculate predictions for a large number of flavour physics observables, both in the SM and in EFTs using the Wilson coefficients specified by `wilson`. While version 0.28 contained mostly B decays observables, electroweak precision observables were added by version 1.5, and Higgs observables in version 2.0.

Predictions for observables in the SM are obtained with the method `sm_prediction`, and in the EFT with the method `np_prediction`. For example, the values of R_D^ℓ and $R_{K^+}^{[1.1,6]}$ in the SM and the SMEFT point of the previous section are calculated with the following code:

```
import flavio
```

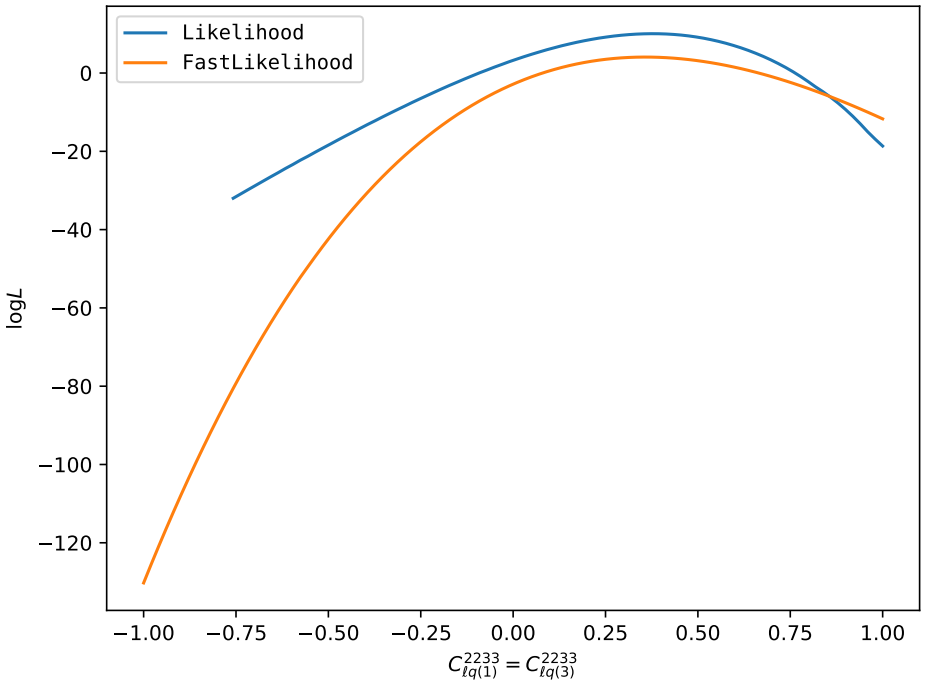

Figure B.1: $\log L$ calculated with the `flavio` classes `Likelihood` and `FastLikelihood`, including the observables $R^{[1.1,6]}_{K^+}$, $R^{[1.1,6]}_{K^*}$, R^{ℓ}_{D} and $R^{\ell}_{D^*}$.

```
RD_SM = flavio.sm_prediction('Rtaul(B->Dlnu)')
RD_SMEFT = flavio.np_prediction('Rtaul(B->Dlnu)', wc_SMEFT)

RK_SM = flavio.sm_prediction('<Rmue>(B+->Kll)', q2min=1.1, q2max=6)
RK_SMEFT = flavio.np_prediction('<Rmue>(B+->Kll)',
                                wc_SMEFT, q2min=1.1, q2max=6)

print('RD:\tSM = ' + str(RD_SM) + '\tSMEFT = ' + str(RD_SMEFT))
print('RK:\tSM = ' + str(RK_SM) + '\tSMEFT = ' + str(RK_SMEFT))
```

The output of the code above is:

```
RD:     SM = 0.303002599436188      SMEFT = 0.3212463003336509
RK:     SM = 1.00077907868083     SMEFT = 0.5021697262791173
```

`flavio` comes with an extense database of experimental measurements, including probability density functions and correlations between observables when available. This allows `flavio` to construct the likelihood function L for any set of observables, with the class `Likelihood`. An approximate version, where all probability distributions are assumed to be Gaussian distributions and the correlations are assumed to depend only on the SM input parameters, is available through the class `FastLikelihood`.

The code below compares the usage of the classes `Likelihood` and `FastLikelihood`, including the observables $R^{[1.1,6]}_{K^+}$, $R^{[1.1,6]}_{K^*}$, R^{ℓ}_{D} and $R^{\ell}_{D^*}$. It calculates the value of $\log L$ in both cases for Wilson coefficients $C^{2233}_{\ell q(1)} = C^{2233}_{\ell q(3)} \in [-1,1]$ and plots them. The result is

included as Fig. B.1.

```
import numpy as np
import matplotlib.pyplot as plt
from flavio.statistics.likelihood import Likelihood, FastLikelihood

SM_par = flavio.default_parameters.get_central_all() #SM input parameters

lh = []
flh = []

observables = ['Rtaul(B->Dlnu)',
               'Rtaul(B->D*lnu)',
               ('<Rmue>(B+->Kll)', 1.1, 6),
               ('<Rmue>(B0->K*ll)', 1.1, 6) ]
lh_function = Likelihood(observables=observables)
flh_function = FastLikelihood(observables=observables, name='')
flh_function.make_measurement() #Pre-calculates \ac{sm} covariance matrix

for c in np.linspace(-1, 1, 100):
        cLambda = c/Lambda_SMEFT**2
        wc = Wilson({'lq1_2233': cLambda, 'lq3_2233': cLambda},
                    scale = Lambda_SMEFT,
                    eft = 'SMEFT', basis = 'Warsaw')
        lh.append(lh_function.log_likelihood(SM_par, wc))
        flh.append(flh_function.log_likelihood(SM_par, wc))

#Plotting
plt.plot(np.linspace(-1,1,100), lh, label=r'$\mathtt{Likelihood}$')
plt.plot(np.linspace(-1,1,100), flh, label=r'$\mathtt{FastLikelihood}$')
plt.legend()
plt.xlabel(r'$C_{\ell q(1)}^{2233} = C_{\ell q(3)}^{2233}$')
plt.ylabel(r'$\log L$')
plt.tight_layout(pad=0.5)
plt.show()
```

The code `flavio` already includes the RG effects of the SMEFT operators on the vev of the Higgs in Eq. (3.39) and the Fermi constant in Eq. (3.40). By default, `flavio` uses the SM values for the entries of the CKM matrix.

Alternatives to `flavio` include:

- `HEPfit` [456].

- `EOS` [457]. Only implements effective operators in the WET.
- `FlavBit` [458] module for `GAMBIT` [459]. Only implements effective operators in the WET.

B.1.3 `smelli`

The package `smelli` [342] implements a likelihood function including all `flavio` observables that are experimentally constrained. That includes electroweak precision tests, B and K decays, meson-antimeson mixing, τ decays and magnetic anomalous moments of leptons. In order to overcome the computational cost of the calculation for the complete likelihood function, it is factorized in two parts: one part for observables whose theoretical uncertainty can be neglected compared to the experimental uncertainty, and another part for observables whose uncertainties can be approximated by Gaussian distributions independent of Wilson coefficients, similar to the `flavio` class `FastLikelihood`.

Starting on version 1.4, `smelli` implements the determination of the CKM matrix from the measurements included in the fit, overwriting the SM values used by `flavio`. The procedure is as explained in Ref. [186], with the exception that $|V_{ub}|^2$ is determined from the inclusive decay $\text{BR}(B \to X_c e \nu_e)$.

B.1.4 Contributions to `flavio` and `smelli`

Version 2.0 of `flavio` introduced a new parameterisation of the $B \to D^*$ for factors [370]. Comparing the uncertainties of the $R_{D^{(*)}}$ ratios with the previous version, I noticed a bug in the implementation of the new form factors, where one of the parameters had a wrong sign in the correlation matrix. I fixed the bug with a pull request that has been merged in the main repository.[1]

The package `flavio` has a function to include new measurements into its database. In the versions 1.x, `smelli` automatically imports every measurement. My code relied on this functionality to investigate the impact of the ILC prospects in the global fit. However, `smelli` 2.0 changed this behaviour, and now it only considers a hard-coded selection of measurements that can not be changed in runtime. The solution was to add a new option to `smelli` to add or remove measurements to the likelihood. It was implemented in a pull request to the main repository.[2]

B.2 Public codes for Machine Learning

The Machine Learning analysis performed in section 7.4 required the use of specialized codes:

[1] https://github.com/flav-io/flavio/pull/160
[2] https://github.com/smelli/smelli/pull/45

- `scikit-learn` [460]: a general-purpose Python package to work with Machine Learning models. We use it to prepare the training and validation datasets, and to provide metrics of the model.
- `xgboost` [385]: Implements the Machine Learning model based on regression trees.
- `shap` [386, 387] calculates an approximation for the SHAP values, which does not require training any additional model. In fact, for tree-based models, the algorithm is of polynomial time [387].

The ideas behind the `xgboost` and `shap` algorithms are explained in Section 7.4.1.

B.3 Custom-made codes

B.3.1 Code used in chapter 5

The code that I wrote in order to produce the results and plots of chapter 5 is publicly available at [461]. The calculation routines are contained in the file `src/bigftit.py`, and the plotting routines can be found in the file `src/plotter.py`.

bigfit.py

The first part of the file includes definitions for later use: the function `myDeltaMS` implements the observable ΔM_s as in Equation (5.4), and the functions `wc_Z` and `wc_LQ` the matching of the Z' and S_3 leptoquark to the Wilson coefficients, as defined in Equations (4.7), (4.8), (4.2) and (4.3). The functions `C9mu`, `C10mu`, `C910mu`, `C9pmu`, `C10pmu`, `C9e`, `C10e`, `C910e`, `C9pe`, `C10pe` define the scenarios with one Wilson coefficient used in Tables 5.1 and 5.2, `CRe910` and `CIm910` define the scenarios with two Wilson coefficients used in Figure 5.2, and `C910Im` is used in 5.1. The code in `save_observables` selects the bins of the angular observables P_4' and P_5' relevant to our analysis, pre-computes the SM prediction and uncertainty for all observables in the fit, and writes them to a file. This file can be later open using `read_observables`, and a sample file is found in `results/observables_ZLQ.yaml`. The function `chi2` computes the χ^2 of the fit as a function of the Wilson coefficients, splitting the contributions of ΔM_s, $A_{\rm CP}^{\rm mix}$ and the rest of observables; the contribution of each individual observables is obtained by `chi2_budget`.

The second part of the file is used to study the impact of one single complex Wilson coefficient at a time. The function `define_fit` creates the `flavio.FastFit` object, that is used by the function `plot` to produce Figure 5.2. The function `predictions` uses `Minuit` to compute the best fit and its pull in the one-dimensional scenarios, as well as the central values and uncertainties for each observable. The results of this function are in Tables 5.1 and 5.2.

The third part of the file is contains the functions relevant for the specific NP models, namely Z' and leptoquark S_3. The function `makefit_complex` scans over the parameter

space of the real and imaginary parts of the coupling constant and the mass of the NP particle, and saves the results to a file. This function was used to generate Figures 5.3, 5.4, 5.5 and 5.6. The function `predmodel` computes, using `Minuit`, the best fit, pull and predictions for the observables, in Tables 5.3 and 5.4.

plotter.py

The function `drawplot` was used to produce Fig. 5.3 and 5.5 depicting the mass versus imaginary coupling for the Z' leptoquark and respectively. The function takes a datafile which contains the mass of the particle in the first column, the coupling in the second, and the likelihoods for the $R_{K^{(*)}}$ observables, the ΔM_S observables and their sum in the following columns. The resulting plot represents the contours of 1, 2 and 3 σ as solid green regions for the global fit, and the contours of 1 and 2 σ for $R_{K^{(*)}}$ and ΔM_S as lines.

The function `plot` was used to generate Fig. 5.4 and 5.6, for the real and imaginary parts of the coupling when the mass of the Z' or leptoquark is kept constant. This function is based on `flavio`'s `likelihood_contour`, but the calculation task is separated from the plotting task, allowing for a more flexible approach as the likelihoods do not need to be re-computed each time that a minor change to the appearance of the plot is needed.

Finally, the function `errorplot` is used for Fig. 5.7 and 5.8. The 1 σ allowed values for the observables are represented as a green (or brown) rectangle for the experimental values, as a yellow rectangle for the SM predictions, and as red or blue errorbars for our results.

B.3.2 Code used in chapters 6 and 7

The code used for the calculations in chapters 6 and 7 can be found in the `GitHub` repository [462], and the `jupyter` notebooks to execute the code, together with the results of the execution, in the repository [463].

The files in the repository [462] are organized as follows:

scenarios

The module `scenarios.py` contains the functions needed to translate the parameters of the fit into the Wilson coefficients.

- For the fits in Chapter 6, the functions `scI` through `scXI` are used.
- The functions corresponding to the fits in Chapter 7 are `rotBI` and `rotBII`, which use the function `idemp` to implement the parameterisation of Eq. (7.13).
- The function `rot2lqU1` matches the Wilson coefficients of these two scenarios into the couplings of a vector U_1 leptoquark of mass M according to Eq. (7.24).

SMEFTglob

The module `SMEFTglob.py` contains basic functions to work with the global likelihood and physical observables:

- `likelihood_global` and `likelihood_fits` return the logarithm of the likelihood function at an specific parameter point for the global fit or a fit restricted to only a sector ($R_{K^{(*)}}$, $R_{D^{(*)}}$, electroweak, etc.) respectively.

- The functions `prediction` and `pull_obs` return the NP prediction and the pull for a single observable.

- The function `newlist` creates a YAML file containing the list of all observables included in the fit, ordered according to their SM pull.

ellipse

The module `ellipse.py` is used to perform the Hessian approximation of Eq. (6.8) around the best-fit point.

- The function `minimum` calculates the minimum of the log-likelihood and returns the best-fit point, the SVD of the Hessian matrix, and the log-likelihood and significance of the fit.

- All this data can be saved to a YAML file and retrieved with the functions `save` and `load`.

- The function `parametrize` maps the points of the unit hypersphere to points in the ellipsoid of (approximate) constant likelihood.

- Finally, the function `notablepoints` creates a table with the points at the 1σ ellipsoid obtained when changing one Wilson coefficient or when moving along the principal axes.

obsuncert

The function `calculate` of the module `obsuncert` calculates the predictions in the fit for the observables $R_{K^{(*)}}$ and $R_{D^{(*)}}$, and saves the results to a YAML file. In order to estimate the uncertainty associated to the fit, the function uses a Montecarlo algorithm to generate a small sample distributed according to the likelihood function. If used with the argument `mode = 'exact'`, the complete log-likelihood is used, and otherwise the Hessian approximation of the likelihood is used instead.

comparepulls

The module `comparepulls` contains functions to compare the pulls of one or more observables between different points in the parameter space.

- The function `compare` generates the tables in Appendix C comparing the pulls in the SM and in the best fit for all the observables included.
- The function `pointpull` identifies the observables whose pulls change the most when comparing the best-fit point to any other given point in parameter space, and the function `notablepulls` does the same between the best-fit point and the points obtained by `notablepoints` of the `ellipse` module.
- Finally, `pullevolution` calculates the change in the pulls of any observable when one Wilson coefficient is modified or when moving along one of the principal axes of the ellipsoid.

plots

The module `plots` contains several functions to graphically plot the results obtained using the previous modules.

- The function `hatch_contour` generalizes `flavio`'s `contour`, allowing the use of any colour and hatch pattern for the contour plots.
- This function is then used by `likelihood_plot`, that processes the likelihoods of parameter points distributed along a grid and adds the axis labels, legend and a marker for the best-fit point. This function, unlike `flavio`'s `likelihood_contour`, separates the plotting from the calculation of the likelihoods, making much more easier to modify the appearance of the plot. This function is an evolution of the function `plot` from the previous section, including more options to change the style of the plot.
- The function `binerrorbox` is used to plot a rectangular box marking the uncertainty of an observable, with an horizontal line for its central value.
- The function `errorplot` plots `binerrorboxes` for the SM predictions and experimental values, and errorbars for predictions in NP scenarios, for the $R_{K^{(*)}}$ and $R_{D^{(*)}}$ observables. This function is an evolution of the one with the same name in the previous section, and now draws an horizontal line for the central value of the observables.
- The function `compare_plot` plots the pull for every observable in the SM and in the best-fit point.

- The function `evolution_plot` plots the pulls of several observables when one Wilson coefficient is modified or when moving along one of the principal axes of the ellipsoid.

All the plots are saved in two vectorial formats: PDF, which can be opened on their own on any operating system, and PGF, which can be included in a TEXfile and compiled.

ml

The module `ml` contains the functions used in the Machine-Learning analysis of section 7.4.

- The function `train` takes a dataset of parameter points and their likelihood and trains an `XGBoost` model to predict them. The function saves the validation dataset, not used for training, and the trained model as a JSON file.
- The function `load_model` opens the JSON file with the trained `XGBoost` model.
- The function `regr` creates a regression plot between the actual likelihoods and the ML predictions in the validation datasets.
- The function `hist` creates a histogram for the likelihoods of the new points generated by the Montecarlo-ML algorithm, and compares it with the probability distribution function of the χ^2 distribution with the corresponding d.o.f..
- The function `SHAP_bf` computes the SHAP values for each parameter in the best-fit point.
- The function `SHAP_summary` calculates the SHAP values for each point in the dataset and plots their frequency.
- The function `SHAP_param` plots the SHAP values against each parameter in the fit.

Jupyter notebooks

The `jupyter` notebooks available at [463] demonstrate the usage of the code described above. The notebooks in the folder `PaperSMEFT` have been used to generate step-by-step all the results in section 6.3, the notebooks in the folder `PaperILC` to generate the results in section 6.4, and the notebooks in the folder `PaperML` to generate the results in chapter 7.

Appendix C

Predictions of the observables

The tables in this appendix contains all observables that contribute to the global fit, as well as their prediction in the NP scenarios of chapters 6 and 7 and their pull in both the scenario (NP pull) and SM (SM pull). Predictions for dimensionful observables are expressed in the corresponding power of GeV (for example, ΔM_s in GeV and σ^0_{had} in GeV^{-2}). The notation $\langle\cdot\rangle$ means that the observable is binned in the invariant mass-squared of the di-lepton system q^2, with the endpoints of the bin in GeV^2 are indicated in the superscript. Observables are ordered according to their SM pull, and color-coded according to the difference between the SM scenario and SM pulls: green observables have a better pull in the NP scenario, red observables have a better pull in the SM and white observables have a similar pull in both cases.

Section C.1 contains the pulls and predictions for the global fit to Scenario VII proposed in Chapter 6, where there are independent New Physics contributions to the Wilson coefficients $C^e_{\ell q}$, $C^\mu_{\ell q}$ and $C^\tau_{\ell q}$. Section C.2 contains the pulls and predictions for the global fit to Scenario II proposed in Chapter 7, where the New Physics contributes to the Wilson coefficient $C^{3333}_{\ell q(1)} = C^{3333}_{\ell q(3)}$ in the interaction basis, which is then rotated to both the first and second generations of fermions in the mass basis. The fits performed in Chapter 5 included fewer observables, so their predictions are included in the body of the Chapter, in Tables 5.3 and 5.4.

C.1 Predictions of the observables in Scenario VII of chapter 6

	Observable	NP prediction	NP pull	SM pull
0	a_μ	0.0011659	4.2 σ	4.2 σ
1	$\langle \frac{d\overline{\text{BR}}}{dq^2} \rangle (B_s \to \phi\mu^+\mu^-)^{[2.5,\,4.0]}$	4.6797×10^{-8}	3.3 σ	4 σ
2	$\langle F_L \rangle (B^+ \to K^{*+}\mu^+\mu^-)^{[2.5,\,4]}$	0.79641	3.3 σ	3.3 σ
3	$R_{\tau\ell}(B \to D^*\ell^+\nu)$	0.25225	2.8 σ	3.3 σ
4	$\langle P_2 \rangle (B^0 \to K^{*0}\mu^+\mu^-)^{[0.1,\,0.98]}$	-0.12728	3.2 σ	3.3 σ
5	$\langle R_{\mu e} \rangle (B^\pm \to K^\pm\ell^+\ell^-)^{[1.1,\,6.0]}$	0.86244	0.38 σ	3.2 σ

	Observable	NP prediction	NP pull	SM pull
6	$\langle \frac{d\overline{\mathrm{BR}}}{dq^2} \rangle (B_s \to \phi\mu^+\mu^-)^{[1.1,\,2.5]}$	5.0154×10^{-8}	2.6 σ	3.2 σ
7	$\langle \frac{d\overline{\mathrm{BR}}}{dq^2} \rangle (B_s \to \phi\mu^+\mu^-)^{[4.0,\,6.0]}$	4.9885×10^{-8}	2.5 σ	3.1 σ
8	$\left\langle \frac{dR}{d\theta} \right\rangle (e^+e^- \to W^+W^-)^{[198.38,\,0.8,\,1.0]}$	7.2259	2.9 σ	3 σ
9	$\langle P_5' \rangle (B^0 \to K^{*0}\mu^+\mu^-)^{[4,\,6]}$	-0.74244	2.7 σ	2.8 σ
10	$\langle \frac{d\mathrm{BR}}{dq^2} \rangle (B_s \to \phi\mu^+\mu^-)^{[0.1,\,0.98]}$	1.0842×10^{-7}	2.3 σ	2.7 σ
11	$\mathrm{BR}(W^\pm \to \tau^\pm \nu)$	0.10824	2.6 σ	2.6 σ
12	$\langle R_{\mu e} \rangle (B^0 \to K^{*0}\ell^+\ell^-)^{[1.1,\,6.0]}$	0.86267	1.6 σ	2.5 σ
13	ϵ'/ϵ	-3.0463×10^{-5}	2.5 σ	2.5 σ
14	$R_{\tau\mu}(B \to D^*\ell^+\nu)$	0.25716	2 σ	2.5 σ
15	$A_{\mathrm{FB}}^{0,b}$	0.10323	2.5 σ	2.4 σ
16	$\langle R_{\mu e} \rangle (B^0 \to K^{*0}\ell^+\ell^-)^{[0.045,\,1.1]}$	0.88927	2.1 σ	2.4 σ
17	$\frac{\langle \mathrm{BR} \rangle}{\mathrm{BR}} (B \to D^*\tau^+\nu)^{[10.4,\,10.93]}$	0.018511	2.3 σ	2.3 σ
18	A_e	0.14725	2.1 σ	2.2 σ
19	$\langle \frac{d\mathrm{BR}}{dq^2} \rangle (B^+ \to K^{*+}\mu^+\mu^-)^{[15.0,\,19.0]}$	5.8443×10^{-8}	1.7 σ	2.2 σ
20	$\left\langle \frac{dR}{d\theta} \right\rangle (e^+e^- \to W^+W^-)^{[189.09,\,0.8,\,1.0]}$	6.2442	2.2 σ	2.2 σ
21	$\langle P_4' \rangle (B^0 \to K^{*0}\mu^+\mu^-)^{[4,\,6]}$	-0.49957	2.1 σ	2.2 σ
22	$\tilde{B}_n^{[0.591]}$	0.98894	2.2 σ	2.2 σ
23	$\langle P_8' \rangle (B^0 \to K^{*0}\mu^+\mu^-)^{[1.1,\,2.5]}$	-0.017094	2.2 σ	2.2 σ
24	$\langle P_1 \rangle (B^0 \to K^{*0}\mu^+\mu^-)^{[1.1,\,2.5]}$	0.028313	2.1 σ	2.1 σ
25	$\langle P_3 \rangle (B^0 \to K^{*0}\mu^+\mu^-)^{[1.1,\,2.5]}$	0.003771	2.1 σ	2.1 σ
26	$\lvert\epsilon_K\rvert$	0.001705	2.4 σ	2.1 σ
27	$\langle \frac{d\mathrm{BR}}{dq^2} \rangle (B^+ \to K^{*+}\mu^+\mu^-)^{[4.0,\,6.0]}$	4.9242×10^{-8}	1.7 σ	2.1 σ
28	$\frac{\langle \mathrm{BR} \rangle}{\mathrm{BR}} (B \to D^*\tau^+\nu)^{[5.07,\,5.6]}$	0.063084	2.1 σ	2.1 σ
29	$\langle \frac{d\mathrm{BR}}{dq^2} \rangle (B^\pm \to K^\pm\mu^+\mu^-)^{[4.0,\,5.0]}$	3.1613×10^{-8}	1.6 σ	2.1 σ
30	$\mathrm{BR}(K_L \to e^+e^-)$	1.8922×10^{-13}	2.1 σ	2.1 σ
31	$\mathrm{BR}(B^\pm \to K^\pm\tau^+\tau^-)$	1.8473×10^{-7}	2 σ	2 σ
32	$\langle \frac{d\mathrm{BR}}{dq^2} \rangle (B^0 \to K^{*0}\mu^+\mu^-)^{[15.0,\,19.0]}$	5.3937×10^{-8}	1.4 σ	2.1 σ
33	$\langle P_5' \rangle (B^+ \to K^{*+}\mu^+\mu^-)^{[15,\,19]}$	-0.59572	2 σ	2 σ
34	$\langle A_{\mathrm{FB}}^{\ell h} \rangle (\Lambda_b \to \Lambda\mu^+\mu^-)^{[15,\,20]}$	0.1631	2.1 σ	2 σ
35	$\langle P_2 \rangle (B^+ \to K^{*+}\mu^+\mu^-)^{[4,\,6]}$	0.27461	2 σ	2.1 σ
36	$\langle \frac{d\overline{\mathrm{BR}}}{dq^2} \rangle (B_s \to \phi\mu^+\mu^-)^{[1.0,\,6.0]}$	4.9208×10^{-8}	1.7 σ	2 σ
37	$\langle P_3 \rangle (B^+ \to K^{*+}\mu^+\mu^-)^{[0.1,\,0.98]}$	0.00148	2 σ	2 σ
38	$\mathrm{BR}(\tau^- \to \mu^-\nu\bar{\nu})$	0.17272	2.3 σ	2 σ
39	$\overline{\mathrm{BR}}(B_s \to \mu^+\mu^-)$	3.3492×10^{-9}	1.1 σ	1.9 σ
40	$\langle P_2 \rangle (B^0 \to K^{*0}\mu^+\mu^-)^{[4,\,6]}$	0.27271	1.7 σ	1.9 σ
41	$\langle \frac{d\mathrm{BR}}{dq^2} \rangle (B^0 \to K^0\mu^+\mu^-)^{[4.0,\,6.0]}$	2.9215×10^{-8}	1.6 σ	2 σ
42	a_e	0.0011597	1.9 σ	1.9 σ
43	$\langle P_5' \rangle (B^0 \to K^{*0}\mu^+\mu^-)^{[2.5,\,4]}$	-0.46464	1.8 σ	1.9 σ
44	$\langle \frac{d\mathrm{BR}}{dq^2} \rangle (B^0 \to K^0\mu^+\mu^-)^{[15.0,\,22.0]}$	1.264×10^{-8}	1.4 σ	1.9 σ
45	$\frac{\langle \mathrm{BR} \rangle}{\mathrm{BR}} (B \to D\tau^+\nu)^{[7.73,\,8.27]}$	0.091527	1.9 σ	1.9 σ
46	$\langle \frac{d\mathrm{BR}}{dq^2} \rangle (B^\pm \to K^\pm\mu^+\mu^-)^{[5.0,\,6.0]}$	3.138×10^{-8}	1.4 σ	1.9 σ
47	$\frac{\langle \mathrm{BR} \rangle}{\mathrm{BR}} (B \to D^*\tau^+\nu)^{[7.2,\,7.73]}$	0.10189	1.9 σ	1.9 σ
48	$\langle \frac{d\mathrm{BR}}{dq^2} \rangle (B^\pm \to K^\pm\mu^+\mu^-)^{[1.1,\,2.0]}$	3.2122×10^{-8}	1.4 σ	1.9 σ
49	$\left\langle \frac{dR}{d\theta} \right\rangle (e^+e^- \to W^+W^-)^{[198.38,\,-0.6,\,-0.4]}$	0.83212	1.9 σ	1.9 σ
50	$\langle P_1 \rangle (B^0 \to K^{*0}\mu^+\mu^-)^{[4.3,\,6]}$	-0.17938	1.9 σ	1.9 σ
51	$\mu_{Zh}(h \to c\bar{c})$	1	1.8 σ	1.8 σ
52	$\left\langle \frac{dR}{d\theta} \right\rangle (e^+e^- \to W^+W^-)^{[198.38,\,0.6,\,0.8]}$	4.4207	1.7 σ	1.8 σ
53	$\langle \frac{d\mathrm{BR}}{dq^2} \rangle (B^0 \to K^{*0}\mu^+\mu^-)^{[1.1,\,2.5]}$	4.3064×10^{-8}	1.3 σ	1.8 σ
54	$\left\langle \frac{dR}{d\theta} \right\rangle (e^+e^- \to W^+W^-)^{[182.66,\,-1.0,\,-0.8]}$	0.69934	1.7 σ	1.8 σ
55	$\langle \frac{d\mathrm{BR}}{dq^2} \rangle (B^0 \to K^{*0}\mu^+\mu^-)^{[4.3,\,6]}$	4.5956×10^{-8}	1.2 σ	1.7 σ
56	$\langle \frac{d\mathrm{BR}}{dq^2} \rangle (B^0 \to K^{*0}\mu^+\mu^-)^{[4.0,\,6.0]}$	4.5477×10^{-8}	1.2 σ	1.7 σ
57	$\left\langle \frac{dR}{d\theta} \right\rangle (e^+e^- \to W^+W^-)^{[198.38,\,-1.0,\,-0.8]}$	0.53951	1.8 σ	1.7 σ
58	m_W	80.359	1.7 σ	1.7 σ

	Observable	NP prediction	NP pull	SM pull
59	$\left\langle \frac{dR}{d\theta} \right\rangle (e^+e^- \to W^+W^-)^{[182.66,\ 0.0,\ 0.2]}$	1.7271	1.7 σ	1.7 σ
60	$\langle \frac{d\mathrm{BR}}{dq^2} \rangle (B^0 \to K^0\mu^+\mu^-)^{[2.0,\ 4.0]}$	2.9586×10^{-8}	1.4 σ	1.7 σ
61	$\mu_{Wh}(h \to \tau^+\tau^-)$	1	1.7 σ	1.7 σ
62	$\left\langle \frac{dR}{d\theta} \right\rangle (e^+e^- \to W^+W^-)^{[205.92,\ 0.2,\ 0.4]}$	2.0516	1.7 σ	1.7 σ
63	$\left\langle \frac{dR}{d\theta} \right\rangle (e^+e^- \to W^+W^-)^{[205.92,\ -0.6,\ -0.4]}$	0.76722	1.7 σ	1.7 σ
64	$\mu_{t\bar{t}h}(h \to W^+W^-)$	1	1.7 σ	1.7 σ
65	$\langle \frac{d\mathrm{BR}}{dq^2} \rangle (\Lambda_b \to \Lambda\mu^+\mu^-)^{[15,\ 20]}$	6.4546×10^{-8}	2 σ	1.7 σ
66	$R(e^+e^- \to W^+W^-)^{[182.7]}$	0.99786	1.7 σ	1.6 σ
67	$A_{\Delta\Gamma}(B_s \to \phi\gamma)$	0.030488	1.7 σ	1.7 σ
68	$\langle \frac{d\mathrm{BR}}{dq^2} \rangle (B^\pm \to K^\pm\mu^+\mu^-)^{[15.0,\ 22.0]}$	1.3721×10^{-8}	0.9 σ	1.6 σ
69	$\mathrm{BR}(K_S \to \pi^+e^+\nu)$	0.00071896	1.6 σ	1.7 σ
70	$\langle P_5' \rangle (B^0 \to K^{*0}\mu^+\mu^-)^{[0.1,\ 0.98]}$	0.6688	1.5 σ	1.7 σ
71	$\frac{\langle \mathrm{BR} \rangle}{\mathrm{BR}} (B \to D\tau^+\nu)^{[9.0,\ 9.5]}$	0.066851	1.6 σ	1.6 σ
72	$R_{\tau\ell}(B \to D\ell^+\nu)$	0.30611	1.3 σ	1.6 σ
73	$\langle P_6' \rangle (B^+ \to K^{*+}\mu^+\mu^-)^{[15,\ 19]}$	-0.0023099	1.6 σ	1.6 σ
74	$\langle F_L \rangle (B^0 \to K^{*0}\mu^+\mu^-)^{[1.1,\ 2.5]}$	0.74681	1.4 σ	1.6 σ
75	$\tau_{B_s \to \mu\mu}$	2.4506×10^{12}	1.6 σ	1.6 σ
76	$\mathrm{BR}(K_L \to \pi^+e^+\nu)$	0.41064	1.4 σ	1.5 σ
77	$\langle D_{P_5'}^{\mu e} \rangle (B^0 \to K^{*0}\ell^+\ell^-)^{[14.18,\ 19.0]}$	0.0015837	1.5 σ	1.5 σ
78	$\langle \frac{d\overline{\mathrm{BR}}}{dq^2} \rangle (B^\pm \to K^\pm\mu^+\mu^-)^{[3.0,\ 4.0]}$	3.1809×10^{-8}	1 σ	1.5 σ
79	$\langle P_6' \rangle (B^0 \to K^{*0}\mu^+\mu^-)^{[4,\ 6]}$	-0.031906	1.5 σ	1.5 σ
80	$\langle P_5' \rangle (B^0 \to K^{*0}\mu^+\mu^-)^{[1.1,\ 2.5]}$	0.17609	1.3 σ	1.5 σ
81	$A_{\mathrm{FB}}^{0,\tau}$	0.016283	1.5 σ	1.5 σ
82	$\langle \frac{d\overline{\mathrm{BR}}}{dq^2} \rangle (B_s \to \phi\mu^+\mu^-)^{[15.0,\ 19.0]}$	5.0587×10^{-8}	0.69 σ	1.5 σ
83	R_μ^0	20.74	1.3 σ	1.5 σ
84	$\langle \frac{d\mathrm{BR}}{dq^2} \rangle (B^0 \to K^{*0}\mu^+\mu^-)^{[2.5,\ 4.0]}$	4.0902×10^{-8}	0.97 σ	1.5 σ
85	$\mathrm{BR}(B^- \to \pi^-\tau^+e^-)$	0	1.5 σ	1.5 σ
86	$\left\langle \frac{dR}{d\theta} \right\rangle (e^+e^- \to W^+W^-)^{[182.66,\ 0.2,\ 0.4]}$	2.1845	1.5 σ	1.5 σ
87	$\langle \overline{S_4} \rangle (B_s \to \phi\mu^+\mu^-)^{[15.0,\ 19.0]}$	-0.30176	1.5 σ	1.5 σ
88	$F_L(B^0 \to D^{*-}\tau^+\nu_\tau)$	0.46989	1.5 σ	1.5 σ
89	$\mathrm{BR}(B^+ \to K^+\nu\bar{\nu})$	4.3186×10^{-6}	1.5 σ	1.4 σ
90	$\mathrm{BR}(K_S \to \mu^+\mu^-)$	5.1859×10^{-12}	1.4 σ	1.4 σ
91	$\frac{\langle \mathrm{BR} \rangle}{\mathrm{BR}} (B \to D^*\tau^+\nu)^{[6.0,\ 6.5]}$	0.080351	1.4 σ	1.4 σ
92	$\mathrm{BR}(W^\pm \to \mu^\pm\nu)$	0.10855	1.5 σ	1.4 σ
93	R_e^0	20.729	1.5 σ	1.4 σ
94	$\langle A_9 \rangle (B^0 \to K^{*0}\mu^+\mu^-)^{[15,\ 19]}$	6.2164×10^{-5}	1.4 σ	1.4 σ
95	$R_{e\mu}(K^+ \to \ell^+\nu)$	2.4693×10^{-5}	2.1 σ	1.4 σ
96	$\langle P_5' \rangle (B^+ \to K^{*+}\mu^+\mu^-)^{[4,\ 6]}$	-0.74882	1.3 σ	1.3 σ
97	$\langle \mathrm{BR} \rangle (B \to X_s e^+e^-)^{[14.2,\ 25.0]}$	3.2516×10^{-7}	1.2 σ	1.4 σ
98	$\mathscr{F}t(^{10}\mathrm{C})$	4.6723×10^{27}	0.57 σ	1.4 σ
99	$\langle \frac{d\mathrm{BR}}{dq^2} \rangle (B^\pm \to K^\pm\mu^+\mu^-)^{[0,\ 2]}$	3.2172×10^{-8}	0.91 σ	1.3 σ
100	$\left\langle \frac{dR}{d\theta} \right\rangle (e^+e^- \to W^+W^-)^{[189.09,\ -0.2,\ 0.0]}$	1.3994	1.3 σ	1.3 σ
101	$\mathrm{BR}(B^+ \to e^+\nu)$	1.1308×10^{-11}	1.3 σ	1.3 σ
102	$\langle D_{P_5'}^{\mu e} \rangle (B^0 \to K^{*0}\ell^+\ell^-)^{[1.0,\ 6.0]}$	0.053944	1.2 σ	1.3 σ
103	$S_{\phi\gamma}$	-0.00025088	1.3 σ	1.3 σ
104	$\overline{\mathrm{BR}}(B_s \to e^+e^-)$	9.0501×10^{-14}	1.3 σ	1.3 σ
105	$\langle P_8' \rangle (B^0 \to K^{*0}\mu^+\mu^-)^{[4,\ 6]}$	-0.011885	1.4 σ	1.3 σ
106	$\langle P_4' \rangle (B^0 \to K^{*0}\mu^+\mu^-)^{[2,\ 4]}$	-0.33273	1.3 σ	1.3 σ
107	$\mathrm{BR}(K_S \to e^+e^-)$	1.6217×10^{-16}	1.3 σ	1.3 σ
108	$\mathrm{BR}(B^0 \to e^+e^-)$	2.5351×10^{-15}	1.3 σ	1.3 σ
109	$\mathrm{BR}(K_L \to \pi^0\nu\bar{\nu})$	3.505×10^{-11}	1.3 σ	1.3 σ
110	$\frac{\langle \mathrm{BR} \rangle}{\mathrm{BR}} (B \to D^*\tau^+\nu)^{[8.27,\ 8.8]}$	0.10324	1.3 σ	1.3 σ
111	$\mathrm{BR}(B^0 \to \rho^0\nu\bar{\nu})$	1.7848×10^{-7}	1.3 σ	1.3 σ
112	$\mathrm{BR}(B^- \to \pi^-e^+\tau^-)$	0	1.3 σ	1.3 σ
113	$\langle R_{\mu e} \rangle (B^0 \to K^0\ell^+\ell^-)^{[4.0,\ 8.12]}$	0.86339	0.93 σ	1.3 σ

	Observable	NP prediction	NP pull	SM pull
114	$\mathrm{BR}(K^+ \to \pi^0 e^+ \nu)$	0.051494	1.2 σ	1.3 σ
115	$\left\langle \frac{dR}{d\theta} \right\rangle (e^+e^- \to W^+W^-)^{[205.92,\ 0.0,\ 0.2]}$	1.5572	1.3 σ	1.3 σ
116	$\mathrm{BR}(B^0 \to K^{*0} \nu \bar{\nu})$	9.3704×10^{-6}	1.3 σ	1.3 σ
117	$\langle F_L \rangle (B^0 \to K^{*0} \mu^+ \mu^-)^{[2,\ 4]}$	0.79504	1.2 σ	1.2 σ
118	$\mu_{t\bar{t}h}(h \to VV)$	1	1.3 σ	1.3 σ
119	$\mathrm{BR}(K_S \to \pi^+ \mu^+ \nu)$	0.00047741	1.3 σ	1.2 σ
120	$\frac{\langle \mathrm{BR} \rangle}{\mathrm{BR}} (B \to D \tau^+ \nu)^{[9.86,\ 10.4]}$	0.052842	1.2 σ	1.2 σ
121	$\langle P_3 \rangle (B^0 \to K^{*0} \mu^+ \mu^-)^{[0.1,\ 0.98]}$	0.0014165	1.2 σ	1.2 σ
122	$S_{\psi K_S}$	0.76793	1.2 σ	1.2 σ
123	$\mu_{\mathrm{VBF}}(h \to b\bar{b})$	1	1.2 σ	1.2 σ
124	$\left\langle \frac{dR}{d\theta} \right\rangle (e^+e^- \to W^+W^-)^{[182.66,\ 0.6,\ 0.8]}$	3.7997	1.2 σ	1.2 σ
125	$\mathrm{BR}(\tau^+ \to K^+ \bar{\nu})$	0.0071074	1.1 σ	1.2 σ
126	$\frac{\langle \mathrm{BR} \rangle}{\mathrm{BR}} (B \to D^* \tau^+ \nu)^{[4.0,\ 4.5]}$	0.026461	1.2 σ	1.2 σ
127	$\langle \frac{d\mathrm{BR}}{dq^2} \rangle (B^0 \to K^{*0} \mu^+ \mu^-)^{[2,\ 4.3]}$	4.1071×10^{-8}	0.66 σ	1.1 σ
128	$\langle F_L \rangle (B^+ \to K^{*+} \mu^+ \mu^-)^{[1.1,\ 2.5]}$	0.75442	1.1 σ	1.2 σ
129	$\mu_{Zh}(h \to b\bar{b})$	1	1.1 σ	1.1 σ
130	$\mathrm{BR}(B^+ \to K^{*+} \nu \bar{\nu})$	1.0088×10^{-5}	1.1 σ	1.1 σ
131	$\mu_{Zh}(h \to W^+W^-)$	1	1.1 σ	1.1 σ
132	$\langle P_4' \rangle (B^+ \to K^{*+} \mu^+ \mu^-)^{[15,\ 19]}$	-0.63457	1.1 σ	1.1 σ
133	$\mu_{Wh}(h \to W^+W^-)$	1	1.1 σ	1.1 σ
134	a_τ	0.0011772	1.2 σ	1.2 σ
135	$\mathrm{R}_{\mu e}(W^\pm \to \ell^\pm \nu)$	1.002	1.2 σ	1.1 σ
136	ΔM_s	1.2278×10^{-11}	0.8 σ	1.1 σ
137	$\langle \frac{d\mathrm{BR}}{dq^2} \rangle (B^\pm \to K^\pm \mu^+ \mu^-)^{[2.0,\ 3.0]}$	3.1977×10^{-8}	0.59 σ	1.1 σ
138	$\langle P_4' \rangle (B^+ \to K^{*+} \mu^+ \mu^-)^{[1.1,\ 2.5]}$	-0.047638	1.1 σ	1.1 σ
139	$\langle P_6' \rangle (B^0 \to K^{*0} \mu^+ \mu^-)^{[1.1,\ 2.5]}$	-0.069838	1.1 σ	1.1 σ
140	$\langle \mathrm{BR} \rangle (B \to X_s \mu^+ \mu^-)^{[1.0,\ 6.0]}$	1.5671×10^{-6}	0.96 σ	1.1 σ
141	$\left\langle \frac{dR}{d\theta} \right\rangle (e^+e^- \to W^+W^-)^{[182.66,\ -0.8,\ -0.6]}$	0.83817	1 σ	1.1 σ
142	$\langle P_8' \rangle (B^+ \to K^{*+} \mu^+ \mu^-)^{[0.1,\ 0.98]}$	-0.03255	1.1 σ	1.1 σ
143	$\mathrm{BR}(K^+ \to \pi^0 \mu^+ \nu)$	0.034081	1.1 σ	1 σ
144	$\langle P_5' \rangle (B^+ \to K^{*+} \mu^+ \mu^-)^{[1.1,\ 2.5]}$	0.14924	1 σ	1 σ
145	$\mathscr{F}t(^{46}\mathrm{V})$	4.6723×10^{27}	0.49 σ	1 σ
146	$\langle P_1 \rangle (B^0 \to K^{*0} \mu^+ \mu^-)^{[4,\ 6]}$	-0.17664	1.1 σ	1.1 σ
147	$\langle \overline{S_3} \rangle (B_s \to \phi \mu^+ \mu^-)^{[15.0,\ 19.0]}$	-0.20988	1.1 σ	1.1 σ
148	$\langle P_1 \rangle (B^0 \to K^{*0} \mu^+ \mu^-)^{[2,\ 4]}$	-0.08703	1.1 σ	1 σ
149	$\mu_{t\bar{t}h}(h \to \gamma\gamma)$	1	1 σ	1 σ
150	$\mu_{gg}(h \to Z\gamma)$	1	1 σ	1 σ
151	$\left\langle \frac{dR}{d\theta} \right\rangle (e^+e^- \to W^+W^-)^{[182.66,\ -0.6,\ -0.4]}$	1.008	0.98 σ	1 σ
152	$\mu_{Wh}(h \to \gamma\gamma)$	1	0.99 σ	0.99 σ
153	$\langle P_3 \rangle (B^0 \to K^{*0} \mu^+ \mu^-)^{[15,\ 19]}$	-0.00041326	1 σ	1 σ
154	$\langle P_5' \rangle (B^0 \to K^{*0} \mu^+ \mu^-)^{[15,\ 19]}$	-0.5926	1 σ	0.99 σ
155	$\langle P_1 \rangle (B^+ \to K^{*+} \mu^+ \mu^-)^{[0.1,\ 0.98]}$	0.044855	0.99 σ	0.99 σ
156	$\frac{\langle \mathrm{BR} \rangle}{\mathrm{BR}} (B \to D^* \tau^+ \nu)^{[10.5,\ 11.0]}$	0.0098782	0.96 σ	0.96 σ
157	$\left\langle \frac{dR}{d\theta} \right\rangle (e^+e^- \to W^+W^-)^{[189.09,\ -0.8,\ -0.6]}$	0.77821	0.98 σ	0.95 σ
158	$A_{\mathrm{CP}}(B \to X_{s+d}\gamma)$	-1.8859×10^{-18}	0.94 σ	0.94 σ
159	$\mu_{\mathrm{VBF}}(h \to W^+W^-)$	1	0.94 σ	0.94 σ
160	$\langle A_7 \rangle (B^0 \to K^{*0} \mu^+ \mu^-)^{[1.1,\ 6]}$	0.0025461	0.94 σ	0.94 σ
161	$\langle P_1 \rangle (B^+ \to K^{*+} \mu^+ \mu^-)^{[4,\ 6]}$	-0.17492	0.96 σ	0.96 σ
162	$\left\langle \frac{dR}{d\theta} \right\rangle (e^+e^- \to W^+W^-)^{[189.09,\ -0.6,\ -0.4]}$	0.92501	0.98 σ	0.94 σ
163	$\frac{\langle \mathrm{BR} \rangle}{\mathrm{BR}} (B \to D^* \tau^+ \nu)^{[7.73,\ 8.27]}$	0.10629	0.94 σ	0.94 σ
164	$\langle P_4' \rangle (B^0 \to K^{*0} \mu^+ \mu^-)^{[0.1,\ 0.98]}$	0.25299	0.96 σ	0.95 σ
165	$R(e^+e^- \to W^+W^-)^{[204.9]}$	0.99771	0.81 σ	0.94 σ
166	$R(e^+e^- \to W^+W^-)^{[188.6]}$	0.99781	0.75 σ	0.92 σ
167	$\langle \mathrm{BR} \rangle (B \to X_s \mu^+ \mu^-)^{[14.2,\ 25.0]}$	3.2225×10^{-7}	1 σ	0.91 σ
168	$\langle P_4' \rangle (B^+ \to K^{*+} \mu^+ \mu^-)^{[0.1,\ 0.98]}$	0.23607	0.84 σ	0.83 σ
169	$\langle D^{\mu e}_{P_4'} \rangle (B^0 \to K^{*0} \ell^+ \ell^-)^{[1.0,\ 6.0]}$	0.022819	0.86 σ	0.91 σ

	Observable	NP prediction	NP pull	SM pull
170	$\frac{\langle \mathrm{BR} \rangle}{\mathrm{BR}}(B \to D\tau^+\nu)^{[10.93,\ 11.47]}$	0.023168	0.9 σ	0.9 σ
171	$\left\langle \frac{dR}{d\theta} \right\rangle (e^+e^- \to W^+W^-)^{[205.92,\ -0.4,\ -0.2]}$	0.96897	0.94 σ	0.9 σ
172	A_τ	0.14743	1 σ	0.9 σ
173	$\frac{\langle \mathrm{BR} \rangle}{\mathrm{BR}}(B \to D\tau^+\nu)^{[6.67,\ 7.2]}$	0.095702	0.89 σ	0.89 σ
174	$\langle A_7 \rangle (B^0 \to K^{*0}\mu^+\mu^-)^{[15,\ 19]}$	0.00010742	0.89 σ	0.89 σ
175	$\tilde{a}_n^{[0.695]}$	-0.09921	0.89 σ	0.89 σ
176	$\mu_{gg}(h \to \mu^+\mu^-)$	1	0.89 σ	0.89 σ
177	$\mu_{Zh}(h \to \gamma\gamma)$	1	0.88 σ	0.88 σ
178	$\langle \overline{S_4} \rangle (B_s \to \phi\mu^+\mu^-)^{[2.0,\ 5.0]}$	-0.14405	0.88 σ	0.87 σ
179	$\mu_{gg}(h \to ZZ)$	1	0.88 σ	0.88 σ
180	$\langle F_L \rangle (B^0 \to K^{*0}\mu^+\mu^-)^{[1,\ 2]}$	0.70831	0.72 σ	0.87 σ
181	$\langle \overline{F_L} \rangle (B_s \to \phi\mu^+\mu^-)^{[2.0,\ 5.0]}$	0.80957	0.87 σ	0.88 σ
182	$\frac{\langle \mathrm{BR} \rangle}{\mathrm{BR}}(B \to D\tau^+\nu)^{[10.0,\ 10.5]}$	0.046209	0.87 σ	0.87 σ
183	$\left\langle \frac{dR}{d\theta} \right\rangle (e^+e^- \to W^+W^-)^{[198.38,\ 0.4,\ 0.6]}$	2.9975	0.83 σ	0.87 σ
184	$\mathrm{BR}(B^- \to K^-e^+\tau^-)$	0	0.87 σ	0.87 σ
185	$\left\langle \frac{dR}{d\theta} \right\rangle (e^+e^- \to W^+W^-)^{[182.66,\ 0.4,\ 0.6]}$	2.8168	0.85 σ	0.87 σ
186	$\frac{\langle \mathrm{BR} \rangle}{\mathrm{BR}}(B \to D\tau^+\nu)^{[8.8,\ 9.33]}$	0.074315	0.86 σ	0.86 σ
187	$\mu_{Vh}(h \to b\bar{b})$	1	0.86 σ	0.86 σ
188	$\frac{\langle \mathrm{BR} \rangle}{\mathrm{BR}}(B \to D\tau^+\nu)^{[5.5,\ 6.0]}$	0.081066	0.86 σ	0.86 σ
189	$\mathrm{BR}(\tau^- \to e^-\nu\bar{\nu})$	0.17716	2 σ	0.84 σ
190	$\frac{\langle \mathrm{BR} \rangle}{\mathrm{BR}}(B \to D^*\tau^+\nu)^{[8.8,\ 9.33]}$	0.097951	0.85 σ	0.85 σ
191	$\frac{\langle \mathrm{BR} \rangle}{\mathrm{BR}}(B \to D^*\tau^+\nu)^{[5.5,\ 6.0]}$	0.069889	0.84 σ	0.84 σ
192	$\frac{\langle \mathrm{BR} \rangle}{\mathrm{BR}}(B \to D\tau^+\nu)^{[7.2,\ 7.73]}$	0.094208	0.84 σ	0.84 σ
193	$\mathscr{F}t(^{22}\mathrm{Mg})$	4.6723×10^{27}	0.35 σ	0.85 σ
194	$\frac{\langle \mathrm{BR} \rangle}{\mathrm{BR}}(B \to D^*\tau^+\nu)^{[6.13,\ 6.67]}$	0.089674	0.83 σ	0.83 σ
195	$\frac{\langle \mathrm{BR} \rangle}{\mathrm{BR}}(B \to D\tau^+\nu)^{[9.5,\ 10.0]}$	0.05713	0.83 σ	0.83 σ
196	$\frac{\langle \mathrm{BR} \rangle}{\mathrm{BR}}(B \to D\tau^+\nu)^{[10.4,\ 10.93]}$	0.038397	0.83 σ	0.83 σ
197	$A_{\mathrm{FB}}^{0,c}$	0.073719	0.86 σ	0.83 σ
198	$\langle A_8 \rangle (B^0 \to K^{*0}\mu^+\mu^-)^{[1.1,\ 6]}$	0.0012012	0.83 σ	0.83 σ
199	$\mathrm{BR}(W^\pm \to e^\pm\nu)$	0.10833	0.77 σ	0.82 σ
200	$\frac{\langle \mathrm{BR} \rangle}{\mathrm{BR}}(B \to D\tau^+\nu)^{[6.13,\ 6.67]}$	0.095556	0.82 σ	0.82 σ
201	$\left\langle \frac{dR}{d\theta} \right\rangle (e^+e^- \to W^+W^-)^{[189.09,\ 0.4,\ 0.6]}$	2.9406	0.78 σ	0.81 σ
202	$\mathscr{F}t(^{26m}\mathrm{Al})$	4.6723×10^{27}	1.4 σ	0.82 σ
203	$\langle P_6' \rangle (B^0 \to K^{*0}\mu^+\mu^-)^{[15,\ 19]}$	-0.0023148	0.82 σ	0.81 σ
204	$\langle A_9 \rangle (B^0 \to K^{*0}\mu^+\mu^-)^{[1.1,\ 6]}$	0.00013597	0.8 σ	0.8 σ
205	$\langle A_{\mathrm{FB}}^{\ell} \rangle (\Lambda_b \to \Lambda\mu^+\mu^-)^{[15,\ 20]}$	-0.35236	0.83 σ	0.81 σ
206	$\mu_{\mathrm{VBF}}(h \to \tau^+\tau^-)$	1	0.8 σ	0.8 σ
207	$\langle A_{\mathrm{FB}} \rangle (B^0 \to K^{*0}\mu^+\mu^-)^{[4.3,\ 6]}$	0.12379	0.75 σ	0.8 σ
208	$\frac{\langle \mathrm{BR} \rangle}{\mathrm{BR}}(B \to D^*\tau^+\nu)^{[6.67,\ 7.2]}$	0.096421	0.8 σ	0.8 σ
209	$\mathrm{BR}(K_L \to \pi^+\mu^+\nu)$	0.27267	0.92 σ	0.78 σ
210	$\frac{\langle \mathrm{BR} \rangle}{\mathrm{BR}}(B \to D\tau^+\nu)^{[6.0,\ 6.5]}$	0.087333	0.78 σ	0.78 σ
211	$\langle P_1 \rangle (B^0 \to K^{*0}\mu^+\mu^-)^{[2.5,\ 4]}$	-0.10919	0.74 σ	0.76 σ
212	$\tilde{A}_n^{[0.586]}$	-0.11027	0.78 σ	0.78 σ
213	$\langle P_4' \rangle (B^+ \to K^{*+}\mu^+\mu^-)^{[4,\ 6]}$	-0.4979	0.75 σ	0.74 σ
214	$\langle P_1 \rangle (B^0 \to K^{*0}e^+e^-)^{[0.000784,\ 0.257]}$	0.032439	0.71 σ	0.71 σ
215	$\left\langle \frac{dR}{d\theta} \right\rangle (e^+e^- \to W^+W^-)^{[189.09,\ -1.0,\ -0.8]}$	0.65839	0.81 σ	0.77 σ
216	$\langle P_2 \rangle (B^0 \to K^{*0}\mu^+\mu^-)^{[2.5,\ 4]}$	-0.10196	0.54 σ	0.78 σ
217	$\left\langle \frac{dR}{d\theta} \right\rangle (e^+e^- \to W^+W^-)^{[205.92,\ 0.8,\ 1.0]}$	7.772	0.72 σ	0.77 σ
218	$R(e^+e^- \to W^+W^-)^{[199.5]}$	0.99774	0.63 σ	0.76 σ
219	$\langle F_L \rangle (B^0 \to K^{*0}\mu^+\mu^-)^{[0,\ 2]}$	0.36926	0.63 σ	0.75 σ
220	$\langle P_3 \rangle (B^+ \to K^{*+}\mu^+\mu^-)^{[2.5,\ 4]}$	0.0040249	0.78 σ	0.78 σ
221	$\frac{\langle \mathrm{BR} \rangle}{\mathrm{BR}}(B \to D\tau^+\nu)^{[7.5,\ 8.0]}$	0.086998	0.75 σ	0.75 σ
222	$\tilde{A}_n^{[0.559]}$	-0.11027	0.75 σ	0.75 σ
223	$\left\langle \frac{dR}{d\theta} \right\rangle (e^+e^- \to W^+W^-)^{[198.38,\ -0.4,\ -0.2]}$	1.0179	0.79 σ	0.75 σ
224	$\langle P_3 \rangle (B^+ \to K^{*+}\mu^+\mu^-)^{[4,\ 6]}$	0.0026242	0.72 σ	0.72 σ
225	$\left\langle \frac{dR}{d\theta} \right\rangle (e^+e^- \to W^+W^-)^{[205.92,\ 0.4,\ 0.6]}$	2.8975	0.7 σ	0.74 σ

	Observable	NP prediction	NP pull	SM pull
226	$\langle P_1\rangle(B^0\to K^{*0}\mu^+\mu^-)^{[2,\,4.3]}$	-0.098168	0.76 σ	0.75 σ
227	R_b^0	0.21582	0.71 σ	0.73 σ
228	$\mu_{\rm VBF}(h\to\gamma\gamma)$	1	0.72 σ	0.72 σ
229	$\langle\overline{F_L}\rangle(B_s\to\phi\mu^+\mu^-)^{[15.0,\,19.0]}$	0.34157	0.72 σ	0.71 σ
230	$\langle F_L\rangle(B^0\to K^{*0}\mu^+\mu^-)^{[4,\,6]}$	0.71323	0.73 σ	0.7 σ
231	$\tau_n^{[0.655]}$	1.3812×10^{27}	0.74 σ	0.71 σ
232	$\langle A_{\rm FB}\rangle(B^0\to K^{*0}\mu^+\mu^-)^{[1,\,2]}$	-0.16334	0.66 σ	0.7 σ
233	$\left\langle\frac{dR}{d\theta}\right\rangle(e^+e^-\to W^+W^-)^{[198.38,\,0.2,\,0.4]}$	2.1565	0.67 σ	0.71 σ
234	$\left\langle\frac{dR}{d\theta}\right\rangle(e^+e^-\to W^+W^-)^{[189.09,\,0.0,\,0.2]}$	1.711	0.73 σ	0.7 σ
235	R_{uc}^0	0.17224	0.69 σ	0.69 σ
236	$\mathscr{F}t(^{34}{\rm Ar})$	4.6723×10^{27}	1.1 σ	0.7 σ
237	$\langle P_2\rangle(B^+\to K^{*+}\mu^+\mu^-)^{[0.1,\,0.98]}$	-0.13065	0.64 σ	0.69 σ
238	$\langle F_L\rangle(B^0\to K^{*0}\mu^+\mu^-)^{[0.1,\,0.98]}$	0.27912	0.4 σ	0.67 σ
239	$A_{\rm FB}^{0,e}$	0.016263	0.71 σ	0.69 σ
240	$\mu_{gg}(h\to b\bar{b})$	1	0.68 σ	0.68 σ
241	$\frac{\langle{\rm BR}\rangle}{\rm BR}(B\to D\tau^+\nu)^{[8.5,\,9.0]}$	0.075222	0.68 σ	0.68 σ
242	${\rm BR}(B^+\to\pi^+\nu\bar{\nu})$	1.115×10^{-7}	0.68 σ	0.68 σ
243	$\frac{\langle{\rm BR}\rangle}{\rm BR}(B\to D^*\tau^+\nu)^{[7.5,\,8.0]}$	0.097746	0.68 σ	0.68 σ
244	$\frac{\langle{\rm BR}\rangle}{\rm BR}(B\to D\tau^+\nu)^{[10.5,\,11.0]}$	0.034069	0.68 σ	0.68 σ
245	$\left\langle\frac{dR}{d\theta}\right\rangle(e^+e^-\to W^+W^-)^{[189.09,\,0.6,\,0.8]}$	4.1152	0.64 σ	0.68 σ
246	${\rm BR}(B^+\to\rho^+\nu\bar{\nu})$	3.8453×10^{-7}	0.68 σ	0.68 σ
247	$\langle P_6'\rangle(B^0\to K^{*0}\mu^+\mu^-)^{[0.1,\,0.98]}$	-0.054674	0.7 σ	0.7 σ
248	$\frac{{\rm BR}(B^0\to K^{*0}\gamma)}{\overline{\rm BR}(B_s\to\phi\gamma)}$	1.0402	0.68 σ	0.68 σ
249	$\mu_{t\bar{t}h}(h\to ZZ)$	1	0.67 σ	0.67 σ
250	$\frac{\langle{\rm BR}\rangle}{\rm BR}(B\to D\tau^+\nu)^{[4.0,\,4.53]}$	0.039797	0.67 σ	0.67 σ
251	$\frac{\langle{\rm BR}\rangle}{\rm BR}(B\to D^*\tau^+\nu)^{[10.0,\,10.5]}$	0.05616	0.66 σ	0.66 σ
252	$\mathscr{F}t(^{38}{\rm Ca})$	4.6723×10^{27}	0.17 σ	0.68 σ
253	$\langle P_5'\rangle(B^0\to K^{*0}\mu^+\mu^-)^{[4.3,\,6]}$	-0.7557	0.7 σ	0.65 σ
254	$\left\langle\frac{dR}{d\theta}\right\rangle(e^+e^-\to W^+W^-)^{[182.66,\,-0.2,\,0.0]}$	1.3984	0.67 σ	0.65 σ
255	${\rm R}_{\tau e}(W^\pm\to\ell^\pm\nu)$	0.99919	0.63 σ	0.65 σ
256	$\langle A_{\rm FB}\rangle(B^0\to K^{*0}\mu^+\mu^-)^{[2,\,4.3]}$	-0.037416	0.55 σ	0.63 σ
257	$\langle F_L\rangle(B^0\to K^{*0}\mu^+\mu^-)^{[2.5,\,4]}$	0.79417	0.6 σ	0.64 σ
258	${\rm BR}(B^0\to\mu^+\mu^-)$	9.313×10^{-11}	0.53 σ	0.66 σ
259	$\left\langle\frac{dR}{d\theta}\right\rangle(e^+e^-\to W^+W^-)^{[205.92,\,-1.0,\,-0.8]}$	0.52962	0.6 σ	0.64 σ
260	${\rm BR}(B^0\to\pi^0\nu\bar{\nu})$	5.1899×10^{-8}	0.63 σ	0.63 σ
261	$S_{K^*\gamma}$	-0.024607	0.58 σ	0.58 σ
262	$\frac{\langle{\rm BR}\rangle}{\rm BR}(B\to D\tau^+\nu)^{[4.0,\,4.5]}$	0.03694	0.63 σ	0.63 σ
263	$\mu_{Wh}(h\to b\bar{b})$	1	0.62 σ	0.62 σ
264	${\rm R}_{\tau\mu}(W^\pm\to\ell^\pm\nu)$	0.99718	0.4 σ	0.61 σ
265	$R(e^+e^-\to W^+W^-)^{[195.5]}$	0.99777	0.74 σ	0.61 σ
266	$\frac{\langle{\rm BR}\rangle}{\rm BR}(B\to D^*\tau^+\nu)^{[4.53,\,5.07]}$	0.047598	0.61 σ	0.61 σ
267	$\left\langle\frac{dR}{d\theta}\right\rangle(e^+e^-\to W^+W^-)^{[205.92,\,-0.8,\,-0.6]}$	0.63944	0.57 σ	0.61 σ
268	$\langle P_3\rangle(B^0\to K^{*0}\mu^+\mu^-)^{[4,\,6]}$	0.0026785	0.62 σ	0.62 σ
269	$\langle F_L\rangle(B^0\to K^{*0}\mu^+\mu^-)^{[4.3,\,6]}$	0.70555	0.6 σ	0.59 σ
270	$\mu_{Zh}(h\to\tau^+\tau^-)$	1	0.6 σ	0.6 σ
271	${\rm BR}(B^0\to\pi^-\tau^+\nu_\tau)$	0.00010418	0.61 σ	0.61 σ
272	Γ_Z	2.4935	0.86 σ	0.6 σ
273	$\mathscr{F}t(^{54}{\rm Co})$	4.6723×10^{27}	1.8 σ	0.6 σ
274	$\langle R_{\mu e}\rangle(B^+\to K^{*+}\ell^+\ell^-)^{[15.0,\,19.0]}$	0.85764	0.8 σ	0.59 σ
275	$\langle A_{\rm FB}\rangle(B^0\to K^{*0}\mu^+\mu^-)^{[0,\,2]}$	-0.10442	0.59 σ	0.58 σ
276	$\langle R_{\mu e}\rangle(B^\pm\to K^\pm\ell^+\ell^-)^{[4.0,\,8.12]}$	0.86338	0.95 σ	0.59 σ
277	D_n	5.0399×10^{-42}	0.58 σ	0.58 σ
278	A_b	0.93471	0.59 σ	0.59 σ
279	$\mu_{gg}(h\to W^+W^-)$	1	0.58 σ	0.58 σ
280	$\langle P_5'\rangle(B^0\to K^{*0}\mu^+\mu^-)^{[0.04,\,2]}$	0.52693	0.47 σ	0.52 σ
281	${\rm BR}(\tau^-\to e^-\mu^+e^-)$	0	0.58 σ	0.58 σ

	Observable	NP prediction	NP pull	SM pull
282	$\mathrm{BR}(B^- \to K^- \tau^+ \mu^-)$	0	0.57 σ	0.57 σ
283	$\langle P_8' \rangle (B^+ \to K^{*+} \mu^+ \mu^-)^{[15,\ 19]}$	0.0005773	0.57 σ	0.57 σ
284	$R_{\mu e}(B \to D^* \ell^+ \nu)$	0.96256	0.71 σ	0.56 σ
285	$\frac{\langle \mathrm{BR} \rangle}{\mathrm{BR}} (B \to D \tau^+ \nu)^{[8.27,\ 8.8]}$	0.083047	0.56 σ	0.56 σ
286	$\langle P_3 \rangle (B^+ \to K^{*+} \mu^+ \mu^-)^{[15,\ 19]}$	-0.00041161	0.58 σ	0.58 σ
287	$\langle P_5' \rangle (B^0 \to K^{*0} \mu^+ \mu^-)^{[1,\ 2]}$	0.3184	0.62 σ	0.54 σ
288	$\langle P_6' \rangle (B^0 \to K^{*0} \mu^+ \mu^-)^{[2.5,\ 4]}$	-0.054331	0.55 σ	0.56 σ
289	$\langle P_5' \rangle (B^+ \to K^{*+} \mu^+ \mu^-)^{[0.1,\ 0.98]}$	0.66506	0.5 σ	0.56 σ
290	$\frac{\langle \mathrm{BR} \rangle}{\mathrm{BR}} (B \to D \tau^+ \nu)^{[4.53,\ 5.07]}$	0.0622	0.53 σ	0.53 σ
291	$\langle R_{\mu e} \rangle (B^0 \to K^0 \ell^+ \ell^-)^{[14.18,\ 19.0]}$	0.86617	0.67 σ	0.53 σ
292	$\lambda_{AB}^{[0.581]}$	-1.251	0.53 σ	0.53 σ
293	$A_{\mathrm{FB}}^{0,\mu}$	0.016213	0.53 σ	0.53 σ
294	$\langle P_1 \rangle (B^+ \to K^{*+} \mu^+ \mu^-)^{[1.1,\ 2.5]}$	0.026958	0.5 σ	0.51 σ
295	$\langle A_8 \rangle (B^0 \to K^{*0} \mu^+ \mu^-)^{[15,\ 19]}$	7.9509×10^{-5}	0.52 σ	0.52 σ
296	$\frac{\langle \mathrm{BR} \rangle}{\mathrm{BR}} (B \to D \tau^+ \nu)^{[11.5,\ 12.0]}$	0.0018997	0.52 σ	0.52 σ
297	$\langle \frac{d\mathrm{BR}}{dq^2} \rangle (B^0 \to K^{*0} \mu^+ \mu^-)^{[0,\ 2]}$	7.9038×10^{-8}	0.7 σ	0.53 σ
298	$\mathrm{BR}(\tau^- \to \mu^- e^+ \mu^-)$	0	0.51 σ	0.51 σ
299	$\mathrm{BR}(\pi^+ \to e^+ \nu)$	0.0001231	0.76 σ	0.51 σ
300	$\langle \frac{d\mathrm{BR}}{dq^2} \rangle (B^+ \to K^{*+} \mu^+ \mu^-)^{[2.0,\ 4.0]}$	4.4449×10^{-8}	0.72 σ	0.48 σ
301	$R(e^+ e^- \to W^+ W^-)^{[206.6]}$	0.99769	0.66 σ	0.5 σ
302	$\langle R_{\mu e} \rangle (B^0 \to K^0 \ell^+ \ell^-)^{[0.1,\ 4.0]}$	0.86182	0.64 σ	0.5 σ
303	$\frac{\langle \mathrm{BR} \rangle}{\mathrm{BR}} (B \to D^* \tau^+ \nu)^{[4.5,\ 5.0]}$	0.042537	0.5 σ	0.5 σ
304	$\mu_{t\bar{t}h}(h \to \tau^+ \tau^-)$	1	0.49 σ	0.49 σ
305	$\left\langle \frac{dR}{d\theta} \right\rangle (e^+ e^- \to W^+ W^-)^{[182.66,\ -0.4,\ -0.2]}$	1.1777	0.51 σ	0.49 σ
306	$\mathrm{BR}(\tau^- \to \mu^- e^+ e^-)$	0	0.49 σ	0.49 σ
307	$\langle F_L \rangle (B^+ \to K^{*+} \mu^+ \mu^-)^{[15,\ 19]}$	0.33821	0.53 σ	0.53 σ
308	$\langle P_2 \rangle (B^+ \to K^{*+} \mu^+ \mu^-)^{[1.1,\ 2.5]}$	-0.45271	0.52 σ	0.52 σ
309	$\mathrm{BR}(B^0 \to K^0 \nu \bar{\nu})$	3.9987×10^{-6}	0.49 σ	0.48 σ
310	$\langle \frac{d\mathrm{BR}}{dq^2} \rangle (B^0 \to K^0 \mu^+ \mu^-)^{[0,\ 2]}$	2.9848×10^{-8}	0.31 σ	0.48 σ
311	$\langle F_L \rangle (B^0 \to K^{*0} \mu^+ \mu^-)^{[0.04,\ 2]}$	0.36926	0.6 σ	0.45 σ
312	$\mathrm{BR}(B_c \to \tau^+ \nu)$	0.023954	0.47 σ	0.46 σ
313	$\frac{\langle \mathrm{BR} \rangle}{\mathrm{BR}} (B \to D^* \tau^+ \nu)^{[7.0,\ 7.5]}$	0.094377	0.45 σ	0.45 σ
314	A_s	0.93552	0.45 σ	0.45 σ
315	$\mathrm{BR}(B^- \to K^{*-} e^+ \mu^-)$	0	0.45 σ	0.45 σ
316	$\left\langle \frac{dR}{d\theta} \right\rangle (e^+ e^- \to W^+ W^-)^{[198.38,\ -0.8,\ -0.6]}$	0.66133	0.41 σ	0.45 σ
317	$\overline{\mathrm{BR}}(B_s \to \phi \gamma)$	3.9614×10^{-5}	0.36 σ	0.43 σ
318	$\frac{\langle \mathrm{BR} \rangle}{\mathrm{BR}} (B \to D^* \tau^+ \nu)^{[9.86,\ 10.4]}$	0.067671	0.44 σ	0.44 σ
319	$\langle P_2 \rangle (B^0 \to K^{*0} \mu^+ \mu^-)^{[15,\ 19]}$	0.37173	0.42 σ	0.45 σ
320	$\langle P_1 \rangle (B^0 \to K^{*0} \mu^+ \mu^-)^{[15,\ 19]}$	-0.62362	0.44 σ	0.44 σ
321	$\langle P_2 \rangle (B^0 \to K^{*0} e^+ e^-)^{[0.000784,\ 0.257]}$	-0.012579	0.45 σ	0.46 σ
322	$\mu_{Wh}(h \to ZZ)$	1	0.43 σ	0.43 σ
323	$\frac{\langle \mathrm{BR} \rangle}{\mathrm{BR}} (B \to D \tau^+ \nu)^{[11.0,\ 11.5]}$	0.019884	0.43 σ	0.43 σ
324	$\langle \frac{d\mathrm{BR}}{dq^2} \rangle (B^\pm \to K^\pm \mu^+ \mu^-)^{[2,\ 4.3]}$	3.1865×10^{-8}	0.03 σ	0.41 σ
325	$\mu_{gg}(h \to \gamma\gamma)$	1	0.42 σ	0.42 σ
326	$\langle \mathrm{BR} \rangle (B \to X_s e^+ e^-)^{[1.0,\ 6.0]}$	1.8785×10^{-6}	0.2 σ	0.42 σ
327	$\langle P_4' \rangle (B^0 \to K^{*0} \mu^+ \mu^-)^{[0.04,\ 2]}$	0.15589	0.42 σ	0.43 σ
328	$\mathrm{BR}(K_L \to \mu^+ \mu^-)$	7.3261×10^{-9}	0.39 σ	0.41 σ
329	$\left\langle \frac{dR}{d\theta} \right\rangle (e^+ e^- \to W^+ W^-)^{[189.09,\ -0.4,\ -0.2]}$	1.1338	0.37 σ	0.41 σ
330	$\langle P_4' \rangle (B^+ \to K^{*+} \mu^+ \mu^-)^{[2.5,\ 4]}$	-0.37795	0.44 σ	0.42 σ
331	$\langle F_L \rangle (B^0 \to K^{*0} \mu^+ \mu^-)^{[2,\ 4.3]}$	0.79028	0.39 σ	0.43 σ
332	$\mathscr{F}t(^{74}\mathrm{Rb})$	4.6723×10^{27}	0.058 σ	0.39 σ
333	a_n	-0.09921	0.39 σ	0.39 σ
334	$\langle \frac{d\mathrm{BR}}{dq^2} \rangle (B^0 \to K^0 \mu^+ \mu^-)^{[2,\ 4.3]}$	2.9561×10^{-8}	0.24 σ	0.4 σ
335	$\langle P_1 \rangle (B^0 \to K^{*0} \mu^+ \mu^-)^{[0.1,\ 0.98]}$	0.043914	0.39 σ	0.38 σ
336	$\left\langle \frac{dR}{d\theta} \right\rangle (e^+ e^- \to W^+ W^-)^{[198.38,\ 0.0,\ 0.2]}$	1.6621	0.41 σ	0.38 σ
337	R_τ^0	20.772	0.16 σ	0.37 σ

	Observable	NP prediction	NP pull	SM pull
338	$\langle P_2\rangle(B^+ \to K^{*+}\mu^+\mu^-)^{[15,\ 19]}$	0.37336	0.35 σ	0.36 σ
339	$\mathscr{F}t(^{34}\mathrm{Cl})$	4.6723×10^{27}	2.1 σ	0.38 σ
340	$\langle R_{\mu e}\rangle(B^0 \to K^{*0}\ell^+\ell^-)^{[0.1,\ 8.0]}$	0.87689	0.066 σ	0.37 σ
341	$\langle R_{\mu e}\rangle(B^0 \to K^{*0}\ell^+\ell^-)^{[15.0,\ 19.0]}$	0.85765	0.72 σ	0.36 σ
342	$\mu_{\mathrm{VBF}}(h \to ZZ)$	1	0.35 σ	0.35 σ
343	$\langle A_{\mathrm{FB}}^{h}\rangle(\Lambda_b \to \Lambda\mu^+\mu^-)^{[15,\ 20]}$	-0.31823	0.34 σ	0.34 σ
344	A_μ	0.1468	0.32 σ	0.34 σ
345	$\overline{\mathrm{BR}}(B_s \to \tau^+\tau^-)$	8.6607×10^{-7}	0.33 σ	0.33 σ
346	$\mu_{t\bar{t}h}(h \to b\bar{b})$	1	0.32 σ	0.32 σ
347	$\langle F_L\rangle(B^+ \to K^{*+}\mu^+\mu^-)^{[4,\ 6]}$	0.71408	0.34 σ	0.32 σ
348	$\frac{\langle \mathrm{BR}\rangle}{\mathrm{BR}}(B \to D\tau^+\nu)^{[6.5,\ 7.0]}$	0.090073	0.32 σ	0.32 σ
349	$\langle P_8'\rangle(B^0 \to K^{*0}\mu^+\mu^-)^{[2.5,\ 4]}$	-0.017558	0.31 σ	0.31 σ
350	$\langle P_8'\rangle(B^+ \to K^{*+}\mu^+\mu^-)^{[4,\ 6]}$	-0.011748	0.29 σ	0.29 σ
351	$\frac{\langle \mathrm{BR}\rangle}{\mathrm{BR}}(B \to D\tau^+\nu)^{[4.5,\ 5.0]}$	0.055942	0.3 σ	0.3 σ
352	$\langle P_1\rangle(B^0 \to K^{*0}\mu^+\mu^-)^{[0.04,\ 2]}$	0.043605	0.29 σ	0.29 σ
353	$\langle F_L\rangle(B^+ \to K^{*+}\mu^+\mu^-)^{[0.1,\ 0.98]}$	0.288	0.38 σ	0.27 σ
354	$\sigma_{\mathrm{had}}^{0}$	0.00010662	1.3 σ	0.3 σ
355	$\mathscr{F}t(^{42}\mathrm{Sc})$	4.6723×10^{27}	1.1 σ	0.32 σ
356	$\mathrm{BR}(\bar{B}^0 \to \bar{K}^{*0}\mu^+e^-)$	0	0.3 σ	0.3 σ
357	$\langle P_2\rangle(B^+ \to K^{*+}\mu^+\mu^-)^{[2.5,\ 4]}$	-0.093553	0.41 σ	0.28 σ
358	R_n	2.1495×10^{-20}	0.32 σ	0.32 σ
359	$\langle R_{\mu e}\rangle(B^\pm \to K^\pm\ell^+\ell^-)^{[14.18,\ 19.0]}$	0.86616	0.78 σ	0.29 σ
360	$\langle R_{\mu e}\rangle(B^\pm \to K^\pm\ell^+\ell^-)^{[0.1,\ 4.0]}$	0.86182	0.25 σ	0.28 σ
361	$\langle P_5'\rangle(B^+ \to K^{*+}\mu^+\mu^-)^{[2.5,\ 4]}$	-0.48271	0.3 σ	0.27 σ
362	$\langle \overline{S_3}\rangle(B_s \to \phi\mu^+\mu^-)^{[2.0,\ 5.0]}$	-0.0080823	0.24 σ	0.24 σ
363	$\langle P_3\rangle(B^0 \to K^{*0}\mu^+\mu^-)^{[2.5,\ 4]}$	0.0040835	0.21 σ	0.21 σ
364	$\Gamma(\pi^+ \to \mu^+\nu)$	2.5233×10^{-17}	0.15 σ	0.25 σ
365	$S_{\psi\phi}$	0.040814	0.24 σ	0.25 σ
366	$\langle P_4'\rangle(B^0 \to K^{*0}\mu^+\mu^-)^{[2.5,\ 4]}$	-0.37916	0.31 σ	0.23 σ
367	$\mathrm{R}(W^+ \to cX)$	0.5	0.25 σ	0.25 σ
368	$x_{12}^{\mathrm{Im},D}$	2.0459×10^{-19}	0.25 σ	0.25 σ
369	$\mathrm{BR}(B^- \to K^{*-}\mu^+e^-)$	0	0.25 σ	0.25 σ
370	$\mu_{\mathrm{VBF}}(h \to \mu^+\mu^-)$	1	0.24 σ	0.24 σ
371	$\langle P_5'\rangle(B^0 \to K^{*0}\mu^+\mu^-)^{[2,\ 4.3]}$	-0.41246	0.34 σ	0.24 σ
372	$\mu_{Zh}(h \to ZZ)$	1	0.23 σ	0.23 σ
373	$\langle P_5'\rangle(B^0 \to K^{*0}\mu^+\mu^-)^{[2,\ 4]}$	-0.37032	0.12 σ	0.23 σ
374	$\langle \frac{d\mathrm{BR}}{dq^2}\rangle(B^+ \to K^{*+}\mu^+\mu^-)^{[0,\ 2]}$	8.2778×10^{-8}	0.17 σ	0.25 σ
375	$\mu_{Vh}(h \to ZZ)$	1	0.23 σ	0.23 σ
376	$\mathrm{BR}(K^+ \to \mu^+\nu)$	0.63441	0.14 σ	0.23 σ
377	$\langle P_6'\rangle(B^+ \to K^{*+}\mu^+\mu^-)^{[1.1,\ 2.5]}$	-0.054307	0.24 σ	0.24 σ
378	$\frac{\langle \mathrm{BR}\rangle}{\mathrm{BR}}(B \to D^*\tau^+\nu)^{[5.6,\ 6.13]}$	0.076832	0.22 σ	0.22 σ
379	$\frac{\langle \mathrm{BR}\rangle}{\mathrm{BR}}(B \to D\tau^+\nu)^{[11.47,\ 12.0]}$	0.002539	0.22 σ	0.22 σ
380	$R(e^+e^- \to W^+W^-)^{[191.6]}$	0.99779	0.14 σ	0.21 σ
381	$\langle F_L\rangle(B^0 \to K^{*0}e^+e^-)^{[0.000784,\ 0.257]}$	0.054518	0.31 σ	0.19 σ
382	$\frac{\langle \mathrm{BR}\rangle}{\mathrm{BR}}(B \to D^*\tau^+\nu)^{[8.5,\ 9.0]}$	0.095922	0.2 σ	0.2 σ
383	$\mu_{Vh}(h \to \gamma\gamma)$	1	0.2 σ	0.2 σ
384	$\left\langle \frac{dR}{d\theta}\right\rangle(e^+e^- \to W^+W^-)^{[189.09,\ 0.2,\ 0.4]}$	2.1824	0.23 σ	0.2 σ
385	$\mathrm{BR}(B^- \to K^-\tau^+e^-)$	0	0.2 σ	0.2 σ
386	$\langle P_1\rangle(B^+ \to K^{*+}\mu^+\mu^-)^{[15,\ 19]}$	-0.62023	0.2 σ	0.2 σ
387	$\left\langle \frac{dR}{d\theta}\right\rangle(e^+e^- \to W^+W^-)^{[205.92,\ 0.6,\ 0.8]}$	4.4376	0.23 σ	0.19 σ
388	$\langle P_1\rangle(B^0 \to K^{*0}\mu^+\mu^-)^{[1,\ 2]}$	0.046592	0.14 σ	0.15 σ
389	$\langle A_T^{\mathrm{Im}}\rangle(B^0 \to K^{*0}e^+e^-)^{[0.000784,\ 0.257]}$	0.00028612	0.21 σ	0.21 σ
390	$\langle P_8'\rangle(B^+ \to K^{*+}\mu^+\mu^-)^{[1.1,\ 2.5]}$	-0.026951	0.21 σ	0.21 σ
391	$\mathrm{BR}(B^- \to \pi^-\tau^+\mu^-)$	0	0.18 σ	0.18 σ
392	$\mathrm{BR}(B \to X_s\gamma)$	0.00033157	0.18 σ	0.18 σ
393	$\mathrm{BR}(\tau^+ \to \pi^+\bar{\nu})$	0.10821	0.025 σ	0.19 σ
394	$\mathrm{BR}(K^+ \to \pi^+\nu\bar{\nu})$	8.2767×10^{-11}	0.19 σ	0.15 σ

	Observable	NP prediction	NP pull	SM pull
395	$\frac{\langle \mathrm{BR} \rangle}{\mathrm{BR}}(B \to D^* \tau^+ \nu)^{[6.5,\ 7.0]}$	0.088536	0.17 σ	0.17 σ
396	$\frac{\langle \mathrm{BR} \rangle}{\mathrm{BR}}(B \to D \tau^+ \nu)^{[7.0,\ 7.5]}$	0.089808	0.17 σ	0.17 σ
397	$\mathrm{BR}(B^0 \to K^{*0} \gamma)$	4.1206×10^{-5}	0.25 σ	0.16 σ
398	Γ_W	2.0913	0.15 σ	0.16 σ
399	$\langle \frac{d\mathrm{BR}}{dq^2} \rangle (B^0 \to K^{*0} \mu^+ \mu^-)^{[1,\ 2]}$	4.518×10^{-8}	0.2 σ	0.15 σ
400	$\langle P_8' \rangle (B^0 \to K^{*0} \mu^+ \mu^-)^{[15,\ 19]}$	0.00057776	0.14 σ	0.14 σ
401	$\left\langle \frac{dR}{d\theta} \right\rangle (e^+ e^- \to W^+ W^-)^{[182.66,\ 0.8,\ 1.0]}$	5.4263	0.13 σ	0.15 σ
402	$\langle P_6' \rangle (B^+ \to K^{*+} \mu^+ \mu^-)^{[4,\ 6]}$	-0.02992	0.14 σ	0.14 σ
403	$\langle F_L \rangle (B^0 \to K^{*0} \mu^+ \mu^-)^{[15,\ 19]}$	0.34049	0.12 σ	0.13 σ
404	$\frac{\langle \mathrm{BR} \rangle}{\mathrm{BR}}(B \to D^* \tau^+ \nu)^{[5.0,\ 5.5]}$	0.05722	0.14 σ	0.14 σ
405	$\langle P_1 \rangle (B^+ \to K^{*+} \mu^+ \mu^-)^{[2.5,\ 4]}$	-0.10947	0.17 σ	0.16 σ
406	$R_T(K^+ \to \pi^0 \mu^+ \nu)$	-9.1454×10^{-19}	0.1 σ	0.1 σ
407	$\langle P_6' \rangle (B^+ \to K^{*+} \mu^+ \mu^-)^{[2.5,\ 4]}$	-0.045641	0.14 σ	0.15 σ
408	$\mathscr{F}t(^{50}\mathrm{Mn})$	4.6723×10^{27}	1.6 σ	0.14 σ
409	$\frac{\langle \mathrm{BR} \rangle}{\mathrm{BR}}(B \to D \tau^+ \nu)^{[8.0,\ 8.5]}$	0.082028	0.13 σ	0.13 σ
410	$\sigma_{\mathrm{trident}} / \sigma^{\mathrm{SM}}_{\mathrm{trident}}$	1.0024	0.14 σ	0.13 σ
411	$\frac{\langle \mathrm{BR} \rangle}{\mathrm{BR}}(B \to D^* \tau^+ \nu)^{[9.33,\ 9.86]}$	0.087022	0.13 σ	0.13 σ
412	$R(e^+ e^- \to W^+ W^-)^{[201.6]}$	0.99773	0.03 σ	0.12 σ
413	$\langle P_4' \rangle (B^0 \to K^{*0} \mu^+ \mu^-)^{[1.1,\ 2.5]}$	-0.046594	0.23 σ	0.12 σ
414	$\left\langle \frac{dR}{d\theta} \right\rangle (e^+ e^- \to W^+ W^-)^{[198.38,\ -0.2,\ 0.0]}$	1.2615	0.14 σ	0.1 σ
415	$\langle R_{\mu e} \rangle (B^+ \to K^{*+} \ell^+ \ell^-)^{[0.1,\ 8.0]}$	0.87648	0.28 σ	0.1 σ
416	$\frac{\langle \mathrm{BR} \rangle}{\mathrm{BR}}(B \to D \tau^+ \nu)^{[5.07,\ 5.6]}$	0.07714	0.1 σ	0.1 σ
417	$\langle P_6' \rangle (B^+ \to K^{*+} \mu^+ \mu^-)^{[0.1,\ 0.98]}$	-0.047636	0.093 σ	0.092 σ
418	$\frac{\langle \mathrm{BR} \rangle}{\mathrm{BR}}(B \to D \tau^+ \nu)^{[5.6,\ 6.13]}$	0.087798	0.1 σ	0.1 σ
419	$\mathrm{BR}(\tau^- \to e^- e^+ e^-)$	0	0.1 σ	0.1 σ
420	$\langle P_3 \rangle (B^+ \to K^{*+} \mu^+ \mu^-)^{[1.1,\ 2.5]}$	0.0038341	0.1 σ	0.1 σ
421	$\left\langle \frac{dR}{d\theta} \right\rangle (e^+ e^- \to W^+ W^-)^{[205.92,\ -0.2,\ 0.0]}$	1.2276	0.13 σ	0.097 σ
422	A_c	0.6675	0.092 σ	0.092 σ
423	$\ln(C)(K^+ \to \pi^0 \mu^+ \nu)$	0.19988	0.084 σ	0.084 σ
424	$\frac{\langle \mathrm{BR} \rangle}{\mathrm{BR}}(B \to D^* \tau^+ \nu)^{[8.0,\ 8.5]}$	0.098402	0.084 σ	0.084 σ
425	$\frac{\langle \mathrm{BR} \rangle}{\mathrm{BR}}(B \to D^* \tau^+ \nu)^{[9.0,\ 9.5]}$	0.089545	0.082 σ	0.082 σ
426	$\langle D^{\mu e}_{P_4'} \rangle (B^0 \to K^{*0} \ell^+ \ell^-)^{[14.18,\ 19.0]}$	-0.0001102	0.072 σ	0.072 σ
427	$\mathscr{F}t(^{14}\mathrm{O})$	4.6723×10^{27}	1.1 σ	0.052 σ
428	$\frac{\langle \mathrm{BR} \rangle}{\mathrm{BR}}(B \to D \tau^+ \nu)^{[5.0,\ 5.5]}$	0.070732	0.066 σ	0.066 σ
429	$\mathrm{BR}(B^+ \to K^{*+} \gamma)$	4.1857×10^{-5}	0.03 σ	0.052 σ
430	$\langle P_2 \rangle (B^0 \to K^{*0} \mu^+ \mu^-)^{[1.1,\ 2.5]}$	-0.45169	0.11 σ	0.11 σ
431	$\frac{\langle \mathrm{BR} \rangle}{\mathrm{BR}}(B \to D^* \tau^+ \nu)^{[9.5,\ 10.0]}$	0.077734	0.053 σ	0.053 σ
432	R_c^0	0.17222	0.04 σ	0.041 σ
433	$\langle P_4' \rangle (B^0 \to K^{*0} \mu^+ \mu^-)^{[15,\ 19]}$	-0.63519	0.046 σ	0.047 σ
434	$\langle P_8' \rangle (B^+ \to K^{*+} \mu^+ \mu^-)^{[2.5,\ 4]}$	-0.018578	0.0092 σ	0.0091 σ
435	$\langle P_8' \rangle (B^0 \to K^{*0} \mu^+ \mu^-)^{[0.1,\ 0.98]}$	-0.0050462	0.0018 σ	0.0043 σ
436	$\mathscr{F}t(^{38m}\mathrm{K})$	4.6723×10^{27}	1.6 σ	0.012 σ
437	$\frac{\langle \mathrm{BR} \rangle}{\mathrm{BR}}(B \to D^* \tau^+ \nu)^{[4.0,\ 4.53]}$	0.028569	0.026 σ	0.026 σ
438	$\mu_{gg}(h \to \tau^+ \tau^-)$	1	0.025 σ	0.025 σ
439	$\mathscr{F}t(^{62}\mathrm{Ga})$	4.6723×10^{27}	0.54 σ	0.0023 σ
440	$\frac{\langle \mathrm{BR} \rangle}{\mathrm{BR}}(B \to D \tau^+ \nu)^{[9.33,\ 9.86]}$	0.063887	0.016 σ	0.016 σ
441	$\mathrm{BR}(B^+ \to \mu^+ \nu)$	4.6652×10^{-7}	0.044 σ	0.017 σ
442	$\langle \frac{d\mathrm{BR}}{dq^2} \rangle (B^+ \to K^{*+} \mu^+ \mu^-)^{[2,\ 4.3]}$	4.4708×10^{-8}	0.11 σ	0.0019 σ
443	$\mathrm{BR}(B^0 \to \tau^+ \tau^-)$	2.4006×10^{-8}	0.0047 σ	0.0045 σ
444	$\mathrm{BR}(\bar{B}^0 \to \bar{K}^{*0} e^+ \mu^-)$	0	0 σ	0 σ
445	$\mathrm{BR}(B^- \to K^- e^+ \mu^-)$	0	0 σ	0 σ
446	$\mathrm{BR}(B^- \to K^- \mu^+ e^-)$	0	0 σ	0 σ
447	$\mathrm{BR}(B^- \to K^- \mu^+ \tau^-)$	0	0 σ	0 σ
448	$\mathrm{BR}(B^- \to \pi^- \mu^+ \tau^-)$	0	0 σ	0 σ
449	$\mathrm{BR}(\bar{B}^0 \to e^\pm \mu^\mp)$	0	0 σ	0 σ
450	$\mathrm{BR}(\bar{B}^0 \to e^\pm \tau^\mp)$	0	0 σ	0 σ

	Observable	NP prediction	NP pull	SM pull
451	$\mathrm{BR}(\bar{B}^0 \to \mu^\pm \tau^\mp)$	0	0 σ	0 σ
452	$\mathrm{BR}(\bar{B}_s \to e^\pm \mu^\mp)$	0	0 σ	0 σ
453	$\mathrm{BR}(\bar{B}_s \to \mu^\pm \tau^\mp)$	0	0 σ	0 σ
454	$\mathrm{BR}(\bar{B}^0 \to \pi^0 e^\pm \mu^\mp)$	0	0 σ	0 σ
455	$\mathrm{BR}(B^- \to \pi^- e^\pm \mu^\mp)$	0	0 σ	0 σ
456	$\mathrm{BR}(K_L \to e^\pm \mu^\mp)$	0	0 σ	0 σ
457	$\mathrm{BR}(\mu^- \to e^- e^+ e^-)$	0	0 σ	0 σ
458	$\mathrm{BR}(\mu \to e\gamma)$	0	0 σ	0 σ
459	$\mathrm{BR}(\tau \to \mu\gamma)$	0	0 σ	0 σ
460	$\mathrm{BR}(\tau^- \to \mu^- \mu^+ \mu^-)$	0	0 σ	0 σ
461	$\mathrm{BR}(\tau^- \to e^- \mu^+ \mu^-)$	0	0 σ	0 σ
462	$\mathrm{BR}(\tau \to e\gamma)$	0	0 σ	0 σ
463	$\mathrm{BR}(\tau^+ \to \rho^0 e^+)$	0	0 σ	0 σ
464	$\mathrm{BR}(\tau^+ \to \rho^0 \mu^+)$	0	0 σ	0 σ
465	$\mathrm{BR}(\tau^+ \to \phi e^+)$	0	0 σ	0 σ
466	$\mathrm{BR}(\tau^+ \to \phi \mu^+)$	0	0 σ	0 σ
467	$CR(\mu - e)$ in $^{48}_{22}\mathrm{Ti}$	0	0 σ	0 σ
468	$CR(\mu - e)$ in $^{197}_{79}\mathrm{Au}$	0	0 σ	0 σ
469	$\mathrm{BR}(Z^0 \to e^\pm \mu^\mp)$	0	0 σ	0 σ
470	$\mathrm{BR}(Z^0 \to e^\pm \tau^\mp)$	0	0 σ	0 σ
471	$\mathrm{BR}(Z^0 \to \mu^\pm \tau^\mp)$	0	0 σ	0 σ

C.2 Predictions of the observables in Scenario II of chapter 7

	Observable	NP prediction	NP pull	SM pull
0	a_μ	0.0011659	4.3 σ	4.3 σ
1	$\langle \frac{d\overline{\mathrm{BR}}}{dq^2} \rangle (B_s \to \phi \mu^+ \mu^-)^{[2.5,\ 4.0]}$	4.5349×10^{-8}	3.1 σ	4 σ
2	$\langle F_L \rangle (B^+ \to K^{*+} \mu^+ \mu^-)^{[2.5,\ 4]}$	0.76718	3.2 σ	3.3 σ
3	$R_{\tau\ell}(B \to D^* \ell^+ \nu)$	0.29444	0.11 σ	3.3 σ
4	$\langle P_2 \rangle (B^0 \to K^{*0} \mu^+ \mu^-)^{[0.1,\ 0.98]}$	-0.13088	3.3 σ	3.3 σ
5	$\langle R_{\mu e} \rangle (B^\pm \to K^\pm \ell^+ \ell^-)^{[1.1,\ 6.0]}$	0.83564	0.25 σ	3.2 σ
6	$\langle \frac{d\overline{\mathrm{BR}}}{dq^2} \rangle (B_s \to \phi \mu^+ \mu^-)^{[1.1,\ 2.5]}$	4.9232×10^{-8}	2.5 σ	3.2 σ
7	$\langle \frac{d\overline{\mathrm{BR}}}{dq^2} \rangle (B_s \to \phi \mu^+ \mu^-)^{[4.0,\ 6.0]}$	4.7857×10^{-8}	2.2 σ	3.1 σ
8	$\left\langle \frac{dR}{d\theta} \right\rangle (e^+ e^- \to W^+ W^-)^{[198.38,\ 0.8,\ 1.0]}$	7.236	3 σ	3 σ
9	$\langle P_5' \rangle (B^0 \to K^{*0} \mu^+ \mu^-)^{[4,\ 6]}$	-0.61471	1.8 σ	2.8 σ
10	$\langle \frac{d\overline{\mathrm{BR}}}{dq^2} \rangle (B_s \to \phi \mu^+ \mu^-)^{[0.1,\ 0.98]}$	1.0947×10^{-7}	2.4 σ	2.7 σ
11	$\mathrm{BR}(W^\pm \to \tau^\pm \nu)$	0.10837	2.6 σ	2.6 σ
12	$\langle R_{\mu e} \rangle (B^0 \to K^{*0} \ell^+ \ell^-)^{[1.1,\ 6.0]}$	0.84252	1.4 σ	2.5 σ
13	ϵ'/ϵ	-2.4922×10^{-5}	2.5 σ	2.5 σ
14	$R_{\tau\mu}(B \to D^* \ell^+ \nu)$	0.29506	0.57 σ	2.5 σ
15	$A_{\mathrm{FB}}^{0,b}$	0.10307	2.4 σ	2.4 σ
16	$\langle R_{\mu e} \rangle (B^0 \to K^{*0} \ell^+ \ell^-)^{[0.045,\ 1.1]}$	0.88458	2.1 σ	2.4 σ
17	$\frac{\langle \mathrm{BR} \rangle}{\mathrm{BR}} (B \to D^* \tau^+ \nu)^{[10.4,\ 10.93]}$	0.018511	2.3 σ	2.3 σ
18	A_e	0.14703	2.2 σ	2.2 σ
19	$\langle \frac{d\mathrm{BR}}{dq^2} \rangle (B^+ \to K^{*+} \mu^+ \mu^-)^{[15.0,\ 19.0]}$	5.4963×10^{-8}	1.4 σ	2.2 σ
20	$\left\langle \frac{dR}{d\theta} \right\rangle (e^+ e^- \to W^+ W^-)^{[189.09,\ 0.8,\ 1.0]}$	6.253	2.2 σ	2.2 σ
21	$\langle P_4' \rangle (B^0 \to K^{*0} \mu^+ \mu^-)^{[4,\ 6]}$	-0.49053	2 σ	2.1 σ
22	$\bar{B}_n^{[0.591]}$	0.98894	2.2 σ	2.2 σ
23	$\langle P_8' \rangle (B^0 \to K^{*0} \mu^+ \mu^-)^{[1.1,\ 2.5]}$	-0.012211	2.2 σ	2.1 σ
24	$\langle P_1 \rangle (B^0 \to K^{*0} \mu^+ \mu^-)^{[1.1,\ 2.5]}$	0.022867	2.2 σ	2.2 σ
25	$\langle P_3 \rangle (B^0 \to K^{*0} \mu^+ \mu^-)^{[1.1,\ 2.5]}$	0.0028863	2.2 σ	2.1 σ

	Observable	NP prediction	NP pull	SM pull
26	$\lvert\epsilon_K\rvert$	0.0016583	2.6 σ	2.1 σ
27	$\langle\frac{d\mathrm{BR}}{dq^2}\rangle(B^+\to K^{*+}\mu^+\mu^-)^{[4.0,\,6.0]}$	4.7359×10^{-8}	1.6 σ	2.1 σ
28	$\frac{\langle\mathrm{BR}\rangle}{\mathrm{BR}}(B\to D^*\tau^+\nu)^{[5.07,\,5.6]}$	0.063084	2.1 σ	2.1 σ
29	$\langle\frac{d\mathrm{BR}}{dq^2}\rangle(B^\pm\to K^\pm\mu^+\mu^-)^{[4.0,\,5.0]}$	2.9582×10^{-8}	1.2 σ	2.1 σ
30	$\mathrm{BR}(K_L\to e^+e^-)$	1.7487×10^{-13}	2.1 σ	2.1 σ
31	$\mathrm{BR}(B^\pm\to K^\pm\tau^+\tau^-)$	5.7453×10^{-5}	2 σ	2 σ
32	$\langle\frac{d\mathrm{BR}}{dq^2}\rangle(B^0\to K^{*0}\mu^+\mu^-)^{[15.0,\,19.0]}$	5.0724×10^{-8}	0.93 σ	2.1 σ
33	$\langle P_5'\rangle(B^+\to K^{*+}\mu^+\mu^-)^{[15,\,19]}$	-0.56699	1.9 σ	2 σ
34	$\langle A_{\mathrm{FB}}^{\ell h}\rangle(\Lambda_b\to\Lambda\mu^+\mu^-)^{[15,\,20]}$	0.15534	2.2 σ	2.1 σ
35	$\langle P_2\rangle(B^+\to K^{*+}\mu^+\mu^-)^{[4,\,6]}$	0.16362	1.5 σ	2.1 σ
36	$\langle\frac{d\overline{\mathrm{BR}}}{dq^2}\rangle(B_s\to\phi\mu^+\mu^-)^{[1.0,\,6.0]}$	4.7692×10^{-8}	1.7 σ	2 σ
37	$\langle P_3\rangle(B^+\to K^{*+}\mu^+\mu^-)^{[0.1,\,0.98]}$	0.0013649	2 σ	2 σ
38	$\mathrm{BR}(\tau^-\to\mu^-\nu\bar{\nu})$	0.17278	2.2 σ	2 σ
39	$\overline{\mathrm{BR}}(B_s\to\mu^+\mu^-)$	3.6616×10^{-9}	1.9 σ	1.9 σ
40	$\langle P_2\rangle(B^0\to K^{*0}\mu^+\mu^-)^{[4,\,6]}$	0.16155	0.65 σ	1.9 σ
41	$\langle\frac{d\mathrm{BR}}{dq^2}\rangle(B^0\to K^0\mu^+\mu^-)^{[4.0,\,6.0]}$	2.7333×10^{-8}	1.3 σ	1.9 σ
42	a_e	0.0011597	1.9 σ	1.9 σ
43	$\langle P_5'\rangle(B^0\to K^{*0}\mu^+\mu^-)^{[2.5,\,4]}$	-0.29333	0.79 σ	1.9 σ
44	$\langle\frac{d\mathrm{BR}}{dq^2}\rangle(B^0\to K^0\mu^+\mu^-)^{[15.0,\,22.0]}$	1.1833×10^{-8}	1 σ	1.9 σ
45	$\frac{\langle\mathrm{BR}\rangle}{\mathrm{BR}}(B\to D\tau^+\nu)^{[7.73,\,8.27]}$	0.091527	1.9 σ	1.9 σ
46	$\langle\frac{d\mathrm{BR}}{dq^2}\rangle(B^\pm\to K^\pm\mu^+\mu^-)^{[5.0,\,6.0]}$	2.9353×10^{-8}	1 σ	1.9 σ
47	$\frac{\langle\mathrm{BR}\rangle}{\mathrm{BR}}(B\to D^*\tau^+\nu)^{[7.2,\,7.73]}$	0.10189	1.9 σ	1.9 σ
48	$\langle\frac{d\mathrm{BR}}{dq^2}\rangle(B^\pm\to K^\pm\mu^+\mu^-)^{[1.1,\,2.0]}$	3.0075×10^{-8}	1.1 σ	1.9 σ
49	$\left\langle\frac{dR}{d\theta}\right\rangle(e^+e^-\to W^+W^-)^{[198.38,\,-0.6,\,-0.4]}$	0.835	1.9 σ	1.9 σ
50	$\langle P_1\rangle(B^0\to K^{*0}\mu^+\mu^-)^{[4.3,\,6]}$	-0.16703	1.9 σ	1.9 σ
51	$\mu_{Zh}(h\to c\bar{c})$	1	1.8 σ	1.8 σ
52	$\left\langle\frac{dR}{d\theta}\right\rangle(e^+e^-\to W^+W^-)^{[198.38,\,0.6,\,0.8]}$	4.428	1.8 σ	1.8 σ
53	$\langle\frac{d\mathrm{BR}}{dq^2}\rangle(B^0\to K^{*0}\mu^+\mu^-)^{[1.1,\,2.5]}$	4.2691×10^{-8}	1.3 σ	1.8 σ
54	$\left\langle\frac{dR}{d\theta}\right\rangle(e^+e^-\to W^+W^-)^{[182.66,\,-1.0,\,-0.8]}$	0.702	1.8 σ	1.8 σ
55	$\langle\frac{d\mathrm{BR}}{dq^2}\rangle(B^0\to K^{*0}\mu^+\mu^-)^{[4.3,\,6]}$	4.4203×10^{-8}	1.1 σ	1.7 σ
56	$\langle\frac{d\mathrm{BR}}{dq^2}\rangle(B^0\to K^{*0}\mu^+\mu^-)^{[4.0,\,6.0]}$	4.3783×10^{-8}	0.99 σ	1.7 σ
57	$\left\langle\frac{dR}{d\theta}\right\rangle(e^+e^-\to W^+W^-)^{[198.38,\,-1.0,\,-0.8]}$	0.542	1.7 σ	1.7 σ
58	m_W	80.359	1.7 σ	1.7 σ
59	$\left\langle\frac{dR}{d\theta}\right\rangle(e^+e^-\to W^+W^-)^{[182.66,\,0.0,\,0.2]}$	1.731	1.7 σ	1.7 σ
60	$\langle\frac{d\mathrm{BR}}{dq^2}\rangle(B^0\to K^0\mu^+\mu^-)^{[2.0,\,4.0]}$	2.7695×10^{-8}	1.1 σ	1.7 σ
61	$\mu_{Wh}(h\to\tau^+\tau^-)$	1	1.7 σ	1.7 σ
62	$\left\langle\frac{dR}{d\theta}\right\rangle(e^+e^-\to W^+W^-)^{[205.92,\,0.2,\,0.4]}$	2.056	1.7 σ	1.7 σ
63	$\left\langle\frac{dR}{d\theta}\right\rangle(e^+e^-\to W^+W^-)^{[205.92,\,-0.6,\,-0.4]}$	0.77	1.7 σ	1.7 σ
64	$\mu_{t\bar{t}h}(h\to W^+W^-)$	1	1.7 σ	1.7 σ
65	$\langle\frac{d\mathrm{BR}}{dq^2}\rangle(\Lambda_b\to\Lambda\mu^+\mu^-)^{[15,\,20]}$	6.0653×10^{-8}	2.1 σ	1.7 σ
66	$R(e^+e^-\to W^+W^-)^{[182.7]}$	1	1.6 σ	1.6 σ
67	$A_{\Delta\Gamma}(B_s\to\phi\gamma)$	0.03051	1.7 σ	1.7 σ
68	$\langle\frac{d\mathrm{BR}}{dq^2}\rangle(B^\pm\to K^\pm\mu^+\mu^-)^{[15.0,\,22.0]}$	1.2845×10^{-8}	0.41 σ	1.6 σ
69	$\mathrm{BR}(K_S\to\pi^+e^+\nu)$	0.00071986	1.6 σ	1.6 σ
70	$\langle P_5'\rangle(B^0\to K^{*0}\mu^+\mu^-)^{[0.1,\,0.98]}$	0.73931	2.1 σ	1.6 σ
71	$\frac{\langle\mathrm{BR}\rangle}{\mathrm{BR}}(B\to D\tau^+\nu)^{[9.0,\,9.5]}$	0.066851	1.6 σ	1.6 σ
72	$R_{\tau\ell}(B\to D\ell^+\nu)$	0.3573	0.35 σ	1.6 σ
73	$\langle P_6'\rangle(B^+\to K^{*+}\mu^+\mu^-)^{[15,\,19]}$	-0.002583	1.5 σ	1.5 σ
74	$\langle F_L\rangle(B^0\to K^{*0}\mu^+\mu^-)^{[1.1,\,2.5]}$	0.70778	0.79 σ	1.6 σ
75	$\tau_{B_s\to\mu\mu}$	2.4506×10^{12}	1.6 σ	1.6 σ
76	$\mathrm{BR}(K_L\to\pi^+e^+\nu)$	0.41115	1.6 σ	1.6 σ
77	$\langle D_{P_5'}^{\mu e}\rangle(B^0\to K^{*0}\ell^+\ell^-)^{[14.18,\,19.0]}$	0.0070533	1.5 σ	1.5 σ
78	$\langle\frac{d\mathrm{BR}}{dq^2}\rangle(B^\pm\to K^\pm\mu^+\mu^-)^{[3.0,\,4.0]}$	2.9773×10^{-8}	0.7 σ	1.5 σ

	Observable	NP prediction	NP pull	SM pull
79	$\langle P_6' \rangle (B^0 \to K^{*0}\mu^+\mu^-)^{[4,\,6]}$	-0.034085	1.5 σ	1.5 σ
80	$\langle P_5' \rangle (B^0 \to K^{*0}\mu^+\mu^-)^{[1.1,\,2.5]}$	0.29796	0.47 σ	1.5 σ
81	$A_{\rm FB}^{0,\tau}$	0.016236	1.5 σ	1.5 σ
82	$\langle \frac{d\overline{\rm BR}}{dq^2} \rangle (B_s \to \phi\mu^+\mu^-)^{[15.0,\,19.0]}$	4.753×10^{-8}	0.21 σ	1.5 σ
83	R_μ^0	20.735	1.5 σ	1.5 σ
84	$\langle \frac{d{\rm BR}}{dq^2} \rangle (B^0 \to K^{*0}\mu^+\mu^-)^{[2.5,\,4.0]}$	3.9895×10^{-8}	0.84 σ	1.5 σ
85	${\rm BR}(B^- \to \pi^-\tau^+e^-)$	2.0924×10^{-9}	1.5 σ	1.5 σ
86	$\left\langle \frac{dR}{d\theta} \right\rangle (e^+e^- \to W^+W^-)^{[182.66,\,0.2,\,0.4]}$	2.189	1.5 σ	1.5 σ
87	$\langle \overline{S_4} \rangle (B_s \to \phi\mu^+\mu^-)^{[15.0,\,19.0]}$	-0.30161	1.5 σ	1.5 σ
88	$F_L(B^0 \to D^{*-}\tau^+\nu_\tau)$	0.46989	1.5 σ	1.5 σ
89	${\rm BR}(B^+ \to K^+\nu\bar{\nu})$	5.943×10^{-6}	1 σ	1.4 σ
90	${\rm BR}(K_S \to \mu^+\mu^-)$	5.1619×10^{-12}	1.4 σ	1.4 σ
91	$\frac{\langle {\rm BR} \rangle}{\rm BR} (B \to D^*\tau^+\nu)^{[6.0,\,6.5]}$	0.080351	1.4 σ	1.4 σ
92	${\rm BR}(W^\pm \to \mu^\pm\nu)$	0.10842	1.4 σ	1.4 σ
93	R_e^0	20.734	1.4 σ	1.4 σ
94	$\langle A_9 \rangle (B^0 \to K^{*0}\mu^+\mu^-)^{[15,\,19]}$	4.1214×10^{-5}	1.4 σ	1.4 σ
95	$R_{e\mu}(K^+ \to \ell^+\nu)$	2.4755×10^{-5}	1.4 σ	1.4 σ
96	$\langle P_5' \rangle (B^+ \to K^{*+}\mu^+\mu^-)^{[4,\,6]}$	-0.62316	0.97 σ	1.3 σ
97	$\langle {\rm BR} \rangle (B \to X_s e^+e^-)^{[14.2,\,25.0]}$	3.182×10^{-7}	1.4 σ	1.4 σ
98	$\mathscr{F}t(^{10}{\rm C})$	4.6665×10^{27}	1.4 σ	1.4 σ
99	$\langle \frac{d{\rm BR}}{dq^2} \rangle (B^\pm \to K^\pm\mu^+\mu^-)^{[0,\,2]}$	3.0119×10^{-8}	0.63 σ	1.3 σ
100	$\left\langle \frac{dR}{d\theta} \right\rangle (e^+e^- \to W^+W^-)^{[189.09,\,-0.2,\,0.0]}$	1.403	1.3 σ	1.3 σ
101	${\rm BR}(B^+ \to e^+\nu)$	9.8005×10^{-12}	1.3 σ	1.3 σ
102	$\langle D_{P_5'}^{\mu e} \rangle (B^0 \to K^{*0}\ell^+\ell^-)^{[1.0,\,6.0]}$	0.080606	1.2 σ	1.3 σ
103	$S_{\phi\gamma}$	-0.00023221	1.3 σ	1.3 σ
104	$\overline{\rm BR}(B_s \to e^+e^-)$	1.0087×10^{-13}	1.3 σ	1.3 σ
105	$\langle P_8' \rangle (B^0 \to K^{*0}\mu^+\mu^-)^{[4,\,6]}$	-0.010099	1.3 σ	1.3 σ
106	$\langle P_4' \rangle (B^0 \to K^{*0}\mu^+\mu^-)^{[2,\,4]}$	-0.3251	1.3 σ	1.3 σ
107	${\rm BR}(K_S \to e^+e^-)$	1.6155×10^{-16}	1.3 σ	1.3 σ
108	${\rm BR}(B^0 \to e^+e^-)$	2.5204×10^{-15}	1.3 σ	1.3 σ
109	${\rm BR}(K_L \to \pi^0\nu\bar{\nu})$	3.537×10^{-11}	1.3 σ	1.3 σ
110	$\frac{\langle {\rm BR} \rangle}{\rm BR} (B \to D^*\tau^+\nu)^{[8.27,\,8.8]}$	0.10324	1.3 σ	1.3 σ
111	${\rm BR}(B^0 \to \rho^0\nu\bar{\nu})$	1.9904×10^{-7}	1.3 σ	1.3 σ
112	${\rm BR}(B^- \to \pi^-e^+\tau^-)$	2.0924×10^{-9}	1.3 σ	1.3 σ
113	$\langle R_{\mu e} \rangle (B^0 \to K^0\ell^+\ell^-)^{[4.0,\,8.12]}$	0.83657	0.86 σ	1.3 σ
114	${\rm BR}(K^+ \to \pi^0e^+\nu)$	0.051558	1.3 σ	1.3 σ
115	$\left\langle \frac{dR}{d\theta} \right\rangle (e^+e^- \to W^+W^-)^{[205.92,\,0.0,\,0.2]}$	1.561	1.3 σ	1.3 σ
116	${\rm BR}(B^0 \to K^{*0}\nu\bar{\nu})$	1.2895×10^{-5}	1.6 σ	1.3 σ
117	$\langle F_L \rangle (B^0 \to K^{*0}\mu^+\mu^-)^{[2,\,4]}$	0.76366	0.98 σ	1.3 σ
118	$\mu_{t\bar{t}h}(h \to VV)$	1	1.3 σ	1.3 σ
119	${\rm BR}(K_S \to \pi^+\mu^+\nu)$	0.00047682	1.3 σ	1.3 σ
120	$\frac{\langle {\rm BR} \rangle}{\rm BR} (B \to D\tau^+\nu)^{[9.86,\,10.4]}$	0.052842	1.2 σ	1.2 σ
121	$\langle P_3 \rangle (B^0 \to K^{*0}\mu^+\mu^-)^{[0.1,\,0.98]}$	0.0013074	1.2 σ	1.2 σ
122	$S_{\psi K_S}$	0.7251	0.6 σ	1.2 σ
123	$\mu_{\rm VBF}(h \to b\bar{b})$	0.99999	1.2 σ	1.2 σ
124	$\left\langle \frac{dR}{d\theta} \right\rangle (e^+e^- \to W^+W^-)^{[182.66,\,0.6,\,0.8]}$	3.806	1.2 σ	1.2 σ
125	${\rm BR}(\tau^+ \to K^+\bar{\nu})$	0.0071474	1.3 σ	1.2 σ
126	$\frac{\langle {\rm BR} \rangle}{\rm BR} (B \to D^*\tau^+\nu)^{[4.0,\,4.5]}$	0.026461	1.2 σ	1.2 σ
127	$\langle \frac{d{\rm BR}}{dq^2} \rangle (B^0 \to K^{*0}\mu^+\mu^-)^{[2,\,4.3]}$	4.0108×10^{-8}	0.56 σ	1.2 σ
128	$\langle F_L \rangle (B^+ \to K^{*+}\mu^+\mu^-)^{[1.1,\,2.5]}$	0.71563	0.9 σ	1.2 σ
129	$\mu_{Zh}(h \to b\bar{b})$	1	1.1 σ	1.1 σ
130	${\rm BR}(B^+ \to K^{*+}\nu\bar{\nu})$	1.3883×10^{-5}	0.83 σ	1.1 σ
131	$\mu_{Zh}(h \to W^+W^-)$	1	1.1 σ	1.1 σ
132	$\langle P_4' \rangle (B^+ \to K^{*+}\mu^+\mu^-)^{[15,\,19]}$	-0.63437	1.1 σ	1.1 σ
133	$\mu_{Wh}(h \to W^+W^-)$	1	1.1 σ	1.1 σ
134	a_τ	0.0011772	1.1 σ	1.1 σ

	Observable	NP prediction	NP pull	SM pull
135	$R_{\mu e}(W^{\pm} \to \ell^{\pm}\nu)$	1	1.1 σ	1.1 σ
136	ΔM_s	1.2465×10^{-11}	1.1 σ	1.1 σ
137	$\langle \frac{d\text{BR}}{dq^2} \rangle (B^{\pm} \to K^{\pm}\mu^+\mu^-)^{[2.0,\ 3.0]}$	2.9936×10^{-8}	0.27 σ	1.1 σ
138	$\langle P_4' \rangle (B^+ \to K^{*+}\mu^+\mu^-)^{[1.1,\ 2.5]}$	-0.07051	1.1 σ	1.1 σ
139	$\langle P_6' \rangle (B^0 \to K^{*0}\mu^+\mu^-)^{[1.1,\ 2.5]}$	-0.069814	1 σ	1 σ
140	$\langle \text{BR} \rangle (B \to X_s\mu^+\mu^-)^{[1.0,\ 6.0]}$	1.495×10^{-6}	0.87 σ	1.1 σ
141	$\left\langle \frac{dR}{d\theta} \right\rangle (e^+e^- \to W^+W^-)^{[182.66,\ -0.8,\ -0.6]}$	0.841	1.1 σ	1.1 σ
142	$\langle P_8' \rangle (B^+ \to K^{*+}\mu^+\mu^-)^{[0.1,\ 0.98]}$	-0.030051	1.1 σ	1.1 σ
143	$\text{BR}(K^+ \to \pi^0\mu^+\nu)$	0.034039	1 σ	1 σ
144	$\langle P_5' \rangle (B^+ \to K^{*+}\mu^+\mu^-)^{[1.1,\ 2.5]}$	0.27169	0.87 σ	1.1 σ
145	$\mathscr{F}t(^{46}\text{V})$	4.6665×10^{27}	1.1 σ	1.1 σ
146	$\langle P_1 \rangle (B^0 \to K^{*0}\mu^+\mu^-)^{[4,\ 6]}$	-0.1637	0.97 σ	1 σ
147	$\langle \overline{S_3} \rangle (B_s \to \phi\mu^+\mu^-)^{[15.0,\ 19.0]}$	-0.2098	1 σ	1 σ
148	$\langle P_1 \rangle (B^0 \to K^{*0}\mu^+\mu^-)^{[2,\ 4]}$	-0.073287	1 σ	1 σ
149	$\mu_{t\bar{t}h}(h \to \gamma\gamma)$	1	1 σ	1 σ
150	$\mu_{gg}(h \to Z\gamma)$	1	1 σ	1 σ
151	$\left\langle \frac{dR}{d\theta} \right\rangle (e^+e^- \to W^+W^-)^{[182.66,\ -0.6,\ -0.4]}$	1.011	1 σ	1 σ
152	$\mu_{Wh}(h \to \gamma\gamma)$	1	0.99 σ	0.99 σ
153	$\langle P_3 \rangle (B^0 \to K^{*0}\mu^+\mu^-)^{[15,\ 19]}$	-0.00052873	1 σ	1 σ
154	$\langle P_5' \rangle (B^0 \to K^{*0}\mu^+\mu^-)^{[15,\ 19]}$	-0.56403	1.4 σ	0.99 σ
155	$\langle P_1 \rangle (B^+ \to K^{*+}\mu^+\mu^-)^{[0.1,\ 0.98]}$	0.042389	0.96 σ	0.95 σ
156	$\frac{\langle \text{BR} \rangle}{\text{BR}} (B \to D^*\tau^+\nu)^{[10.5,\ 11.0]}$	0.0098782	0.96 σ	0.96 σ
157	$\left\langle \frac{dR}{d\theta} \right\rangle (e^+e^- \to W^+W^-)^{[189.09,\ -0.8,\ -0.6]}$	0.781	0.95 σ	0.95 σ
158	$A_{\text{CP}}(B \to X_{s+d}\gamma)$	0	0.93 σ	0.93 σ
159	$\mu_{\text{VBF}}(h \to W^+W^-)$	1	0.94 σ	0.94 σ
160	$\langle A_7 \rangle (B^0 \to K^{*0}\mu^+\mu^-)^{[1.1,\ 6]}$	0.0025767	0.94 σ	0.94 σ
161	$\langle P_1 \rangle (B^+ \to K^{*+}\mu^+\mu^-)^{[4,\ 6]}$	-0.16215	0.92 σ	0.91 σ
162	$\left\langle \frac{dR}{d\theta} \right\rangle (e^+e^- \to W^+W^-)^{[189.09,\ -0.6,\ -0.4]}$	0.928	0.94 σ	0.94 σ
163	$\frac{\langle \text{BR} \rangle}{\text{BR}} (B \to D^*\tau^+\nu)^{[7.73,\ 8.27]}$	0.10629	0.94 σ	0.94 σ
164	$\langle P_4' \rangle (B^0 \to K^{*0}\mu^+\mu^-)^{[0.1,\ 0.98]}$	0.20359	0.56 σ	0.95 σ
165	$R(e^+e^- \to W^+W^-)^{[204.9]}$	1	0.94 σ	0.94 σ
166	$R(e^+e^- \to W^+W^-)^{[188.6]}$	1	0.92 σ	0.92 σ
167	$\langle \text{BR} \rangle (B \to X_s\mu^+\mu^-)^{[14.2,\ 25.0]}$	3.0603×10^{-7}	1 σ	0.88 σ
168	$\langle P_4' \rangle (B^+ \to K^{*+}\mu^+\mu^-)^{[0.1,\ 0.98]}$	0.19845	0.75 σ	0.85 σ
169	$\langle D^{\mu e}_{P_4'} \rangle (B^0 \to K^{*0}\ell^+\ell^-)^{[1.0,\ 6.0]}$	0.025677	0.85 σ	0.91 σ
170	$\frac{\langle \text{BR} \rangle}{\text{BR}} (B \to D\tau^+\nu)^{[10.93,\ 11.47]}$	0.023168	0.9 σ	0.9 σ
171	$\left\langle \frac{dR}{d\theta} \right\rangle (e^+e^- \to W^+W^-)^{[205.92,\ -0.4,\ -0.2]}$	0.972	0.9 σ	0.9 σ
172	A_τ	0.14723	0.95 σ	0.9 σ
173	$\frac{\langle \text{BR} \rangle}{\text{BR}} (B \to D\tau^+\nu)^{[6.67,\ 7.2]}$	0.095702	0.89 σ	0.89 σ
174	$\langle A_7 \rangle (B^0 \to K^{*0}\mu^+\mu^-)^{[15,\ 19]}$	0.0001129	0.89 σ	0.89 σ
175	$\tilde{a}_n^{[0.695]}$	-0.09921	0.89 σ	0.89 σ
176	$\mu_{gg}(h \to \mu^+\mu^-)$	1	0.89 σ	0.89 σ
177	$\mu_{Zh}(h \to \gamma\gamma)$	1	0.88 σ	0.88 σ
178	$\langle \overline{S_4} \rangle (B_s \to \phi\mu^+\mu^-)^{[2.0,\ 5.0]}$	-0.14749	0.87 σ	0.87 σ
179	$\mu_{gg}(h \to ZZ)$	1	0.88 σ	0.88 σ
180	$\langle F_L \rangle (B^0 \to K^{*0}\mu^+\mu^-)^{[1,\ 2]}$	0.66878	0.35 σ	0.85 σ
181	$\langle \overline{F_L} \rangle (B_s \to \phi\mu^+\mu^-)^{[2.0,\ 5.0]}$	0.7851	0.71 σ	0.88 σ
182	$\frac{\langle \text{BR} \rangle}{\text{BR}} (B \to D\tau^+\nu)^{[10.0,\ 10.5]}$	0.046209	0.87 σ	0.87 σ
183	$\left\langle \frac{dR}{d\theta} \right\rangle (e^+e^- \to W^+W^-)^{[198.38,\ 0.4,\ 0.6]}$	3.003	0.87 σ	0.87 σ
184	$\text{BR}(B^- \to K^-e^+\tau^-)$	5.896×10^{-7}	0.91 σ	0.87 σ
185	$\left\langle \frac{dR}{d\theta} \right\rangle (e^+e^- \to W^+W^-)^{[182.66,\ 0.4,\ 0.6]}$	2.822	0.87 σ	0.87 σ
186	$\frac{\langle \text{BR} \rangle}{\text{BR}} (B \to D\tau^+\nu)^{[8.8,\ 9.33]}$	0.074315	0.86 σ	0.86 σ
187	$\mu_{Vh}(h \to b\bar{b})$	1	0.86 σ	0.86 σ
188	$\frac{\langle \text{BR} \rangle}{\text{BR}} (B \to D\tau^+\nu)^{[5.5,\ 6.0]}$	0.081066	0.86 σ	0.86 σ
189	$\text{BR}(\tau^- \to e^-\nu\bar{\nu})$	0.17765	1.1 σ	0.84 σ
190	$\frac{\langle \text{BR} \rangle}{\text{BR}} (B \to D^*\tau^+\nu)^{[8.8,\ 9.33]}$	0.097951	0.85 σ	0.85 σ

	Observable	NP prediction	NP pull	SM pull
191	$\frac{\langle \mathrm{BR} \rangle}{\mathrm{BR}}(B \to D^* \tau^+ \nu)^{[5.5,\ 6.0]}$	0.069889	0.84 σ	0.84 σ
192	$\frac{\langle \mathrm{BR} \rangle}{\mathrm{BR}}(B \to D \tau^+ \nu)^{[7.2,\ 7.73]}$	0.094208	0.84 σ	0.84 σ
193	$\mathscr{F}t(^{22}\mathrm{Mg})$	4.6665×10^{27}	0.82 σ	0.81 σ
194	$\frac{\langle \mathrm{BR} \rangle}{\mathrm{BR}}(B \to D^* \tau^+ \nu)^{[6.13,\ 6.67]}$	0.089674	0.83 σ	0.83 σ
195	$\frac{\langle \mathrm{BR} \rangle}{\mathrm{BR}}(B \to D \tau^+ \nu)^{[9.5,\ 10.0]}$	0.05713	0.83 σ	0.83 σ
196	$\frac{\langle \mathrm{BR} \rangle}{\mathrm{BR}}(B \to D \tau^+ \nu)^{[10.4,\ 10.93]}$	0.038397	0.83 σ	0.83 σ
197	$A_{\mathrm{FB}}^{0,c}$	0.07361	0.83 σ	0.83 σ
198	$\langle A_8 \rangle(B^0 \to K^{*0} \mu^+ \mu^-)^{[1.1,\ 6]}$	0.00056089	0.82 σ	0.83 σ
199	$\mathrm{BR}(W^\pm \to e^\pm \nu)$	0.10842	0.83 σ	0.82 σ
200	$\frac{\langle \mathrm{BR} \rangle}{\mathrm{BR}}(B \to D \tau^+ \nu)^{[6.13,\ 6.67]}$	0.095556	0.82 σ	0.82 σ
201	$\left\langle \frac{dR}{d\theta} \right\rangle (e^+ e^- \to W^+ W^-)^{[189.09,\ 0.4,\ 0.6]}$	2.946	0.81 σ	0.81 σ
202	$\mathscr{F}t(^{26m}\mathrm{Al})$	4.6665×10^{27}	0.81 σ	0.81 σ
203	$\langle P_6' \rangle(B^0 \to K^{*0} \mu^+ \mu^-)^{[15,\ 19]}$	-0.0025886	0.81 σ	0.81 σ
204	$\langle A_9 \rangle(B^0 \to K^{*0} \mu^+ \mu^-)^{[1.1,\ 6]}$	7.3603×10^{-5}	0.8 σ	0.8 σ
205	$\langle A_{\mathrm{FB}}^{\ell} \rangle(\Lambda_b \to \Lambda \mu^+ \mu^-)^{[15,\ 20]}$	-0.33481	1.2 σ	0.8 σ
206	$\mu_{\mathrm{VBF}}(h \to \tau^+ \tau^-)$	0.99999	0.8 σ	0.8 σ
207	$\langle A_{\mathrm{FB}} \rangle(B^0 \to K^{*0} \mu^+ \mu^-)^{[4.3,\ 6]}$	0.08224	0.45 σ	0.77 σ
208	$\frac{\langle \mathrm{BR} \rangle}{\mathrm{BR}}(B \to D^* \tau^+ \nu)^{[6.67,\ 7.2]}$	0.096421	0.8 σ	0.8 σ
209	$\mathrm{BR}(K_L \to \pi^+ \mu^+ \nu)$	0.27234	0.77 σ	0.77 σ
210	$\frac{\langle \mathrm{BR} \rangle}{\mathrm{BR}}(B \to D \tau^+ \nu)^{[6.0,\ 6.5]}$	0.087333	0.78 σ	0.78 σ
211	$\langle P_1 \rangle(B^0 \to K^{*0} \mu^+ \mu^-)^{[2.5,\ 4]}$	-0.092975	0.7 σ	0.76 σ
212	$\tilde{A}_n^{[0.586]}$	-0.11027	0.78 σ	0.78 σ
213	$\langle P_4' \rangle(B^+ \to K^{*+} \mu^+ \mu^-)^{[4,\ 6]}$	-0.48861	0.8 σ	0.77 σ
214	$\langle P_1 \rangle(B^0 \to K^{*0} e^+ e^-)^{[0.000784,\ 0.257]}$	0.03227	0.78 σ	0.77 σ
215	$\left\langle \frac{dR}{d\theta} \right\rangle (e^+ e^- \to W^+ W^-)^{[189.09,\ -1.0,\ -0.8]}$	0.661	0.77 σ	0.77 σ
216	$\langle P_2 \rangle(B^0 \to K^{*0} \mu^+ \mu^-)^{[2.5,\ 4]}$	-0.20976	0.12 σ	0.78 σ
217	$\left\langle \frac{dR}{d\theta} \right\rangle (e^+ e^- \to W^+ W^-)^{[205.92,\ 0.8,\ 1.0]}$	7.783	0.77 σ	0.77 σ
218	$R(e^+ e^- \to W^+ W^-)^{[199.5]}$	1	0.76 σ	0.76 σ
219	$\langle F_L \rangle(B^0 \to K^{*0} \mu^+ \mu^-)^{[0,\ 2]}$	0.34491	0.52 σ	0.8 σ
220	$\langle P_3 \rangle(B^+ \to K^{*+} \mu^+ \mu^-)^{[2.5,\ 4]}$	0.0030891	0.74 σ	0.74 σ
221	$\frac{\langle \mathrm{BR} \rangle}{\mathrm{BR}}(B \to D \tau^+ \nu)^{[7.5,\ 8.0]}$	0.086998	0.75 σ	0.75 σ
222	$\tilde{A}_n^{[0.559]}$	-0.11027	0.75 σ	0.75 σ
223	$\left\langle \frac{dR}{d\theta} \right\rangle (e^+ e^- \to W^+ W^-)^{[198.38,\ -0.4,\ -0.2]}$	1.021	0.75 σ	0.75 σ
224	$\langle P_3 \rangle(B^+ \to K^{*+} \mu^+ \mu^-)^{[4,\ 6]}$	0.002185	0.7 σ	0.7 σ
225	$\left\langle \frac{dR}{d\theta} \right\rangle (e^+ e^- \to W^+ W^-)^{[205.92,\ 0.4,\ 0.6]}$	2.903	0.74 σ	0.74 σ
226	$\langle P_1 \rangle(B^0 \to K^{*0} \mu^+ \mu^-)^{[2,\ 4.3]}$	-0.083388	0.79 σ	0.74 σ
227	R_b^0	0.21581	0.73 σ	0.73 σ
228	$\mu_{\mathrm{VBF}}(h \to \gamma\gamma)$	0.99999	0.72 σ	0.72 σ
229	$\langle \overline{F_L} \rangle(B_s \to \phi \mu^+ \mu^-)^{[15.0,\ 19.0]}$	0.34101	0.69 σ	0.69 σ
230	$\langle F_L \rangle(B^0 \to K^{*0} \mu^+ \mu^-)^{[4,\ 6]}$	0.69525	0.44 σ	0.71 σ
231	$\tau_n^{[0.655]}$	1.3795×10^{27}	0.71 σ	0.71 σ
232	$\langle A_{\mathrm{FB}} \rangle(B^0 \to K^{*0} \mu^+ \mu^-)^{[1,\ 2]}$	-0.18814	0.51 σ	0.7 σ
233	$\left\langle \frac{dR}{d\theta} \right\rangle (e^+ e^- \to W^+ W^-)^{[198.38,\ 0.2,\ 0.4]}$	2.161	0.71 σ	0.71 σ
234	$\left\langle \frac{dR}{d\theta} \right\rangle (e^+ e^- \to W^+ W^-)^{[189.09,\ 0.0,\ 0.2]}$	1.715	0.7 σ	0.7 σ
235	R_{uc}^0	0.17225	0.69 σ	0.69 σ
236	$\mathscr{F}t(^{34}\mathrm{Ar})$	4.6665×10^{27}	0.72 σ	0.73 σ
237	$\langle P_2 \rangle(B^+ \to K^{*+} \mu^+ \mu^-)^{[0.1,\ 0.98]}$	-0.13427	0.69 σ	0.7 σ
238	$\langle F_L \rangle(B^0 \to K^{*0} \mu^+ \mu^-)^{[0.1,\ 0.98]}$	0.25971	0.076 σ	0.67 σ
239	$A_{\mathrm{FB}}^{0,e}$	0.016214	0.69 σ	0.69 σ
240	$\mu_{gg}(h \to b\bar{b})$	1	0.68 σ	0.68 σ
241	$\frac{\langle \mathrm{BR} \rangle}{\mathrm{BR}}(B \to D \tau^+ \nu)^{[8.5,\ 9.0]}$	0.075222	0.68 σ	0.68 σ
242	$\mathrm{BR}(B^+ \to \pi^+ \nu \bar{\nu})$	1.2435×10^{-7}	0.68 σ	0.68 σ
243	$\frac{\langle \mathrm{BR} \rangle}{\mathrm{BR}}(B \to D^* \tau^+ \nu)^{[7.5,\ 8.0]}$	0.097746	0.68 σ	0.68 σ
244	$\frac{\langle \mathrm{BR} \rangle}{\mathrm{BR}}(B \to D \tau^+ \nu)^{[10.5,\ 11.0]}$	0.034069	0.68 σ	0.68 σ
245	$\left\langle \frac{dR}{d\theta} \right\rangle (e^+ e^- \to W^+ W^-)^{[189.09,\ 0.6,\ 0.8]}$	4.122	0.68 σ	0.68 σ
246	$\mathrm{BR}(B^+ \to \rho^+ \nu \bar{\nu})$	4.2883×10^{-7}	0.67 σ	0.68 σ

	Observable	NP prediction	NP pull	SM pull
247	$\langle P_6' \rangle (B^0 \to K^{*0} \mu^+ \mu^-)^{[0.1,\ 0.98]}$	-0.057819	0.72 σ	0.69 σ
248	$\frac{\mathrm{BR}(B^0 \to K^{*0}\gamma)}{\overline{\mathrm{BR}}(B_s \to \phi\gamma)}$	1.0404	0.66 σ	0.66 σ
249	$\mu_{t\bar{t}h}(h \to ZZ)$	1	0.67 σ	0.67 σ
250	$\frac{\langle \mathrm{BR} \rangle}{\mathrm{BR}} (B \to D\tau^+\nu)^{[4.0,\ 4.53]}$	0.039797	0.67 σ	0.67 σ
251	$\frac{\langle \mathrm{BR} \rangle}{\mathrm{BR}} (B \to D^*\tau^+\nu)^{[10.0,\ 10.5]}$	0.05616	0.66 σ	0.66 σ
252	$\mathscr{F}t(^{38}\mathrm{Ca})$	4.6665×10^{27}	0.68 σ	0.67 σ
253	$\langle P_5' \rangle (B^0 \to K^{*0} \mu^+ \mu^-)^{[4.3,\ 6]}$	-0.63167	1.2 σ	0.67 σ
254	$\left\langle \frac{dR}{d\theta} \right\rangle (e^+e^- \to W^+W^-)^{[182.66,\ -0.2,\ 0.0]}$	1.402	0.65 σ	0.65 σ
255	$\mathrm{R}_{\tau e}(W^\pm \to \ell^\pm \nu)$	0.99953	0.64 σ	0.65 σ
256	$\langle A_{\mathrm{FB}} \rangle (B^0 \to K^{*0} \mu^+ \mu^-)^{[2,\ 4.3]}$	-0.076594	0.25 σ	0.65 σ
257	$\langle F_L \rangle (B^0 \to K^{*0} \mu^+ \mu^-)^{[2.5,\ 4]}$	0.76472	0.14 σ	0.64 σ
258	$\mathrm{BR}(B^0 \to \mu^+\mu^-)$	1.0213×10^{-10}	0.65 σ	0.65 σ
259	$\left\langle \frac{dR}{d\theta} \right\rangle (e^+e^- \to W^+W^-)^{[205.92,\ -1.0,\ -0.8]}$	0.532	0.64 σ	0.64 σ
260	$\mathrm{BR}(B^0 \to \pi^0 \nu\bar{\nu})$	5.7879×10^{-8}	0.63 σ	0.63 σ
261	$S_{K^*\gamma}$	-0.023305	0.64 σ	0.63 σ
262	$\frac{\langle \mathrm{BR} \rangle}{\mathrm{BR}} (B \to D\tau^+\nu)^{[4.0,\ 4.5]}$	0.03694	0.63 σ	0.63 σ
263	$\mu_{Wh}(h \to b\bar{b})$	1	0.62 σ	0.62 σ
264	$\mathrm{R}_{\tau\mu}(W^\pm \to \ell^\pm \nu)$	0.99953	0.58 σ	0.61 σ
265	$R(e^+e^- \to W^+W^-)^{[195.5]}$	1	0.61 σ	0.61 σ
266	$\frac{\langle \mathrm{BR} \rangle}{\mathrm{BR}} (B \to D^*\tau^+\nu)^{[4.53,\ 5.07]}$	0.047598	0.61 σ	0.61 σ
267	$\left\langle \frac{dR}{d\theta} \right\rangle (e^+e^- \to W^+W^-)^{[205.92,\ -0.8,\ -0.6]}$	0.642	0.61 σ	0.61 σ
268	$\langle P_3 \rangle (B^0 \to K^{*0} \mu^+ \mu^-)^{[4,\ 6]}$	0.0022292	0.6 σ	0.6 σ
269	$\langle F_L \rangle (B^0 \to K^{*0} \mu^+ \mu^-)^{[4.3,\ 6]}$	0.68834	0.48 σ	0.6 σ
270	$\mu_{Zh}(h \to \tau^+\tau^-)$	1	0.6 σ	0.6 σ
271	$\mathrm{BR}(B^0 \to \pi^-\tau^+\nu_\tau)$	0.00010418	0.63 σ	0.63 σ
272	Γ_Z	2.494	0.66 σ	0.6 σ
273	$\mathscr{F}t(^{54}\mathrm{Co})$	4.6665×10^{27}	0.57 σ	0.57 σ
274	$\langle R_{\mu e} \rangle (B^+ \to K^{*+} \ell^+ \ell^-)^{[15.0,\ 19.0]}$	0.83103	0.83 σ	0.59 σ
275	$\langle A_{\mathrm{FB}} \rangle (B^0 \to K^{*0} \mu^+ \mu^-)^{[0,\ 2]}$	-0.11537	0.65 σ	0.61 σ
276	$\langle R_{\mu e} \rangle (B^\pm \to K^\pm \ell^+ \ell^-)^{[4.0,\ 8.12]}$	0.83656	1 σ	0.59 σ
277	D_n	2.8379×10^{-25}	0.6 σ	0.6 σ
278	A_b	0.93471	0.59 σ	0.59 σ
279	$\mu_{gg}(h \to W^+W^-)$	1	0.58 σ	0.58 σ
280	$\langle P_5' \rangle (B^0 \to K^{*0} \mu^+ \mu^-)^{[0.04,\ 2]}$	0.60523	0.19 σ	0.49 σ
281	$\mathrm{BR}(\tau^- \to e^-\mu^+e^-)$	2.1035×10^{-89}	0.58 σ	0.58 σ
282	$\mathrm{BR}(B^- \to K^-\tau^+\mu^-)$	1.6205×10^{-20}	0.57 σ	0.57 σ
283	$\langle P_8' \rangle (B^+ \to K^{*+} \mu^+ \mu^-)^{[15,\ 19]}$	0.00077581	0.56 σ	0.56 σ
284	$R_{\mu e}(B \to D^* \ell^+ \nu)$	0.99583	0.53 σ	0.56 σ
285	$\frac{\langle \mathrm{BR} \rangle}{\mathrm{BR}} (B \to D\tau^+\nu)^{[8.27,\ 8.8]}$	0.083047	0.56 σ	0.56 σ
286	$\langle P_3 \rangle (B^+ \to K^{*+} \mu^+ \mu^-)^{[15,\ 19]}$	-0.00052625	0.52 σ	0.52 σ
287	$\langle P_5' \rangle (B^0 \to K^{*0} \mu^+ \mu^-)^{[1,\ 2]}$	0.42384	0.91 σ	0.52 σ
288	$\langle P_6' \rangle (B^0 \to K^{*0} \mu^+ \mu^-)^{[2.5,\ 4]}$	-0.055302	0.54 σ	0.56 σ
289	$\langle P_5' \rangle (B^+ \to K^{*+} \mu^+ \mu^-)^{[0.1,\ 0.98]}$	0.73584	0.76 σ	0.59 σ
290	$\frac{\langle \mathrm{BR} \rangle}{\mathrm{BR}} (B \to D\tau^+\nu)^{[4.53,\ 5.07]}$	0.0622	0.53 σ	0.53 σ
291	$\langle R_{\mu e} \rangle (B^0 \to K^0 \ell^+ \ell^-)^{[14.18,\ 19.0]}$	0.83977	0.7 σ	0.53 σ
292	$\lambda_{AB}^{[0.581]}$	-1.251	0.53 σ	0.53 σ
293	$A_{\mathrm{FB}}^{0,\mu}$	0.016214	0.53 σ	0.53 σ
294	$\langle P_1 \rangle (B^+ \to K^{*+} \mu^+ \mu^-)^{[1.1,\ 2.5]}$	0.02184	0.53 σ	0.53 σ
295	$\langle A_8 \rangle (B^0 \to K^{*0} \mu^+ \mu^-)^{[15,\ 19]}$	5.4076×10^{-5}	0.52 σ	0.52 σ
296	$\frac{\langle \mathrm{BR} \rangle}{\mathrm{BR}} (B \to D\tau^+\nu)^{[11.5,\ 12.0]}$	0.0018997	0.52 σ	0.52 σ
297	$\langle \frac{d\mathrm{BR}}{dq^2} \rangle (B^0 \to K^{*0} \mu^+ \mu^-)^{[0,\ 2]}$	7.9467×10^{-8}	0.68 σ	0.53 σ
298	$\mathrm{BR}(\tau^- \to \mu^-e^+\mu^-)$	8.6274×10^{-59}	0.51 σ	0.51 σ
299	$\mathrm{BR}(\pi^+ \to e^+\nu)$	0.0001234	0.51 σ	0.51 σ
300	$\langle \frac{d\mathrm{BR}}{dq^2} \rangle (B^+ \to K^{*+} \mu^+ \mu^-)^{[2.0,\ 4.0]}$	4.3362×10^{-8}	0.8 σ	0.49 σ
301	$R(e^+e^- \to W^+W^-)^{[206.6]}$	1	0.5 σ	0.5 σ
302	$\langle R_{\mu e} \rangle (B^0 \to K^0 \ell^+ \ell^-)^{[0.1,\ 4.0]}$	0.83503	0.66 σ	0.5 σ

	Observable	NP prediction	NP pull	SM pull
303	$\frac{\langle \mathrm{BR} \rangle}{\mathrm{BR}}(B \to D^* \tau^+ \nu)^{[4.5,\ 5.0]}$	0.042537	0.5 σ	0.5 σ
304	$\mu_{t\bar{t}h}(h \to \tau^+ \tau^-)$	1	0.49 σ	0.49 σ
305	$\left\langle \frac{dR}{d\theta} \right\rangle (e^+ e^- \to W^+ W^-)^{[182.66,\ -0.4,\ -0.2]}$	1.181	0.49 σ	0.49 σ
306	$\mathrm{BR}(\tau^- \to \mu^- e^+ e^-)$	7.1088×10^{-26}	0.49 σ	0.49 σ
307	$\langle F_L \rangle (B^+ \to K^{*+} \mu^+ \mu^-)^{[15,\ 19]}$	0.33762	0.5 σ	0.5 σ
308	$\langle P_2 \rangle (B^+ \to K^{*+} \mu^+ \mu^-)^{[1.1,\ 2.5]}$	-0.4585	0.5 σ	0.48 σ
309	$\mathrm{BR}(B^0 \to K^0 \nu \bar{\nu})$	5.5029×10^{-6}	0.33 σ	0.48 σ
310	$\langle \frac{d\mathrm{BR}}{dq^2} \rangle (B^0 \to K^0 \mu^+ \mu^-)^{[0,\ 2]}$	2.7943×10^{-8}	0.19 σ	0.47 σ
311	$\langle F_L \rangle (B^0 \to K^{*0} \mu^+ \mu^-)^{[0.04,\ 2]}$	0.34491	0.79 σ	0.43 σ
312	$\mathrm{BR}(B_c \to \tau^+ \nu)$	0.028435	0.56 σ	0.46 σ
313	$\frac{\langle \mathrm{BR} \rangle}{\mathrm{BR}}(B \to D^* \tau^+ \nu)^{[7.0,\ 7.5]}$	0.094377	0.45 σ	0.45 σ
314	A_s	0.93552	0.45 σ	0.45 σ
315	$\mathrm{BR}(B^- \to K^{*-} e^+ \mu^-)$	2.8849×10^{-22}	0.45 σ	0.45 σ
316	$\left\langle \frac{dR}{d\theta} \right\rangle (e^+ e^- \to W^+ W^-)^{[198.38,\ -0.8,\ -0.6]}$	0.664	0.45 σ	0.45 σ
317	$\overline{\mathrm{BR}}(B_s \to \phi \gamma)$	4.0162×10^{-5}	0.42 σ	0.43 σ
318	$\frac{\langle \mathrm{BR} \rangle}{\mathrm{BR}}(B \to D^* \tau^+ \nu)^{[9.86,\ 10.4]}$	0.067671	0.44 σ	0.44 σ
319	$\langle P_2 \rangle (B^0 \to K^{*0} \mu^+ \mu^-)^{[15,\ 19]}$	0.35191	0.24 σ	0.43 σ
320	$\langle P_1 \rangle (B^0 \to K^{*0} \mu^+ \mu^-)^{[15,\ 19]}$	-0.62265	0.42 σ	0.43 σ
321	$\langle P_2 \rangle (B^0 \to K^{*0} e^+ e^-)^{[0.000784,\ 0.257]}$	-0.013205	0.41 σ	0.43 σ
322	$\mu_{Wh}(h \to ZZ)$	1	0.43 σ	0.43 σ
323	$\frac{\langle \mathrm{BR} \rangle}{\mathrm{BR}}(B \to D \tau^+ \nu)^{[11.0,\ 11.5]}$	0.019884	0.43 σ	0.43 σ
324	$\langle \frac{d\mathrm{BR}}{dq^2} \rangle (B^\pm \to K^\pm \mu^+ \mu^-)^{[2,\ 4.3]}$	2.9828×10^{-8}	0.22 σ	0.41 σ
325	$\mu_{gg}(h \to \gamma\gamma)$	1	0.42 σ	0.42 σ
326	$\langle \mathrm{BR} \rangle (B \to X_s e^+ e^-)^{[1.0,\ 6.0]}$	1.8341×10^{-6}	0.28 σ	0.42 σ
327	$\langle P_4' \rangle (B^0 \to K^{*0} \mu^+ \mu^-)^{[0.04,\ 2]}$	0.12201	0.5 σ	0.45 σ
328	$\mathrm{BR}(K_L \to \mu^+ \mu^-)$	7.3597×10^{-9}	0.42 σ	0.41 σ
329	$\left\langle \frac{dR}{d\theta} \right\rangle (e^+ e^- \to W^+ W^-)^{[189.09,\ -0.4,\ -0.2]}$	1.137	0.41 σ	0.41 σ
330	$\langle P_4' \rangle (B^+ \to K^{*+} \mu^+ \mu^-)^{[2.5,\ 4]}$	-0.36596	0.43 σ	0.41 σ
331	$\langle F_L \rangle (B^0 \to K^{*0} \mu^+ \mu^-)^{[2,\ 4.3]}$	0.76007	0.024 σ	0.4 σ
332	$\mathscr{F}t(^{74}\mathrm{Rb})$	4.6665×10^{27}	0.39 σ	0.39 σ
333	a_n	-0.09921	0.39 σ	0.39 σ
334	$\langle \frac{d\mathrm{BR}}{dq^2} \rangle (B^0 \to K^0 \mu^+ \mu^-)^{[2,\ 4.3]}$	2.767×10^{-8}	0.13 σ	0.39 σ
335	$\langle P_1 \rangle (B^0 \to K^{*0} \mu^+ \mu^-)^{[0.1,\ 0.98]}$	0.041514	0.4 σ	0.38 σ
336	$\left\langle \frac{dR}{d\theta} \right\rangle (e^+ e^- \to W^+ W^-)^{[198.38,\ 0.0,\ 0.2]}$	1.666	0.38 σ	0.38 σ
337	R_τ^0	20.777	0.27 σ	0.37 σ
338	$\langle P_2 \rangle (B^+ \to K^{*+} \mu^+ \mu^-)^{[15,\ 19]}$	0.35346	0.13 σ	0.36 σ
339	$\mathscr{F}t(^{34}\mathrm{Cl})$	4.6665×10^{27}	0.39 σ	0.39 σ
340	$\langle R_{\mu e} \rangle (B^0 \to K^{*0} \ell^+ \ell^-)^{[0.1,\ 8.0]}$	0.85895	0.022 σ	0.37 σ
341	$\langle R_{\mu e} \rangle (B^0 \to K^{*0} \ell^+ \ell^-)^{[15.0,\ 19.0]}$	0.83104	0.79 σ	0.36 σ
342	$\mu_{\mathrm{VBF}}(h \to ZZ)$	1	0.35 σ	0.35 σ
343	$\langle A_{\mathrm{FB}}^h \rangle (\Lambda_b \to \Lambda \mu^+ \mu^-)^{[15,\ 20]}$	-0.31831	0.31 σ	0.31 σ
344	A_μ	0.14703	0.34 σ	0.34 σ
345	$\overline{\mathrm{BR}}(B_s \to \tau^+ \tau^-)$	0.00026434	0.42 σ	0.33 σ
346	$\mu_{t\bar{t}h}(h \to b\bar{b})$	1	0.32 σ	0.32 σ
347	$\langle F_L \rangle (B^+ \to K^{*+} \mu^+ \mu^-)^{[4,\ 6]}$	0.69599	0.17 σ	0.29 σ
348	$\frac{\langle \mathrm{BR} \rangle}{\mathrm{BR}}(B \to D \tau^+ \nu)^{[6.5,\ 7.0]}$	0.090073	0.32 σ	0.32 σ
349	$\langle P_8' \rangle (B^0 \to K^{*0} \mu^+ \mu^-)^{[2.5,\ 4]}$	-0.013804	0.26 σ	0.28 σ
350	$\langle P_8' \rangle (B^+ \to K^{*+} \mu^+ \mu^-)^{[4,\ 6]}$	-0.010087	0.28 σ	0.28 σ
351	$\frac{\langle \mathrm{BR} \rangle}{\mathrm{BR}}(B \to D \tau^+ \nu)^{[4.5,\ 5.0]}$	0.055942	0.3 σ	0.3 σ
352	$\langle P_1 \rangle (B^0 \to K^{*0} \mu^+ \mu^-)^{[0.04,\ 2]}$	0.040328	0.33 σ	0.34 σ
353	$\langle F_L \rangle (B^+ \to K^{*+} \mu^+ \mu^-)^{[0.1,\ 0.98]}$	0.26798	0.57 σ	0.3 σ
354	σ_{had}^0	0.00010655	0.47 σ	0.3 σ
355	$\mathscr{F}t(^{42}\mathrm{Sc})$	4.6665×10^{27}	0.33 σ	0.32 σ
356	$\mathrm{BR}(\bar{B}^0 \to \bar{K}^{*0} \mu^+ e^-)$	2.6796×10^{-22}	0.3 σ	0.3 σ
357	$\langle P_2 \rangle (B^+ \to K^{*+} \mu^+ \mu^-)^{[2.5,\ 4]}$	-0.20266	0.77 σ	0.28 σ
358	R_n	9.7994×10^{-21}	0.33 σ	0.33 σ

	Observable	NP prediction	NP pull	SM pull
359	$\langle R_{\mu e}\rangle(B^{\pm}\to K^{\pm}\ell^{+}\ell^{-})^{[14.18,\ 19.0]}$	0.83975	0.87 σ	0.29 σ
360	$\langle R_{\mu e}\rangle(B^{\pm}\to K^{\pm}\ell^{+}\ell^{-})^{[0.1,\ 4.0]}$	0.83503	0.35 σ	0.28 σ
361	$\langle P_5'\rangle(B^{+}\to K^{*+}\mu^{+}\mu^{-})^{[2.5,\ 4]}$	-0.31369	0.41 σ	0.26 σ
362	$\langle \overline{S_3}\rangle(B_s\to\phi\mu^{+}\mu^{-})^{[2.0,\ 5.0]}$	-0.0072466	0.26 σ	0.25 σ
363	$\langle P_3\rangle(B^{0}\to K^{*0}\mu^{+}\mu^{-})^{[2.5,\ 4]}$	0.0031278	0.23 σ	0.22 σ
364	$\Gamma(\pi^{+}\to\mu^{+}\nu)$	2.5202×10^{-17}	0.25 σ	0.25 σ
365	$S_{\psi\phi}$	0.037986	0.14 σ	0.23 σ
366	$\langle P_4'\rangle(B^{0}\to K^{*0}\mu^{+}\mu^{-})^{[2.5,\ 4]}$	-0.36793	0.39 σ	0.25 σ
367	$\mathrm{R}(W^{+}\to cX)$	0.50001	0.25 σ	0.25 σ
368	$x_{12}^{\mathrm{Im},D}$	4.2076×10^{-18}	0.24 σ	0.24 σ
369	$\mathrm{BR}(B^{-}\to K^{*-}\mu^{+}e^{-})$	2.8849×10^{-22}	0.25 σ	0.25 σ
370	$\mu_{\mathrm{VBF}}(h\to\mu^{+}\mu^{-})$	0.99999	0.24 σ	0.24 σ
371	$\langle P_5'\rangle(B^{0}\to K^{*0}\mu^{+}\mu^{-})^{[2,\ 4.3]}$	-0.24463	0.8 σ	0.26 σ
372	$\mu_{Zh}(h\to ZZ)$	1	0.23 σ	0.23 σ
373	$\langle P_5'\rangle(B^{0}\to K^{*0}\mu^{+}\mu^{-})^{[2,\ 4]}$	-0.20115	0.35 σ	0.24 σ
374	$\langle\frac{d\mathrm{BR}}{dq^2}\rangle(B^{+}\to K^{*+}\mu^{+}\mu^{-})^{[0,\ 2]}$	8.315×10^{-8}	0.17 σ	0.24 σ
375	$\mu_{Vh}(h\to ZZ)$	1	0.23 σ	0.23 σ
376	$\mathrm{BR}(K^{+}\to\mu^{+}\nu)$	0.63364	0.22 σ	0.22 σ
377	$\langle P_6'\rangle(B^{+}\to K^{*+}\mu^{+}\mu^{-})^{[1.1,\ 2.5]}$	-0.054332	0.24 σ	0.24 σ
378	$\frac{\langle\mathrm{BR}\rangle}{\mathrm{BR}}(B\to D^{*}\tau^{+}\nu)^{[5.6,\ 6.13]}$	0.076832	0.22 σ	0.22 σ
379	$\frac{\langle\mathrm{BR}\rangle}{\mathrm{BR}}(B\to D\tau^{+}\nu)^{[11.47,\ 12.0]}$	0.002539	0.22 σ	0.22 σ
380	$R(e^{+}e^{-}\to W^{+}W^{-})^{[191.6]}$	1	0.21 σ	0.21 σ
381	$\langle F_L\rangle(B^{0}\to K^{*0}e^{+}e^{-})^{[0.000784,\ 0.257]}$	0.05191	0.24 σ	0.21 σ
382	$\frac{\langle\mathrm{BR}\rangle}{\mathrm{BR}}(B\to D^{*}\tau^{+}\nu)^{[8.5,\ 9.0]}$	0.095922	0.2 σ	0.2 σ
383	$\mu_{Vh}(h\to\gamma\gamma)$	1	0.2 σ	0.2 σ
384	$\left\langle\frac{dR}{d\theta}\right\rangle(e^{+}e^{-}\to W^{+}W^{-})^{[189.09,\ 0.2,\ 0.4]}$	2.187	0.2 σ	0.2 σ
385	$\mathrm{BR}(B^{-}\to K^{-}\tau^{+}e^{-})$	5.896×10^{-7}	0.14 σ	0.2 σ
386	$\langle P_1\rangle(B^{+}\to K^{*+}\mu^{+}\mu^{-})^{[15,\ 19]}$	-0.61926	0.18 σ	0.18 σ
387	$\left\langle\frac{dR}{d\theta}\right\rangle(e^{+}e^{-}\to W^{+}W^{-})^{[205.92,\ 0.6,\ 0.8]}$	4.445	0.19 σ	0.19 σ
388	$\langle P_1\rangle(B^{0}\to K^{*0}\mu^{+}\mu^{-})^{[1,\ 2]}$	0.038646	0.16 σ	0.15 σ
389	$\langle A_T^{\mathrm{Im}}\rangle(B^{0}\to K^{*0}e^{+}e^{-})^{[0.000784,\ 0.257]}$	0.00026076	0.21 σ	0.21 σ
390	$\langle P_8'\rangle(B^{+}\to K^{*+}\mu^{+}\mu^{-})^{[1.1,\ 2.5]}$	-0.022549	0.19 σ	0.19 σ
391	$\mathrm{BR}(B^{-}\to\pi^{-}\tau^{+}\mu^{-})$	5.7464×10^{-23}	0.18 σ	0.18 σ
392	$\mathrm{BR}(B\to X_s\gamma)$	0.00033107	0.16 σ	0.18 σ
393	$\mathrm{BR}(\tau^{+}\to\pi^{+}\bar{\nu})$	0.10837	0.12 σ	0.18 σ
394	$\mathrm{BR}(K^{+}\to\pi^{+}\nu\bar{\nu})$	8.3437×10^{-11}	0.19 σ	0.16 σ
395	$\frac{\langle\mathrm{BR}\rangle}{\mathrm{BR}}(B\to D^{*}\tau^{+}\nu)^{[6.5,\ 7.0]}$	0.088536	0.17 σ	0.17 σ
396	$\frac{\langle\mathrm{BR}\rangle}{\mathrm{BR}}(B\to D\tau^{+}\nu)^{[7.0,\ 7.5]}$	0.089808	0.17 σ	0.17 σ
397	$\mathrm{BR}(B^{0}\to K^{*0}\gamma)$	4.1783×10^{-5}	0.18 σ	0.16 σ
398	Γ_W	2.0917	0.16 σ	0.16 σ
399	$\langle\frac{d\mathrm{BR}}{dq^2}\rangle(B^{0}\to K^{*0}\mu^{+}\mu^{-})^{[1,\ 2]}$	4.4957×10^{-8}	0.21 σ	0.16 σ
400	$\langle P_8'\rangle(B^{0}\to K^{*0}\mu^{+}\mu^{-})^{[15,\ 19]}$	0.00077655	0.14 σ	0.14 σ
401	$\left\langle\frac{dR}{d\theta}\right\rangle(e^{+}e^{-}\to W^{+}W^{-})^{[182.66,\ 0.8,\ 1.0]}$	5.434	0.15 σ	0.15 σ
402	$\langle P_6'\rangle(B^{+}\to K^{*+}\mu^{+}\mu^{-})^{[4,\ 6]}$	-0.031992	0.13 σ	0.14 σ
403	$\langle F_L\rangle(B^{0}\to K^{*0}\mu^{+}\mu^{-})^{[15,\ 19]}$	0.33989	0.14 σ	0.13 σ
404	$\frac{\langle\mathrm{BR}\rangle}{\mathrm{BR}}(B\to D^{*}\tau^{+}\nu)^{[5.0,\ 5.5]}$	0.05722	0.14 σ	0.14 σ
405	$\langle P_1\rangle(B^{+}\to K^{*+}\mu^{+}\mu^{-})^{[2.5,\ 4]}$	-0.093246	0.12 σ	0.1 σ
406	$R_T(K^{+}\to\pi^{0}\mu^{+}\nu)$	1.5878×10^{-36}	0.1 σ	0.1 σ
407	$\langle P_6'\rangle(B^{+}\to K^{*+}\mu^{+}\mu^{-})^{[2.5,\ 4]}$	-0.04655	0.12 σ	0.12 σ
408	$\mathscr{F}t(^{50}\mathrm{Mn})$	4.6665×10^{27}	0.12 σ	0.12 σ
409	$\frac{\langle\mathrm{BR}\rangle}{\mathrm{BR}}(B\to D\tau^{+}\nu)^{[8.0,\ 8.5]}$	0.082028	0.13 σ	0.13 σ
410	$\sigma_{\mathrm{trident}}/\sigma_{\mathrm{trident}}^{\mathrm{SM}}$	1	0.13 σ	0.13 σ
411	$\frac{\langle\mathrm{BR}\rangle}{\mathrm{BR}}(B\to D^{*}\tau^{+}\nu)^{[9.33,\ 9.86]}$	0.087022	0.13 σ	0.13 σ
412	$R(e^{+}e^{-}\to W^{+}W^{-})^{[201.6]}$	1	0.12 σ	0.12 σ
413	$\langle P_4'\rangle(B^{0}\to K^{*0}\mu^{+}\mu^{-})^{[1.1,\ 2.5]}$	-0.071117	0.073 σ	0.12 σ
414	$\left\langle\frac{dR}{d\theta}\right\rangle(e^{+}e^{-}\to W^{+}W^{-})^{[198.38,\ -0.2,\ 0.0]}$	1.265	0.1 σ	0.1 σ
415	$\langle R_{\mu e}\rangle(B^{+}\to K^{*+}\ell^{+}\ell^{-})^{[0.1,\ 8.0]}$	0.85835	0.32 σ	0.1 σ

	Observable	NP prediction	NP pull	SM pull
416	$\frac{\langle \mathrm{BR} \rangle}{\mathrm{BR}}(B \to D\tau^+\nu)^{[5.07,\ 5.6]}$	0.07714	0.1 σ	0.1 σ
417	$\langle P_6' \rangle (B^+ \to K^{*+}\mu^+\mu^-)^{[0.1,\ 0.98]}$	-0.050366	0.087 σ	0.079 σ
418	$\frac{\langle \mathrm{BR} \rangle}{\mathrm{BR}}(B \to D\tau^+\nu)^{[5.6,\ 6.13]}$	0.087798	0.1 σ	0.1 σ
419	$\mathrm{BR}(\tau^- \to e^- e^+ e^-)$	3.8425×10^{-12}	0.1 σ	0.1 σ
420	$\langle P_3 \rangle (B^+ \to K^{*+}\mu^+\mu^-)^{[1.1,\ 2.5]}$	0.0029324	0.084 σ	0.085 σ
421	$\left\langle \frac{dR}{d\theta} \right\rangle (e^+e^- \to W^+W^-)^{[205.92,\ -0.2,\ 0.0]}$	1.231	0.097 σ	0.097 σ
422	A_c	0.66752	0.092 σ	0.092 σ
423	$\ln(C)(K^+ \to \pi^0\mu^+\nu)$	0.19988	0.084 σ	0.084 σ
424	$\frac{\langle \mathrm{BR} \rangle}{\mathrm{BR}}(B \to D^*\tau^+\nu)^{[8.0,\ 8.5]}$	0.098402	0.084 σ	0.084 σ
425	$\frac{\langle \mathrm{BR} \rangle}{\mathrm{BR}}(B \to D^*\tau^+\nu)^{[9.0,\ 9.5]}$	0.089545	0.082 σ	0.082 σ
426	$\langle D^{\mu e}_{P_4'} \rangle (B^0 \to K^{*0}\ell^+\ell^-)^{[14.18,\ 19.0]}$	-7.9298×10^{-5}	0.072 σ	0.072 σ
427	$\mathscr{F}t(^{14}\mathrm{O})$	4.6665×10^{27}	0.041 σ	0.043 σ
428	$\frac{\langle \mathrm{BR} \rangle}{\mathrm{BR}}(B \to D\tau^+\nu)^{[5.0,\ 5.5]}$	0.070732	0.066 σ	0.066 σ
429	$\mathrm{BR}(B^+ \to K^{*+}\gamma)$	4.2462×10^{-5}	0.04 σ	0.055 σ
430	$\langle P_2 \rangle (B^0 \to K^{*0}\mu^+\mu^-)^{[1.1,\ 2.5]}$	-0.45667	0.12 σ	0.074 σ
431	$\frac{\langle \mathrm{BR} \rangle}{\mathrm{BR}}(B \to D^*\tau^+\nu)^{[9.5,\ 10.0]}$	0.077734	0.053 σ	0.053 σ
432	R_c^0	0.17223	0.042 σ	0.041 σ
433	$\langle P_4' \rangle (B^0 \to K^{*0}\mu^+\mu^-)^{[15,\ 19]}$	-0.63499	0.04 σ	0.038 σ
434	$\langle P_8' \rangle (B^+ \to K^{*+}\mu^+\mu^-)^{[2.5,\ 4]}$	-0.015318	0.028 σ	0.029 σ
435	$\langle P_8' \rangle (B^0 \to K^{*0}\mu^+\mu^-)^{[0.1,\ 0.98]}$	-0.001826	0.036 σ	0.0032 σ
436	$\mathscr{F}t(^{38m}\mathrm{K})$	4.6665×10^{27}	0.017 σ	0.014 σ
437	$\frac{\langle \mathrm{BR} \rangle}{\mathrm{BR}}(B \to D^*\tau^+\nu)^{[4.0,\ 4.53]}$	0.028569	0.026 σ	0.026 σ
438	$\mu_{gg}(h \to \tau^+\tau^-)$	1	0.025 σ	0.025 σ
439	$\mathscr{F}t(^{62}\mathrm{Ga})$	4.6665×10^{27}	0.016 σ	0.017 σ
440	$\frac{\langle \mathrm{BR} \rangle}{\mathrm{BR}}(B \to D\tau^+\nu)^{[9.33,\ 9.86]}$	0.063887	0.016 σ	0.016 σ
441	$\mathrm{BR}(B^+ \to \mu^+\nu)$	4.1832×10^{-7}	0.17 σ	0.013 σ
442	$\langle \frac{d\mathrm{BR}}{dq^2} \rangle (B^+ \to K^{*+}\mu^+\mu^-)^{[2,\ 4.3]}$	4.356×10^{-8}	0.14 σ	0.0085 σ
443	$\mathrm{BR}(B^0 \to \tau^+\tau^-)$	1.0176×10^{-6}	0.031 σ	0.0045 σ
444	$\mathrm{BR}(\bar{B}^0 \to \bar{K}^{*0}e^+\mu^-)$	2.6796×10^{-22}	8.4×10^{-8} σ	0 σ
445	$\mathrm{BR}(B^- \to K^- e^+\mu^-)$	1.2368×10^{-22}	0 σ	0 σ
446	$\mathrm{BR}(B^- \to K^-\mu^+ e^-)$	1.2368×10^{-22}	8.4×10^{-8} σ	0 σ
447	$\mathrm{BR}(B^- \to K^-\mu^+\tau^-)$	1.6205×10^{-20}	0 σ	0 σ
448	$\mathrm{BR}(B^- \to \pi^-\mu^+\tau^-)$	5.7464×10^{-23}	0 σ	0 σ
449	$\mathrm{BR}(\bar{B}^0 \to e^\pm\mu^\mp)$	2.3614×10^{-27}	0 σ	0 σ
450	$\mathrm{BR}(\bar{B}^0 \to e^\pm\tau^\mp)$	3.9357×10^{-9}	0.00026 σ	0 σ
451	$\mathrm{BR}(\bar{B}^0 \to \mu^\pm\tau^\mp)$	1.0858×10^{-22}	0 σ	0 σ
452	$\mathrm{BR}(\bar{B}_s \to e^\pm\mu^\mp)$	6.77×10^{-25}	0 σ	0 σ
453	$\mathrm{BR}(\bar{B}_s \to \mu^\pm\tau^\mp)$	3.1385×10^{-20}	0 σ	0 σ
454	$\mathrm{BR}(\bar{B}^0 \to \pi^0 e^\pm\mu^\mp)$	3.4752×10^{-25}	0 σ	0 σ
455	$\mathrm{BR}(B^- \to \pi^- e^\pm\mu^\mp)$	7.4665×10^{-25}	0 σ	0 σ
456	$\mathrm{BR}(K_L \to e^\pm\mu^\mp)$	2.5388×10^{-24}	0 σ	0 σ
457	$\mathrm{BR}(\mu^- \to e^- e^+ e^-)$	3.0781×10^{-27}	0 σ	0 σ
458	$\mathrm{BR}(\mu \to e\gamma)$	2.4192×10^{-36}	0 σ	0 σ
459	$\mathrm{BR}(\tau \to \mu\gamma)$	7.6018×10^{-35}	0 σ	0 σ
460	$\mathrm{BR}(\tau^- \to \mu^-\mu^+\mu^-)$	1.0555×10^{-25}	0 σ	0 σ
461	$\mathrm{BR}(\tau^- \to e^-\mu^+\mu^-)$	2.5878×10^{-12}	0 σ	0 σ
462	$\mathrm{BR}(\tau \to e\gamma)$	2.787×10^{-21}	0 σ	0 σ
463	$\mathrm{BR}(\tau^+ \to \rho^0 e^+)$	2.4383×10^{-12}	0.00022 σ	0 σ
464	$\mathrm{BR}(\tau^+ \to \rho^0\mu^+)$	6.6168×10^{-26}	0 σ	0 σ
465	$\mathrm{BR}(\tau^+ \to \phi e^+)$	9.6464×10^{-9}	0.51 σ	0 σ
466	$\mathrm{BR}(\tau^+ \to \phi\mu^+)$	2.6082×10^{-22}	0 σ	0 σ
467	$CR(\mu - e)$ in $^{48}_{22}\mathrm{Ti}$	4.598×10^{-26}	0 σ	0 σ
468	$CR(\mu - e)$ in $^{197}_{79}\mathrm{Au}$	5.4131×10^{-26}	0 σ	0 σ
469	$\mathrm{BR}(Z^0 \to e^\pm\mu^\mp)$	1.0657×10^{-27}	0 σ	0 σ
470	$\mathrm{BR}(Z^0 \to e^\pm\tau^\mp)$	8.0094×10^{-12}	0.0026 σ	0 σ
471	$\mathrm{BR}(Z^0 \to \mu^\pm\tau^\mp)$	2.2002×10^{-25}	0 σ	0 σ

Bibliography

[1] J. Alda, J. Guasch, and S. Penaranda. "Some results on Lepton Flavour Universality Violation". In: *Eur. Phys. J. C* 79.7 (2019), p. 588. DOI: 10.1140/epjc/s10052-019-7092-x. arXiv: 1805.03636 [hep-ph].

[2] J. Alda, J. Guasch, and S. Peñaranda. "Anomalies in B mesons decays: A phenomenological approach". In: *Eur. Phys. J. Plus* 137 (Feb. 2022), p. 217. DOI: 10.1140/epjp/s13360-022-02405-3. arXiv: 2012.14799 [hep-ph].

[3] J. Alda, J. Guasch, and S. Penaranda. "Anomalies in B mesons decays: Present status and future collider prospects". In: *International Workshop on Future Linear Colliders*. May 2021. arXiv: 2105.05095 [hep-ph].

[4] J. Alda, J. Guasch, and S. Penaranda. "Using Machine Learning techniques in phenomenological studies in flavour physics". In: (Sept. 2021). arXiv: 2109.07405 [hep-ph].

[5] J. Alda, J. Guasch, and S. Penaranda. "Exploring B-physics anomalies at colliders". In: *European Physical Society Conference on High Energy Physics 2021*. Vol. EPS-HEP2021. Oct. 2021, p. 494. DOI: 10.22323/1.398.0494. arXiv: 2110.12240 [hep-ph].

[6] J. Alda, A. W. M. Guerrera, S. Peñaranda, and S. Rigolin. "Leptonic Meson Decays into Invisible ALP". In: (Nov. 2021). arXiv: 2111.02536 [hep-ph].

[7] S. L. Glashow. "Partial Symmetries of Weak Interactions". In: *Nucl. Phys.* 22 (1961), pp. 579–588. DOI: 10.1016/0029-5582(61)90469-2.

[8] S. Weinberg. "A Model of Leptons". In: *Phys. Rev. Lett.* 19 (1967), pp. 1264–1266. DOI: 10.1103/PhysRevLett.19.1264.

[9] A. Salam. "Weak and Electromagnetic Interactions". In: *Conf. Proc. C* 680519 (1968), pp. 367–377. DOI: 10.1142/9789812795915_0034.

[10] F. Englert and R. Brout. "Broken Symmetry and the Mass of Gauge Vector Mesons". In: *Phys. Rev. Lett.* 13 (1964). Ed. by J. C. Taylor, pp. 321–323. DOI: 10.1103/PhysRevLett.13.321.

[11] P. W. Higgs. "Broken Symmetries and the Masses of Gauge Bosons". In: *Phys. Rev. Lett.* 13 (1964). Ed. by J. C. Taylor, pp. 508–509. DOI: 10.1103/PhysRevLett.13.508.

[12] G. Aad *et al.* "Observation of a new particle in the search for the Standard Model Higgs boson with the ATLAS detector at the LHC". In: *Phys. Lett. B* 716 (2012), pp. 1–29. DOI: 10.1016/j.physletb.2012.08.020. arXiv: 1207.7214 [hep-ex].

[13] S. Chatrchyan *et al.* "Observation of a New Boson at a Mass of 125 GeV with the CMS Experiment at the LHC". In: *Phys. Lett. B* 716 (2012), pp. 30–61. DOI: 10.1016/j.physletb.2012.08.021. arXiv: 1207.7235 [hep-ex].

[14] G. 't Hooft. "Symmetry Breaking Through Bell-Jackiw Anomalies". In: *Phys. Rev. Lett.* 37 (1976). Ed. by M. A. Shifman, pp. 8–11. DOI: 10.1103/PhysRevLett.37.8.

[15] C. Quigg. *Gauge Theories of the Strong, Weak, and Electromagnetic Interactions: Second Edition*. USA: Princeton University Press, Sept. 2013. ISBN: 978-0-691-13548-9, 978-1-4008-4822-5.

[16] M. E. Peskin and D. V. Schroeder. *An Introduction to quantum field theory*. Reading, USA: Addison-Wesley, 1995. ISBN: 978-0-201-50397-5.

[17] S. Weinberg. *The Quantum theory of fields. Vol. 1: Foundations*. Cambridge University Press, June 2005. ISBN: 978-0-521-67053-1, 978-0-511-25204-4.

[18] S. Weinberg. *The quantum theory of fields. Vol. 2: Modern applications*. Cambridge University Press, Aug. 2013. ISBN: 978-1-139-63247-8, 978-0-521-67054-8, 978-0-521-55002-4.

[19] D. J. Gross and R. Jackiw. "Effect of anomalies on quasirenormalizable theories". In: *Phys. Rev. D* 6 (1972), pp. 477–493. DOI: 10.1103/PhysRevD.6.477.

[20] H. Georgi and S. L. Glashow. "Gauge theories without anomalies". In: *Phys. Rev. D* 6 (1972), p. 429. DOI: 10.1103/PhysRevD.6.429.

[21] D. Decamp *et al.* "A Precise Determination of the Number of Families With Light Neutrinos and of the Z Boson Partial Widths". In: *Phys. Lett. B* 235 (1990), pp. 399–411. DOI: 10.1016/0370-2693(90)91984-J.

[22] S. Schael *et al.* "Precision electroweak measurements on the Z resonance". In: *Phys. Rept.* 427 (2006), pp. 257–454. DOI: 10.1016/j.physrep.2005.12.006. arXiv: hep-ex/0509008.

[23] N. Aghanim *et al.* "Planck 2018 results. VI. Cosmological parameters". In: *Astron. Astrophys.* 641 (2020). [Erratum: Astron.Astrophys. 652, C4 (2021)], A6. DOI: 10.1051/0004-6361/201833910. arXiv: 1807.06209 [astro-ph.CO].

[24] A. D. Sakharov. "Violation of CP Invariance, C asymmetry, and baryon asymmetry of the universe". In: *Pisma Zh. Eksp. Teor. Fiz.* 5 (1967), pp. 32–35. DOI: 10.1070/PU1991v034n05ABEH002497.

[25] P. Huet and E. Sather. "Electroweak baryogenesis and standard model CP violation". In: *Phys. Rev. D* 51 (1995), pp. 379–394. DOI: 10.1103/PhysRevD.51.379. arXiv: hep-ph/9404302.

[26] Y. Fukuda *et al.* "Evidence for oscillation of atmospheric neutrinos". In: *Phys. Rev. Lett.* 81 (1998), pp. 1562–1567. DOI: 10.1103/PhysRevLett.81.1562. arXiv: hep-ex/9807003.

[27] Q. R. Ahmad *et al.* "Direct evidence for neutrino flavor transformation from neutral current interactions in the Sudbury Neutrino Observatory". In: *Phys. Rev. Lett.* 89 (2002), p. 011301. DOI: 10.1103/PhysRevLett.89.011301. arXiv: nucl-ex/0204008.

[28] K. Eguchi *et al.* "First results from KamLAND: Evidence for reactor anti-neutrino disappearance". In: *Phys. Rev. Lett.* 90 (2003), p. 021802. DOI: 10.1103/PhysRevLett.90.021802. arXiv: hep-ex/0212021.

[29] B. Pontecorvo. "Mesonium and anti-mesonium". In: *Sov. Phys. JETP* 6 (1957), p. 429.

[30] B. Pontecorvo. "Inverse beta processes and nonconservation of lepton charge". In: *Zh. Eksp. Teor. Fiz.* 34 (1957), p. 247.

[31] C. Giganti, S. Lavignac, and M. Zito. "Neutrino oscillations: The rise of the PMNS paradigm". In: *Prog. Part. Nucl. Phys.* 98 (2018), pp. 1–54. DOI: 10.1016/j.ppnp.2017.10.001. arXiv: 1710.00715 [hep-ex].

[32] A. De Simone. "Introduction to cosmology and dark matter". In: *CERN Yellow Rep. School Proc.* 6 (2019). Ed. by M. Mulders and C. Duhr, pp. 145–180. DOI: 10.23730/CYRSP-2019-006.145.

[33] O. Fischer *et al.* "Unveiling Hidden Physics at the LHC". In: (Sept. 2021). arXiv: 2109.06065 [hep-ph].

[34] A. Pich. "The Standard Model of Electroweak Interactions". In: *2010 European School of High Energy Physics*. Jan. 2012, pp. 1–50. arXiv: 1201.0537 [hep-ph].

[35] A. Pich. "Flavour Dynamics and Violations of the CP Symmetry". In: *CERN Yellow Rep. School Proc.* 4 (2018). Ed. by M. Mulders and G. Zanderighi, p. 63. DOI: 10.23730/CYRSP-2018-004.63. arXiv: 1805.08597 [hep-ph].

[36] R. M. Godbole. "Field Theory and the Electro-Weak Standard Model". In: *2nd Asia-Europe-Pacific School of High-Energy Physics*. 2017, pp. 1–61. DOI: 10.23730/CYRSP-2017-002.1. arXiv: 1703.04978 [hep-ph].

[37] P. A. Zyla *et al.* "Review of Particle Physics". In: *PTEP* 2020.8 (2020), p. 083C01. DOI: 10.1093/ptep/ptaa104.

[38] J. Charles, A. Hocker, H. Lacker, S. Laplace, F. R. Le Diberder, *et al.* "CP violation and the CKM matrix: Assessing the impact of the asymmetric *B* factories". In: *Eur. Phys. J. C* 41.1 (2005). updated results and plots available at http://ckmfitter.in2p3.fr/, pp. 1–131. DOI: 10.1140/epjc/s2005-02169-1. arXiv: hep-ph/0406184.

[39] L. Wolfenstein. "Parametrization of the Kobayashi-Maskawa Matrix". In: *Phys. Rev. Lett.* 51 (1983), p. 1945. DOI: 10.1103/PhysRevLett.51.1945.

[40] Z. Maki, M. Nakagawa, and S. Sakata. "Remarks on the unified model of elementary particles". In: *Prog. Theor. Phys.* 28 (1962), pp. 870–880. DOI: 10.1143/PTP.28.870.

[41] G. Buchalla, A. J. Buras, and M. K. Harlander. "Penguin box expansion: Flavor changing neutral current processes and a heavy top quark". In: *Nucl. Phys. B* 349 (1991), pp. 1–47. DOI: 10.1016/0550-3213(91)90186-2.

[42] Y. Nir. "Flavour physics and CP violation". In: *CERN Yellow Rep. School Proc.* 5 (2020). Ed. by M. Mulders and J. Trân Thanh Vân, pp. 79–128. DOI: 10.23730/CYRSP-2020-005.79.

[43] S. L. Glashow, J. Iliopoulos, and L. Maiani. "Weak Interactions with Lepton-Hadron Symmetry". In: *Phys. Rev. D* 2 (1970), pp. 1285–1292. DOI: 10.1103/PhysRevD.2.1285.

[44] S. T. Petcov. "The Processes $\mu \to e + \gamma, \mu \to e + \overline{e}, \nu' \to \nu + \gamma$ in the Weinberg-Salam Model with Neutrino Mixing". In: *Sov. J. Nucl. Phys.* 25 (1977). [Erratum: Sov.J.Nucl.Phys. 25, 698 (1977), Erratum: Yad.Fiz. 25, 1336 (1977)], p. 340.

[45] S. M. Bilenky, S. T. Petcov, and B. Pontecorvo. "Lepton Mixing, mu –> e + gamma Decay and Neutrino Oscillations". In: *Phys. Lett. B* 67 (1977), p. 309. DOI: 10.1016/0370-2693(77)90379-3.

[46] A. Pich. "Rare kaon decays and CP violation". In: *PoS* Beauty2019 (2020), p. 027. DOI: 10.22323/1.377.0027. arXiv: 2001.11350 [hep-ph].

[47] P. Chang, K.-F. Chen, and W.-S. Hou. "Flavor Physics and CP Violation". In: *Prog. Part. Nucl. Phys.* 97 (2017), pp. 261–311. DOI: 10.1016/j.ppnp.2017.07.001. arXiv: 1708.03793 [hep-ph].

[48] T. Blake, G. Lanfranchi, and D. M. Straub. "Rare B Decays as Tests of the Standard Model". In: *Prog. Part. Nucl. Phys.* 92 (2017), pp. 50–91. DOI: 10.1016/j.ppnp.2016.10.001. arXiv: 1606.00916 [hep-ph].

[49] P. Koppenburg, Z. Dolezal, and M. Smizanska. "Rare decays of b hadrons". In: *Scholarpedia* 11 (2016), p. 32643. DOI: 10.4249/scholarpedia.32643. arXiv: 1606.00999 [hep-ex].

[50] A. Ali. "Rare B-Meson Decays at the Crossroads". In: *Int. J. Mod. Phys. A* 31.23 (2016), p. 1630036. DOI: 10.1142/S0217751X16300362. arXiv: 1607.04918 [hep-ph].

[51] S. Bifani, S. Descotes-Genon, A. Romero Vidal, and M.-H. Schune. "Review of Lepton Universality tests in B decays". In: *J. Phys. G* 46.2 (2019), p. 023001. DOI: 10.1088/1361-6471/aaf5de. arXiv: 1809.06229 [hep-ex].

[52] G. Lanfranchi. "Rare b-hadron decays as probe of new physics". In: *Int. J. Mod. Phys. A* 33.14n15 (2018), p. 1830012. DOI: 10.1142/S0217751X18300120. arXiv: 1805.05399 [hep-ex].

[53] U. Egede and J. Serrano. "Rare b-hadron decays". In: *Comptes Rendus Physique* 21.1 (2020), pp. 93–106. DOI: 10.5802/crphys.10.

[54] S. Stone. "New physics from flavour". In: *PoS* ICHEP2012 (2013). Ed. by A. Limosani, p. 033. DOI: 10.22323/1.174.0033. arXiv: 1212.6374 [hep-ph].

[55] M. Artuso, G. Borissov, and A. Lenz. "CP violation in the B_s^0 system". In: *Rev. Mod. Phys.* 88.4 (2016). [Addendum: Rev.Mod.Phys. 91, 049901 (2019)], p. 045002. DOI: 10.1103/RevModPhys.88.045002. arXiv: 1511.09466 [hep-ph].

[56] R. Ammar *et al.* "Evidence for penguins: First observation of B —> K* (892) gamma". In: *Phys. Rev. Lett.* 71 (1993), pp. 674–678. DOI: 10.1103/PhysRevLett.71.674.

[57] M. S. Alam *et al.* "First measurement of the rate for the inclusive radiative penguin decay $b \to s\gamma$". In: *Phys. Rev. Lett.* 74 (1995), pp. 2885–2889. DOI: 10.1103/PhysRevLett.74.2885.

[58] R. Aaij *et al.* "First Evidence for the Decay $B_s^0 \to \mu^+\mu^-$". In: *Phys. Rev. Lett.* 110.2 (2013), p. 021801. DOI: 10.1103/PhysRevLett.110.021801. arXiv: 1211.2674 [hep-ex].

[59] S. Chatrchyan *et al.* "Measurement of the $B_s^0 \to \mu^+\mu^-$ Branching Fraction and Search for $B^0 \to \mu^+\mu^-$ with the CMS Experiment". In: *Phys. Rev. Lett.* 111 (2013), p. 101804. DOI: 10.1103/PhysRevLett.111.101804. arXiv: 1307.5025 [hep-ex].

[60] C. Bobeth, M. Gorbahn, T. Hermann, M. Misiak, E. Stamou, *et al.* "$B_{s,d} \to l^+l^-$ in the Standard Model with Reduced Theoretical Uncertainty". In: *Phys. Rev. Lett.* 112 (2014), p. 101801. DOI: 10.1103/PhysRevLett.112.101801. arXiv: 1311.0903 [hep-ph].

[61] R. Aaij *et al.* "Measurement of the $B_s^0 \to \mu^+\mu^-$ decay properties and search for the $B^0 \to \mu^+\mu^-$ and $B_s^0 \to \mu^+\mu^-\gamma$ decays". In: *Phys. Rev. D* 105.1 (2022), p. 012010. DOI: 10.1103/PhysRevD.105.012010. arXiv: 2108.09283 [hep-ex].

[62] R. Aaij *et al.* "Analysis of Neutral B-Meson Decays into Two Muons". In: *Phys. Rev. Lett.* 128.4 (2022), p. 041801. DOI: 10.1103/PhysRevLett.128.041801. arXiv: 2108.09284 [hep-ex].

[63] W. Altmannshofer and P. Stangl. "New physics in rare B decays after Moriond 2021". In: *Eur. Phys. J. C* 81.10 (2021), p. 952. DOI: 10.1140/epjc/s10052-021-09725-1. arXiv: 2103.13370 [hep-ph].

[64] B. Aubert *et al.* "A search for the rare decay $B^0 \to \tau^+\tau^-$ at BABAR". In: *Phys. Rev. Lett.* 96 (2006), p. 241802. DOI: 10.1103/PhysRevLett.96.241802. arXiv: hep-ex/0511015.

[65] R. Aaij *et al.* "Search for the decays $B_s^0 \to \tau^+\tau^-$ and $B^0 \to \tau^+\tau^-$". In: *Phys. Rev. Lett.* 118.25 (2017), p. 251802. DOI: 10.1103/PhysRevLett.118.251802. arXiv: 1703.02508 [hep-ex].

[66] E. Kurbatov. "LHCb results on rare leptonic decays of B-mesons". In: *EPJ Web Conf.* 222 (2019). Ed. by D. Melikhov and I. Volobuev, p. 02008. DOI: 10.1051/epjconf/201922202008.

[67] R. Fleischer. "Probing New Physics with Leptonic Rare B Decays". In: *PoS* CORFU2019 (2020), p. 021. DOI: 10.22323/1.376.0021.

[68] C. Cornella, G. Isidori, M. König, S. Liechti, P. Owen, *et al.* "Hunting for $B^+ \to K^+\tau^+\tau^-$ imprints on the $B^+ \to K^+\mu^+\mu^-$ dimuon spectrum". In: *Eur. Phys. J. C* 80.12 (2020), p. 1095. DOI: 10.1140/epjc/s10052-020-08674-5. arXiv: 2001.04470 [hep-ph].

[69] T. Aaltonen *et al.* "Measurement of the Forward-Backward Asymmetry in the $B \to K^{(*)}\mu^+\mu^-$ Decay and First Observation of the $B_s^0 \to \phi\mu^+\mu^-$ Decay". In: *Phys. Rev. Lett.* 106 (2011), p. 161801. DOI: 10.1103/PhysRevLett.106.161801. arXiv: 1101.1028 [hep-ex].

[70] R. Aaij *et al.* "Differential branching fraction and angular analysis of the decay $B_s^0 \to \phi\mu^+\mu^-$". In: *JHEP* 07 (2013), p. 084. DOI: 10.1007/JHEP07(2013)084. arXiv: 1305.2168 [hep-ex].

[71] R. Aaij *et al.* "Angular analysis and differential branching fraction of the decay $B_s^0 \to \phi\mu^+\mu^-$". In: *JHEP* 09 (2015), p. 179. DOI: 10.1007/JHEP09(2015)179. arXiv: 1506.08777 [hep-ex].

[72] R. Aaij *et al.* "Branching Fraction Measurements of the Rare $B_s^0 \to \phi\mu^+\mu^-$ and $B_s^0 \to f_2'(1525)\mu^+\mu^-$ - Decays". In: *Phys. Rev. Lett.* 127.15 (2021), p. 151801. DOI: 10.1103/PhysRevLett.127.151801. arXiv: 2105.14007 [hep-ex].

[73] R. Aaij *et al.* "Angular analysis of the rare decay $B_s^0 \to \phi\mu^+\mu^-$". In: *JHEP* 11 (2021), p. 043. DOI: 10.1007/JHEP11(2021)043. arXiv: 2107.13428 [hep-ex].

[74] T. Aaltonen *et al.* "Observation of the Baryonic Flavor-Changing Neutral Current Decay $\Lambda_b \to \Lambda\mu^+\mu^-$". In: *Phys. Rev. Lett.* 107 (2011), p. 201802. DOI: 10.1103/PhysRevLett.107.201802. arXiv: 1107.3753 [hep-ex].

[75] R. Aaij *et al.* "Differential branching fraction and angular analysis of $\Lambda_b^0 \to \Lambda\mu^+\mu^-$ decays". In: *JHEP* 06 (2015). [Erratum: JHEP 09, 145 (2018)], p. 115. DOI: 10.1007/JHEP06(2015)115. arXiv: 1503.07138 [hep-ex].

[76] R. Aaij *et al.* "Angular moments of the decay $\Lambda_b^0 \to \Lambda\mu^+\mu^-$ at low hadronic recoil". In: *JHEP* 09 (2018), p. 146. DOI: 10.1007/JHEP09(2018)146. arXiv: 1808.00264 [hep-ex].

[77] R. Aaij *et al.* "Measurement of the phase difference between short- and long-distance amplitudes in the $B^+ \to K^+\mu^+\mu^-$ decay". In: *Eur. Phys. J. C* 77.3 (2017), p. 161. DOI: 10.1140/epjc/s10052-017-4703-2. arXiv: 1612.06764 [hep-ex].

[78] A. Khodjamirian, T. Mannel, A. A. Pivovarov, and Y. .-. Wang. "Charm-loop effect in $B \to K^{(*)}\ell^+\ell^-$ and $B \to K^*\gamma$". In: *JHEP* 09 (2010), p. 089. DOI: 10.1007/JHEP09(2010)089. arXiv: 1006.4945 [hep-ph].

[79] A. Khodjamirian, T. Mannel, and Y. M. Wang. "$B \to K\ell^+\ell^-$ decay at large hadronic recoil". In: *JHEP* 02 (2013), p. 010. DOI: 10.1007/JHEP02(2013)010. arXiv: 1211.0234 [hep-ph].

[80] S. Descotes-Genon, L. Hofer, J. Matias, and J. Virto. "QCD uncertainties in the prediction of B $\to K^*\mu^+\mu^-$ observables". In: *Nucl. Part. Phys. Proc.* 273-275 (2016). Ed. by M. Aguilar-Benítez, J. Fuster, S. Martí-García, and A. Santamaría, pp. 1442–1447. DOI: 10.1016/j.nuclphysbps.2015.09.233. arXiv: 1411.0922 [hep-ph].

[81] C. Bobeth, G. Hiller, and G. Piranishvili. "Angular distributions of $\bar{B} \to \bar{K}\ell^+\ell^-$ decays". In: *JHEP* 12 (2007), p. 040. DOI: 10.1088/1126-6708/2007/12/040. arXiv: 0709.4174 [hep-ph].

[82] F. Kruger, L. M. Sehgal, N. Sinha, and R. Sinha. "Angular distribution and CP asymmetries in the decays $\bar{B} \to K^-\pi^+e^-e^+$ and $\bar{B} \to \pi^-\pi^+e^-e^+$". In: *Phys. Rev. D* 61 (2000). [Erratum: Phys.Rev.D 63, 019901 (2001)], p. 114028. DOI: 10.1103/PhysRevD.61.114028. arXiv: hep-ph/9907386.

[83] W. Altmannshofer, P. Ball, A. Bharucha, A. J. Buras, D. M. Straub, *et al.* "Symmetries and Asymmetries of $B \to K^*\mu^+\mu^-$ Decays in the Standard Model and Beyond". In: *JHEP* 01 (2009), p. 019. DOI: 10.1088/1126-6708/2009/01/019. arXiv: 0811.1214 [hep-ph].

[84] S. Descotes-Genon, J. Matias, M. Ramon, and J. Virto. "Implications from clean observables for the binned analysis of $B- > K* \mu^+\mu^-$ at large recoil". In: *JHEP* 01 (2013), p. 048. DOI: 10.1007/JHEP01(2013)048. arXiv: 1207.2753 [hep-ph].

[85] M. De Cian. "Track Reconstruction Efficiency and Analysis of $B^0 \to K^{*0}\mu^+\mu^-$ at the LHCb Experiment". PhD thesis. Zurich U., 2013. DOI: 10.5167/uzh-85745.

[86] A. Ali, P. Ball, L. T. Handoko, and G. Hiller. "A Comparative study of the decays $B \to (K, K^*)\ell^+\ell^-$ in standard model and supersymmetric theories". In: *Phys. Rev. D* 61 (2000), p. 074024. DOI: 10.1103/PhysRevD.61.074024. arXiv: hep-ph/9910221.

[87] P. Ball and R. Zwicky. "New results on $B \to \pi, K, \eta$ decay formfactors from light-cone sum rules". In: *Phys. Rev. D* 71 (2005), p. 014015. DOI: 10.1103/PhysRevD.71.014015. arXiv: hep-ph/0406232.

[88] A. Bharucha, T. Feldmann, and M. Wick. "Theoretical and Phenomenological Constraints on Form Factors for Radiative and Semi-Leptonic B-Meson Decays". In: *JHEP* 09 (2010), p. 090. DOI: 10.1007/JHEP09(2010)090. arXiv: 1004.3249 [hep-ph].

[89] N. Gubernari, A. Kokulu, and D. van Dyk. "$B \to P$ and $B \to V$ Form Factors from B-Meson Light-Cone Sum Rules beyond Leading Twist". In: *JHEP* 01 (2019), p. 150. DOI: 10.1007/JHEP01(2019)150. arXiv: 1811.00983 [hep-ph].

[90] C. Bouchard, G. P. Lepage, C. Monahan, H. Na, and J. Shigemitsu. "Rare decay $B \to K\ell^+\ell^-$ form factors from lattice QCD". In: *Phys. Rev. D* 88.5 (2013). [Erratum: Phys.Rev.D 88, 079901 (2013)], p. 054509. DOI: 10.1103/PhysRevD.88.054509. arXiv: 1306.2384 [hep-lat].

[91] R. R. Horgan, Z. Liu, S. Meinel, and M. Wingate. "Lattice QCD calculation of form factors describing the rare decays $B \to K^*\ell^+\ell^-$ and $B_s \to \phi\ell^+\ell^-$". In: *Phys. Rev. D* 89.9 (2014), p. 094501. DOI: 10.1103/PhysRevD.89.094501. arXiv: 1310.3722 [hep-lat].

[92] R. R. Horgan, Z. Liu, S. Meinel, and M. Wingate. "Rare B decays using lattice QCD form factors". In: *PoS* LATTICE2014 (2015), p. 372. DOI: 10.22323/1.214.0372. arXiv: 1501.00367 [hep-lat].

[93] G. Hiller and F. Kruger. "More model-independent analysis of $b \to s$ processes". In: *Phys. Rev. D* 69 (2004), p. 074020. DOI: 10.1103/PhysRevD.69.074020. arXiv: hep-ph/0310219.

[94] B. Capdevila, S. Descotes-Genon, J. Matias, and J. Virto. "Assessing lepton-flavour non-universality from $B \to K^*\ell\ell$ angular analyses". In: *JHEP* 10 (2016), p. 075. DOI: 10.1007/JHEP10(2016)075. arXiv: 1605.03156 [hep-ph].

[95] D. Becirevic, S. Fajfer, I. Nisandzic, and A. Tayduganov. "Angular distributions of $\bar{B} \to D^{(*)}\ell\bar{\nu}_\ell$ decays and search of New Physics". In: *Nucl. Phys. B* 946 (2019), p. 114707. DOI: 10.1016/j.nuclphysb.2019.114707. arXiv: 1602.03030 [hep-ph].

[96] A. Peñuelas Martínez. "Phenomenology of the LHC and flavour factories". PhD thesis. U. Valencia (main), 2020.

[97] J. A. Bailey *et al.* "B→D$\ell\nu$ form factors at nonzero recoil and $|V_{cb}|$ from 2+1-flavor lattice QCD". In: *Phys. Rev. D* 92.3 (2015), p. 034506. DOI: 10.1103/PhysRevD.92.034506. arXiv: 1503.07237 [hep-lat].

[98] H. Na, C. M. Bouchard, G. P. Lepage, C. Monahan, and J. Shigemitsu. "$B \to Dl\nu$ form factors at nonzero recoil and extraction of $|V_{cb}|$". In: *Phys. Rev. D* 92.5 (2015). [Erratum: Phys.Rev.D 93, 119906 (2016)], p. 054510. DOI: 10.1103/PhysRevD.93.119906. arXiv: 1505.03925 [hep-lat].

[99] S. Fajfer, J. F. Kamenik, and I. Nisandzic. "On the $B \to D^* \tau \bar{\nu}_\tau$ Sensitivity to New Physics". In: *Phys. Rev. D* 85 (2012), p. 094025. DOI: 10.1103/PhysRevD.85.094025. arXiv: 1203.2654 [hep-ph].

[100] J. F. Kamenik and F. Mescia. "$B \to D\tau\nu$ Branching Ratios: Opportunity for Lattice QCD and Hadron Colliders". In: *Phys. Rev. D* 78 (2008), p. 014003. DOI: 10.1103/PhysRevD.78.014003. arXiv: 0802.3790 [hep-ph].

[101] G. Isidori and O. Sumensari. "Optimized lepton universality tests in $B \to V \ell \bar{\nu}$ decays". In: *Eur. Phys. J. C* 80.11 (2020), p. 1078. DOI: 10.1140/epjc/s10052-020-08653-w. arXiv: 2007.08481 [hep-ph].

[102] A. Abdesselam *et al.* "Precise determination of the CKM matrix element $|V_{cb}|$ with $\bar{B}^0 \to D^{*+} \ell^- \bar{\nu}_\ell$ decays with hadronic tagging at Belle". In: (Feb. 2017). arXiv: 1702.01521 [hep-ex].

[103] E. Waheed *et al.* "Measurement of the CKM matrix element $|V_{cb}|$ from $B^0 \to D^{*-} \ell^+ \nu_\ell$ at Belle". In: *Phys. Rev. D* 100.5 (2019). [Erratum: Phys.Rev.D 103, 079901 (2021)], p. 052007. DOI: 10.1103/PhysRevD.100.052007. arXiv: 1809.03290 [hep-ex].

[104] M. Jung and D. M. Straub. "Constraining new physics in $b \to c\ell\nu$ transitions". In: *JHEP* 01 (2019), p. 009. DOI: 10.1007/JHEP01(2019)009. arXiv: 1801.01112 [hep-ph].

[105] S. Jaiswal, S. Nandi, and S. K. Patra. "Extraction of $|V_{cb}|$ from $B \to D^{(*)} \ell \nu_\ell$ and the Standard Model predictions of $R(D^{(*)})$". In: *JHEP* 12 (2017), p. 060. DOI: 10.1007/JHEP12(2017)060. arXiv: 1707.09977 [hep-ph].

[106] E. Hernandez, J. Nieves, and J. M. Verde-Velasco. "Study of exclusive semileptonic and non-leptonic decays of B_c - in a nonrelativistic quark model". In: *Phys. Rev. D* 74 (2006), p. 074008. DOI: 10.1103/PhysRevD.74.074008. arXiv: hep-ph/0607150.

[107] M. Blanke, A. Crivellin, S. de Boer, T. Kitahara, M. Moscati, *et al.* "Impact of polarization observables and $B_c \to \tau\nu$ on new physics explanations of the $b \to c\tau\nu$ anomaly". In: *Phys. Rev. D* 99.7 (2019), p. 075006. DOI: 10.1103/PhysRevD.99.075006. arXiv: 1811.09603 [hep-ph].

[108] A. J. Bevan *et al.* "The Physics of the B Factories". In: *Eur. Phys. J. C* 74 (2014), p. 3026. DOI: 10.1140/epjc/s10052-014-3026-9. arXiv: 1406.6311 [hep-ex].

[109] B. Aubert *et al.* "The BaBar detector". In: *Nucl. Instrum. Meth. A* 479 (2002), pp. 1–116. DOI: 10.1016/S0168-9002(01)02012-5. arXiv: hep-ex/0105044.

[110] D. Boutigny *et al. The BABAR physics book: Physics at an asymmetric B factory.* Oct. 1998. DOI: 10.2172/979931.

[111] B. Aubert *et al.* "The BABAR Detector: Upgrades, Operation and Performance". In: *Nucl. Instrum. Meth. A* 729 (2013), pp. 615–701. DOI: 10.1016/j.nima.2013.05.107. arXiv: 1305.3560 [physics.ins-det].

[112] A. Abashian *et al.* "The Belle Detector". In: *Nucl. Instrum. Meth. A* 479 (2002), pp. 117–232. DOI: 10.1016/S0168-9002(01)02013-7.

[113] I. Adachi, T. E. Browder, P. Križan, S. Tanaka, and Y. Ushiroda. "Detectors for extreme luminosity: Belle II". In: *Nucl. Instrum. Meth. A* 907 (2018), pp. 46–59. DOI: 10.1016/j.nima.2018.03.068.

[114] W. Altmannshofer *et al.* "The Belle II Physics Book". In: *PTEP* 2019.12 (2019). Ed. by E. Kou and P. Urquijo. [Erratum: PTEP 2020, 029201 (2020)], p. 123C01. DOI: 10.1093/ptep/ptz106. arXiv: 1808.10567 [hep-ex].

[115] A. A. Alves Jr. *et al.* "The LHCb Detector at the LHC". In: *JINST* 3 (2008), S08005. DOI: 10.1088/1748-0221/3/08/S08005.

[116] A. Perrin. "Contribution to the Inner Tracker design and penguin sensitivity studies for the measurement of sin 2 β in LHCb". PhD thesis. Ecole Polytechnique, Lausanne, 2008.

[117] B. Adeva *et al.* "Roadmap for selected key measurements of LHCb". In: (Dec. 2009). arXiv: 0912.4179 [hep-ex].

[118] K. Abe *et al.* "Observation of the decay $B \to K\ell^+\ell^-$". In: *Phys. Rev. Lett.* 88 (2002), p. 021801. DOI: 10.1103/PhysRevLett.88.021801. arXiv: hep-ex/0109026.

[119] A. Ishikawa *et al.* "Observation of B —> K* l+ l-". In: *Phys. Rev. Lett.* 91 (2003). Ed. by H. W. K. Cheung and T. S. Pratt, p. 261601. DOI: 10.1103/PhysRevLett.91.261601. arXiv: hep-ex/0308044.

[120] J. .-. Wei *et al.* "Measurement of the Differential Branching Fraction and Forward-Backward Asymmetry for $B \to K^{(*)}\ell^+\ell^-$". In: *Phys. Rev. Lett.* 103 (2009), p. 171801. DOI: 10.1103/PhysRevLett.103.171801. arXiv: 0904.0770 [hep-ex].

[121] J. P. Lees *et al.* "Measurement of Branching Fractions and Rate Asymmetries in the Rare Decays $B \to K^{(*)}l^+l^-$". In: *Phys. Rev. D* 86 (2012), p. 032012. DOI: 10.1103/PhysRevD.86.032012. arXiv: 1204.3933 [hep-ex].

[122] R. Aaij *et al.* "Test of lepton universality using $B^+ \to K^+\ell^+\ell^-$ decays". In: *Phys. Rev. Lett.* 113 (2014), p. 151601. DOI: 10.1103/PhysRevLett.113.151601. arXiv: 1406.6482 [hep-ex].

[123] R. Aaij *et al.* "Search for lepton-universality violation in $B^+ \to K^+\ell^+\ell^-$ decays". In: *Phys. Rev. Lett.* 122.19 (2019), p. 191801. DOI: 10.1103/PhysRevLett.122.191801. arXiv: 1903.09252 [hep-ex].

[124] R. Aaij *et al.* "Test of lepton universality with $B^0 \to K^{*0}\ell^+\ell^-$ decays". In: *JHEP* 08 (2017), p. 055. DOI: 10.1007/JHEP08(2017)055. arXiv: 1705.05802 [hep-ex].

[125] S. Bifani. "Search for new physics with $b \to s\ell^+\ell^-$ decays at LHCb". In: *LHC Seminar*. Apr. 2017. URL: https://indico.cern.ch/event/580620/.

[126] A. Oyanguren. "B decay anomalies at LHCb". In: *EPJ Web Conf.* 175 (2018). Ed. by M. Della Morte, P. Fritzsch, E. Gámiz Sánchez, and C. Pena Ruano, p. 01004. DOI: 10.1051/epjconf/201817501004.

[127] A. Abdesselam *et al.* "Test of Lepton-Flavor Universality in $B \to K^*\ell^+\ell^-$ Decays at Belle". In: *Phys. Rev. Lett.* 126.16 (2021), p. 161801. DOI: 10.1103/PhysRevLett.126.161801. arXiv: 1904.02440 [hep-ex].

[128] S. Choudhury *et al.* "Test of lepton flavor universality and search for lepton flavor violation in $B \to K\ell\ell$ decays". In: *JHEP* 03 (2021), p. 105. DOI: 10.1007/JHEP03(2021)105. arXiv: 1908.01848 [hep-ex].

[129] R. Aaij *et al.* "Test of lepton universality in beauty-quark decays". In: (Mar. 2021). arXiv: 2103.11769 [hep-ex].

[130] R. Aaij *et al.* "Tests of lepton universality using $B^0 \to K^0_S\ell^+\ell^-$ and $B^+ \to K^{*+}\ell^+\ell^-$ decays". In: (Oct. 2021). arXiv: 2110.09501 [hep-ex].

[131] R. Aaij *et al.* "Measurement of Form-Factor-Independent Observables in the Decay $B^0 \to K^{*0}\mu^+\mu^-$". In: *Phys. Rev. Lett.* 111 (2013), p. 191801. DOI: 10.1103/PhysRevLett.111.191801. arXiv: 1308.1707 [hep-ex].

[132] R. Aaij *et al.* "Differential branching fractions and isospin asymmetries of $B \to K^{(*)}\mu^+\mu^-$ decays". In: *JHEP* 06 (2014), p. 133. DOI: 10.1007/JHEP06(2014)133. arXiv: 1403.8044 [hep-ex].

[133] R. Aaij *et al.* "Angular analysis of the $B^0 \to K^{*0}\mu^+\mu^-$ decay using 3 fb^{-1} of integrated luminosity". In: *JHEP* 02 (2016), p. 104. DOI: 10.1007/JHEP02(2016)104. arXiv: 1512.04442 [hep-ex].

[134] A. Abdesselam *et al.* "Angular analysis of $B^0 \to K^*(892)^0\ell^+\ell^-$". In: *LHC Ski 2016: A First Discussion of 13 TeV Results*. Apr. 2016. arXiv: 1604.04042 [hep-ex].

[135] S. Wehle *et al.* "Lepton-Flavor-Dependent Angular Analysis of $B \to K^*\ell^+\ell^-$". In: *Phys. Rev. Lett.* 118.11 (2017), p. 111801. DOI: 10.1103/PhysRevLett.118.111801. arXiv: 1612.05014 [hep-ex].

[136] R. Aaij *et al.* "Measurements of the S-wave fraction in $B^0 \to K^+\pi^-\mu^+\mu^-$ decays and the $B^0 \to K^*(892)^0\mu^+\mu^-$ differential branching fraction". In: *JHEP* 11 (2016). [Erratum: JHEP 04, 142 (2017)], p. 047. DOI: 10.1007/JHEP11(2016)047. arXiv: 1606.04731 [hep-ex].

[137] M. Aaboud *et al.* "Angular analysis of $B^0_d \to K^*\mu^+\mu^-$ decays in pp collisions at $\sqrt{s}$ = 8 TeV with the ATLAS detector". In: *JHEP* 10 (2018), p. 047. DOI: 10.1007/JHEP10(2018)047. arXiv: 1805.04000 [hep-ex].

[138] R. Aaij *et al.* "Measurement of *CP*-Averaged Observables in the $B^0 \to K^{*0}\mu^+\mu^-$ Decay". In: *Phys. Rev. Lett.* 125.1 (2020), p. 011802. DOI: 10.1103/PhysRevLett.125.011802. arXiv: 2003.04831 [hep-ex].

[139] S. Descotes-Genon, L. Hofer, J. Matias, and J. Virto. "On the impact of power corrections in the prediction of $B \to K^*\mu^+\mu^-$ observables". In: *JHEP* 12 (2014), p. 125. DOI: 10.1007/JHEP12(2014)125. arXiv: 1407.8526 [hep-ph].

[140] A. Matyja *et al.* "Observation of B0 —> D*- tau+ nu(tau) decay at Belle". In: *Phys. Rev. Lett.* 99 (2007), p. 191807. DOI: 10.1103/PhysRevLett.99.191807. arXiv: 0706.4429 [hep-ex].

[141] J. P. Lees *et al.* "Evidence for an excess of $\bar{B} \to D^{(*)}\tau^-\bar{\nu}_\tau$ decays". In: *Phys. Rev. Lett.* 109 (2012), p. 101802. DOI: 10.1103/PhysRevLett.109.101802. arXiv: 1205.5442 [hep-ex].

[142] I. Adachi *et al.* "Measurement of B —> D(*) tau nu using full reconstruction tags". In: *24th International Symposium on Lepton-Photon Interactions at High Energy (LP09)*. Oct. 2009. arXiv: 0910.4301 [hep-ex].

[143] M. Huschle *et al.* "Measurement of the branching ratio of $\bar{B} \to D^{(*)}\tau^-\bar{\nu}_\tau$ relative to $\bar{B} \to D^{(*)}\ell^-\bar{\nu}_\ell$ decays with hadronic tagging at Belle". In: *Phys. Rev. D* 92.7 (2015), p. 072014. DOI: 10.1103/PhysRevD.92.072014. arXiv: 1507.03233 [hep-ex].

[144] R. Aaij *et al.* "Measurement of the ratio of branching fractions $\mathcal{B}(\bar{B}^0 \to D^{*+}\tau^-\bar{\nu}_\tau)/\mathcal{B}(\bar{B}^0 \to D^{*+}\mu^-\bar{\nu}_\mu)$". In: *Phys. Rev. Lett.* 115.11 (2015). [Erratum: Phys.Rev.Lett. 115, 159901 (2015)], p. 111803. DOI: 10.1103/PhysRevLett.115.111803. arXiv: 1506.08614 [hep-ex].

[145] S. Hirose *et al.* "Measurement of the τ lepton polarization and $R(D^*)$ in the decay $\bar{B} \to D^*\tau^-\bar{\nu}_\tau$". In: *Phys. Rev. Lett.* 118.21 (2017), p. 211801. DOI: 10.1103/PhysRevLett.118.211801. arXiv: 1612.00529 [hep-ex].

[146] R. Aaij *et al.* "Measurement of the ratio of the $B^0 \to D^{*-}\tau^+\nu_\tau$ and $B^0 \to D^{*-}\mu^+\nu_\mu$ branching fractions using three-prong τ-lepton decays". In: *Phys. Rev. Lett.* 120.17 (2018), p. 171802. DOI: 10.1103/PhysRevLett.120.171802. arXiv: 1708.08856 [hep-ex].

[147] A. Abdesselam *et al.* "Measurement of $\mathcal{R}(D)$ and $\mathcal{R}(D^*)$ with a semileptonic tagging method". In: (Apr. 2019). arXiv: 1904.08794 [hep-ex].

[148] Y. S. Amhis *et al.* "Averages of b-hadron, c-hadron, and τ-lepton properties as of 2018". In: *Eur. Phys. J. C* 81.3 (2021), p. 226. DOI: 10.1140/epjc/s10052-020-8156-7. arXiv: 1909.12524 [hep-ex].

[149] A. Abdesselam *et al.* "Measurement of the D^{*-} polarization in the decay $B^0 \to D^{*-}\tau^+\nu_\tau$". In: *10th International Workshop on the CKM Unitarity Triangle*. Mar. 2019. arXiv: 1903.03102 [hep-ex].

[150] R. Aaij *et al.* "Measurement of the ratio of branching fractions $\mathscr{B}(B_c^+ \to J/\psi\tau^+\nu_\tau)/\mathscr{B}(B_c^+ \to J/\psi\mu^+\nu_\mu)$". In: *Phys. Rev. Lett.* 120.12 (2018), p. 121801. DOI: 10.1103/PhysRevLett.120.121801. arXiv: 1711.05623 [hep-ex].

[151] A. Dobado, A. Gomez-Nicola, A. L. Maroto, and J. R. Pelaez. *Effective lagrangians for the standard model*. 1997.

[152] I. Z. Rothstein. "TASI lectures on effective field theories". In: Aug. 2003. arXiv: hep-ph/0308266.

[153] A. Falkowski. "Effective Field Theories". In: *GDR-Intensity Frontier lectures*. Sept. 2020. URL: https://indico.in2p3.fr/event/22195/.

[154] T. Appelquist and J. Carazzone. "Infrared Singularities and Massive Fields". In: *Phys. Rev. D* 11 (1975), p. 2856. DOI: 10.1103/PhysRevD.11.2856.

[155] D. B. Kaplan. "Effective field theories". In: *7th Summer School in Nuclear Physics Symmetries*. June 1995. arXiv: nucl-th/9506035.

[156] A. V. Manohar. "Effective field theories". In: *Lect. Notes Phys.* 479 (1997). Ed. by H. Latal and W. Schweiger, pp. 311–362. DOI: 10.1007/BFb0104294. arXiv: hep-ph/9606222.

[157] A. Pich. "Effective field theory: Course". In: *Les Houches Summer School in Theoretical Physics, Session 68: Probing the Standard Model of Particle Interactions*. June 1998, pp. 949–1049. arXiv: hep-ph/9806303.

[158] A. V. Manohar. "Introduction to Effective Field Theories". In: (Apr. 2018). Ed. by S. Davidson, P. Gambino, M. Laine, M. Neubert, and C. Salomon. DOI: 10.1093/oso/9780198855743.003.0002. arXiv: 1804.05863 [hep-ph].

[159] D. J. Gross and F. Wilczek. "Ultraviolet Behavior of Nonabelian Gauge Theories". In: *Phys. Rev. Lett.* 30 (1973). Ed. by J. C. Taylor, pp. 1343–1346. DOI: 10.1103/PhysRevLett.30.1343.

[160] H. D. Politzer. "Reliable Perturbative Results for Strong Interactions?" In: *Phys. Rev. Lett.* 30 (1973). Ed. by J. C. Taylor, pp. 1346–1349. DOI: 10.1103/PhysRevLett.30.1346.

[161] H. Euler. "On the scattering of light by light according to Dirac's theory". In: *Annalen Phys.* 26.5 (1936), pp. 398–448. DOI: 10.1002/andp.19364180503.

[162] W. Heisenberg and H. Euler. "Consequences of Dirac's theory of positrons". In: *Z. Phys.* 98.11-12 (1936), pp. 714–732. DOI: 10.1007/BF01343663. arXiv: physics/0605038.

[163] Y. Liang and A. Czarnecki. "Photon-photon scattering: A Tutorial". In: *Can. J. Phys.* 90 (2012), pp. 11–26. DOI: 10.1139/p11-144. arXiv: 1111.6126 [hep-ph].

[164] H. Georgi. "Effective field theory". In: *Ann. Rev. Nucl. Part. Sci.* 43 (1993), pp. 209–252. DOI: 10.1146/annurev.ns.43.120193.001233.

[165] S. Weinberg. "Phenomenological Lagrangians". In: *Physica A* 96.1-2 (1979). Ed. by S. Deser, pp. 327–340. DOI: 10.1016/0378-4371(79)90223-1.

[166] J. Gasser and H. Leutwyler. "Chiral Perturbation Theory to One Loop". In: *Annals Phys.* 158 (1984), p. 142. DOI: 10.1016/0003-4916(84)90242-2.

[167] J. Gasser and H. Leutwyler. "Chiral Perturbation Theory: Expansions in the Mass of the Strange Quark". In: *Nucl. Phys. B* 250 (1985), pp. 465–516. DOI: 10.1016/0550-3213(85)90492-4.

[168] W. Buchmuller and D. Wyler. "Effective Lagrangian Analysis of New Interactions and Flavor Conservation". In: *Nucl. Phys. B* 268 (1986), pp. 621–653. DOI: 10.1016/0550-3213(86)90262-2.

[169] B. Grzadkowski, M. Iskrzynski, M. Misiak, and J. Rosiek. "Dimension-Six Terms in the Standard Model Lagrangian". In: *JHEP* 10 (2010), p. 085. DOI: 10.1007/JHEP10(2010)085. arXiv: 1008.4884 [hep-ph].

[170] H. Elvang. "Effective Field Theories from Amplitudes". In: (Oct. 2020). URL: https://indico.cern.ch/event/958298/.

[171] B. Henning, X. Lu, T. Melia, and H. Murayama. "Operator bases, S-matrices, and their partition functions". In: *JHEP* 10 (2017), p. 199. DOI: 10.1007/JHEP10(2017)199. arXiv: 1706.08520 [hep-th].

[172] R. M. Fonseca. "Enumerating the operators of an effective field theory". In: *Phys. Rev. D* 101.3 (2020), p. 035040. DOI: 10.1103/PhysRevD.101.035040. arXiv: 1907.12584 [hep-ph].

[173] F. Feruglio. "A Note on Gauge Anomaly Cancellation in Effective Field Theories". In: *JHEP* 03 (2021), p. 128. DOI: 10.1007/JHEP03(2021)128. arXiv: 2012.13989 [hep-ph].

[174] E. Fermi. "An attempt of a theory of beta radiation." In: *Z. Phys.* 88 (1934), pp. 161–177. DOI: 10.1007/BF01351864.

[175] E. Fermi. "Trends to a Theory of beta Radiation. (In Italian)". In: *Nuovo Cim.* 11 (1934), pp. 1–19. DOI: 10.1007/BF02959820.

[176] C. S. Wu. "The Universal Fermi Interaction and the Conserved Vector Current in Beta Decay". In: *Rev. Mod. Phys.* 36 (1964), p. 618. DOI: 10.1103/RevModPhys.36.618.

[177] G. Arnison *et al.* "Experimental Observation of Isolated Large Transverse Energy Electrons with Associated Missing Energy at $\sqrt{s} = 540$ GeV". In: *Phys. Lett. B* 122 (1983), pp. 103–116. DOI: 10.1016/0370-2693(83)91177-2.

[178] G. Arnison *et al.* "Further Evidence for Charged Intermediate Vector Bosons at the SPS Collider". In: *Phys. Lett. B* 129 (1983), pp. 273–282. DOI: 10.1016/0370-2693(83)90860-2.

[179] G. F. Giudice, C. Grojean, A. Pomarol, and R. Rattazzi. "The Strongly-Interacting Light Higgs". In: *JHEP* 06 (2007), p. 045. DOI: 10.1088/1126-6708/2007/06/045. arXiv: hep-ph/0703164.

[180] R. Contino, M. Ghezzi, C. Grojean, M. Muhlleitner, and M. Spira. "Effective Lagrangian for a light Higgs-like scalar". In: *JHEP* 07 (2013), p. 035. DOI: 10.1007/JHEP07(2013)035. arXiv: 1303.3876 [hep-ph].

[181] R. S. Gupta, A. Pomarol, and F. Riva. "BSM Primary Effects". In: *Phys. Rev. D* 91.3 (2015), p. 035001. DOI: 10.1103/PhysRevD.91.035001. arXiv: 1405.0181 [hep-ph].

[182] L. Lehman. "Extending the Standard Model Effective Field Theory with the Complete Set of Dimension-7 Operators". In: *Phys. Rev. D* 90.12 (2014), p. 125023. DOI: 10.1103/PhysRevD.90.125023. arXiv: 1410.4193 [hep-ph].

[183] B. Henning, X. Lu, T. Melia, and H. Murayama. "2, 84, 30, 993, 560, 15456, 11962, 261485, ...: Higher dimension operators in the SM EFT". In: *JHEP* 08 (2017). [Erratum: JHEP 09, 019 (2019)], p. 016. DOI: 10.1007/JHEP08(2017)016. arXiv: 1512.03433 [hep-ph].

[184] R. Alonso, E. E. Jenkins, A. V. Manohar, and M. Trott. "Renormalization Group Evolution of the Standard Model Dimension Six Operators III: Gauge Coupling Dependence and Phenomenology". In: *JHEP* 04 (2014), p. 159. DOI: 10.1007/JHEP04(2014)159. arXiv: 1312.2014 [hep-ph].

[185] E. E. Jenkins, A. V. Manohar, and P. Stoffer. "Low-Energy Effective Field Theory below the Electroweak Scale: Operators and Matching". In: *JHEP* 03 (2018), p. 016. DOI: 10.1007/JHEP03(2018)016. arXiv: 1709.04486 [hep-ph].

[186] S. Descotes-Genon, A. Falkowski, M. Fedele, M. González-Alonso, and J. Virto. "The CKM parameters in the SMEFT". In: *JHEP* 05 (2019), p. 172. DOI: 10.1007/JHEP05(2019)172. arXiv: 1812.08163 [hep-ph].

[187] E. E. Jenkins, A. V. Manohar, and M. Trott. "Renormalization Group Evolution of the Standard Model Dimension Six Operators I: Formalism and lambda Dependence". In: *JHEP* 10 (2013), p. 087. DOI: 10.1007/JHEP10(2013)087. arXiv: 1308.2627 [hep-ph].

[188] E. E. Jenkins, A. V. Manohar, and M. Trott. "Renormalization Group Evolution of the Standard Model Dimension Six Operators II: Yukawa Dependence". In: *JHEP* 01 (2014), p. 035. DOI: 10.1007/JHEP01(2014)035. arXiv: 1310.4838 [hep-ph].

[189] R. Alonso, H.-M. Chang, E. E. Jenkins, A. V. Manohar, and B. Shotwell. "Renormalization group evolution of dimension-six baryon number violating operators". In: *Phys. Lett. B* 734 (2014), pp. 302–307. DOI: 10.1016/j.physletb.2014.05.065. arXiv: 1405.0486 [hep-ph].

[190] E. E. Jenkins, A. V. Manohar, and P. Stoffer. "Low-Energy Effective Field Theory below the Electroweak Scale: Anomalous Dimensions". In: *JHEP* 01 (2018), p. 084. DOI: 10.1007/JHEP01(2018)084. arXiv: 1711.05270 [hep-ph].

[191] J. Aebischer, M. Fael, C. Greub, and J. Virto. "B physics Beyond the Standard Model at One Loop: Complete Renormalization Group Evolution below the Electroweak Scale". In: *JHEP* 09 (2017), p. 158. DOI: 10.1007/JHEP09(2017)158. arXiv: 1704.06639 [hep-ph].

[192] H.-L. Li, Z. Ren, M.-L. Xiao, J.-H. Yu, and Y.-H. Zheng. "Low energy effective field theory operator basis at d ≤ 9". In: *JHEP* 06 (2021), p. 138. DOI: 10.1007/JHEP06(2021)138. arXiv: 2012.09188 [hep-ph].

[193] A. J. Buras and M. Munz. "Effective Hamiltonian for B —> X(s) e+ e- beyond leading logarithms in the NDR and HV schemes". In: *Phys. Rev. D* 52 (1995), pp. 186–195. DOI: 10.1103/PhysRevD.52.186. arXiv: hep-ph/9501281.

[194] G. Buchalla, A. J. Buras, and M. E. Lautenbacher. "Weak decays beyond leading logarithms". In: *Rev. Mod. Phys.* 68 (1996), pp. 1125–1144. DOI: 10.1103/RevModPhys.68.1125. arXiv: hep-ph/9512380.

[195] D. M. Straub. "flavio: a Python package for flavour and precision phenomenology in the Standard Model and beyond". In: (Oct. 2018). arXiv: 1810.08132 [hep-ph].

[196] J. Aebischer *et al.* "WCxf: an exchange format for Wilson coefficients beyond the Standard Model". In: *Comput. Phys. Commun.* 232 (2018), pp. 71–83. DOI: 10.1016/j.cpc.2018.05.022. arXiv: 1712.05298 [hep-ph].

[197] C. Bobeth, M. Misiak, and J. Urban. "Photonic penguins at two loops and m_t dependence of $BR[B \to X_s l^+ l^-]$". In: *Nucl. Phys. B* 574 (2000), pp. 291–330. DOI: 10.1016/S0550-3213(00)00007-9. arXiv: hep-ph/9910220.

[198] C. Bobeth, G. Hiller, and D. van Dyk. "General analysis of $\bar{B} \to \bar{K}^{(*)} \ell^+ \ell^-$ decays at low recoil". In: *Phys. Rev. D* 87.3 (2013), p. 034016. DOI: 10.1103/PhysRevD.87.034016. arXiv: 1212.2321 [hep-ph].

[199] M. Tanaka and R. Watanabe. "New physics in the weak interaction of $\bar{B} \to D^{(*)} \tau \bar{\nu}$". In: *Phys. Rev. D* 87.3 (2013), p. 034028. DOI: 10.1103/PhysRevD.87.034028. arXiv: 1212.1878 [hep-ph].

[200] J. Aebischer, A. Crivellin, M. Fael, and C. Greub. "Matching of gauge invariant dimension-six operators for $b \to s$ and $b \to c$ transitions". In: *JHEP* 05 (2016), p. 037. DOI: 10.1007/JHEP05(2016)037. arXiv: 1512.02830 [hep-ph].

[201] B. Bhattacharya, A. Datta, J.-P. Guévin, D. London, and R. Watanabe. "Simultaneous Explanation of the R_K and $R_{D^{(*)}}$ Puzzles: a Model Analysis". In: *JHEP* 01 (2017), p. 015. DOI: 10.1007/JHEP01(2017)015. arXiv: 1609.09078 [hep-ph].

[202] F. Feruglio, P. Paradisi, and A. Pattori. "On the Importance of Electroweak Corrections for B Anomalies". In: *JHEP* 09 (2017), p. 061. DOI: 10.1007/JHEP09(2017)061. arXiv: 1705.00929 [hep-ph].

[203] L. Di Luzio, M. Kirk, and A. Lenz. "B_s-$\bar{B}_s$ mixing interplay with B anomalies". In: *10th International Workshop on the CKM Unitarity Triangle*. Nov. 2018. arXiv: 1811.12884 [hep-ph].

[204] A. J. Buras, M. Jamin, and P. H. Weisz. "Leading and Next-to-leading QCD Corrections to ϵ Parameter and $B^0 - \bar{B}^0$ Mixing in the Presence of a Heavy Top Quark". In: *Nucl. Phys. B* 347 (1990), pp. 491–536. DOI: 10.1016/0550-3213(90)90373-L.

[205] T. Inami and C. S. Lim. "Effects of Superheavy Quarks and Leptons in Low-Energy Weak Processes k(L) —> mu anti-mu, K+ —> pi+ Neutrino anti-neutrino and K0 <—> anti-K0". In: *Prog. Theor. Phys.* 65 (1981). [Erratum: Prog.Theor.Phys. 65, 1772 (1981)], p. 297. DOI: 10.1143/PTP.65.297.

[206] A. Crivellin, G. D'Ambrosio, and J. Heeck. "Addressing the LHC flavor anomalies with horizontal gauge symmetries". In: *Phys. Rev. D* 91.7 (2015), p. 075006. DOI: 10.1103/PhysRevD.91.075006. arXiv: 1503.03477 [hep-ph].

[207] B. Gripaios, M. Nardecchia, and S. A. Renner. "Linear flavour violation and anomalies in B physics". In: *JHEP* 06 (2016), p. 083. DOI: 10.1007/JHEP06(2016)083. arXiv: 1509.05020 [hep-ph].

[208] P. Arnan, L. Hofer, F. Mescia, and A. Crivellin. "Loop effects of heavy new scalars and fermions in $b \to s\mu^+\mu^-$". In: *JHEP* 04 (2017), p. 043. DOI: 10.1007/JHEP04(2017)043. arXiv: 1608.07832 [hep-ph].

[209] A. K. Alok, B. Bhattacharya, A. Datta, D. Kumar, J. Kumar, *et al.* "New Physics in $b \to s\mu^+\mu^-$ after the Measurement of R_{K^*}". In: *Phys. Rev. D* 96.9 (2017), p. 095009. DOI: 10.1103/PhysRevD.96.095009. arXiv: 1704.07397 [hep-ph].

[210] C. Hati and U. Sarkar. "$B - L$ violating nucleon decays as a probe of leptoquarks and implications for baryogenesis". In: *Nucl. Phys. B* 954 (2020), p. 114985. DOI: 10.1016/j.nuclphysb.2020.114985. arXiv: 1805.06081 [hep-ph].

[211] P. Stangl. "Flavour anomalies and (fundamental) partial compositeness". In: *PoS* CORFU2018 (2019). Ed. by K. Anagnostopoulos *et al.*, p. 033. DOI: 10.22323/1.347.0033. arXiv: 1907.05158 [hep-ph].

[212] J. Heeck and D. Teresi. "Pati-Salam and lepton universality in B decays". In: *54th Rencontres de Moriond on Electroweak Interactions and Unified Theories*. 2019, pp. 333–338. arXiv: 1905.05211 [hep-ph].

[213] J.-P. Lee. "B anomalies in the nonminimal universal extra dimension model". In: *Phys. Rev. D* 100.7 (2019), p. 075005. DOI: 10.1103/PhysRevD.100.075005. arXiv: 1906.07345 [hep-ph].

[214] Z.-L. Han, R. Ding, S.-J. Lin, and B. Zhu. "Gauged $U(1)_{L_\mu - L_\tau}$ scotogenic model in light of $R_{K^{(*)}}$ anomaly and AMS-02 positron excess". In: *Eur. Phys. J. C* 79.12 (2019), p. 1007. DOI: 10.1140/epjc/s10052-019-7526-5. arXiv: 1908.07192 [hep-ph].

[215] A. Datta, J. L. Feng, S. Kamali, and J. Kumar. "Resolving the $(g-2)_\mu$ and B Anomalies with Leptoquarks and a Dark Higgs Boson". In: *Phys. Rev. D* 101.3 (2020), p. 035010. DOI: 10.1103/PhysRevD.101.035010. arXiv: 1908.08625 [hep-ph].

[216] R. R. Volkas. "Radiative neutrino mass models and the flavour anomalies". In: *PoS* NuFact2019 (2019), p. 105. DOI: 10.22323/1.369.0105.

[217] D. London. "Anomalies in B Decays: A Sign of New Physics?" In: *11th International Symposium on Quantum Theory and Symmetries*. Nov. 2019. arXiv: 1911.06238 [hep-ph].

[218] Q.-Y. Hu and L.-L. Huang. "Explaining $b \to s\ell^+\ell^-$ data by sneutrinos in the R -parity violating MSSM". In: *Phys. Rev. D* 101.3 (2020), p. 035030. DOI: 10.1103/PhysRevD.101.035030. arXiv: 1912.03676 [hep-ph].

[219] E. Gabrielli and M. Palmiotto. "Magnetic-dipole corrections to R_K and R_{K*} in the Standard Model and dark photon scenarios". In: *JHEP* 10 (2020), p. 145. DOI: 10.1007/JHEP10(2020)145. arXiv: 1910.14385 [hep-ph].

[220] S. Balaji and M. A. Schmidt. "Unified SU(4) theory for the $R_{D^{(*)}}$ and $R_{K^{(*)}}$ anomalies". In: *Phys. Rev. D* 101.1 (2020), p. 015026. DOI: 10.1103/PhysRevD.101.015026. arXiv: 1911.08873 [hep-ph].

[221] A. Vicente. "Theory status and implications of $R_K^{(*)}$". In: *PoS* Beauty2019 (2020), p. 029. DOI: 10.22323/1.377.0029. arXiv: 2001.04788 [hep-ph].

[222] L. Darmé, M. Fedele, K. Kowalska, and E. M. Sessolo. "Flavour anomalies from a split dark sector". In: *JHEP* 08 (2020), p. 148. DOI: 10.1007/JHEP08(2020)148. arXiv: 2002.11150 [hep-ph].

[223] W. Altmannshofer, P. S. B. Dev, A. Soni, and Y. Sui. "Addressing $R_{D^{(*)}}$, $R_{K^{(*)}}$, muon $g-2$ and ANITA anomalies in a minimal R-parity violating supersymmetric framework". In: *Phys. Rev. D* 102.1 (2020), p. 015031. DOI: 10.1103/PhysRevD.102.015031. arXiv: 2002.12910 [hep-ph].

[224] S. Lebbal, N. Mebarki, and J. Mimouni. "Lepton Flavor Universality Violation in a 331 Model in $b \to s l^+ l^-$ Processes". In: Mar. 2020. arXiv: 2003.03230 [hep-ph].

[225] R. Aoude, T. Hurth, S. Renner, and W. Shepherd. "The impact of flavour data on global fits of the MFV SMEFT". In: *JHEP* 12 (2020), p. 113. DOI: 10.1007/JHEP12(2020)113. arXiv: 2003.05432 [hep-ph].

[226] D. Boubaa, S. Khalil, and S. Moretti. "Explaining B decays anomalies in SUSY models". In: *J. Phys. Conf. Ser.* 1766.1 (2021), p. 012018. DOI: 10.1088/1742-6596/1766/1/012018. arXiv: 2004.07939 [hep-ph].

[227] D. Guadagnoli, M. Reboud, and P. Stangl. "The Dark Side of 4321". In: *JHEP* 10 (2020), p. 084. DOI: 10.1007/JHEP10(2020)084. arXiv: 2005.10117 [hep-ph].

[228] S. Baek. "A connection between flavour anomaly, neutrino mass, and axion". In: *JHEP* 10 (2020), p. 111. DOI: 10.1007/JHEP10(2020)111. arXiv: 2006.02050 [hep-ph].

[229] K. Kowalska, E. M. Sessolo, and Y. Yamamoto. "Flavor anomalies from asymptotically safe gravity". In: *Eur. Phys. J. C* 81.4 (2021), p. 272. DOI: 10.1140/epjc/s10052-021-09072-1. arXiv: 2007.03567 [hep-ph].

[230] D. Huang, A. P. Morais, and R. Santos. "Anomalies in B-meson decays and the muon $g-2$ from dark loops". In: *Phys. Rev. D* 102.7 (2020), p. 075009. DOI: 10.1103/PhysRevD.102.075009. arXiv: 2007.05082 [hep-ph].

[231] K. S. Babu, P. S. B. Dev, S. Jana, and A. Thapa. "Unified framework for B-anomalies, muon $g-2$ and neutrino masses". In: *JHEP* 03 (2021), p. 179. DOI: 10.1007/JHEP03(2021)179. arXiv: 2009.01771 [hep-ph].

[232] B. C. Allanach. "$U(1)_{B_3-L_2}$ explanation of the neutral current $B-$anomalies". In: *Eur. Phys. J. C* 81.1 (2021). [Erratum: Eur.Phys.J.C 81, 321 (2021)], p. 56. DOI: 10.1140/epjc/s10052-021-08855-w. arXiv: 2009.02197 [hep-ph].

[233] J.-P. Lee. "B anomalies with unparticles". In: *Mod. Phys. Lett. A* 36.30 (2021), p. 2150219. DOI: 10.1142/S0217732321502199. arXiv: 2012.11852 [hep-ph].

[234] D. London and J. Matias. "B Flavour Anomalies: 2021 Theoretical Status Report". In: (Oct. 2021). DOI: 10.1146/annurev-nucl-102020-090209. arXiv: 2110.13270 [hep-ph].

[235] H. Georgi and S. L. Glashow. "Unity of All Elementary Particle Forces". In: *Phys. Rev. Lett.* 32 (1974), pp. 438–441. DOI: 10.1103/PhysRevLett.32.438.

[236] J. C. Pati and A. Salam. "Lepton Number as the Fourth Color". In: *Phys. Rev. D* 10 (1974). [Erratum: Phys.Rev.D 11, 703–703 (1975)], pp. 275–289. DOI: 10.1103/PhysRevD.10.275.

[237] H. Georgi. "The State of the Art—Gauge Theories". In: *AIP Conf. Proc.* 23 (1975). Ed. by H. C. C. E. W. Carlson, pp. 575–582. DOI: 10.1063/1.2947450.

[238] S. Dimopoulos and L. Susskind. "Mass Without Scalars". In: *Nucl. Phys. B* 155 (1979). Ed. by A. Zichichi, pp. 237–252. DOI: 10.1016/0550-3213(79)90364-X.

[239] E. Farhi and L. Susskind. "Technicolor". In: *Phys. Rept.* 74 (1981), p. 277. DOI: 10.1016/0370-1573(81)90173-3.

[240] I. Doršner, S. Fajfer, A. Greljo, J. F. Kamenik, and N. Košnik. "Physics of leptoquarks in precision experiments and at particle colliders". In: *Phys. Rept.* 641 (2016), pp. 1–68. DOI: 10.1016/j.physrep.2016.06.001. arXiv: 1603.04993 [hep-ph].

[241] N. Kosnik. "Model independent constraints on leptoquarks from $b \to s\ell^+\ell^-$ processes". In: *Phys. Rev. D* 86 (2012), p. 055004. DOI: 10.1103/PhysRevD.86.055004. arXiv: 1206.2970 [hep-ph].

[242] Y. Sakaki, M. Tanaka, A. Tayduganov, and R. Watanabe. "Testing leptoquark models in $\bar{B} \to D^{(*)}\tau\bar{\nu}$". In: *Phys. Rev. D* 88.9 (2013), p. 094012. DOI: 10.1103/PhysRevD.88.094012. arXiv: 1309.0301 [hep-ph].

[243] K. Cheung, Z.-R. Huang, H.-D. Li, C.-D. Lü, Y.-N. Mao, *et al.* "Revisit to the $b \to c\tau\nu$ transition: In and beyond the SM". In: *Nucl. Phys. B* 965 (2021), p. 115354. DOI: 10.1016/j.nuclphysb.2021.115354. arXiv: 2002.07272 [hep-ph].

[244] D. Buttazzo, A. Greljo, G. Isidori, and D. Marzocca. "B-physics anomalies: a guide to combined explanations". In: *JHEP* 11 (2017), p. 044. DOI: 10.1007/JHEP11(2017)044. arXiv: 1706.07808 [hep-ph].

[245] L. Di Luzio, A. Greljo, and M. Nardecchia. "Gauge leptoquark as the origin of B-physics anomalies". In: *Phys. Rev. D* 96.11 (2017), p. 115011. DOI: 10.1103/PhysRevD.96.115011. arXiv: 1708.08450 [hep-ph].

[246] L. Calibbi, A. Crivellin, and T. Li. "Model of vector leptoquarks in view of the *B*-physics anomalies". In: *Phys. Rev. D* 98.11 (2018), p. 115002. DOI: 10.1103/PhysRevD.98.115002. arXiv: 1709.00692 [hep-ph].

[247] A. Angelescu, D. Bečirević, D. A. Faroughy, and O. Sumensari. "Closing the window on single leptoquark solutions to the *B*-physics anomalies". In: *JHEP* 10 (2018), p. 183. DOI: 10.1007/JHEP10(2018)183. arXiv: 1808.08179 [hep-ph].

[248] C. Cornella, J. Fuentes-Martin, and G. Isidori. "Revisiting the vector leptoquark explanation of the B-physics anomalies". In: *JHEP* 07 (2019), p. 168. DOI: 10.1007/JHEP07(2019)168. arXiv: 1903.11517 [hep-ph].

[249] M. Bordone, O. Catà, and T. Feldmann. "Effective Theory Approach to New Physics with Flavour: General Framework and a Leptoquark Example". In: *JHEP* 01 (2020), p. 067. DOI: 10.1007/JHEP01(2020)067. arXiv: 1910.02641 [hep-ph].

[250] A. Crivellin, D. Müller, and T. Ota. "Simultaneous explanation of $R(D^{(*)})$ and $b \to s\mu^+\mu^-$: the last scalar leptoquarks standing". In: *JHEP* 09 (2017), p. 040. DOI: 10.1007/JHEP09(2017)040. arXiv: 1703.09226 [hep-ph].

[251] C. Hati, J. Kriewald, J. Orloff, and A. M. Teixeira. "A nonunitary interpretation for a single vector leptoquark combined explanation to the *B*-decay anomalies". In: *JHEP* 12 (2019), p. 006. DOI: 10.1007/JHEP12(2019)006. arXiv: 1907.05511 [hep-ph].

[252] I. Bigaran, J. Gargalionis, and R. R. Volkas. "A near-minimal leptoquark model for reconciling flavour anomalies and generating radiative neutrino masses". In: *JHEP* 10 (2019), p. 106. DOI: 10.1007/JHEP10(2019)106. arXiv: 1906.01870 [hep-ph].

[253] A. Crivellin, D. Müller, and F. Saturnino. "Flavor Phenomenology of the Leptoquark Singlet-Triplet Model". In: *JHEP* 06 (2020), p. 020. DOI: 10.1007/JHEP06(2020)020. arXiv: 1912.04224 [hep-ph].

[254] S. Saad. "Combined explanations of $(g-2)_\mu$, $R_{D^{(*)}}$, $R_{K^{(*)}}$ anomalies in a two-loop radiative neutrino mass model". In: *Phys. Rev. D* 102.1 (2020), p. 015019. DOI: 10.1103/PhysRevD.102.015019. arXiv: 2005.04352 [hep-ph].

[255] M. Bordone, O. Catà, T. Feldmann, and R. Mandal. "Constraining flavour patterns of scalar leptoquarks in the effective field theory". In: *JHEP* 03 (2021), p. 122. DOI: 10.1007/JHEP03(2021)122. arXiv: 2010.03297 [hep-ph].

[256] C. Hati, J. Kriewald, J. Orloff, and A. M. Teixeira. "The fate of $\mathbf{V_1}$ vector leptoquarks: the impact of future flavour data". In: *Eur. Phys. J. C* 81.12 (2021), p. 1066. DOI: 10.1140/epjc/s10052-021-09824-z. arXiv: 2012.05883 [hep-ph].

[257] J. Kriewald, C. Hati, J. Orloff, and A. M. Teixeira. "A combined explanation of the B-decay anomalies with a single vector leptoquark". In: *PoS* ICHEP2020 (2021), p. 258. DOI: 10.22323/1.390.0258. arXiv: 2012.06315 [hep-ph].

[258] J. Kriewald, C. Hati, J. Orloff, and A. M. Teixeira. "Leptoquarks facing flavour tests and $b \to s\ell\ell$ after Moriond 2021". In: *55th Rencontres de Moriond on Electroweak Interactions and Unified Theories*. Mar. 2021. arXiv: 2104.00015 [hep-ph].

[259] F. del Aguila, J. de Blas, and M. Perez-Victoria. "Electroweak Limits on General New Vector Bosons". In: *JHEP* 09 (2010), p. 033. DOI: 10.1007/JHEP09(2010)033. arXiv: 1005.3998 [hep-ph].

[260] L. Di Luzio, M. Kirk, and A. Lenz. "Updated B_s-mixing constraints on new physics models for $b \to s\ell^+\ell^-$ anomalies". In: *Phys. Rev. D* 97.9 (2018), p. 095035. DOI: 10.1103/PhysRevD.97.095035. arXiv: 1712.06572 [hep-ph].

[261] C. Bobeth and A. J. Buras. "Leptoquarks meet ε'/ε and rare Kaon processes". In: *JHEP* 02 (2018), p. 101. DOI: 10.1007/JHEP02(2018)101. arXiv: 1712.01295 [hep-ph].

[262] M. Aaboud *et al.* "Search for scalar leptoquarks in pp collisions at $\sqrt{s} = 13$ TeV with the ATLAS experiment". In: *New J. Phys.* 18.9 (2016), p. 093016. DOI: 10.1088/1367-2630/18/9/093016. arXiv: 1605.06035 [hep-ex].

[263] A. M. Sirunyan *et al.* "Constraints on models of scalar and vector leptoquarks decaying to a quark and a neutrino at $\sqrt{s} = 13$ TeV". In: *Phys. Rev. D* 98.3 (2018), p. 032005. DOI: 10.1103/PhysRevD.98.032005. arXiv: 1805.10228 [hep-ex].

[264] J. de Blas, J. M. Lizana, and M. Perez-Victoria. "Combining searches of Z' and W' bosons". In: *JHEP* 01 (2013), p. 166. DOI: 10.1007/JHEP01(2013)166. arXiv: 1211.2229 [hep-ph].

[265] D. Pappadopulo, A. Thamm, R. Torre, and A. Wulzer. "Heavy Vector Triplets: Bridging Theory and Data". In: *JHEP* 09 (2014), p. 060. DOI: 10.1007/JHEP09(2014)060. arXiv: 1402.4431 [hep-ph].

[266] B. Capdevila, A. Crivellin, C. A. Manzari, and M. Montull. "Explaining $b \to s\ell^+\ell^-$ and the Cabibbo angle anomaly with a vector triplet". In: *Phys. Rev. D* 103.1 (2021), p. 015032. DOI: 10.1103/PhysRevD.103.015032. arXiv: 2005.13542 [hep-ph].

[267] X.-G. He and G. Valencia. "B decays with τ leptons in nonuniversal left-right models". In: *Phys. Rev. D* 87.1 (2013), p. 014014. DOI: 10.1103/PhysRevD.87.014014. arXiv: 1211.0348 [hep-ph].

[268] J. D. Gómez, N. Quintero, and E. Rojas. "Charged current $b \to c\tau\bar{\nu}_\tau$ anomalies in a general W' boson scenario". In: *Phys. Rev. D* 100.9 (2019), p. 093003. DOI: 10.1103/PhysRevD.100.093003. arXiv: 1907.08357 [hep-ph].

[269] A. Hayreter, X.-G. He, and G. Valencia. "LHC constraints on W', Z' that couple mainly to third generation fermions". In: *Eur. Phys. J. C* 80.10 (2020), p. 912. DOI: 10.1140/epjc/s10052-020-08499-2. arXiv: 1912.06344 [hep-ph].

[270] W. Altmannshofer and D. M. Straub. "New Physics in $B \to K^*\mu\mu$?" In: *Eur. Phys. J. C* 73 (2013), p. 2646. DOI: 10.1140/epjc/s10052-013-2646-9. arXiv: 1308.1501 [hep-ph].

[271] A. J. Buras and J. Girrbach. "Left-handed Z' and Z FCNC quark couplings facing new $b \to s\mu^+\mu^-$ data". In: *JHEP* 12 (2013), p. 009. DOI: 10.1007/JHEP12(2013)009. arXiv: 1309.2466 [hep-ph].

[272] A. Crivellin, L. Hofer, J. Matias, U. Nierste, S. Pokorski, *et al.* "Lepton-flavour violating B decays in generic Z' models". In: *Phys. Rev. D* 92.5 (2015), p. 054013. DOI: 10.1103/PhysRevD.92.054013. arXiv: 1504.07928 [hep-ph].

[273] M. Heiles, M. König, and M. Neubert. "Effective Field Theory for Heavy Vector Resonances Coupled to the Standard Model". In: *Journal of High Energy Physics* 2021.2, 204 (Feb. 2021), p. 204. DOI: 10.1007/JHEP02(2021)204. arXiv: 2011.08205 [hep-ph].

[274] M. Aaboud *et al.* "Combination of searches for heavy resonances decaying into bosonic and leptonic final states using 36 fb^{-1} of proton-proton collision data at $\sqrt{s} = 13$ TeV with the ATLAS detector". In: *Phys. Rev. D* 98.5 (2018), p. 052008. DOI: 10.1103/PhysRevD.98.052008. arXiv: 1808.02380 [hep-ex].

[275] A. M. Sirunyan *et al.* "Combination of CMS searches for heavy resonances decaying to pairs of bosons or leptons". In: *Phys. Lett. B* 798 (2019), p. 134952. DOI: 10.1016/j.physletb.2019.134952. arXiv: 1906.00057 [hep-ex].

[276] J. E. Kim and G. Carosi. "Axions and the Strong CP Problem". In: *Rev. Mod. Phys.* 82 (2010). [Erratum: Rev.Mod.Phys. 91, 049902 (2019)], pp. 557–602. DOI: 10.1103/RevModPhys.82.557. arXiv: 0807.3125 [hep-ph].

[277] J. E. Kim. "A Review on axions and the strong CP problem". In: *AIP Conf. Proc.* 1200.1 (2010). Ed. by G. Alverson, B. Nelson, and P. Nath, pp. 83–92. DOI: 10.1063/1.3327743. arXiv: 0909.3908 [hep-ph].

[278] M. Kawasaki and K. Nakayama. "Axions: Theory and Cosmological Role". In: *Ann. Rev. Nucl. Part. Sci.* 63 (2013), pp. 69–95. DOI: 10.1146/annurev-nucl-102212-170536. arXiv: 1301.1123 [hep-ph].

[279] I. G. Irastorza and J. Redondo. "New experimental approaches in the search for axion-like particles". In: *Prog. Part. Nucl. Phys.* 102 (2018), pp. 89–159. DOI: 10.1016/j.ppnp.2018.05.003. arXiv: 1801.08127 [hep-ph].

[280] I. G. Irastorza. "An introduction to axions and their detection". In: *Les Houches summer school on Dark Matter*. Sept. 2021. arXiv: 2109.07376 [hep-ph].

[281] T. Banks, Y. Nir, and N. Seiberg. "Missing (up) mass, accidental anomalous symmetries, and the strong CP problem". In: *2nd IFT Workshop on Yukawa Couplings and the Origins of Mass*. Feb. 1994, pp. 26–41. arXiv: hep-ph/9403203.

[282] G. M. de Divitiis, R. Frezzotti, V. Lubicz, G. Martinelli, R. Petronzio, *et al.* "Leading isospin breaking effects on the lattice". In: *Phys. Rev. D* 87.11 (2013), p. 114505. DOI: 10.1103/PhysRevD.87.114505. arXiv: 1303.4896 [hep-lat].

[283] S. Basak *et al.* "Electromagnetic effects on the light hadron spectrum". In: *J. Phys. Conf. Ser.* 640.1 (2015). Ed. by A. Sandvik, D. Campbell, D. Coker, and Y. Tang, p. 012052. DOI: 10.1088/1742-6596/640/1/012052. arXiv: 1510.04997 [hep-lat].

[284] R. Horsley *et al.* "Isospin splittings of meson and baryon masses from three-flavor lattice QCD + QED". In: *J. Phys. G* 43.10 (2016), 10LT02. DOI: 10.1088/0954-3899/43/10/10LT02. arXiv: 1508.06401 [hep-lat].

[285] G. Grilli di Cortona, E. Hardy, J. Pardo Vega, and G. Villadoro. "The QCD axion, precisely". In: *JHEP* 01 (2016), p. 034. DOI: 10.1007/JHEP01(2016)034. arXiv: 1511.02867 [hep-ph].

[286] C. Alexandrou, J. Finkenrath, L. Funcke, K. Jansen, B. Kostrzewa, *et al.* "Ruling Out the Massless Up-Quark Solution to the Strong ***CP*** Problem by Computing the Topological Mass Contribution with Lattice QCD". In: *Phys. Rev. Lett.* 125.23 (2020), p. 232001. DOI: 10.1103/PhysRevLett.125.232001. arXiv: 2002.07802 [hep-lat].

[287] C. Abel *et al.* "Measurement of the permanent electric dipole moment of the neutron". In: *Phys. Rev. Lett.* 124.8 (2020), p. 081803. DOI: 10.1103/PhysRevLett.124.081803. arXiv: 2001.11966 [hep-ex].

[288] R. D. Peccei and H. R. Quinn. "Constraints imposed by CP conservation in the presence of pseudoparticles". In: *Phys. Rev. D* 16 (6 Sept. 1977), pp. 1791–1797. DOI: 10.1103/PhysRevD.16.1791. URL: https://link.aps.org/doi/10.1103/PhysRevD.16.1791.

[289] R. Peccei and H. R. Quinn. "CP Conservation in the Presence of Instantons". In: *Phys. Rev. Lett.* 38 (1977), pp. 1440–1443. DOI: 10.1103/PhysRevLett.38.1440.

[290] S. Weinberg. "A New Light Boson?" In: *Phys. Rev. Lett.* 40 (4 Jan. 1978), pp. 223–226. DOI: 10.1103/PhysRevLett.40.223. URL: https://link.aps.org/doi/10.1103/PhysRevLett.40.223.

[291] F. Wilczek. "Problem of Strong P and T Invariance in the Presence of Instantons". In: *Phys. Rev. Lett.* 40 (5 Jan. 1978), pp. 279–282. DOI: 10.1103/PhysRevLett.40.279. URL: https://link.aps.org/doi/10.1103/PhysRevLett.40.279.

[292] C. Vafa and E. Witten. "Parity Conservation in QCD". In: *Phys. Rev. Lett.* 53 (1984), p. 535. DOI: 10.1103/PhysRevLett.53.535.

[293] M. Spalinski. "CHIRAL CORRECTIONS TO THE AXION MASS". In: *Z. Phys. C* 41 (1988), pp. 87–90. DOI: 10.1007/BF01412582.

[294] Y.-Y. Mao and T.-W. Chiu. "Topological Susceptibility to the One-Loop Order in Chiral Perturbation Theory". In: *Phys. Rev. D* 80 (2009), p. 034502. DOI: 10.1103/PhysRevD.80.034502. arXiv: 0903.2146 [hep-lat].

[295] E. Masso. "Axions and their relatives". In: *Lect. Notes Phys.* 741 (2008). Ed. by M. Kuster, G. Raffelt, and B. Beltran, pp. 83–94. DOI: 10.1007/978-3-540-73518-2_5. arXiv: hep-ph/0607215.

[296] A. Arvanitaki, S. Dimopoulos, S. Dubovsky, N. Kaloper, and J. March-Russell. "String Axiverse". In: *Phys. Rev. D* 81 (2010), p. 123530. DOI: 10.1103/PhysRevD.81.123530. arXiv: 0905.4720 [hep-th].

[297] A. Ringwald. "Searching for axions and ALPs from string theory". In: *J. Phys. Conf. Ser.* 485 (2014). Ed. by M. Mondragón, A. Bashir, D. Delepine, F. Larios, O. Loaiza, *et al.*, p. 012013. DOI: 10.1088/1742-6596/485/1/012013. arXiv: 1209.2299 [hep-ph].

[298] H. Georgi, D. B. Kaplan, and L. Randall. "Manifesting the Invisible Axion at Low-energies". In: *Phys. Lett. B* 169 (1986), pp. 73–78. DOI: 10.1016/0370-2693(86)90688-X.

[299] J. Bonilla, I. Brivio, M. B. Gavela, and V. Sanz. "One-loop corrections to ALP couplings". In: *JHEP* 11 (2021), p. 168. DOI: 10.1007/JHEP11(2021)168. arXiv: 2107.11392 [hep-ph].

[300] M. Bauer, M. Neubert, S. Renner, M. Schnubel, and A. Thamm. "The Low-Energy Effective Theory of Axions and ALPs". In: *JHEP* 04 (2021), p. 063. DOI: 10.1007/JHEP04(2021)063. arXiv: 2012.12272 [hep-ph].

[301] A. M. Galda, M. Neubert, and S. Renner. "ALP — SMEFT interference". In: *JHEP* 06 (2021), p. 135. DOI: 10.1007/JHEP06(2021)135. arXiv: 2105.01078 [hep-ph].

[302] Y. Aditya, K. J. Healey, and A. A. Petrov. "Searching for super-WIMPs in leptonic heavy meson decays". In: *Phys. Lett. B* 710 (2012), pp. 118–124. DOI: 10.1016/j.physletb.2012.02.042. arXiv: 1201.1007 [hep-ph].

[303] R. S. Chivukula and H. Georgi. "Composite Technicolor Standard Model". In: *Phys. Lett. B* 188 (1987), pp. 99–104. DOI: 10.1016/0370-2693(87)90713-1.

[304] G. D'Ambrosio, G. F. Giudice, G. Isidori, and A. Strumia. "Minimal flavor violation: An Effective field theory approach". In: *Nucl. Phys. B* 645 (2002), pp. 155–187. DOI: 10.1016/S0550-3213(02)00836-2. arXiv: hep-ph/0207036.

[305] A. J. Buras. "Minimal flavor violation". In: *Acta Phys. Polon. B* 34 (2003). Ed. by M. Praszalowicz, pp. 5615–5668. arXiv: hep-ph/0310208.

[306] C. Smith. "Minimal Flavor Violation". PhD thesis. LPSC, Grenoble, Sept. 2016.

[307] T. Hurth, G. Isidori, J. F. Kamenik, and F. Mescia. "Constraints on New Physics in MFV models: A Model-independent analysis of $\Delta F = 1$ processes". In: *Nucl. Phys. B* 808 (2009), pp. 326–346. DOI: 10.1016/j.nuclphysb.2008.09.040. arXiv: 0807.5039 [hep-ph].

[308] G. Isidori and S. Trifinopoulos. "Exploring the flavour structure of the high-scale MSSM". In: *Eur. Phys. J. C* 80.3 (2020), p. 291. DOI: 10.1140/epjc/s10052-020-7821-1. arXiv: 1912.09940 [hep-ph].

[309] A. Buras. "Flavour Expedition to the Zeptouniverse". In: *PoS* FWNP (2015), p. 003. DOI: 10.22323/1.220.0003. arXiv: 1505.00618 [hep-ph].

[310] R. Barbieri, G. Isidori, J. Jones-Perez, P. Lodone, and D. M. Straub. "$U(2)$ and Minimal Flavour Violation in Supersymmetry". In: *Eur. Phys. J. C* 71 (2011), p. 1725. DOI: 10.1140/epjc/s10052-011-1725-z. arXiv: 1105.2296 [hep-ph].

[311] F. Arias-Aragón, C. Bouthelier-Madre, J. M. Cano, and L. Merlo. "Data Driven Flavour Model". In: *Eur. Phys. J. C* 80.9 (2020), p. 854. DOI: 10.1140/epjc/s10052-020-8398-4. arXiv: 2003.05941 [hep-ph].

[312] M. Bordone, G. Isidori, and A. Pattori. "On the Standard Model predictions for R_K and R_{K^*}". In: *Eur. Phys. J. C* 76.8 (2016), p. 440. DOI: 10.1140/epjc/s10052-016-4274-7. arXiv: 1605.07633 [hep-ph].

[313] W. Altmannshofer, C. Niehoff, P. Stangl, and D. M. Straub. "Status of the $B \to K^* \mu^+ \mu^-$ anomaly after Moriond 2017". In: *Eur. Phys. J. C* 77.6 (2017), p. 377. DOI: 10.1140/epjc/s10052-017-4952-0. arXiv: 1703.09189 [hep-ph].

[314] A. Bazavov *et al.* "$B^0_{(s)}$-mixing matrix elements from lattice QCD for the Standard Model and beyond". In: *Phys. Rev. D* 93.11 (2016), p. 113016. DOI: 10.1103/PhysRevD.93.113016. arXiv: 1602.03560 [hep-lat].

[315] T. Jubb, M. Kirk, A. Lenz, and G. Tetlalmatzi-Xolocotzi. "On the ultimate precision of meson mixing observables". In: *Nucl. Phys. B* 915 (2017), pp. 431–453. DOI: 10.1016/j.nuclphysb.2016.12.020. arXiv: 1603.07770 [hep-ph].

[316] A. J. Buras and F. De Fazio. "331 Models Facing the Tensions in $\Delta F = 2$ Processes with the Impact on ε'/ε, $B_s \to \mu^+\mu^-$ and $B \to K^*\mu^+\mu^-$". In: *JHEP* 08 (2016), p. 115. DOI: 10.1007/JHEP08(2016)115. arXiv: 1604.02344 [hep-ph].

[317] M. Kirk, A. Lenz, and T. Rauh. "Dimension-six matrix elements for meson mixing and lifetimes from sum rules". In: *JHEP* 12 (2017). [Erratum: JHEP 06, 162 (2020)], p. 068. DOI: 10.1007/JHEP12(2017)068. arXiv: 1711.02100 [hep-ph].

[318] Y. Amhis *et al.* "Averages of b-hadron, c-hadron, and τ-lepton properties as of summer 2016". In: *Eur. Phys. J. C* 77.12 (2017), p. 895. DOI: 10.1140/epjc/s10052-017-5058-4. arXiv: 1612.07233 [hep-ex].

[319] A. K. Alok, B. Bhattacharya, D. Kumar, J. Kumar, D. London, *et al.* "New physics in $b \to s\mu^+\mu^-$: Distinguishing models through CP-violating effects". In: *Phys. Rev. D* 96.1 (2017), p. 015034. DOI: 10.1103/PhysRevD.96.015034. arXiv: 1703.09247 [hep-ph].

[320] A. Lenz and U. Nierste. "Theoretical update of $B_s - \bar{B}_s$ mixing". In: *JHEP* 06 (2007), p. 072. DOI: 10.1088/1126-6708/2007/06/072. arXiv: hep-ph/0612167.

[321] T. Hurth, F. Mahmoudi, and S. Neshatpour. "On the anomalies in the latest LHCb data". In: *Nucl. Phys. B* 909 (2016), pp. 737–777. DOI: 10.1016/j.nuclphysb.2016.05.022. arXiv: 1603.00865 [hep-ph].

[322] B. Capdevila, S. Descotes-Genon, L. Hofer, and J. Matias. "Hadronic uncertainties in $B \to K^*\mu^+\mu^-$: a state-of-the-art analysis". In: *JHEP* 04 (2017), p. 016. DOI: 10.1007/JHEP04(2017)016. arXiv: 1701.08672 [hep-ph].

[323] B. Capdevila, A. Crivellin, S. Descotes-Genon, J. Matias, and J. Virto. "Patterns of New Physics in $b \to s\ell^+\ell^-$ transitions in the light of recent data". In: *JHEP* 01 (2018), p. 093. DOI: 10.1007/JHEP01(2018)093. arXiv: 1704.05340 [hep-ph].

[324] W. Altmannshofer, P. Stangl, and D. M. Straub. "Interpreting Hints for Lepton Flavor Universality Violation". In: *Phys. Rev. D* 96.5 (2017), p. 055008. DOI: 10.1103/PhysRevD.96.055008. arXiv: 1704.05435 [hep-ph].

[325] G. D'Amico, M. Nardecchia, P. Panci, F. Sannino, A. Strumia, *et al.* "Flavour anomalies after the R_{K^*} measurement". In: *JHEP* 09 (2017), p. 010. DOI: 10.1007/JHEP09(2017)010. arXiv: 1704.05438 [hep-ph].

[326] G. Hiller and I. Nisandzic. "R_K and R_{K^*} beyond the standard model". In: *Phys. Rev. D* 96.3 (2017), p. 035003. DOI: 10.1103/PhysRevD.96.035003. arXiv: 1704.05444 [hep-ph].

[327] L.-S. Geng, B. Grinstein, S. Jäger, J. Martin Camalich, X.-L. Ren, *et al.* "Towards the discovery of new physics with lepton-universality ratios of $b \to s\ell\ell$ decays". In: *Phys. Rev. D* 96.9 (2017), p. 093006. DOI: 10.1103/PhysRevD.96.093006. arXiv: 1704.05446 [hep-ph].

[328] M. Ciuchini, A. M. Coutinho, M. Fedele, E. Franco, A. Paul, *et al.* "On Flavourful Easter eggs for New Physics hunger and Lepton Flavour Universality violation". In: *Eur. Phys. J. C* 77.10 (2017), p. 688. DOI: 10.1140/epjc/s10052-017-5270-2. arXiv: 1704.05447 [hep-ph].

[329] C. Patrignani *et al.* "Review of Particle Physics". In: *Chin. Phys. C* 40.10 (2016), p. 100001. DOI: 10.1088/1674-1137/40/10/100001.

[330] G. Hiller and M. Schmaltz. "Diagnosing lepton-nonuniversality in $b \to s\ell\ell$". In: *JHEP* 02 (2015), p. 055. DOI: 10.1007/JHEP02(2015)055. arXiv: 1411.4773 [hep-ph].

[331] "Angular analysis of $B_d^0 \to K^*\mu^+\mu^-$ decays in pp collisions at $\sqrt{s} = 8$ TeV with the ATLAS detector". In: (Apr. 2017). Ed. by E. Auge, J. Dumarchez, and J. Tran Thanh Van.

[332] A. M. Sirunyan *et al.* "Measurement of angular parameters from the decay $B^0 \to K^{*0}\mu^+\mu^-$ in proton-proton collisions at $\sqrt{s} = 8$ TeV". In: *Phys. Lett. B* 781 (2018), pp. 517–541. DOI: 10.1016/j.physletb.2018.04.030. arXiv: 1710.02846 [hep-ex].

[333] S. Aoki *et al.* "FLAG Review 2019: Flavour Lattice Averaging Group (FLAG)". In: *Eur. Phys. J. C* 80.2 (2020), p. 113. DOI: 10.1140/epjc/s10052-019-7354-7. arXiv: 1902.08191 [hep-lat].

[334] D. King, A. Lenz, and T. Rauh. "B_s mixing observables and $|V_{td}/V_{ts}|$ from sum rules". In: *JHEP* 05 (2019), p. 034. DOI: 10.1007/JHEP05(2019)034. arXiv: 1904.00940 [hep-ph].

[335] R. J. Dowdall, C. T. H. Davies, R. R. Horgan, G. P. Lepage, C. J. Monahan, *et al.* "Neutral B-meson mixing from full lattice QCD at the physical point". In: *Phys. Rev. D* 100.9 (2019), p. 094508. DOI: 10.1103/PhysRevD.100.094508. arXiv: 1907.01025 [hep-lat].

[336] P. A. Boyle, L. Del Debbio, N. Garron, A. Juttner, A. Soni, *et al.* "SU(3)-breaking ratios for $D_{(s)}$ and $B_{(s)}$ mesons". In: (Dec. 2018). arXiv: 1812.08791 [hep-lat].

[337] L. Di Luzio, M. Kirk, A. Lenz, and T. Rauh. "ΔM_s theory precision confronts flavour anomalies". In: *JHEP* 12 (2019), p. 009. DOI: 10.1007/JHEP12(2019)009. arXiv: 1909.11087 [hep-ph].

[338] R. Barbieri, D. Buttazzo, F. Sala, and D. M. Straub. "Flavour physics from an approximate $U(2)^3$ symmetry". In: *JHEP* 07 (2012), p. 181. DOI: 10.1007/JHEP07(2012)181. arXiv: 1203.4218 [hep-ph].

[339] D. Barducci *et al.* "Interpreting top-quark LHC measurements in the standard-model effective field theory". In: (Feb. 2018). Ed. by J. A. Aguilar-Saavedra, C. Degrande, G. Durieux, F. Maltoni, E. Vryonidou, *et al.* arXiv: 1802.07237 [hep-ph].

[340] R. Coy, M. Frigerio, F. Mescia, and O. Sumensari. "New physics in $b \to s\ell\ell$ transitions at one loop". In: *Eur. Phys. J. C* 80.1 (2020), p. 52. DOI: 10.1140/epjc/s10052-019-7581-y. arXiv: 1909.08567 [hep-ph].

[341] J. Aebischer, J. Kumar, and D. M. Straub. "Wilson: a Python package for the running and matching of Wilson coefficients above and below the electroweak scale". In: *Eur. Phys. J. C* 78.12 (2018), p. 1026. DOI: 10.1140/epjc/s10052-018-6492-7. arXiv: 1804.05033 [hep-ph].

[342] J. Aebischer, J. Kumar, P. Stangl, and D. M. Straub. "A Global Likelihood for Precision Constraints and Flavour Anomalies". In: *Eur. Phys. J. C* 79.6 (2019), p. 509. DOI: 10.1140/epjc/s10052-019-6977-z. arXiv: 1810.07698 [hep-ph].

[343] A. Celis, J. Fuentes-Martin, A. Vicente, and J. Virto. "Gauge-invariant implications of the LHCb measurements on lepton-flavor nonuniversality". In: *Phys. Rev. D* 96.3 (2017), p. 035026. DOI: 10.1103/PhysRevD.96.035026. arXiv: 1704.05672 [hep-ph].

[344] J. E. Camargo-Molina, A. Celis, and D. A. Faroughy. "Anomalies in Bottom from new physics in Top". In: *Phys. Lett. B* 784 (2018), pp. 284–293. DOI: 10.1016/j.physletb.2018.07.051. arXiv: 1805.04917 [hep-ph].

[345] J. Aebischer, W. Altmannshofer, D. Guadagnoli, M. Reboud, P. Stangl, *et al.* "B-decay discrepancies after Moriond 2019". In: *Eur. Phys. J. C* 80.3 (2020), p. 252. DOI: 10.1140/epjc/s10052-020-7817-x. arXiv: 1903.10434 [hep-ph].

[346] K. A. Olive *et al.* "Review of Particle Physics". In: *Chin. Phys. C* 38 (2014), p. 090001. DOI: 10.1088/1674-1137/38/9/090001.

[347] S. Aoki *et al.* "Review of lattice results concerning low-energy particle physics". In: *Eur. Phys. J. C* 77.2 (2017), p. 112. DOI: 10.1140/epjc/s10052-016-4509-7. arXiv: 1607.00299 [hep-lat].

[348] A. Bazavov *et al.* "Up-, down-, strange-, charm-, and bottom-quark masses from four-flavor lattice QCD". In: *Phys. Rev. D* 98.5 (2018), p. 054517. DOI: 10.1103/PhysRevD.98.054517. arXiv: 1802.04248 [hep-lat].

[349] S. Descotes-Genon, L. Hofer, J. Matias, and J. Virto. "Global analysis of $b \to s\ell\ell$ anomalies". In: *JHEP* 06 (2016), p. 092. DOI: 10.1007/JHEP06(2016)092. arXiv: 1510.04239 [hep-ph].

[350] B. Capdevila, U. Laa, and G. Valencia. "Anatomy of a six-parameter fit to the $b \to s\ell^+\ell^-$ anomalies". In: *Eur. Phys. J. C* 79.6 (2019), p. 462. DOI: 10.1140/epjc/s10052-019-6944-8. arXiv: 1811.10793 [hep-ph].

[351] B. Capdevila, A. Crivellin, S. Descotes-Genon, L. Hofer, and J. Matias. "Searching for New Physics with $b \to s\tau^+\tau^-$ processes". In: *Phys. Rev. Lett.* 120.18 (2018), p. 181802. DOI: 10.1103/PhysRevLett.120.181802. arXiv: 1712.01919 [hep-ph].

[352] F. Feruglio. "B-anomalies related to leptons and lepton flavour violation: new directions in model building". In: *PoS* BEAUTY2018 (2018). Ed. by R. Fleischer, N. Harnew, G. Wilkinson, F. Palla, and G. Punzi, p. 029. DOI: 10.22323/1.326.0029. arXiv: 1808.01502 [hep-ph].

[353] D. A. Faroughy, A. Greljo, and J. F. Kamenik. "Confronting lepton flavor universality violation in B decays with high-p_T tau lepton searches at LHC". In: *Phys. Lett. B* 764 (2017), pp. 126–134. DOI: 10.1016/j.physletb.2016.11.011. arXiv: 1609.07138 [hep-ph].

[354] A. Greljo, J. Martin Camalich, and J. D. Ruiz-Álvarez. "Mono-τ Signatures at the LHC Constrain Explanations of B-decay Anomalies". In: *Phys. Rev. Lett.* 122.13 (2019), p. 131803. DOI: 10.1103/PhysRevLett.122.131803. arXiv: 1811.07920 [hep-ph].

[355] A. Falkowski, M. González-Alonso, and O. Naviliat-Cuncic. "Comprehensive analysis of beta decays within and beyond the Standard Model". In: *JHEP* 04 (2021), p. 126. DOI: 10.1007/JHEP04(2021)126. arXiv: 2010.13797 [hep-ph].

[356] J. C. Hardy and I. S. Towner. "Superallowed $0^+ \to 0^+$ nuclear β decays: 2020 critical survey, with implications for V_{ud} and CKM unitarity". In: *Phys. Rev. C* 102.4 (2020), p. 045501. DOI: 10.1103/PhysRevC.102.045501.

[357] F. Feruglio, P. Paradisi, and A. Pattori. "Revisiting Lepton Flavor Universality in B Decays". In: *Phys. Rev. Lett.* 118.1 (2017), p. 011801. DOI: 10.1103/PhysRevLett.118.011801. arXiv: 1606.00524 [hep-ph].

[358] H. Aihara *et al.* "The International Linear Collider. A Global Project". In: (Jan. 2019). arXiv: 1901.09829 [hep-ex].

[359] A. Robson, P. N. Burrows, N. Catalan Lasheras, L. Linssen, M. Petric, *et al.* "The Compact Linear e^+e^- Collider (CLIC): Accelerator and Detector". In: (Dec. 2018). arXiv: 1812.07987 [physics.acc-ph].

[360] F. Bordry, M. Benedikt, O. Brüning, J. Jowett, L. Rossi, *et al.* "Machine Parameters and Projected Luminosity Performance of Proposed Future Colliders at CERN". In: (Oct. 2018). arXiv: 1810.13022 [physics.acc-ph].

[361] A. Irles, R. Pöschl, F. Richard, and H. Yamamoto. "Complementarity between ILC250 and ILC-GigaZ". In: *Linear Collider Community Meeting*. May 2019. arXiv: 1905.00220 [hep-ex].

[362] N. Alipour Tehrani *et al.* "FCC-ee: Your Questions Answered". In: *CERN Council Open Symposium on the Update of European Strategy for Particle Physics*. Ed. by A. Blondel and P. Janot. June 2019. arXiv: 1906.02693 [hep-ph].

[363] F. Maltoni, L. Mantani, and K. Mimasu. "Top-quark electroweak interactions at high energy". In: *JHEP* 10 (2019), p. 004. DOI: 10.1007/JHEP10(2019)004. arXiv: 1904.05637 [hep-ph].

[364] R. K. Ellis *et al.* "Physics Briefing Book: Input for the European Strategy for Particle Physics Update 2020". In: (Oct. 2019). arXiv: 1910.11775 [hep-ex].

[365] G. Durieux, M. Perelló, M. Vos, and C. Zhang. "Global and optimal probes for the top-quark effective field theory at future lepton colliders". In: *JHEP* 10 (2018), p. 168. DOI: 10.1007/JHEP10(2018)168. arXiv: 1807.02121 [hep-ph].

[366] J. de Blas *et al.* "The CLIC Potential for New Physics". In: 3/2018 (Dec. 2018). DOI: 10.23731/CYRM-2018-003. arXiv: 1812.02093 [hep-ph].

[367] M. Algueró, B. Capdevila, A. Crivellin, S. Descotes-Genon, P. Masjuan, *et al.* "Emerging patterns of New Physics with and without Lepton Flavour Universal contributions". In: *Eur. Phys. J. C* 79.8 (2019). [Addendum: Eur.Phys.J.C 80, 511 (2020)], p. 714. DOI: 10.1140/epjc/s10052-019-7216-3. arXiv: 1903.09578 [hep-ph].

[368] M. Algueró, B. Capdevila, S. Descotes-Genon, J. Matias, and M. Novoa-Brunet. "$b \to s\ell\ell$ Global Fits after R_{K_S} and $R_{K^{*+}}$". In: Apr. 2021. arXiv: 2104.08921 [hep-ph].

[369] G. Hiller and M. Schmaltz. "R_K and future $b \to s\ell\ell$ physics beyond the standard model opportunities". In: *Phys. Rev. D* 90 (2014), p. 054014. DOI: 10.1103/PhysRevD.90.054014. arXiv: 1408.1627 [hep-ph].

[370] M. Bordone, M. Jung, and D. van Dyk. "Theory determination of $\bar{B} \to D^{(*)}\ell^-\bar{\nu}$ form factors at $\mathcal{O}(1/m_c^2)$". In: *Eur. Phys. J. C* 80.2 (2020), p. 74. DOI: 10.1140/epjc/s10052-020-7616-4. arXiv: 1908.09398 [hep-ph].

[371] M. Aaboud *et al.* "Study of the rare decays of B_s^0 and B^0 mesons into muon pairs using data collected during 2015 and 2016 with the ATLAS detector". In: *JHEP* 04 (2019), p. 098. DOI: 10.1007/JHEP04(2019)098. arXiv: 1812.03017 [hep-ex].

[372] V. Khachatryan *et al.* "Observation of the rare $B_s^0 \to \mu^+\mu^-$ decay from the combined analysis of CMS and LHCb data". In: *Nature* 522 (2015), pp. 68–72. DOI: 10.1038/nature14474. arXiv: 1411.4413 [hep-ex].

[373] A. Datta, J. Kumar, and D. London. "The B anomalies and new physics in $b \to se^+e^-$". In: *Phys. Lett. B* 797 (2019), p. 134858. DOI: 10.1016/j.physletb.2019.134858. arXiv: 1903.10086 [hep-ph].

[374] D. Marzocca and S. Trifinopoulos. "Minimal Explanation of Flavor Anomalies: B-Meson Decays, Muon Magnetic Moment, and the Cabibbo Angle". In: *Phys. Rev. Lett.* 127.6 (2021), p. 061803. DOI: 10.1103/PhysRevLett.127.061803. arXiv: 2104.05730 [hep-ph].

[375] C. Cornella, F. Feruglio, and P. Paradisi. "Low-energy Effects of Lepton Flavour Universality Violation". In: *JHEP* 11 (2018), p. 012. DOI: 10.1007/JHEP11(2018)012. arXiv: 1803.00945 [hep-ph].

[376] A. Celis, J. Fuentes-Martin, A. Vicente, and J. Virto. "DsixTools: The Standard Model Effective Field Theory Toolkit". In: *Eur. Phys. J. C* 77.6 (2017), p. 405. DOI: 10.1140/epjc/s10052-017-4967-6. arXiv: 1704.04504 [hep-ph].

[377] C. Cornella, D. A. Faroughy, J. Fuentes-Martin, G. Isidori, and M. Neubert. "Reading the footprints of the B-meson flavor anomalies". In: *JHEP* 08 (2021), p. 050. DOI: 10.1007/JHEP08(2021)050. arXiv: 2103.16558 [hep-ph].

[378] A. K. Alok, A. Dighe, S. Gangal, and D. Kumar. "Continuing search for new physics in $b \to s\mu\mu$ decays: two operators at a time". In: *JHEP* 06 (2019), p. 089. DOI: 10.1007/JHEP06(2019)089. arXiv: 1903.09617 [hep-ph].

[379] D. Kumar, K. Kowalska, and E. M. Sessolo. "Global Bayesian Analysis of new physics in $b \to s\mu\mu$ transitions after Moriond-2019". In: *17th Conference on Flavor Physics and CP Violation*. June 2019. arXiv: 1906.08596 [hep-ph].

[380] B. Capdevila, U. Laa, and G. Valencia. "Fitting in or odd one out? Pulls vs residual responses in $b \to s\ell^+\ell^-$". In: (Aug. 2019). arXiv: 1908.03338 [hep-ph].

[381] S. Bhattacharya, A. Biswas, S. Nandi, and S. K. Patra. "Exhaustive model selection in $b \to s\ell\ell$ decays: Pitting cross-validation against the Akaike information criterion". In: *Phys. Rev. D* 101.5 (2020), p. 055025. DOI: 10.1103/PhysRevD.101.055025. arXiv: 1908.04835 [hep-ph].

[382] A. Biswas, S. Nandi, S. K. Patra, and I. Ray. "New physics in b $\to$ s$\ell\ell$ decays with complex Wilson coefficients". In: *Nucl. Phys. B* 969 (2021), p. 115479. DOI: 10.1016/j.nuclphysb.2021.115479. arXiv: 2004.14687 [hep-ph].

[383] J. Bhom, M. Chrzaszcz, F. Mahmoudi, M. T. Prim, P. Scott, *et al.* "A model-independent analysis of $b \to s\mu^+\mu^-$ transitions with GAMBIT 's FlavBit". In: *Eur. Phys. J. C* 81.12 (2021), p. 1076. DOI: 10.1140/epjc/s10052-021-09840-z. arXiv: 2006.03489 [hep-ph].

[384] S. Bhattacharya, S. Nandi, S. K. Patra, and S. Sahoo. "'Deep' Dive into $b \to c$ Anomalies: Standardized and Future-proof Model Selection Using Self-normalizing Neural Networks". In: (Aug. 2020). arXiv: 2008.04316 [hep-ph].

[385] T. Chen and C. Guestrin. "XGBoost: A Scalable Tree Boosting System". In: *arXiv e-prints*, arXiv:1603.02754 (Mar. 2016), arXiv:1603.02754. arXiv: 1603.02754 [cs.LG].

[386] S. Lundberg and S.-I. Lee. "A Unified Approach to Interpreting Model Predictions". In: *arXiv e-prints* (May 2017). arXiv: 1705.07874 [cs.AI].

[387] S. M. Lundberg, G. G. Erion, and S.-I. Lee. "Consistent Individualized Feature Attribution for Tree Ensembles". In: *arXiv e-prints* (Feb. 2018). arXiv: 1802.03888 [cs.LG].

[388] L. S. Shapley. "17. A Value for n-Person Games". In: *Contributions to the Theory of Games (AM-28), Volume II*. Ed. by H. W. Kuhn and A. W. Tucker. Princeton University Press, 2016, pp. 307–318. DOI: doi:10.1515/9781400881970-018.

[389] J. Grygier *et al.* "Search for $B \to h\nu\bar{\nu}$ decays with semileptonic tagging at Belle". In: *Phys. Rev. D* 96.9 (2017). [Addendum: Phys.Rev.D 97, 099902 (2018)], p. 091101. DOI: 10.1103/PhysRevD.96.091101. arXiv: 1702.03224 [hep-ex].

[390] F. Dattola. "Search for $B^+ \to K^+\nu\bar{\nu}$ decays with an inclusive tagging method at the Belle II experiment". In: *55th Rencontres de Moriond on Electroweak Interactions and Unified Theories*. May 2021. arXiv: 2105.05754 [hep-ex].

[391] T. E. Browder, N. G. Deshpande, R. Mandal, and R. Sinha. "Impact of B→K$\nu\nu^-$ measurements on beyond the Standard Model theories". In: *Phys. Rev. D* 104.5 (2021), p. 053007. DOI: 10.1103/PhysRevD.104.053007. arXiv: 2107.01080 [hep-ph].

[392] "Constraints on models of scalar and vector leptoquarks decaying to a quark and a neutrino at $\sqrt{s} = 13$ TeV". In: (2018).

[393] A. Bhaskar, D. Das, T. Mandal, S. Mitra, and C. Neeraj. "Precise limits on the charge-2/3 U1 vector leptoquark". In: *Phys. Rev. D* 104.3 (2021), p. 035016. DOI: 10.1103/PhysRevD.104.035016. arXiv: 2101.12069 [hep-ph].

[394] K. Mimasu and V. Sanz. "ALPs at Colliders". In: *JHEP* 06 (2015), p. 173. DOI: 10.1007/JHEP06(2015)173. arXiv: 1409.4792 [hep-ph].

[395] J. Jaeckel and M. Spannowsky. "Probing MeV to 90 GeV axion-like particles with LEP and LHC". In: *Phys. Lett. B* 753 (2016), pp. 482–487. DOI: 10.1016/j.physletb.2015.12.037. arXiv: 1509.00476 [hep-ph].

[396] M. Bauer, M. Neubert, and A. Thamm. "Collider Probes of Axion-Like Particles". In: *JHEP* 12 (2017), p. 044. DOI: 10.1007/JHEP12(2017)044. arXiv: 1708.00443 [hep-ph].

[397] I. Brivio, M. Gavela, L. Merlo, K. Mimasu, J. No, *et al.* "ALPs Effective Field Theory and Collider Signatures". In: *Eur. Phys. J. C* 77.8 (2017), p. 572. DOI: 10.1140/epjc/s10052-017-5111-3. arXiv: 1701.05379 [hep-ph].

[398] G. Alonso-Álvarez, M. Gavela, and P. Quilez. "Axion couplings to electroweak gauge bosons". In: *Eur. Phys. J. C* 79.3 (2019), p. 223. DOI: 10.1140/epjc/s10052-019-6732-5. arXiv: 1811.05466 [hep-ph].

[399] C. Baldenegro, S. Fichet, G. von Gersdorff, and C. Royon. "Searching for axion-like particles with proton tagging at the LHC". In: *JHEP* 06 (2018), p. 131. DOI: 10.1007/JHEP06(2018)131. arXiv: 1803.10835 [hep-ph].

[400] L. Harland-Lang, J. Jaeckel, and M. Spannowsky. "A fresh look at ALP searches in fixed target experiments". In: *Phys. Lett. B* 793 (2019), pp. 281–289. DOI: 10.1016/j.physletb.2019.04.045. arXiv: 1902.04878 [hep-ph].

[401] J. Martin Camalich, M. Pospelov, P. N. H. Vuong, R. Ziegler, and J. Zupan. "Quark Flavor Phenomenology of the QCD Axion". In: *Phys. Rev. D* 102.1 (2020), p. 015023. DOI: 10.1103/PhysRevD.102.015023. arXiv: 2002.04623 [hep-ph].

[402] L. Di Luzio, R. Gröber, and P. Paradisi. "Hunting for CP-violating axionlike particle interactions". In: *Phys. Rev. D* 104.9 (2021), p. 095027. DOI: 10.1103/PhysRevD.104.095027. arXiv: 2010.13760 [hep-ph].

[403] A. W. M. Guerrera and S. Rigolin. "Revisiting $K \to \pi a$ decays". In: (June 2021). arXiv: 2106.05910 [hep-ph].

[404] D. Cadamuro and J. Redondo. "Cosmological bounds on pseudo Nambu-Goldstone bosons". In: *JCAP* 02 (2012), p. 032. DOI: 10.1088/1475-7516/2012/02/032. arXiv: 1110.2895 [hep-ph].

[405] M. Millea, L. Knox, and B. Fields. "New Bounds for Axions and Axion-Like Particles with keV-GeV Masses". In: *Phys. Rev. D* 92.2 (2015), p. 023010. DOI: 10.1103/PhysRevD.92.023010. arXiv: 1501.04097 [astro-ph.CO].

[406] L. Di Luzio, F. Mescia, and E. Nardi. "Redefining the Axion Window". In: *Phys. Rev. Lett.* 118.3 (2017), p. 031801. DOI: 10.1103/PhysRevLett.118.031801. arXiv: 1610.07593 [hep-ph].

[407] P. Agrawal *et al.* "Feebly-interacting particles: FIPs 2020 workshop report". In: *Eur. Phys. J. C* 81.11 (2021), p. 1015. DOI: 10.1140/epjc/s10052-021-09703-7. arXiv: 2102.12143 [hep-ph].

[408] G. Lucente and P. Carenza. "Supernova bound on axionlike particles coupled with electrons". In: *Phys. Rev. D* 104.10 (2021), p. 103007. DOI: 10.1103/PhysRevD.104.103007. arXiv: 2107.12393 [hep-ph].

[409] R. Essig *et al.* "Working Group Report: New Light Weakly Coupled Particles". In: *Community Summer Study 2013: Snowmass on the Mississippi*. Oct. 2013. arXiv: 1311.0029 [hep-ph].

[410] A. V. Artamonov *et al.* "Study of the decay $K^+ \to \pi^+ \nu\bar{\nu}$ in the momentum region $140 < P_\pi < 199$ MeV/c". In: *Phys. Rev. D* 79 (2009), p. 092004. DOI: 10.1103/PhysRevD.79.092004. arXiv: 0903.0030 [hep-ex].

[411] A. Artamonov *et al.* "New measurement of the $K^+ \to \pi^+ \nu\bar{\nu}$ branching ratio". In: *Phys. Rev. Lett.* 101 (2008), p. 191802. DOI: 10.1103/PhysRevLett.101.191802. arXiv: 0808.2459 [hep-ex].

[412] S. Adler *et al.* "Measurement of the K+ –> pi+ nu nu branching ratio". In: *Phys. Rev. D* 77 (2008), p. 052003. DOI: 10.1103/PhysRevD.77.052003. arXiv: 0709.1000 [hep-ex].

[413] E. Cortina Gil *et al.* "Search for a feebly interacting particle X in the decay $K^+ \to \pi^+ X$". In: *JHEP* 03 (2021), p. 058. DOI: 10.1007/JHEP03(2021)058. arXiv: 2011.11329 [hep-ex].

[414] E. Cortina Gil *et al.* "Measurement of the very rare $K^+ \to \pi^+ \nu\bar{\nu}$ decay". In: *JHEP* 06 (2021), p. 093. DOI: 10.1007/JHEP06(2021)093. arXiv: 2103.15389 [hep-ex].

[415] J. Ahn *et al.* "Search for the $K_L \to \pi^0 \nu\bar{\nu}$ and $K_L \to \pi^0 X^0$ decays at the J-PARC KOTO experiment". In: *Phys. Rev. Lett.* 122.2 (2019), p. 021802. DOI: 10.1103/PhysRevLett.122.021802. arXiv: 1810.09655 [hep-ex].

[416] S. Alekhin *et al.* "A facility to Search for Hidden Particles at the CERN SPS: the SHiP physics case". In: *Rept. Prog. Phys.* 79.12 (2016), p. 124201. DOI: 10.1088/0034-4885/79/12/124201. arXiv: 1504.04855 [hep-ph].

[417] K. J. Kelly, S. Kumar, and Z. Liu. "Heavy axion opportunities at the DUNE near detector". In: *Phys. Rev. D* 103.9 (2021), p. 095002. DOI: 10.1103/PhysRevD.103.095002. arXiv: 2011.05995 [hep-ph].

[418] R. Aaij *et al.* "Search for hidden-sector bosons in $B^0 \to K^{*0} \mu^+ \mu^-$ decays". In: *Phys. Rev. Lett.* 115.16 (2015), p. 161802. DOI: 10.1103/PhysRevLett.115.161802. arXiv: 1508.04094 [hep-ex].

[419] R. Aaij *et al.* "Search for long-lived scalar particles in $B^+ \to K^+ \chi(\mu^+\mu^-)$ decays". In: *Phys. Rev. D* 95.7 (2017), p. 071101. DOI: 10.1103/PhysRevD.95.071101. arXiv: 1612.07818 [hep-ex].

[420] E. Masso and R. Toldra. "On a light spinless particle coupled to photons". In: *Phys. Rev. D* 52 (1995), pp. 1755–1763. DOI: 10.1103/PhysRevD.52.1755. arXiv: hep-ph/9503293.

[421] A. Bevan *et al.* "The Physics of the B Factories". In: *Eur. Phys. J. C* 74 (2014), p. 3026. DOI: 10.1140/epjc/s10052-014-3026-9. arXiv: 1406.6311 [hep-ex].

[422] E. Izaguirre, T. Lin, and B. Shuve. "Searching for Axionlike Particles in Flavor-Changing Neutral Current Processes". In: *Phys. Rev. Lett.* 118.11 (2017), p. 111802. DOI: 10.1103/PhysRevLett.118.111802. arXiv: 1611.09355 [hep-ph].

[423] M. J. Dolan, T. Ferber, C. Hearty, F. Kahlhoefer, and K. Schmidt-Hoberg. "Revised constraints and Belle II sensitivity for visible and invisible axion-like particles". In: *JHEP* 12 (2017), p. 094. DOI: 10.1007/JHEP12(2017)094. arXiv: 1709.00009 [hep-ph].

[424] W. Altmannshofer *et al.* "The Belle II Physics Book". In: *PTEP* 2019.12 (2019). Ed. by E. Kou and P. Urquijo. [Erratum: PTEP 2020, 029201 (2020)], p. 123C01. DOI: 10.1093/ptep/ptz106. arXiv: 1808.10567 [hep-ex].

[425] X. Cid Vidal, A. Mariotti, D. Redigolo, F. Sala, and K. Tobioka. "New Axion Searches at Flavor Factories". In: *JHEP* 01 (2019). [Erratum: JHEP 06, 141 (2020)], p. 113. DOI: 10.1007/JHEP01(2019)113. arXiv: 1810.09452 [hep-ph].

[426] P. deNiverville, H.-S. Lee, and M.-S. Seo. "Implications of the dark axion portal for the muon g-2, B-factories, fixed target neutrino experiments and beam dumps". In: *Phys. Rev. D* 98.11 (2018), p. 115011. DOI: 10.1103/PhysRevD.98.115011. arXiv: 1806.00757 [hep-ph].

[427] M. Gavela, R. Houtz, P. Quilez, R. Del Rey, and O. Sumensari. "Flavor constraints on electroweak ALP couplings". In: *Eur. Phys. J. C* 79.5 (2019), p. 369. DOI: 10.1140/epjc/s10052-019-6889-y. arXiv: 1901.02031 [hep-ph].

[428] L. Merlo, F. Pobbe, S. Rigolin, and O. Sumensari. "Revisiting the production of ALPs at B-factories". In: *JHEP* 06 (2019), p. 091. DOI: 10.1007/JHEP06(2019)091. arXiv: 1905.03259 [hep-ph].

[429] G. Lepage and S. J. Brodsky. "Exclusive Processes in Perturbative Quantum Chromodynamics". In: *Phys. Rev. D* 22 (1980), p. 2157. DOI: 10.1103/PhysRevD.22.2157.

[430] A. Szczepaniak, E. M. Henley, and S. J. Brodsky. "Perturbative {QCD} Effects in Heavy Meson Decays". In: *Phys. Lett. B* 243 (1990), pp. 287–292. DOI: 10.1016/0370-2693(90)90853-X.

[431] N. Satoyama *et al.* "A Search for the rare leptonic decays B+ —> mu+ nu(mu) and B+ —> e+ nu(nu)". In: *Phys. Lett. B* 647 (2007), pp. 67–73. DOI: 10.1016/j.physletb.2007.01.068. arXiv: hep-ex/0611045.

[432] M. T. Prim *et al.* "Search for $B^+ \to \mu^+ \nu_\mu$ and $B^+ \to \mu^+ N$ with inclusive tagging". In: *Phys. Rev. D* 101.3 (2020), p. 032007. DOI: 10.1103/PhysRevD.101.032007. arXiv: 1911.03186 [hep-ex].

[433] I. Adachi *et al.* "Evidence for $B^- \to \tau^- \bar{\nu}_\tau$ with a Hadronic Tagging Method Using the Full Data Sample of Belle". In: *Phys. Rev. Lett.* 110.13 (2013), p. 131801. DOI: 10.1103/PhysRevLett.110.131801. arXiv: 1208.4678 [hep-ex].

[434] B. Eisenstein *et al.* "Precision Measurement of $B(D^+ \to \mu^+ \nu)$ and the Pseudoscalar Decay Constant $f(D^+)$". In: *Phys. Rev. D* 78 (2008), p. 052003. DOI: 10.1103/PhysRevD.78.052003. arXiv: 0806.2112 [hep-ex].

[435] M. Ablikim *et al.* "Precision measurements of $B(D^+ \to \mu^+\nu_\mu)$, the pseudoscalar decay constant f_{D^+}, and the quark mixing matrix element $|V_{cd}|$". In: *Phys. Rev. D* 89.5 (2014), p. 051104. DOI: 10.1103/PhysRevD.89.051104. arXiv: 1312.0374 [hep-ex].

[436] M. Ablikim *et al.* "Determination of the pseudoscalar decay constant $f_{D_s^+}$ via $D_s^+ \to \mu^+\nu_\mu$". In: *Phys. Rev. Lett.* 122.7 (2019), p. 071802. DOI: 10.1103/PhysRevLett.122.071802. arXiv: 1811.10890 [hep-ex].

[437] M. Ablikim *et al.* "Measurement of the $D_s^+ \to \ell^+\nu_\ell$ branching fractions and the decay constant $f_{D_s^+}$". In: *Phys. Rev. D* 94.7 (2016), p. 072004. DOI: 10.1103/PhysRevD.94.072004. arXiv: 1608.06732 [hep-ex].

[438] M. Ablikim *et al.* "Observation of the leptonic decay $D^+ \to \tau^+\nu_\tau$". In: *Phys. Rev. Lett.* 123.21 (2019), p. 211802. DOI: 10.1103/PhysRevLett.123.211802. arXiv: 1908.08877 [hep-ex].

[439] A. Zupanc *et al.* "Measurements of branching fractions of leptonic and hadronic D_s^+ meson decays and extraction of the D_s^+ meson decay constant". In: *JHEP* 09 (2013), p. 139. DOI: 10.1007/JHEP09(2013)139. arXiv: 1307.6240 [hep-ex].

[440] C. Lazzeroni *et al.* "Precision Measurement of the Ratio of the Charged Kaon Leptonic Decay Rates". In: *Phys. Lett. B* 719 (2013), pp. 326–336. DOI: 10.1016/j.physletb.2013.01.037. arXiv: 1212.4012 [hep-ex].

[441] F. Ambrosino *et al.* "Measurement of the charged kaon lifetime with the KLOE detector". In: *JHEP* 01 (2008), p. 073. DOI: 10.1088/1126-6708/2008/01/073. arXiv: 0712.1112 [hep-ex].

[442] S. J. Brodsky and G. P. Lepage. "Large Angle Two Photon Exclusive Channels in Quantum Chromodynamics". In: *Phys. Rev. D* 24 (1981), p. 1808. DOI: 10.1103/PhysRevD.24.1808.

[443] E. Armengaud *et al.* "Searches for electron interactions induced by new physics in the EDELWEISS-III Germanium bolometers". In: *Phys. Rev. D* 98.8 (2018), p. 082004. DOI: 10.1103/PhysRevD.98.082004. arXiv: 1808.02340 [hep-ex].

[444] A. Berlin, N. Blinov, G. Krnjaic, P. Schuster, and N. Toro. "Dark Matter, Millicharges, Axion and Scalar Particles, Gauge Bosons, and Other New Physics with LDMX". In: *Phys. Rev. D* 99.7 (2019), p. 075001. DOI: 10.1103/PhysRevD.99.075001. arXiv: 1807.01730 [hep-ph].

[445] J. B. Dent, B. Dutta, D. Kim, S. Liao, R. Mahapatra, *et al.* "New Directions for Axion Searches via Scattering at Reactor Neutrino Experiments". In: *Phys. Rev. Lett.* 124.21 (2020), p. 211804. DOI: 10.1103/PhysRevLett.124.211804. arXiv: 1912.05733 [hep-ph].

[446] J.-F. Fortin, H.-K. Guo, S. P. Harris, D. Kim, K. Sinha, *et al.* "Axions: From magnetars and neutron star mergers to beam dumps and BECs". In: *Int. J. Mod. Phys. D* 30.07 (2021), p. 2130002. DOI: 10.1142/S0218271821300020. arXiv: 2102.12503 [hep-ph].

[447] W. Altmannshofer and D. M. Straub. "New physics in $b \to s$ transitions after LHC run 1". In: *Eur. Phys. J. C* 75.8 (2015), p. 382. DOI: 10.1140/epjc/s10052-015-3602-7. arXiv: 1411.3161 [hep-ph].

[448] S. Descotes-Genon, T. Hurth, J. Matias, and J. Virto. "Optimizing the basis of $B \to K^* ll$ observables in the full kinematic range". In: *JHEP* 05 (2013), p. 137. DOI: 10.1007/JHEP05(2013)137. arXiv: 1303.5794 [hep-ph].

[449] J. D. Hunter. "Matplotlib: A 2D graphics environment". In: *Computing in Science & Engineering* 9.3 (2007), pp. 90–95. DOI: 10.1109/MCSE.2007.55.

[450] C. R. Harris, K. J. Millman, S. J. van der Walt, R. Gommers, P. Virtanen, *et al.* "Array programming with NumPy". In: *Nature* 585.7825 (Sept. 2020), pp. 357–362. DOI: 10.1038/s41586-020-2649-2. URL: https://doi.org/10.1038/s41586-020-2649-2.

[451] P. Virtanen, R. Gommers, T. E. Oliphant, M. Haberland, T. Reddy, *et al.* "SciPy 1.0: Fundamental Algorithms for Scientific Computing in Python". In: *Nature Methods* 17 (2020), pp. 261–272. DOI: 10.1038/s41592-019-0686-2.

[452] W. McKinney *et al.* "Data structures for statistical computing in python". In: *Proceedings of the 9th Python in Science Conference*. Vol. 445. Austin, TX. 2010, pp. 51–56.

[453] H. Dembinski, P. Ongmongkolkul, C. Deil, D. M. Hurtado, H. Schreiner, *et al. scikit-hep/iminuit: v1.5.4*. Version v1.5.4. Nov. 2020. DOI: 10.5281/zenodo.4283509. URL: https://doi.org/10.5281/zenodo.4283509.

[454] F. James and M. Roos. "Minuit: A System for Function Minimization and Analysis of the Parameter Errors and Correlations". In: *Comput. Phys. Commun.* 10 (1975), pp. 343–367. DOI: 10.1016/0010-4655(75)90039-9.

[455] J. Fuentes-Martin, P. Ruiz-Femenia, A. Vicente, and J. Virto. "DsixTools 2.0: The Effective Field Theory Toolkit". In: *Eur. Phys. J. C* 81.2 (2021), p. 167. DOI: 10.1140/epjc/s10052-020-08778-y. arXiv: 2010.16341 [hep-ph].

[456] J. De Blas *et al.* "HEPfit: a code for the combination of indirect and direct constraints on high energy physics models". In: *Eur. Phys. J. C* 80.5 (2020), p. 456. DOI: 10.1140/epjc/s10052-020-7904-z. arXiv: 1910.14012 [hep-ph].

[457] D. van Dyk *et al.* "EOS – A Software for Flavor Physics Phenomenology". In: (Nov. 2021). arXiv: 2111.15428 [hep-ph].

[458] F. U. Bernlochner *et al.* "FlavBit: A GAMBIT module for computing flavour observables and likelihoods". In: *Eur. Phys. J. C* 77.11 (2017), p. 786. DOI: 10.1140/epjc/s10052-017-5157-2. arXiv: 1705.07933 [hep-ph].

[459] P. Athron *et al.* "GAMBIT: The Global and Modular Beyond-the-Standard-Model Inference Tool". In: *Eur. Phys. J. C* 77.11 (2017). [Addendum: Eur.Phys.J.C 78, 98 (2018)], p. 784. DOI: 10.1140/epjc/s10052-017-5321-8. arXiv: 1705.07908 [hep-ph].

[460] F. Pedregosa, G. Varoquaux, A. Gramfort, V. Michel, B. Thirion, *et al.* "Scikit-learn: Machine Learning in Python". In: *Journal of Machine Learning Research* 12 (2011), pp. 2825–2830.

[461] J. Alda. "imagWC GitHub code repository". Version v2.0. In: *Zenodo* (May 2019). DOI: 10.5281/zenodo.1160549. URL: https://github.com/Jorge-Alda/imagWC/tree/v2.0.

[462] J. Alda. "SMEFT19 GitHub code repository". Version v3.0.1. In: *Zenodo* (Dec. 2021). DOI: 10.5281/zenodo.5855926. URL: https://github.com/Jorge-Alda/SMEFT19/tree/v3.0.1.

[463] J. Alda. "SMEFT19-notebooks GitHub code repository". Version v1.0.1. In: *Zenodo* (Dec. 2021). DOI: 10.5281/zenodo.5859466. URL: https://github.com/Jorge-Alda/SMEFT19-notebooks/tree/v1.0.1.